A Study of the Reaction $\gamma d \to \pi^+\pi^- d$

(From Vector Mesons to Possible Dibaryons)

A dissertation presented to

the faculty of

the College of Arts and Sciences of Ohio University

In partial fulfillment

of the requirements for the degree

Doctor of Philosophy

Taya Chetry

May 2019

This dissertation titled

A Study of the Reaction $\gamma d \rightarrow \pi^+\pi^- d$

(From Vector Mesons to Possible Dibaryons)

by

TAYA CHETRY

has been approved for

the Department of Physics and Astronomy

and the College of Arts and Sciences by

Kenneth H. Hicks

Professor of Physics and Astronomy

Joseph Shields

Interim Dean, College of Arts and Sciences

Abstract

CHETRY, TAYA, Ph.D., May 2019, Physics and Astronomy

A Study of the Reaction $\gamma d \to \pi^+\pi^- d$ (From Vector Mesons to Possible Dibaryons) (224 pp.)

Director of Dissertation: Kenneth H. Hicks

The work presented in this thesis is based on the g10 experiment performed at the Hall B of the Jefferson Laboratory, where tagged photons with beam energies between 0.8 and 3.5 GeV were incident on a deuterium target. With three final state particles detected (two charged pions and a deuteron), various reaction channels can be studied. This work focuses on three of many possible processes using the same reaction sample:

$$\gamma d \to \begin{cases} \rho d \to \pi^+\pi^- d, \\ \omega d \to \pi^+\pi^- d(\pi^0), \\ N\Delta \equiv d^*\pi^\pm \to \pi^+\pi^- d. \end{cases} \tag{0.1}$$

The first two channels deal with the photoproduction of vector mesons. Differential cross sections as a function of the momentum transfer, t, are calculated for various photon energies. Using a phenomenological model based on the theory of Vector Meson Dominance, the Vector Meson-Nucleon scattering cross section (σ_{VN}) were extracted for ω and ρ.

The third reaction, on the other hand primarily focuses on the production of possible dibaryon resonances. This work establishes the possibility of three dibaryonic charge states (possible $N\Delta$ configuration) and presents a preliminary differential cross section for one of the charged states.

Dedication

To my best friend and wife,

GORI

Acknowledgements

This dissertation has been the most significant academic challenge I have ever had to face. Without the support, patience and guidance of the following people, this study would not have been possible. It is to them who I owe my deepest gratitude.

First, I would like to express my sincere gratitude to my advisor Dr. Kenneth Hicks, whose wisdom, knowledge and commitment to the highest standards always inspired and motivated me. His continuous support and guidance helped me in all the time during my research and writing of this thesis. I still remember our first meeting on the 24th of March 2014 at 1 pm in his office, where we talked about possible research areas using the CLAS data. It was one of the inspirational moments of my life, where I strongly felt optimism about my future and career. I always believed in *plan-your-work-work-your-plan* attitude. He was a perfect example. In fact, he is the most organized person I have ever met. Dr. Hicks is also very patient towards his students. He never rushed my learning process and let my understanding grow at my own pace. Our discussions helped me to understand a great deal about the CLAS detector and the underlying physics of the research projects I accomplished during the last five years at Ohio University (OU). He strongly believed in exposing ongoing research at different conferences and therefore provided various opportunities to present my work at these platforms. Besides academic help, he understood that being away from home is difficult and appreciated my effort as an international student in the US and offered help in various forms. I cannot imagine having a better advisor and mentor than him. Thank you, Dr. Hicks!

I would also like to thank the rest of my dissertation committee: Prof. Julie Roche, Prof. Zachary Meisel and Prof. Eric Masson, for their insightful comments and encouragement, but also for the questions that incentivized me to widen my research from various perspectives. I want to thank Prof. Madappa Prakash for his wonderful feedback when I presented my proposal for the dissertation. Due to time conflicts, he could not

be on my committee and Dr. Meisel was kind enough to agree to be on my committee even on a short notice. I would especially like to acknowledge Dr. Julie Roche for her encouragement. As my teacher, she has taught me more than I could give her credit for here. She has shown, by her example, what a good scientist (and person) should be.

For my understanding of physics and the approaches I developed to solve problems, I am grateful to all the instructors of various Physics courses at OU and Tribhuvan University (TU), Nepal. I want to acknowledge Prof. Raju Khanal (TU), my advisor and mentor for my M.S. thesis, who introduced me to research and instilled in me its importance in our understanding of matter (plasma). I am grateful to Dr. Daniel Phillips (OU), who inspired me to be a disciplined teacher, who works hard and inspires the students to do the same. Without the support and encouragements from Profs. Mark Lucas, Horacio Castillo, Paul King, I would not be as confident as I am. Thank you, my teachers!

Physics students know how to work hard and have fun at the same time. Extended hours of graduate course work can make anyone insane, and my friends helped me to be less crazy (pun intended). I want to thank my friends at OU, Mamun, Oscar, Zhejie (*Jerry*), Sudhanva, Rajib, Tyler and Nick, for their unparalleled help and support throughout my Ph.D. Thank you, my friends!

Nobody has been more important to me in the pursuit of this degree than my family. I would like to thank my mother (*aama*), my brother (*dada*) and my sisters (*didi-haru*), whose love and guidance were with me in every step. I am here because of them. I am also grateful to my brother-in-law, Jhala Neupane (*bhai*), for his unfaltering support and love.

Last but not the least, I want to thank with all my heart to my loving wife, my best friend, Purnima Neupane (*gori*), for all the unwavering support at every stage of my life since we first me. She is my unending inspiration. Even at the most difficult time, she was there for me; her encouragement and boosting talks made me going. It is to her, I dedicate this dissertations. I love you *gori*!

Table of Contents

List of Tables

Table Page

List of Figures

Figure Page

1 Introduction

From philosophers to scientists, the quest for an understanding of the basic building blocks of matter and their interactions has captivated their interests for centuries. In fact, one of the forefronts of fundamental research at present is to understand the constituents of matter and their interactions. Initially, the atom was taken as the basic structure, but was found to actually consist of electrons and nucleons (protons and neutrons). With the advancements in experimental techniques, many subatomic particles were discovered and it is well established now that even the nucleons are made up of smaller constituents, quarks and gluons. The interaction between these entities, however, is still not completely understood. The best of our current understanding can be encapsulated in a theory, Quantum Chromodynamics (QCD), that deals with the strong force mediated by the gluons between quarks [Gri08].

QCD has been a very successful tool, especially in the high energy regime, where approximations and perturbative approaches can be used. Despite its success in the perturbative regime, the approximate methods do not completely describe the structure of the nucleon, for example, or other low energy phenomena. Therefore, the spectrum of the nucleon cannot be calculated analytically, and must be explored using empirical measurements of certain observables describing the properties of the nucleons coupled with phenomenological models. These tools and models that physicists resort to complement QCD and hence add to our understanding about the basic constituents of matter.

This chapter will start with a brief overview of the QCD along with its limitations. Information on some tools, such as the hadron spectroscopy, using photoproduction to get an insight at the non-perturbative QCD regime. The discussion will then follow to a historical overview of photoproduction reactions involving vector mesons and a phenomenological model of the Vector Meson Dominance. Furthermore, motivation for

the need for extraction of the differential cross section[1] for vector mesons ρ and ω in this thesis will be discussed. Historical evidence of some exotic resonances will also be compiled towards the end in this chapter.

1.1 Quantum Chromodynamics (QCD)

QCD is a theory that describes the action of the strong force, one of the four fundamental forces of nature along with electromagnetic, gravitational and the weak nuclear force. It was constructed in analogy to Quantum Electrodynamics (QED), the low energy manifestation of the fundamental theory of electromagnetism. The photon is described in QED as a massless force-carrier vector boson that transmits the electromagnetic force between charged particles (electrons, protons, etc.). By the same token, QCD predicts the existence of force-carrier particles called gluons, also massless vector bosons, which transmit the strong force between quarks, gluons or both. Quarks are fundamental in the sense that they are not made up of smaller particles. They come in six different flavors, occurring in pairs, or generations. Table 1.1 shows some quantum numbers associated with the different quark flavors.

[1] The differential cross section is defined as an effective area of collision between two particles. It is in proportion to the probability by which a given reaction will occur at a certain energy and scattering angle (sometimes defined in terms of other variables such as the momentum transfer, t). This probability provides an insight into the production mechanism for any intermediate or final states. The differential cross section for pion beam experiments is on the order of millibarns, while photoproduction experiments are generally on the order of microbarns.

Table 1.1: The family of the quarks, their flavors and approximate constituent masses in GeV/c^2 along with their electric charges Q in units of e as quoted in [MS08]. Also shown are the values of baryon number B, strangeness S, charm C, bottom $\tilde{B}$ and top T. The values for the corresponding antiquarks are equal in magnitude, but opposite in sign.

Generation	**Flavor**	**Mass**	$\boldsymbol{Q}$	$\boldsymbol{B}$	$\boldsymbol{S}$	$\boldsymbol{C}$	$\boldsymbol{\tilde{B}}$	$\boldsymbol{T}$
First	d	$m_d \approx 0.3$	$-1/3$	$1/3$	0	0	0	0
	u	$m_u \approx 0.3$	$2/3$	$1/3$	0	0	0	0
Second	s	$m_s \approx 0.5$	$-1/3$	$1/3$	-1	0	0	0
	c	$m_c \approx 1.5$	$2/3$	$1/3$	0	1	0	0
Third	b	$m_b \approx 4.5$	$-1/3$	$1/3$	0	0	-1	0
	t	$m_t \approx 174$	$2/3$	$1/3$	0	0	0	1

QCD has three types of charge as opposed to the single type found in electromagnetism, referred to as the red, green and blue which are collectively called the color charge, hence the name QCD. Each quark carries a color charge, an electric charge, a mass and also a weak charge. Antiquarks have the opposite color charge of quarks, referred to as anti-red, anti-green and anti-blue, along with the opposite electric charge. Unlike a photon, a gluon carries the color charge. Therefore, interactions in QCD can be categorized into two groups - a quark emitting/absorbing a gluon ($q - g$ interaction) and a gluon emitting/absorbing a gluon ($g - g$ interaction). The direct $g - g$ coupling makes QCD a lot more complicated than QED. Virtual gluons in the quantum vacuum carry color charge that influences the effective color charge. This property of the gluons gives rise to the phenomena of the asymptotic

freedom[2] and the confinement[3]. This complication has led to the development of a number of techniques for obtaining approximate solutions to the full theory. At very high energies, the strong force becomes weaker and perturbative techniques can be applied (perturbative QCD, Deep Inelastic Scattering) [GS94]; however, at medium low energies, orders of a few GeV, perturbative techniques fail to describe the behavior of quarks and gluons. In the absence of analytical answers, experimental advancements play a significant role in investigating nucleon systems. Input from cross sections from reactions off of a nucleon with certain final states are useful to phenomenological models.

1.1.1 Hadrons

The particles that consist of the quarks and the gluons are called as the hadrons. The general classification of the hadrons consists of particles that interact strongly. The particles are categorized into two main groups: baryons and mesons. Baryons (anti-baryons) are relatively massive particles which are made up of three quarks[4], qqq ($\bar{q}\bar{q}\bar{q}$) in the Standard Model[5]. Baryons are distinct from mesons in that mesons are composed of a quark-antiquark ($q\bar{q}$) pair. Baryons are fermions, while the mesons are bosons.

Other than the two types of hadrons that are fairly observed, in principle, QCD allows hadrons made of two quarks and two antiquarks (tetraquarks: $qq\bar{q}\bar{q}$), four quarks and an antiquark (pentaquarks: $qqqq\bar{q}$), six quarks (hexaquarks or dibaryons: $qqqqqq$) and

[2] At short distances, or equivalently at high energies or momentum transfers, the quarks behave as if they are asymptotically free. This means that the strong coupling constant, α_s, which is a measure of the strength of the strong force, vanishes asymptotically at short distances. In other words, the force between two quarks becomes small when they move close together but grows large when they move apart.

[3] It is the phenomenon that the quarks and gluons cannot be isolated, and therefore cannot be directly observed in normal conditions.

[4] A set of quarks that provide the quantum numbers associated with the hadrons are referred to as the 'valence quarks'. The gluons, like photons, are the quanta of the 'color' field. Also, there is large number of quark-antiquark pairs, not contributing to the quantum number of the hadron, are known as the 'sea quarks'. The quarks (antiquarks) used in the text are the valence quarks (antiquarks).

[5] Around 1970, a theory of fundamental particles and how they interact was formulated, that not only incorporated all that was known at the time but at the same time helped in the prediction of the existence of additional particles. The theory was named the Standard Model of Particle Physics.

infinitely many other configurations. Recently, physicists studying the spectrum of heavy mesons formed with charm and bottom quarks have uncovered evidence that supports the existence of tetraquark (a list of experiments are provided in a table in Reference [A$^+$17]) and pentaquark hadrons [A$^+$15a]. Dibaryons are discussed later in the chapter.

1.1.2 Hadron Spectroscopy

In atomic spectroscopy, the electromagnetic interactions that bind electrons to the nucleus is studied. Similarly, hadron spectroscopy focuses on the QCD interactions ($g - q$ or $g - g$) between quarks and/or gluons. Energetic collisions by particle accelerators can create hadrons, that potentially decay into other hadrons. These hadronic decays enable us to measure many properties such as the mass, charge, angular momentum or some useful physical observables such as the cross sections, etc. These observables provide insight into a better understanding of the QCD.

There are several ways to inject energy into hadrons. Much of our knowledge about nucleons came from pion-beam experiments, which provided an initial look at the field. This was preferred as it provided larger cross sections (typically in millibarns). However, the number of observables extracted were limited in such experiments. Therefore, physicists started to rely on methods such as the electro- and the photoproduction experiments, which enabled the extraction of many polarization variables, providing an insight to not only intermediate hadronic states but also the study of other indirect vector meson beam experiments, which would not be possible otherwise due to their short lifetimes.

Photoproduction has become a powerful tool to study the structure of hadrons. An initial state hadron is bombarded with photons which interact with the constituents (quarks) via electric charge or magnetic moments enabling the study of several final states possibilities. For a scattering reaction such as $\gamma + 2 \rightarrow 3 + 4$, the kinematics

of the interactions can be best described by three Mandelstam variables. These are sometimes referred to as the Mandelstam channels depending on the kinematics, as shown in Figure 1.1. These channels represent different Feynman diagrams where the interaction involves the exchange of an intermediate particle whose squared four-momentum equals s, t and u, respectively.

An s-channel interaction represents a nucleon resonance while the t-channel represents an interaction where most of the momentum of the photon is transferred to the intermediate mesons (in photoproduction experiments). The u-channel is another type where the momentum transferred to the baryon is maximum. Mathematically, these momentum transfers can be written as

$$s = (p_\gamma + p_2)^2 = (p_3 + p_4)^2$$
$$t = (p_\gamma - p_3)^2 = (p_2 - p_4)^2$$
$$u = (p_\gamma - p_4)^2 = (p_2 - p_3)^2,$$

where p_i is the four momentum corresponding to particle i. During photoproduction, many processes involving these channels are seen in the experiments. With certain experimental techniques, it is possible to tap out major channels to be studied separately. In this work, the vector meson photoproduction is studied primarily using the t-channel, while the dibaryon resonances are investigated as an s-channel process.

1.2 Vector Meson Photoproduction

Vector mesons are mesons with total spin 1 and odd parity ($J^P = 1^-$). These have been seen in experiments since the 1960s. The ρ-meson was discovered first, in 1961 [EMWW61], and the ω, ϕ and K^* mesons were found shortly thereafter. Around that time, Vector Meson Dominance (VMD), introduced by J. J. Sakurai [Sak60], became a fundamental concept in the understanding of the photon interaction with hadrons. As

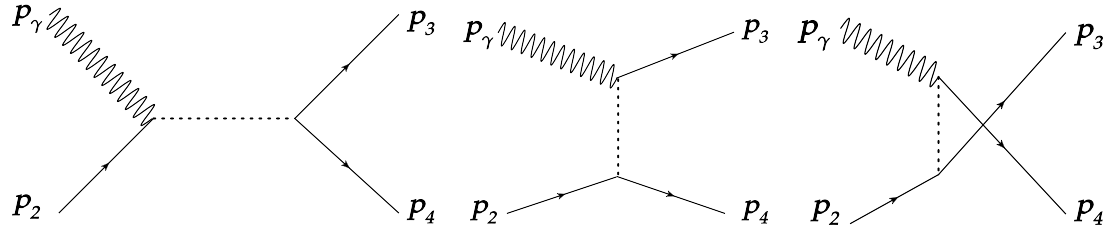

(a) s-channel. (b) t-channel. (c) u-channel.

Figure 1.1: The three Mandelstam Channels. Vector meson production is represented by the t-channel while the s-channel represents the resonance production.

photons have the same spin-parity as the vector mesons, VMD treats them as equivalent to a superposition of the strongly interacting vector mesons.

To make the concept clear, consider an analogy to QED where the photon is thought of as making repeated virtual transitions to electron-positron pairs such that the presence of a massive charged body nearby absorbs the necessary momentum transfer causing the e^-, e^+ pair to materialize as real particles. Similarly, the photon can be thought of as making repeated virtual transitions to vector meson states and in the presence of an appropriate "charged" massive body (which can absorb the necessary momentum transfer) can materialize the vector mesons. The charge in VMD is equivalent to the strength of the vector meson coupling to it (see Figure 1.2).

For a coherent photoproduction of vector mesons (V) from an unpolarized deuterium target, given by

$$\gamma + d \rightarrow V + d \tag{1.1}$$

the corresponding amplitudes can have two pieces. The first is the single scattering term, related to the production of vector mesons off of one nucleon, while the second term is related to the double scattering, where the interaction of the photon with one of the nucleons inside deuterium produce an intermediate virtual vector meson, which then re-scatters from

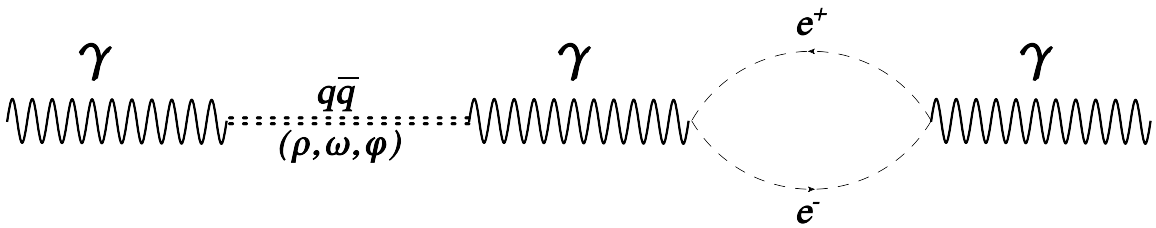

Figure 1.2: Different fluctuations of a photon in terms of the $q\bar{q}$ transition in QCD and a e^+e^- pair loop is shown in this conceptual diagram. The $q\bar{q}$ can scatter as a light vector meson in appropriate conditions mentioned in the text. Similarly in the presence of external massive charged object, the e^+e^- pair can be materialized.

the other nucleon forming the final state V. These are shown with the help of Feynman diagrams in Figure 1.3.

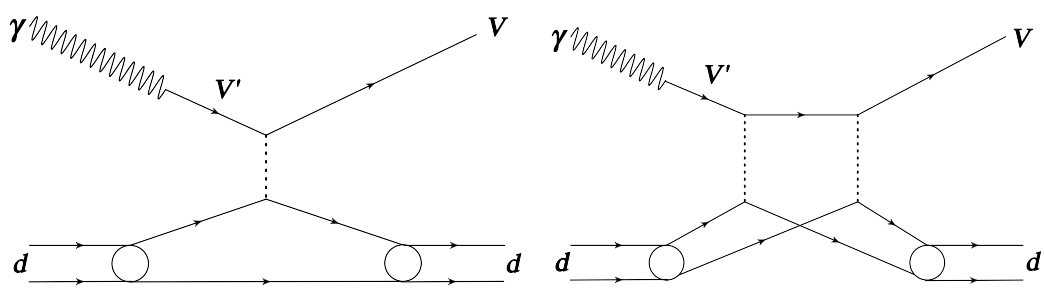

Figure 1.3: The two interactions during the photoproduction of a vector meson using a deuterium target.

At intermediate and high energies, the exclusive photoproduction of vector mesons is dominated by single scattering. This is well understood in terms of the VMD. At low energies (or large momentum transfer[6], $Q^2 >> 1$ GeV^2), the contributions from re-

[6] If $\vec{q}$ is the momentum of a photon with energy E_γ, then the momentum transfer between the photon and the vector meson is given by $Q^2 = -|\vec{q}|^2$. This is equivalent to the Mandelstam t for this process.

scattering increases [FKM+97]. Therefore, at the energy scales of this work, the increased magnitude of the double scattering contribution enables the study of the vector meson-nucleon ($V - N$) interaction, which is otherwise not possible by direct techniques.

A phenomenological model on the vector meson photoproduction is outlined in Reference [FKM+97], where the vector meson production amplitude was derived within the eikonal approximation[7]. As the vector mesons are produced either from the proton or the neutron, a non-relativistic treatment of the deuteron target and the final pn system gives the single scattering amplitude,

$$F^{(single)} = f^{\gamma^* p \to Vp} \left(S_{df}^{jj'} \right)_p + f^{\gamma^* n \to Vn} \left(S_{df}^{jj'} \right)_n , \tag{1.2}$$

where f refers to the photon-nucleon production amplitude explicitly written for proton, p, and neutron, n; and S is the non-relativistic transition form factor. The spin quantum numbers for the deuteron wave function is represented by j, while j' is the same for the final pn system.

Another piece of the scattering amplitude, F^{double}, can be derived by considering the production of the vector meson via an intermediate hadronic state h along with the inclusion of the terms representing the recoil of the two-nucleon final state. The derivation was done on the assumption that the diffractive amplitudes f solely depend on transverse momentum transfers. For the double scattering, the amplitude reduces to the conventional approach of the Glauber model [FG66], where the recoil of the final pn system was not included by ignoring the intermediate hadronic state and replacing the transition of the virtual photon to the intermediate hadron by a vector meson. The vector meson production amplitude can then be calculated by taking into account for all possible intermediate hadronic states [FKM+97].

[7] This method is an approximate approach to solve scattering equations where the multi-variate differential equation is reduced to a single variable equation.

The model used in this work is based on the above outline, which allows to extract total cross section for the VN scattering, σ_{VN}. The scattering amplitude of $\gamma N \to VN$ is given by,

$$f^{\gamma N \to VN} = \sigma_{\gamma^* V}(i + \alpha_{\gamma N})e^{\frac{-b_{\gamma N}}{2}t}, \tag{1.3}$$

that deals with the single scattering. Here b is the slope of the diffractive process involved. A similar equation can be also written for the scattering amplitude of $VN \to VN$ that measures the contribution of the rescattering [FKM+97]. The quantity $\sigma_{\gamma^* V}$ is the differential cross section of $\gamma N \to VN$ reaction at $t = 0$. The initial guess for this parameter can be made using published differential cross section results from photoproduction data (for $V \equiv \rho, \omega$) on proton targets. At intermediate and higher photon energies, VMD assumes the slope factors of the corresponding amplitudes, $b_{\gamma N}$ and b_{VN}, to be equal. The variables, $\alpha_{\gamma N}$ and α_{VN}, are defined as the ratio of the real to imaginary parts of the corresponding scattering amplitudes. In general, the real part of the scattering amplitudes for proton and neutron targets are not exactly the same. Therefore these parameters are varied in the model according to the reaction channel under investigation. For the ωN interaction, for example, these can be kept fixed at a phenomenological value since ω production from d is dominated by isospin averaged amplitudes [FKM+97]. The quantity σ_{VN} can then be extracted using fits to the experimental differential cross section in the double scattering region ($|t| \gtrsim 0.5$ GeV^2). This model has already been successful in describing the ρ-photoproduction data from SLAC [A+71, FKM+97] and ϕ-photoproduction using the g10 data ([M+07]) off of deuterium target.

Along with the understanding some of the theories relevant to this thesis, it is quite useful to review some experimental progress made in the past. The following subsections briefly address some of them.

1.2.1 Previous Experimental Results on ρ-Photoproduction

One of the main results for the differential cross section measurements for the coherent photoproduction of ρ-meson off deuterium, $\gamma d \rightarrow \rho d$, was studied at the Stanford Linear Accelerator Center (SLAC) where data was taken for incident photon energies of 6, 12, and 18 GeV [A$^+$71]. The study was for the values of the four-momentum transfer t from -0.15 to -1.4 (GeV$/c)^2$. They interpreted their results based on Glauber theory [FG66] which was found to be in good agreement.

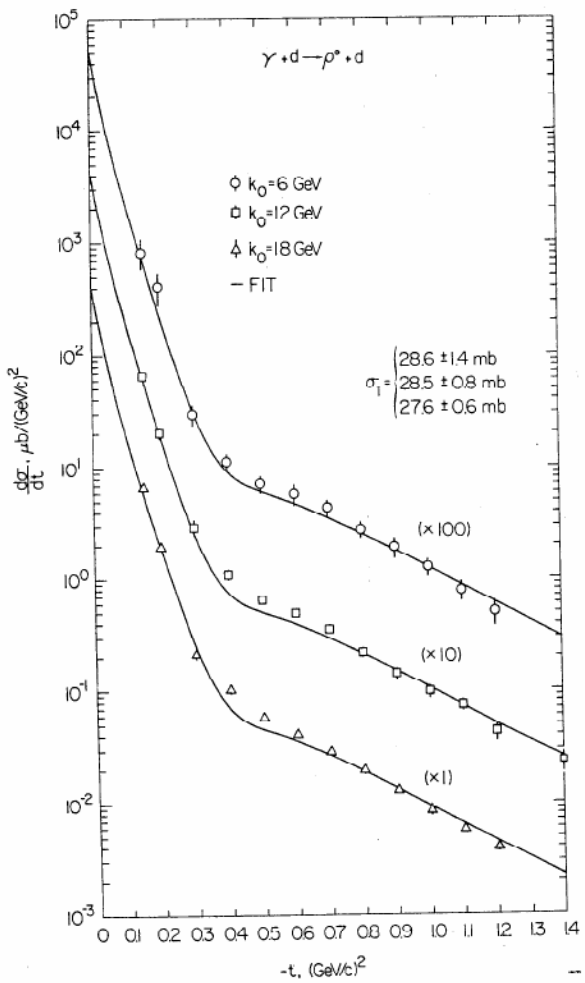

Figure 1.4: Cross sections measured at SLAC at 6, 12 and 18 GeV are plotted as $d\sigma/dt$ in $\mu b/(\mathrm{GeV}/c^2)$ versus $|t|$ in (GeV/c^2). The corresponding value of the total ρ^0-nucleon cross sections $\sigma_T(\rho^0 N)$ are also shown. Image source: [A+71]. License number: RNP/19/JAN/010675.

The observed t-dependence is characteristic for an elastic process on deuterium; the data consisted of a single-scattering region where the cross section decreases rapidly with increasing $|t|$, a flattening out around $t = -0.5$ $(\mathrm{GeV}/c)^2$ where the interference terms and the contributions from the D state in deuterium are important, and then finally for $|t| \gtrsim 0.5$

$(\mathrm{GeV}/c)^2$ a region where the cross section is dominated by contributions from the double-scattering terms. These results can be seen in Figure 1.4. The solid line is a least square fit of the form Ae^{Bt+ct^2} (A, B, C are fit parameters) to the data including the interference term between the single- and double-scattering amplitudes.

Most of the experiments performed to measure the photoproduction observables for ρ-meson photoproduction are only performed at relatively higher photon energies and studied at low momentum transfer (Behrend *et. al.*[BLTW70], P. Bapu *et. al.* [B$^+$77], P. Benz *et. al.* [B$^+$74]). These investigations all use energies much higher beam energies than the vector meson production threshold and were limited in statistics and precision. In other words, data for $E_\gamma < 6$ GeV and $t \geq 0.4$ GeV$^2/c^2$ is limited. Therefore, extension of these studies to lower photon energy and higher momentum transfer will contribute to world data and improve knowledge of the underlying physics.

1.2.2 Previous Experimental Results on ω-Photoproduction

Omega photoproduction off deuterium is yet another interesting channel. Few studies on this vector meson have so far been done. Gupta *et. al.* studied $\gamma + d \rightarrow \omega + d$ at 5.5 GeV photon energy at SLAC in 1976 [G$^+$76]. However, due to low statistics they were unable to make a mass fit, although there were indications of ω production in the mass distributions. In fact, the best data on the reaction $\gamma d \rightarrow \omega d$ were from the Weizmann Institute, that used a 4.3 GeV photon beam at $|t| < 0.2$ GeV^2. Again, it failed to see the double scattering effects. A list of bubble chamber experiments is shown in Table 1.2. As can be seen, that no data could extract $\sigma_{\omega N}$ because of limited statistics in higher $|t|$.

Table 1.2: A table summarizing a list of experiments on ω meson photoproduction. Table source: [BSYP78]. License Number: RNP/19/JAN/010676.

Experiment	Energy [GeV]	Target	Measured observables	$\sigma_{\omega N}$ [mb]	Assumptions	Comments
SLAC-Berkeley Ballam *et al.* (1973)	9.3	H	$\frac{d\sigma}{dt}$	-	$\sigma_{\omega N} = 27$ mb $\alpha_{\omega N} = -0.24$ $\frac{d\sigma}{dt}\|_{t=0} = 11.4\pm2.1\ \mu$b	No corrections for A_2 exchange
Rochester Abramson *et al.* (1976)	8.3	D, Be, C, Al, Cu, Pb	$\frac{d\sigma}{dt}\|_{t=0}$	25.4±2.7	$\alpha_{\omega N} = -0.24$	Corrected for A_2 exchange
Tel Aviv Alexandar *et al.* (1975)	7.5	D	$\frac{d\sigma}{dt}\|_{\omega}$	-	$\sigma_{\omega N} = 27$ mb $\alpha_{\omega N} = -0.24$	-
Pisa-Bonn Braccini *et al.* (1970)	5.7	C, Al, Zn, Ta, Ag, Pb	Smeared cross section	27.0±5.7	$\alpha_{\omega N} = -0.3$	Poor t resolution Huge uncertainty.
Weizmann Eisenberg *et al.* (1976)	4.3	D	$\frac{d\sigma}{dt}\|_{\omega}$ $\frac{d\sigma}{dt}\|_{\rho}/\frac{d\sigma}{dt}\|_{\omega}$	-	$\sigma_{\omega N} = 27$ mb $\alpha_{\omega N} = -0.24$	-
Harvard - CEA Gladding *et al.* (1973)	4.2	H	$\frac{d\sigma}{dt}\|_{\omega}$ $\frac{d\sigma}{dt}\|_{\rho}/\frac{d\sigma}{dt}\|_{\omega}$	-	The ratio of forward amplitudes for the two vector mesons is equal to the ratio of their differential cross sections	No correction for A_2 exchange
ABHHM Benz *et al.* (1974)	1.3-5.3	D	$\sigma_{\rho,\omega}$ $\sigma_{\rho}/\sigma_{\omega}$	-	The ratio of forward amplitudes for the two vector mesons is equal to the ratio of their differential cross sections	-
Lancaster Morris *et al.* (1976)	3.9	D	$\frac{d\sigma}{dt}\|_{\rho,\omega}$		The ratio of forward amplitudes for the two vector mesons is equal to the ratio of their differential cross sections	Poor resolution experiment

The world data lacks differential cross-section for ω-photoproduction as a function of momentum transfer. Also, photoproduction off proton targets are only studied [B$^+$03]. Therefore, a study of photoproduction observables in $\gamma d \rightarrow \omega d$, as done in this thesis, will provide a completely new set of results which can be used to extract $\omega - N$ scattering cross-sections.

1.2.3 Vector mesons from the Lattice

Due to non-linear nature of the strong force and large coupling constant at low energies, perturbative solutions in low energy QCD fails. A completely different approach to investigate QCD of quarks and gluons non-perturbatively has now been well established. This is a lattice gauge theory known as the Lattice QCD (LQCD). In LQCD, quark and gluon fields are defined at the lattice sites and their links respectively. This lattice may have some finite size, which is later approximated to approach continuum QCD by reducing the spacing between the lattice sites to zero. Basically, LQCD can solve QCD. Interestingly, the biggest problem with LQCD is not related to the physics but is limitations of current technology. The computational cost of numerical simulations increases with the decrease in the lattice spacing. Nonetheless, within certain assumptions and limits, it is possible to extract meson-meson scattering phase shifts directly using lattice calculations [WBnD$^+$15]. Recently the Hadron Spectroscopy Collaboration have presented very promising results by determining elastic and coupled-channel amplitudes for isospin-1 meson meson scattering in the P-wave using lattice QCD [WBnD$^+$15]. In this work, they were able to reproduce the ρ resonance by investigating the energy dependence for the phase shift in the elastic $\pi\pi$ scattering region. Therefore, it is timely to measure σ_{VN} experimentally that can be verified by LQCD in the future.

1.3 Dibaryon Resonance

A dibaryon in strict sense just denotes any object with baryon number, $B = 2$. In this sense, the first and the simplest dibaryon is the deuteron discovered in 1932 [UBM32]. A dibaryon is composed of six valence quarks. It may be of molecular type, like deuteron, with two quark bags (protons and neutrons) or in exotic sense all six quarks in a single quark bag. Usually, its the latter definition that is used whenever the term is used.

Dibaryons have a long outstanding history where many experimental claims for a discovery could not be verified when carefully repeated. There has been a renewed interest recently after lattice QCD calculations [BCD$^+$11, IIA$^+$11] provided evidence for a bound H-dibaryon which Jaffe predicted in 1977 [Jaf77] (using the quark bag model) that gluon-exchange forces can bind six quarks to form a stable 'dihyperon' at 2150 MeV and 2335 MeV in the $\Lambda\Lambda$ invariant mass plots. In the absence of any experimental evidence, the verification of this resonance is still pending.

In the paper on the quark model [GMZ61], Gell-Mann showed that QCD does not prohibit colorless multiples of three quarks. Based on this, Dyson and Xuong [DX64] demonstrated that a multiplet of six non-strange dibaryon states can be denoted by D_{IJ} with IJ = 01, 10, 12, 21, 03, 30, where I is the isospin and J is the spin of the resonance state. They formulated a mass formula for these states listed in Table 1.3.

Table 1.3: The summary of the prediction of Dyson and Xuong about a sextet of non-strange dibaryon states based on SU(6) symmetry. The states are denoted by D_{IJ} , where I denotes the isospin and J is the total spin of the state. The associated asymptotic baryon-baryon (BB) configurations and the masses calculated from their mass formulae are also shown. They identified $M = A + B\,[I(I+1) + J(J+1)]$ with the NN threshold at 1876 MeV, $B \approx 47$ MeV was found based on previous measurements.

Dibaryon	I	J	BB configuration	Mass formula	Predicted Mass [MeV]
D_{01}	0	1	deuteron	A	1876
D_{10}	1	0	NN virtual state	A	1876
D_{12}	1	2	$N\Delta$	$A + 6B$	2160
D_{21}	2	1	$N\Delta$	$A + 6B$	2160
D_{03}	0	3	$\Delta\Delta$	$A + 10B$	2350
D_{30}	3	0	$\Delta\Delta$	$A + 10B$	2350

In the pp elastic scattering using the reaction $\pi^+ d \rightarrow pp$ by the SAID data analysis group [ASWB93], a prominent resonance pole was seen in the $^1D_2$ wave. The partial wave analysis performed on the data confirmed the structure at $2148 - i63$ MeV, where the total scattering cross section σ_{total} for the $^1D_2$ pp state was consistent with the sum of the inelastic pp cross section, σ_{in} and the one extracted from $\pi^+ d$, $\sigma_{\pi d}$ (see Figure 1.5). Although the theoretical interpretation were inconclusive because of larger width and the peak being right at the $N\Delta$ threshold [Hos92, Hos93], it calls upon more studies investigate the $^1D_2$ resonance.

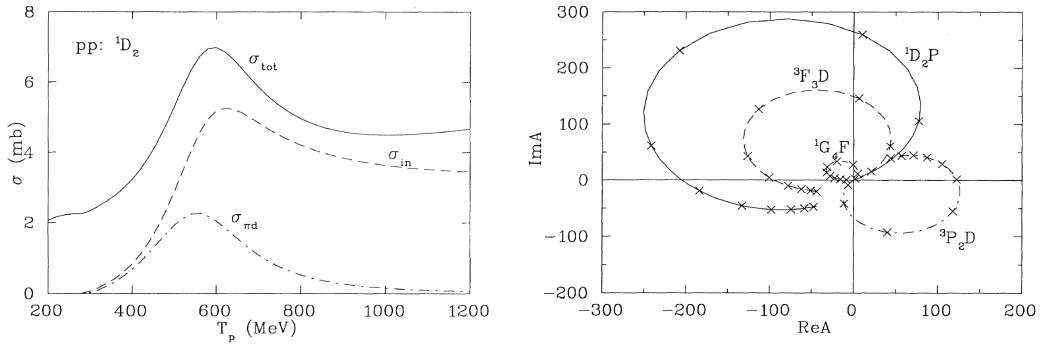

(a) (b)

Figure 1.5: The partial cross section of $^1D_2$ pp state in (a). An Argand diagram of the selected partial-wave amplitudes is shown in (b) exhibiting a pronounced looping. Image source: [ASWB93]. License Number: RNP/19/JAN/010677.

A series of studies performed by the WASA-at-COSY Collaboration establishes the resonance structure in two-pion production as a genuine s-channel resonance in the proton-neutron system [A$^+$11, A$^+$13, ea14]. They studied an exclusive double-pionic fusion reaction $pn \to d\pi^0\pi^0$ over full energy region of the Abashian-Booth-Crowe (ABC) effect and found that the cross-section is consistent with a narrow resonance at 2370 GeV. They reported the width of about 70 MeV and $I(J^P) = 0(3^+)$ in both pn and $\Delta\Delta$ systems. The total cross section is shown in Figure 1.6. The dynamic decay properties of this state point to an asymptotic $\Delta\Delta$ configuration that was predicted by Dyson and Xuong.

The g10 data uses the reaction $\gamma d \to \pi^+\pi^- d$ to study possible resonance states. The spins of the initial state photon, $J = 1$ and deuteron, $J = 1$ can be combined to have possible $J = \{0, 1, 2\}$, while the isospins can be combined to get a set $I = \{0, 1\}$ in the final state suggesting a possibility of studying an $N\Delta$ configuration for the D_{12} state.

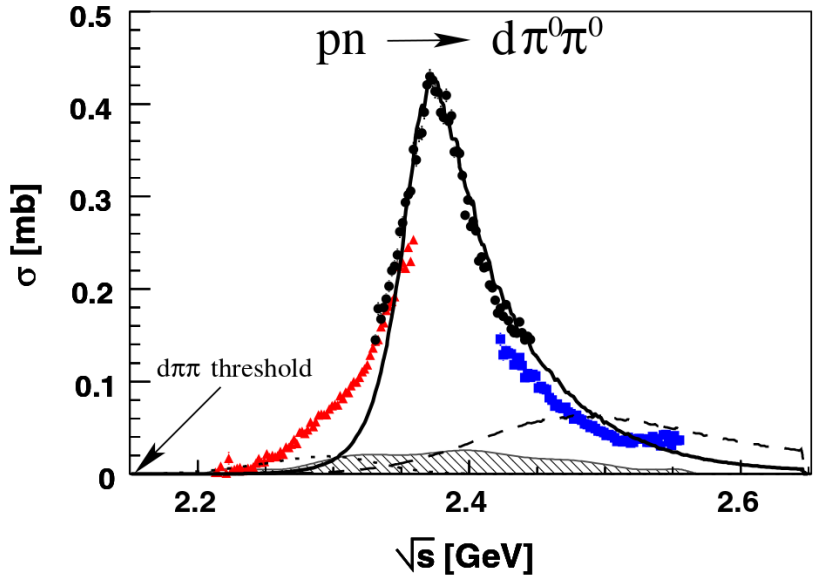

Figure 1.6: The total cross-sections for $pd \rightarrow d\pi^0\pi^0 + p_{spectator}$ for the independently normalized beam energies 1.0 GeV (triangles), 1.2 GeV (dots), and 1.4 GeV (squares). The systematic uncertainties are shown by the hatched area. Expected cross sections a Roper excitation process is shown by the dotted line while the dashed line is from the calculations considering the contributions from the t-channel $\Delta\Delta$ interaction. The solid line is the calculation using $m = 2370$ MeV and width of 68 MeV for a s-channel resonance. Image source: [A$^+$11]. License Number: RNP/19/JAN/010678.

1.4 Summary

The reaction $\gamma d \rightarrow \pi^+\pi^- d$ offers a unique opportunity to gather insight into light vector meson channels. Due to their short lifetimes, a beam of vector mesons is not possible in a lab, therefore information on the VN scattering cannot be assessed by direct means. This thesis presents new sets of high precision measurements of the differential cross section for the vector meson channels at large t and intermediate energies (a few GeV), showing significant contribution of the rescattering, and enables us to extract the σ_{VN}. Information

on the meson-nucleon scattering can provide us more insight in the baryon spectrum of QCD. This work complements a previous measurement of coherent ϕ-photoproduction cross section [M$^+$07] from the g10 experiment, hence completing the trio of light vector mesons: ρ, ω and ϕ.

In addition to the vector meson channels, the thesis will show that the same data can be used to extract the $N\Delta$ attraction predicted by theory, but not measured previously using photoproduction reactions. More experimental observation of such resonances can add to our understanding of the exotic hadrons.

All in all, the results presented in this thesis use the most basic tools of nuclear science, to measure meson-nucleon and baryon-baryon cross sections, which tells us about the nuclear force, and how it varies for different particles made from quarks. For example, NN and $N\Delta$ are different. Another example would be the interaction of pions with nucleons is not equivalent to that of the ω and the nucleons, although both are mesons.

The thesis is organized as follows: Chapter 2 deals with the experimental facility and the detector used to record the data. A discussion on various selection cuts and corrections on the detected events for different channels under investigation is presented in Chapter 3. The details on the simulation and detector acceptance is covered in Chapter 4. Chapters 5, 6 and 7 present the results for the three channels $\gamma d \rightarrow \omega d$, $\gamma d \rightarrow \rho d$ and $\gamma d \rightarrow d^{*++}\pi^- \rightarrow \pi^+\pi^- d$ respectively. A special membership project to calibrate a new subsystem of the upgraded CLAS12 detector of the CLAS collaboration is outlined in Chapter 8. Finally, a conclusion will be presented in Chapter 9.

2 Experimental Setup

The analyses presented in this thesis use data from the g10 experiment at the CEBAF Large Acceptance Spectrometer (CLAS). The g10 dataset was collected in the spring of 2004 at the Thomas Jefferson National Accelerator Facility (TJNAF), commonly referred to as Jefferson Laboratory (JLab). The g10 experiment was originally intended for a high statistics measurement of a pentaquark, an exotic baryon[8] with quark configuration ($qqqq\bar{q}$). Although no evidence of the theoretically predicted pentaquark θ^+ was observed, the run quoted an upper limit. Nonetheless, the g10 dataset is full of potential and this work proves the point that 'no data is redundant'.

JLab's main research facility is the Continuous Electron Beam Accelerator Facility (CEBAF), which produces continuous electron beams. The electron beam is directed to four experimental Halls (named A, B, C and D). Each hall contains specialized detectors to record final state particles produced from the collision of electron beam or with real photons with a stationary target. The g10 experiment was carried out in the experimental Hall B, which houses the CLAS, which was optimized for multi-particle final state detection. CLAS is notable in the hadronic physics community for its large acceptance (referred also as a 4π detector). However, physical gaps between the individual components reduce the coverage by about 40%. Hall B also contained a photon tagging spectrometer, commonly known as the photon tagger, which is useful to determine the energy of the incident photons. There are various components of the detector, see Figure 2.1, that are vital in the recording of an event in the experiments performed in the Hall B including g10. The following sections briefly discuss about them.

[8] The experiment was dedicated to the discovery of θ^+ with a quark configuration of $uudd\bar{s}$

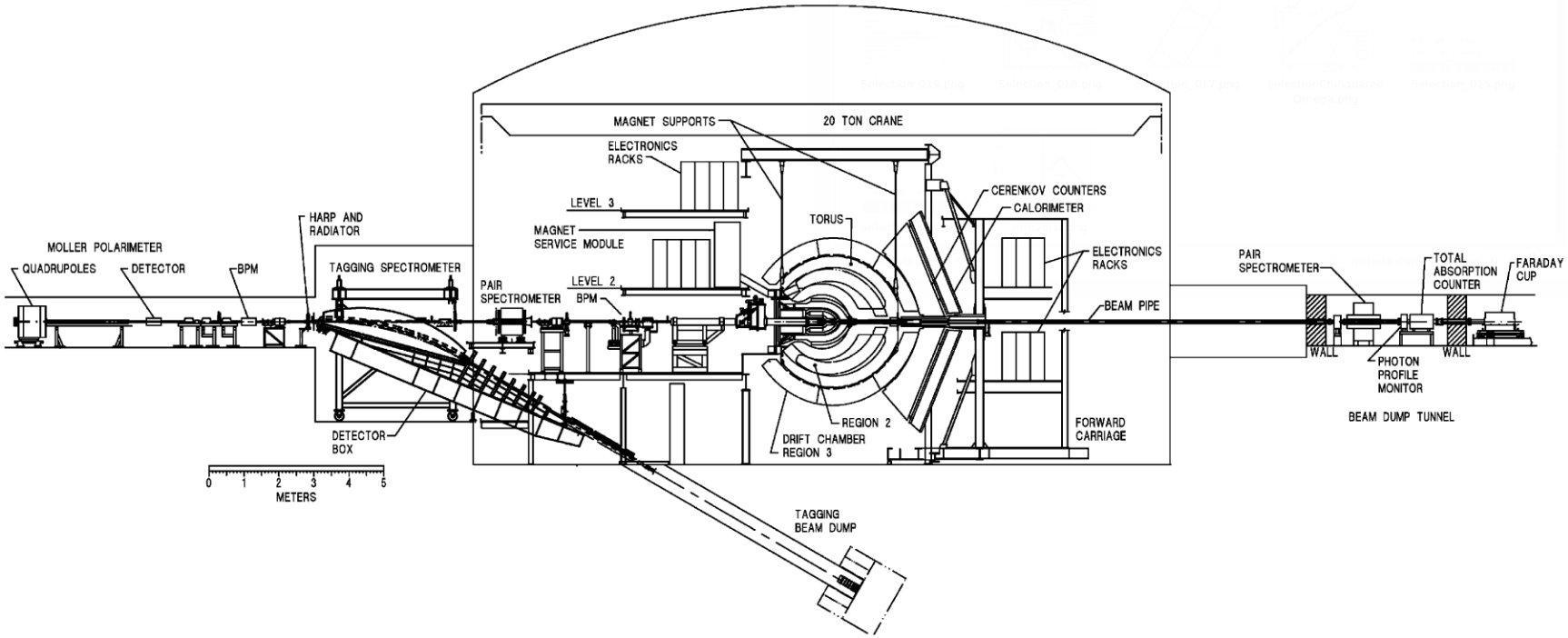

Figure 2.1: Side View of CLAS detector. Image Source: [M+03]. Elsevier License Number: 4501610231672.

2.1 CEBAF

CEBAF is an underground, racetrack-shaped electron accelerator that delivers continuous electron beam to different halls (Figure 2.2). Superconducting radio frequency (SRF) cavities were used to accelerate the electron bunches. When compared to previously used copper cavities in many facilities, the SRF were cheaper to operate. In addition, there was no resistive heating enabling 100% duty cycles. This ensured a continuous high-quality electron beam, enabling high statistics data collection even at low currents [LDK01]. The linear particle accelerators (LINACs) were each composed of 168 superconducting cavities making CEBAF the world's largest implementation of the SRF technology at the time.

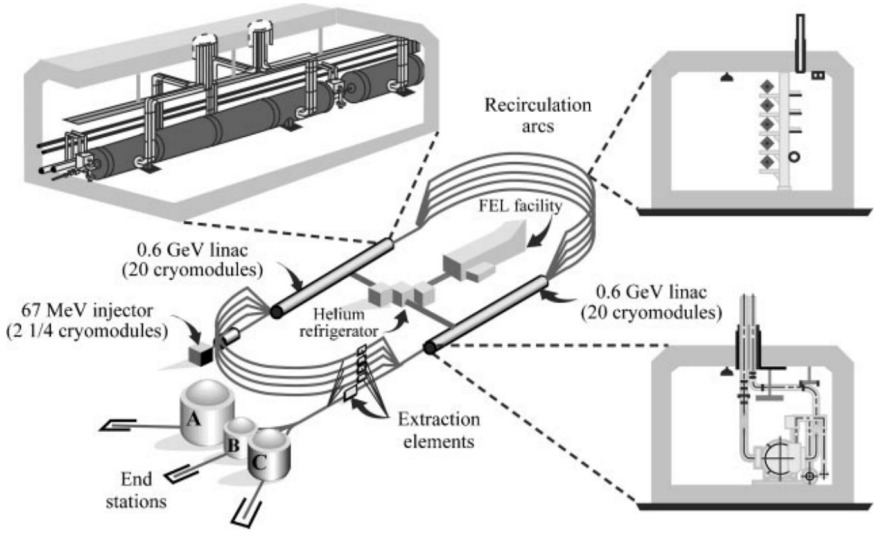

Figure 2.2: Schematic CEBAF accelerator overview. Image source: [LDK01]. Image Licensed from ANNUAL REVIEWS using Copyright Clearance Center License Number: 4506190311828.

Another major innovation associated with the CEBAF was the use of multipass beam recirculation. It not only minimized the cost of SRF implementation but at the same

time accommodated the possibility of energy upgrades because of a large enough bend radii [LDK01]. The electrons passed five times through the SRF LINAC simultaneously delivered electron beams of up to 200 μA corresponding to energy of ~6 GeV with 75% polarization to the Halls A, B and C. Currently, the CEBAF is able to accelerate electrons up to an energy of 12 GeV. After the beam bunch is directed towards a specific Hall, that Hall could measure and control the beam position and focus them. An electron beam of energy up to 3.8 GeV was used during the g10 experiment in Hall B. The general layout of Hall B can be seen in Figure 2.1.

2.2 Photon Tagger

Many experiments at JLAB, including those in Hall B during the 6 GeV era, use photoproduction which is useful to eliminate the complications associated with electron virtuality to the final measurements. Real photons for the process were created using the process of bremsstrahlung radiation, where an energetic electron incident on a radiator and emits a photon as it decelerates under the electromagnetic field within the nuclei. The radiator is usually a high-Z nucleus to ensure a strong field. For the g10 experiment, a gold foil was used as a radiator such that the reaction reads,

$$e + Au \rightarrow Au + e' + \gamma \tag{2.1}$$

The scattered electron e' can be detected to identify, or 'tag', the energy of the outgoing photon. The tagger used in Hall B to tag each photon can be seen in Figure 2.3. The tagger itself detects scattered electrons in the range of roughly 20%-95% times the incident electron energy, E_0.

Photons from the bremsstrahlung process are created with a range of energies. The energy of these photons are calculated by measuring the energy of the scattered electrons from the radiator. Measuring the electron energies is accomplished through the use of a dipole magnet to bend these electrons through toward "E" and "T" scintillators (energy

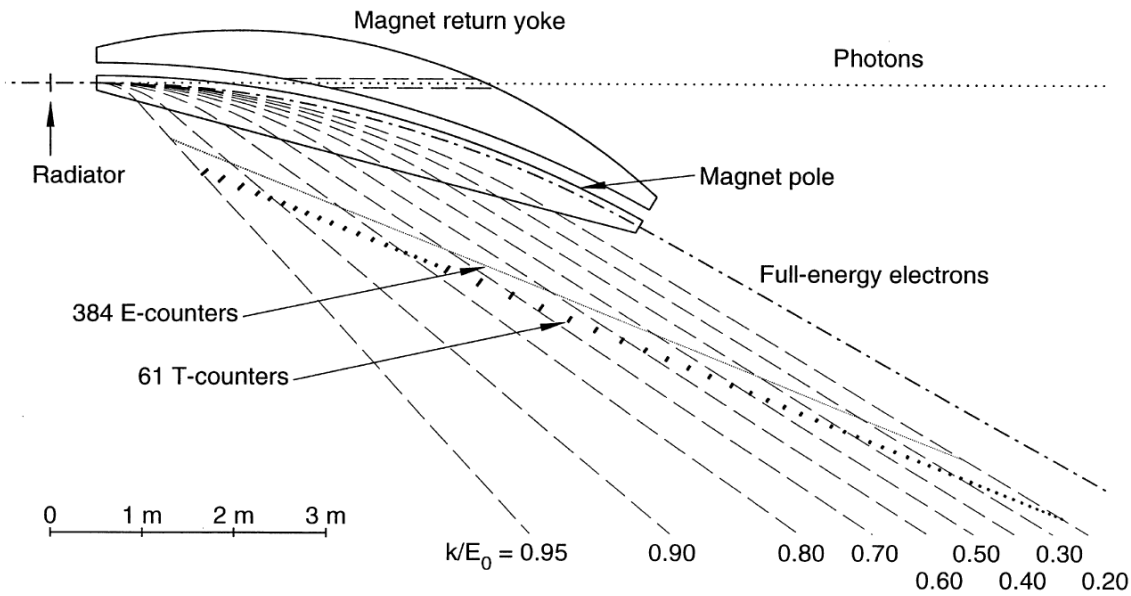

Figure 2.3: Overall geometry of the photon tagger system. Image source: [SCL+00]. Elsevier License Number: 4501620681663.

and time respectively) within the tagger. These scintillator planes are constructed as hodoscopes. These hodoscopes are placed such that there is overlap between them. The electrons that are roughly between 20% - 95% of E_0 will be directed toward these counters by the dipole magnet spectrometer. The full energy electrons were directed away from the beam line into a separate beam dump, leaving only the generated photons to continue onto the deuterium target. The photon energy was calculated by,

$$E_\gamma = E_0 - E_{e'}, \tag{2.2}$$

where $E_{e'}$ is the energy of the scattered electron. This energy is known to a resolution of $10^{-3}E_0$, due to the overlap of the E-Counters. Trajectories of the bent electrons also allow the determination of whether the event was a good geometrical hit in the hodoscopes, and if so a good status was assigned to the event photon. Each photon then has an energy (from its EID), time (from its TID), and status associated with it recorded in each event for analysis.

2.3 The CLAS Detector

To measure charged particles with good momentum resolution, to provide larger geometrical coverage of the charged particles, and to keep the target free of magnetic-field, the CLAS detector was designed based on a toroidal magnetic field.

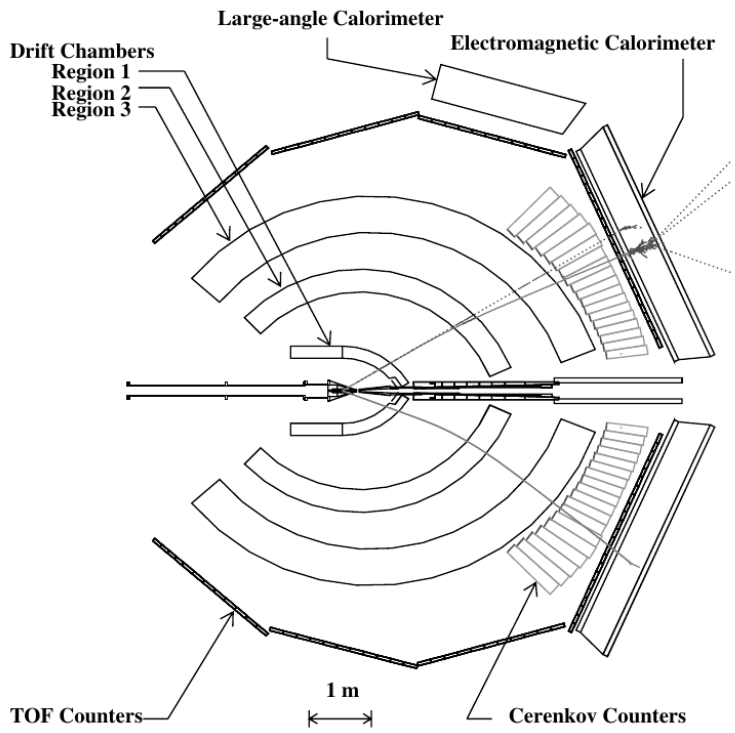

Figure 2.4: A schematic top view of the CLAS detector cut along the beam line. Typical photon, electron, and proton tracks (from top to bottom) from an interaction in the target are superimposed on the figure. Image Source: [M+03]. Elsevier License Number: 4501610231672.

The particle detection system consisted of six sets of drift chambers to determine charged-particle trajectories, gas Cherenkov counters to identify electrons, scintillator counters for measuring the time-of-flight (TOF) and electromagnetic calorimeters (EC)

to detect neutrons and showering particles such as electrons. These segments were instrumented individually so that they formed actually independent magnetic spectrometers with a common target, trigger and data-acquisition system. Different views along with major components of the CLAS detector are shown in Figures 2.4 and 2.5.

2.3.1 Target

The g10 experiment used a cylindrical target cell, 24 cm in length and 4 cm in diameter. The target material used in CLAS can be changed depending on the experiment proposed. An unpolarized liquid deuterium target was utilized for g10 experiment. The target cell was centered at 25 cm upstream from the CLAS center. This location was used to maximize the acceptance for the proposed channels of study.

2.3.2 Start Counter

The Start Counter (SC) records the start time of a particle traversing through CLAS that originated in the target. This time is very important to correctly identify an outgoing particle. The SC is constructed with six pieces of scintillators in a coupled paddle configuration. This effectively provides three sectors of scintillator in the forward direction and the other three in the backward direction resulting in six channels, each corresponding to the six sectors of CLAS [TAD$^+$01]. Each sector had its own Photo-Multiplier Tube (PMT) to receive a signal. The trigger to record an event required at least one hit from the SC and two hits in the TOF counters in two different sectors.

2.3.3 Toroidal Magnet

For the momentum analysis of charged particles, a toroidal magnetic field was generated by placing six superconducting coils around the beamline maintaining azimuthal symmetry in between each of the six sectors of CLAS. The toroidal field shape will bend charged particle tracks towards or away from the beam line depending on the polarity. The

maximum design current for the setting was 3860 A. The g10 experiment used two field settings: one at +2250 A and other at +3375 A. The positive current curves negatively charged tracks towards the beam line. The data used in this thesis are from the former torus setting (+2250 A) which has higher probability of detecting low momentum pions.

2.3.4 Drift Chambers

The construction of the detector was simplified by designing 18 separate pieces of the drift chambers (DC). These were located at three radial positions (regions) in each of the six sectors, each piece to be mounted between two magnet coils as shown in Figure 2.5.

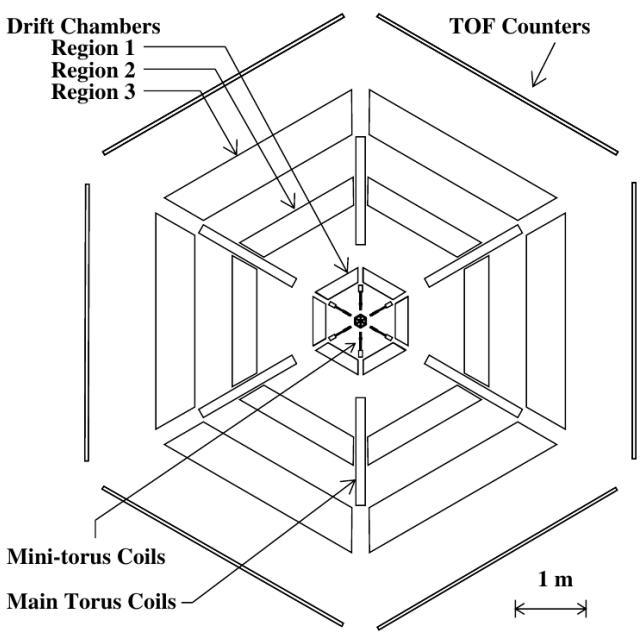

Figure 2.5: Schematic view of the CLAS detector, showing a cut perpendicular to beam. Also shown is the mini-torus used only for electron runs. Image source: [M$^+$03]. Elsevier License Number: 4501610231672.

The six “Region One” chambers surround the target in low magnetic field area, the six “Region Two” chambers are located in high field region while the six “Region Three” chambers are located outside of the magnet coils. Within the 18 drift chambers are a total of 35,148 individually instrumented hexagonal drift cells. The novel geometry of these chambers provided for good tracking resolution and efficiency, along with large acceptance [M$^+$03].

2.3.5 Time-of-flight Counters

The time-of-flight (TOF) counters cover a total of 134^0 of the polar angular range between 8^0 and 142^0 and all active region in azimuth totaling to about 206 m^2. The counters are placed radially outside the tracking system and the Cherenkov counters (in front of the calorimeters). The TOF structure can be seen in Figure 2.6. There are 57 scinitillator paddles in each sector, with the last 18 paddles coupled into nine logical pairs giving a total of 48 logical counters per sector. This detector subsystem was used to measure the laboratory time of the charged tracks leaving CLAS. The difference in the time recorded from the TOF counter and the event start time can be used to identify the mass of specific tracks in an event.

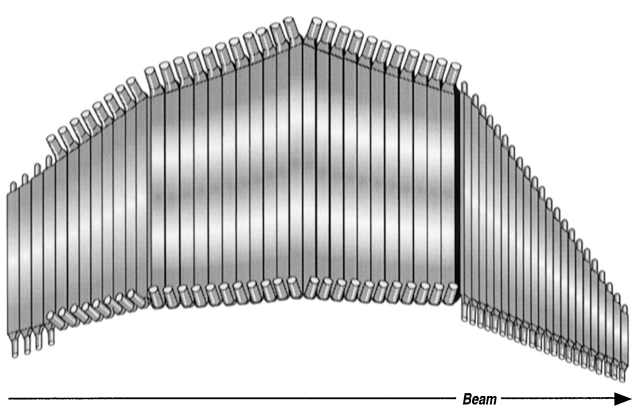

Figure 2.6: View of TOF counters in one sector. Image source: [SCD$^+$99]. Elsevier License Number: 4501621024301.

2.3.6 Cherenkov Counters

The Cherenkov Counters (CC) are used to trigger on electrons and separate electrons from pions [ABC+01]. This is most useful in electroproduction experiments, where the electron flux inside CLAS is much higher. These detectors use Cherenkov radiation given from the tracks traveling through the trapped gas. The emitted light is reflected through a process of curved mirrors allowing a cone of light to be detected. The information obtained from this unit is collected only in the ϕ direction, thus preserving the polar angle trajectory determined by the charge, momentum, and magnetic field.

2.3.7 Electromagnetic Calorimeter

The Electromagnetic Calorimeter (EC) served as the primary electron trigger for CLAS. It was also used to reject pions, reconstruct π^0 and η decays and detect neutrons. In a more general sense, the EC was used to detect neutral particles which travel unaffected by the magnetic field [AAB+01].

The design of the EC is similar to other components of CLAS, except the fact that it is not curved. It is also divided in six sectors. Each sector is in the shape of an equilateral triangle with 39 layers of scintillator strips alternating with sheets of lead. Each neighboring layer of scintillator strip (labeled as U, V and W planes) is rotated by 120^0 to cover the geometry of CLAS. Each layer of lead is intended to create electromagnet showers in an effort to stop the ionizing radiation allowing the scintillators and corresponding PMTs to collect the light output. An exploded view of the calorimeter can be seen in Figure 2.7.

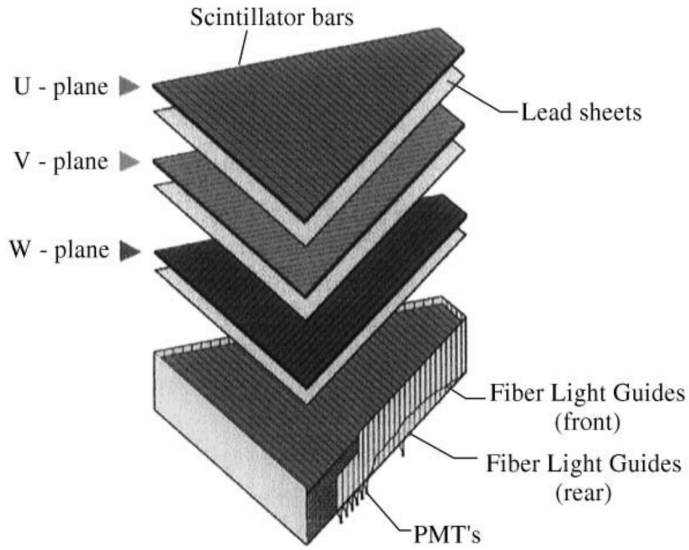

Figure 2.7: An exploded view of one of the six CLAS EC. Image source: [AAB+01]. Elsevier License Number: 4501621206608.

2.4 Summary

This chapter outlined the experimental apparatus and setup used to conduct many experiments in Hall B including the g10 experiment. The g10 dataset, with unpolarized beam, was collected in the spring of 2004 using the CEBAF and CLAS at JLab. CLAS was designed around six superconducting coils arranged in a toroidal configuration that produced a field in the azimuthal direction. The particle detection system consisted of six sets of drift chambers to determine charged-particle trajectories, gas Cherenkov counters to identify electrons, scintillator counters for measuring the time-of-flight (TOF) and electromagnetic calorimeters to detect neutrons and showering particles such as electrons. These segments were instrumented individually so that they formed actually independent magnetic spectrometers with a common target, trigger and data-acquisition system.

The g10 experiment used a continuous electron beam with incident electron energy, E_e = 3.767 GeV. This beam produced bremsstrahlung photons when passed through a thin

gold radiator. The tagger system was used to measure the energy of the photons, which interacted with an unpolarized liquid deuterium target measuring 24 cm in length and 4 cm in diameter. The reaction products traversed the large drift chambers and timing detectors.

The data acquisition trigger required two charged particles detected in coincidence with the tagged photon. The time of flight of a particle was determined using the scintillator paddles in the start counter that surrounded the target and the TOF scintillator paddles that surrounded the exterior of CLAS. The dataset corresponds to the lower magnetic field (torus magnet current set at 2250 A) to optimize the acceptance for low-momentum in-bending π^-.

The next chapters will describe in detail about the selection of final state products and the events that were selected for the three channels presented in this thesis.

3 Event Selection

In order to perform physics analysis of any data collected during an experimental run, it is very important to convert the raw signal information into meaningful and accessible physical values. Therefore, the recorded events ("raw" data) for the g10 experiment were "cooked" into a form suitable for physics analysis . During the cooking, all the detector subsystems (photon tagger, RF, drift chambers, etc.) were calibrated. The calibration constants were stored in a centralized system to reconstruct physical information in various banks using reconstruction and analysis software packages. The cooking procedure determines the tracking and momentum information. These physics events contain multiple detected particles that can be associated with single photon events within the target volume. A detailed description about how the events were cooked is outlined in the PhD Thesis of Bryan McKinnon [McK06]. The analysis efforts in this study began after the data was "cooked".

3.1 Experimental Runs

The g10 dataset used in this study are listed in Table A.1 in Appendix B. Experimental run information is listed at https://clasweb.jlab.org/shift/g10/runsum.txt and is summarized in Table 3.1.

Table 3.1: List of g10 runs and corresponding settings. These details are extracted from https://clasweb.jlab.org/clasonline/prodrunsearch.html.

g10 Run Settings						
Run Number		**Target**	**Beam Energy**	**Beam Current**	**Magnetic Field**	**EC in**
Begin	**End**		**(GeV)**	**(nA)**	**(A)**	**Trigger**
42299	42307	Empty	3.779	5	2250	Yes

Table 3.1 continued from previous page

42309	42315	H_2	3.779	5-30	2250	No
42316	42323	H_2	3.779	30	2250	Yes
EC thresholds changing: 42340-42360						
42340	42360	D_2	3.779	30	2250	Yes
42361	42364	D_2	3.779	25	2250	Yes
Trigger Test with ASYNC: 42366-42370						
42366	42370	D_2	3.779	5	2250	Yes
42371	42373	D_2	3.779	25	2250	Yes
42374	42376	D_2	3.779	25	2250	No
No ASYNC: 42377-42378						
42377	42378	D_2	3.779	25	2250	Yes
42379	42406	D_2	3.779	25	2250	Yes
42428	42431	D_2	3.779	35	2250	Yes
Test of Trigger: 42443-42448						
42433	42522	D_2	3.779	35	2250	Yes
42523	42523	D_2	Cosmic	-	2250	Yes
Big hole in DC Region 2 Sector 2: 42525-42529						
42525	42529	D_2	3.779	35	2250	Yes
42530	42530	D_2	Cosmic	-	2250	Yes
42531	42567	D_2	3.779	35	2250	Yes
42572	42586	D_2	3.779	35	2250	Yes
42587	42601	D_2	3.779	32	2250	Yes
42603	42640	D_2	3.779	32	2250	Yes
42642	42698	D_2	3.779	32	2250	Yes

Table 3.1 continued from previous page

DAQ Test: 42699-42717						
42699	42717	D_2	3.779	32	2250	Yes
42718	42723	D_2	3.779	32	2250	Yes
42729	42731	D_2	3.779	33-35	2250	Yes
42732	42737	D_2	3.779	20-25	2250	No
42738	42742	D_2	3.779	25	3375	No
42743	42765	D_2	3.779	25	2250	No
42770	42779	D_2	3.779	25	2250	No
42780	42863	D_2	3.779	15-25	2250	No
42864	42864	D_2	Cosmic	-	2250	No
42865	42875	D_2	3.779	25	2250	No
Tests: 42876-42888						
42876	42888	D_2	3.779	5	2250	No
42889	42916	D_2	3.779	25	2250	No
42918	42922	D_2	3.779	25	2250	No
Higher Torus Setting: 42923-43257						
42923	43232	D_2	3.779	25-30	3375	No
43233	43233	Empty	3.779	28	3375	No
43238	43241	Empty	3.779	30	3375	No
43242	43257	H_2	3.779	35	3375	No

3.2 Skimming

The cooked data contain a lot of information saved in different banks[9]. In order to process faster, the size of the original files were reduced by keeping only the information absolutely needed by the analyses along with various flags storing information about beam trip files (Section 3.2.1), flux files (Section 3.2.2), and the EC trigger condition. Particles of interest were selected on the basis of a time-of-flight method and the charge of the particles. The selection of events are outlined in Table 3.2. These cuts are explained in the following subsections.

Table 3.2: Summary of the cuts used in this study which are explained in the outlined sections.

Label	**Description**	**Section**
C1	$d\pi^+\pi^-$ skimming	Section 3.2
C2	EC Flag	Section 3.5
C3	Minimum $\|p\|$ cut	Section 3.6.1
C4	z-vertex Cut	Section 3.6.2
C5	50% Fiducial Cut	Section 3.6.3
C6	SC Paddle Cut	Section 3.6.4

3.2.1 Tripped Events

In the course of beam delivery to an experimental hall, the accelerator sometimes trips resulting in a loss of incident beam onto the target. Therefore, to try to maintain a constant incident photon flux, events that occurred during a beam trip

[9] Each data file corresponds to a certain run number. The information on these runs can be accessed from the experimental log book found at http://clasweb.jlab.org/clasonline/prodrunsearch.html.

were removed from the analyses. The beam trip information were recorded in trip files as explained in [BP05]. These are located in JLab's mass storage silo at: `/mss/clas/g10a/production/pass2/trip.tgz`. The trip files contain twelve columns of numbers, a portion of which is shown in Table 3.3.

These files were read in along with the data files. If the corresponding trip file was not found for a data file, the data file was removed from the analysis. For each event, there is a flag assigned (a portion of a trip file is shown in Table 3.3). The scaler interval status can have different flags: 0 good, 1 trip, -1 start file, -2 end of file. The document [BP05] mentions that "Event must be ignored if TRIP is not 0". Therefore, events with flag other than 0 were rejected from the analysis.

Table 3.3: A portion of a trip file for run: 42344, sub-run: 00 showing the Flag. Events with a non-zero flag are excluded from the analysis.

...	Interval Status	1st Event #	Last Event #	...	Live Time
...	-1	3	25206	...	0.759760
...	0	25209	64053	...	0.761274
...	0	64054	101723	...	0.757940
...	0	101724	138780	...	0.749716
...	0	138781	175415	...	0.755933
.	.	.	.	.	.
.	.	.	.	.	.

3.2.2 Flux Files

Over the course of a specific run, the number of incident photons is calculated using the method of photon flux determination [BP05]. The basic idea of this method is counting "good" electrons in the tagger hodoscope and comparing this number with the number of photons on the target measured with a different detector having a well known efficiency. [BP05] explains that the photon flux at the target is determined as a function of energy by using "good" electrons detected at the tagger which were not involved in the physics event trigger. In other words, when the time of hit on the left and right TDC of a T-Counter matches with that for one E-counter, the electron is considered good regardless of the corresponding photon's involvement in any physics event.

The number of "good" electrons per T-counter for a particular data file gives the photon flux per T-counter. The T-counters could be mapped to the E-counters which were used to store flux information. This information is stored in *gflux* files and is located on JLab's storage silo at: `/mss/clas/g10a/production/pass2/`. Every run has a corresponding *gflux*-file. In case there does not exist a pair, the data file was excluded from the analysis.

3.3 Particle Identification

Particle identification (PID) is the process of using information left by a particle passing through a particle detector to identify the type of particle (typically by its mass). Only those events which produced pions and deuterons were kept. Particle identification was done using the TOF technique, where the time of flight of any particle produced during an event was compared with the calculated time for the path for the measured momentum and an assumed mass;

$$\delta t = t_{meas} - t_{calc}, \tag{3.1}$$

where t_{meas} is the measured TOF and t_{calc} is the calculated time. The measured TOF is given by

$$t_{meas} = t_{SC} - t_{\gamma} \tag{3.2}$$

where t_{SC} is the time at which the particle struck the CLAS TOF scintillators and t_{γ} is the trigger time (`tr_time` from `EVNT` bank.). The calculated TOF is given by,

$$t_{calc} = \frac{d_{path}}{c}\frac{E_i}{p_i} \tag{3.3}$$

where d_{path} is the path length from the target to the scinitillator, c is the speed of light and $E = \sqrt{p_i^2 + m_i^2}$ is the energy of the particle with given momentum p_i and an assumed mass m_i. The quantity, δt, is expected to peak at zero assuming all the calibrations are correct. In order to minimize misidentified tracks, a timing cut was placed around the peak. This cut is explained in Appendix B.1. Once the cuts were applied, the timing distributions for the detected particles in both data and MC can be seen in Figure 3.1.

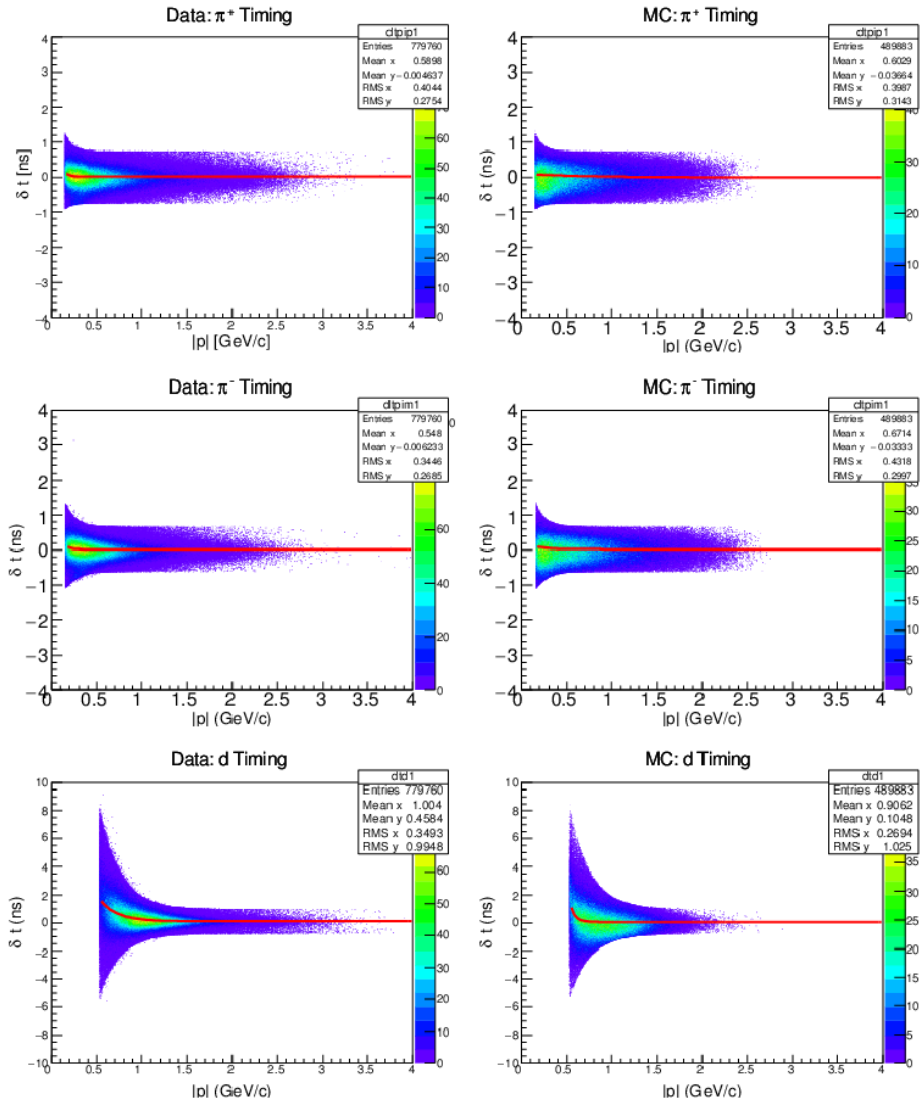

Figure 3.1: Timing distribution used for particle identification for both data (left) and simulation (right) as a function of particle momentum. A 3σ momentum dependent timing cut for both the data and MC is applied. The red curves represent the fit to the centroids extracted using Gaussian fits (Appendix B.1) [Plots are after cut level C1 and C3 of Table 3.2, Energy loss corrections were not applied].

3.4 Photon Selection

Photon selection was done based on its "good hit" status and the timing difference cut. Each tagged photon was assigned a status to it. The photon with a hit status of 7 or 15 is considered a "good" photon, or in other words the hit is said to be a good hit. Status 7 means one unambiguous hit was reconstructed in the tagger, and status 15 means more than one unambiguous hits were reconstructed [Che10]. This information was stored in the `taggoodhit` bank.

In order to ensure that each event was associated with at least one "good" photon, a time difference (t_{diff}) between a photon and a track was required to be within $\pm 1\ ns$, i.e.,

$$t_{diff} = |t_\gamma - t_{vertex}| < 1\ ns \tag{3.4}$$

where t_γ is the trigger time (which is `tr_time` from `EVNT` bank) and t_{vertex} is the vertex time (`vertex_time` from `TGPB` bank). In CLAS, there was an offset of about 0.8 ns in determining the vertex time [Com16]. Therefore, the difference did not exactly peak at zero as shown in Figure 3.2a. This, however, did not affect the selection of photons as the condition was met anyway. This difference was found to be within 1 ns as shown.

To summarize, a multiplicity cut was employed on each event for photon selection. The tagged photons were categorized into two, with the first category requiring photons with a status of 7 or 15 and $t_{diff} < 1\ ns$. The second contained the number of events where only one photon meets the requirements from the first category. The number of photons in the first category is shown in Figure 3.2b and the unambiguous photons account for 93.22%($\equiv \frac{N_{N_\gamma=1}}{N_{N_\gamma>0}}$) of the total "good" photons requiring a correction factor of 6.78%. Only events with one photon and three charged particles (π^+, π^- and d) were kept for further analysis.

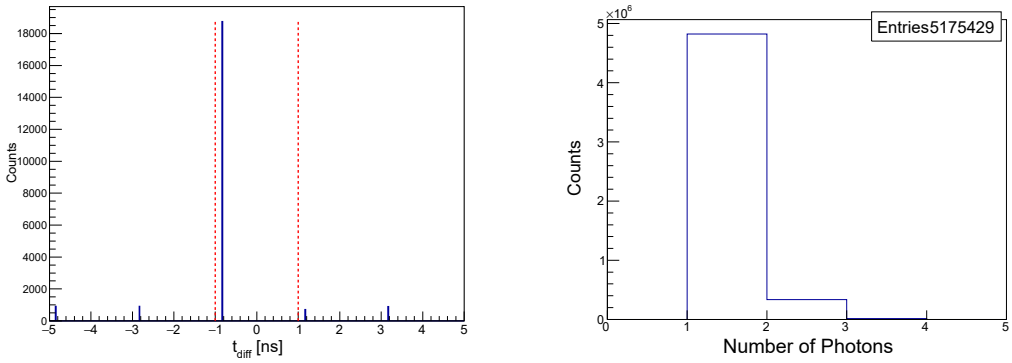

(a) (b)

Figure 3.2: Plots related to photon selection and multiplicity. (a) Shown is the "good" photon time difference, t_{diff}, for a subset of the data files used in this analysis. Also, the number of entries are those events with $N_\gamma > 0$ and detected particles defined by the cut level C1. (b) Number of "good" photons after the PID cut was applied. Number of events associated with only one photon is $N_{N_\gamma=1} = 4.82 \times 10^6$ while total number of photons in first category is $N_{N_\gamma>0} = 5.18 \times 10^6$.

3.5 EC Trigger

The forward region of each sector of CLAS is equipped with Electromagnetic Calorimeter (EC) to provide good energy and position resolution [AAB+01]. During the $g10$ run, trigger conditions based on hits in the EC were recorded. There were three different EC trigger conditions for the low field setting: `noEC` (EC information was not used in the trigger), `withEC` (EC information was in the trigger), `withEC_noASYNC` (EC was used, but the tagger was not in the trigger) [Che10].

In this study, tracks with at least one hit in the EC (`ec` in `gpart` bank) were only passed to the next analysis step. This information was stored in the form of a flag. Turning

the flag ON ensured a consistent normalized yield (See Section 5.5.1) for all $g10$ runs at low field.

3.6 Detector Cuts

3.6.1 Minimum Momentum Cuts

Low momentum deuterons are difficult to model in CLAS. They lose a lot of energy as they pass through material in the detector. This affects not only the accuracy of the energy loss corrections, but causes problems in finding the acceptance as well. Therefore, for the detected particles, an additional minimum momentum cut was added.

Minimum momentum conditions on the detected particles were made in both data and simulation. Events with $|p_{\pi^\pm}| < 0.15$ GeV/c and $p_d| < 0.54$ GeV/c were removed from the analyses, where $|p|$ represents the magnitude of a particle's momentum. These values were calculated by taking the momentum value corresponding to 50% of the height of the total distribution (momentum projection from δt versus $|p|$ distribution within the missing mass cut depending on the reaction channel). The distributions along with the position of cuts are shown in Figure 3.3. Using the same prescription, the minimum momentum cuts for simulation were applied for each channel.

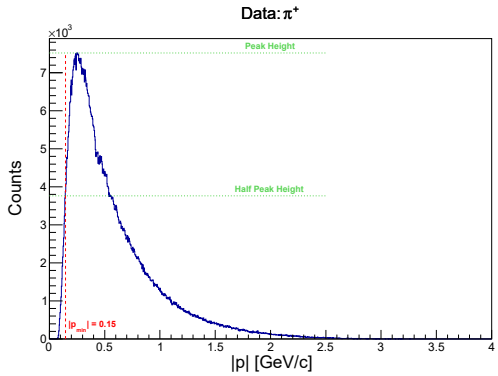

(a) Minimum Momentum Cut for π^+ in data.

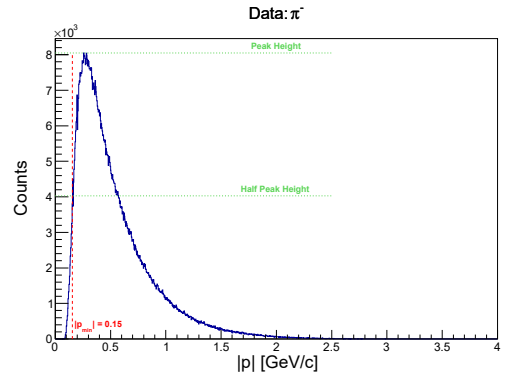

(b) Minimum Momentum Cut for π^- in data.

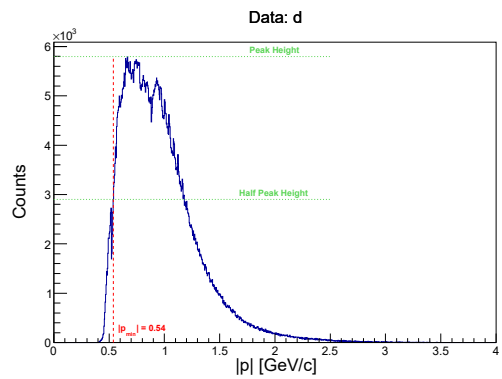

(c) Minimum Momentum Cut for d in data.

Figure 3.3: Momentum distributions in data for the channel $\gamma d \rightarrow \pi^+\pi^- d(\pi^0)$.

3.6.2 z-Vertex Cuts

The $g10$ target cell measured 24 cm in length with a diameter of 4 cm. It was positioned at a distance of 25 cm upstream from the CLAS center, $z = 0$. In terms of the CLAS coordinate, the target cell is placed such that $|z + 25| < 12$. Ideally, the reaction vertices should be within the target cell. In CLAS, all vertices are given as the point of the trajectory that is closest to the z-axis. However, they may not coincide. For this analysis, the point where the ω, ρ or d^* and outgoing deuterons or pions emerge out is reaction vertex which lies within the target cell. In order to find this point, the charged particles

were extrapolated back to where the decay occurred. The vertex of the charged pions are therefore changed from the point closest to the z-axis, to a point that corresponds to that of the outgoing deuteron. This was done by implementing the Distance of Closest Approach (DOCA) technique in which tracks of the particles are compared to find the point at which the distance between them is the smallest.

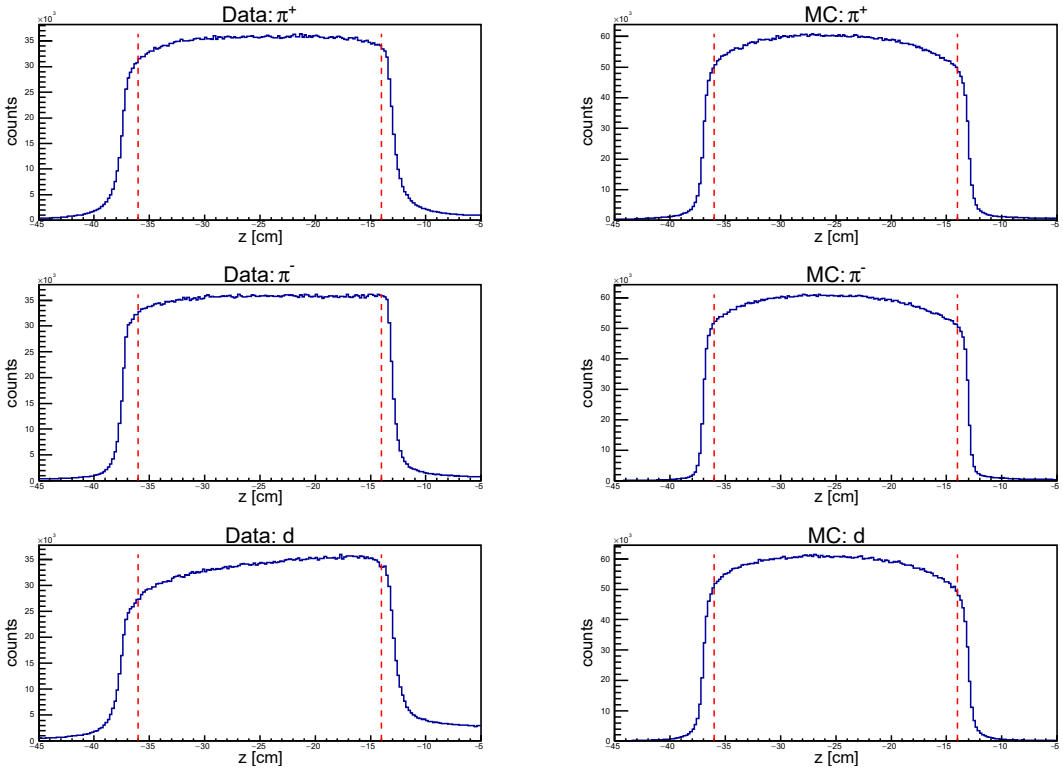

Figure 3.4: z-vertex distribution for the identified particles for both data (left) and simulation (right). Red dotted line is drawn to show the cuts. Events outside this cut are not included in the analysis. [Plots shown here are drawn after cut C1 of Table 3.2].

To ensure events outside of the target cell are rejected, a cut of $|z + 25| < 11$ (cm) was made, where z is calculated using DOCA. This cut was applied to all the particles in both data and simulation. An outline of the cut is shown in Figure 3.4.

3.6.3 Fiducial Cuts

The CLAS detector can be mapped in ϕ and θ for each track. Some particles are tracked back to unreliable regions/angles in the detector such as the edges of the drift chambers. Also, the magnetic field generated by the torus magnet were non-uniform near the cryostat surfaces, which sometimes caused an inaccurate reconstruction of tracks. As a result, the acceptance in these regions changes rapidly or are not well-known, and is thus difficult to model accurately. Therefore, such regions are rejected from both the experimental data and simulation to properly calculate the detector acceptance by employing fiducial cuts. To define fiducial cuts for this analysis, correlation between the polar angle measured by CLAS, θ^{CLAS}, versus the azimuthal angle measured by CLAS, ϕ^{CLAS}, was studied.

Figure 3.5 shows the distribution of events over the azimuthal and polar angles for the detected particles for both data and simulation. The events were projected onto the ϕ^{CLAS} axis in 500 bins of θ^{CLAS}. One such bin is shown in Appendix B.2. For each bin, the height of the projections for the range $-\pi/6 < \phi^{CLAS} < \pi/6$ ($-30^o < \phi^{CLAS} < 30^o$) was calculated. The ϕ^{CLAS} corresponding to 50% of the height made a distribution as a function of θ^{CLAS}. This was fit to an exponential function of the form,

$$\phi = ae^{b\theta} + c \tag{3.5}$$

where a, b and c are the fit parameters. As CLAS is symmetric in ϕ, this equation can be used to fit all the represented edges of the six sectors by shifting by an angle of 60^0. More details can be found in Appendix B.2.

In addition to the cut in the azimuthal angle, a minimum polar angle cut is also made. Events within $0 < \theta_{\pi^+,d} < 0.1$ [rad] and $0 < \theta_{\pi^-} < 0.25$ [rad] were removed from the analysis.

Assuming detector simulations (GSIM) could accurately model the decrease in efficiency in the outermost regions of each sector (Sector 3 has a bad TOF paddle at around $\theta = 0.7$ rad in both data and simulation), angular cuts may not have been needed. However, due to the unknown precision of the GSIM model, the acceptance cannot be reliably determined outside of the fiducial region. Therefore, it is important to apply the fiducial cuts in both azimuthal and polar distributions for the simulated events as well. The angular cuts for both data and MC are shown in Figure 3.5.

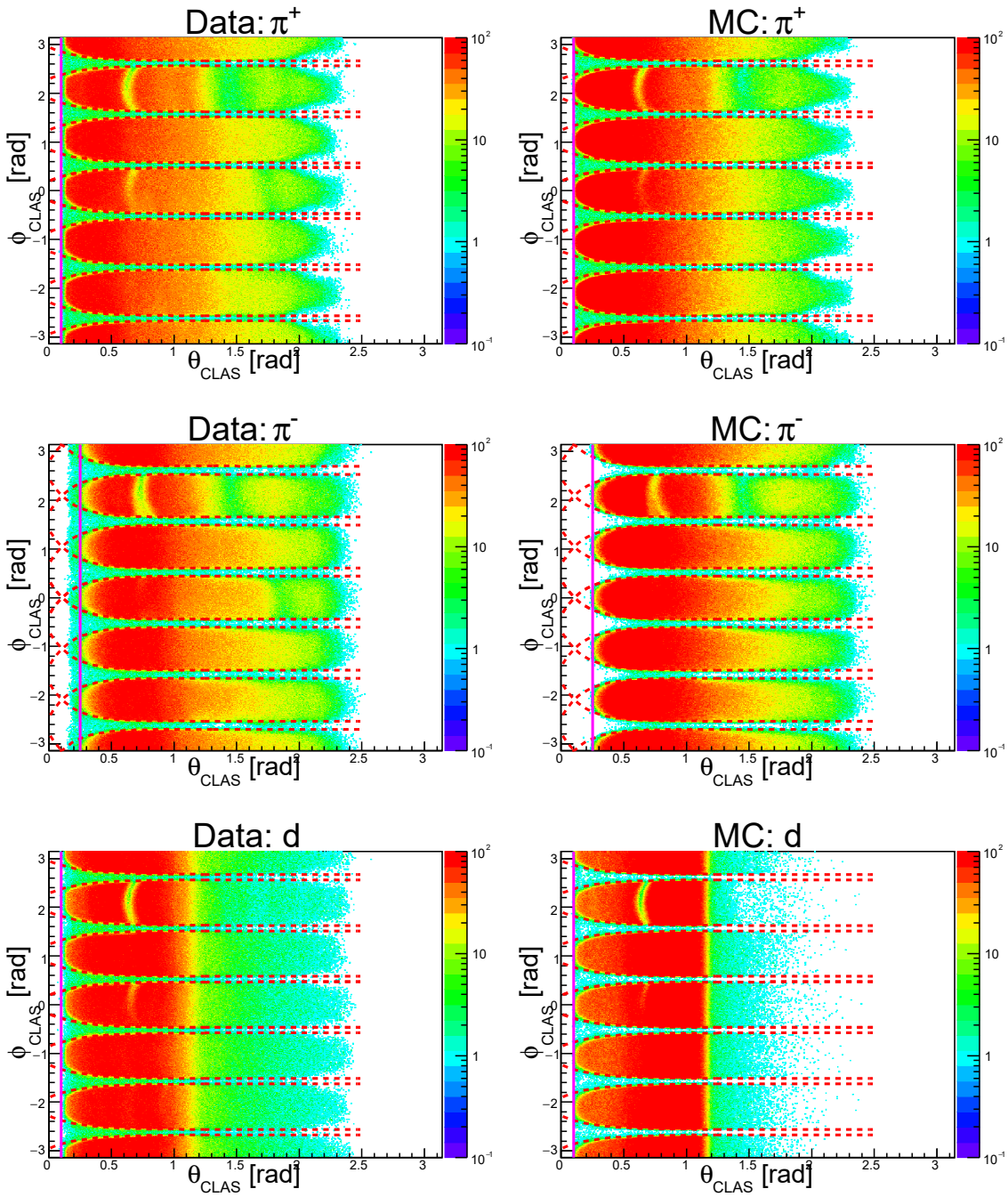

Figure 3.5: ϕ versus θ distributions for π^+, π^-, d are shown. Only events within these fits for each sector were selected. Vertical red lines are drawn to show θ cuts as well. [Plots shown here are drawn after cut C1 of Table 3.2. Energy loss corrections were not applied. Also the plots are scaled on the z-axis for a better comparison].

3.6.4 SC Paddle Cuts

The CLAS has 48 logical paddles or scintillator strips in each of the six sectors. Over time the scintillators may go bad and the data may not capture the physical event. To find the bad paddles, timing distributions δt, were used. For each detected particle, each of the six sectors was investigated by looking at the timing distributions. Selection of bad paddles was done based on the number of events, N_k, in each paddle k. If

$$N_k \ll \frac{N_{k-1} + N_{k+1}}{2}; \quad 1 < k < 48, \tag{3.6}$$

then k was listed as a possible bad paddle. An example of the distribution for π^+ in sector 5 can be seen in Figure 3.6. The number of events in paddle 23 is clearly much less than its neighboring paddles making it a bad paddle. Therefore, the paddle 23 was removed from the analysis.

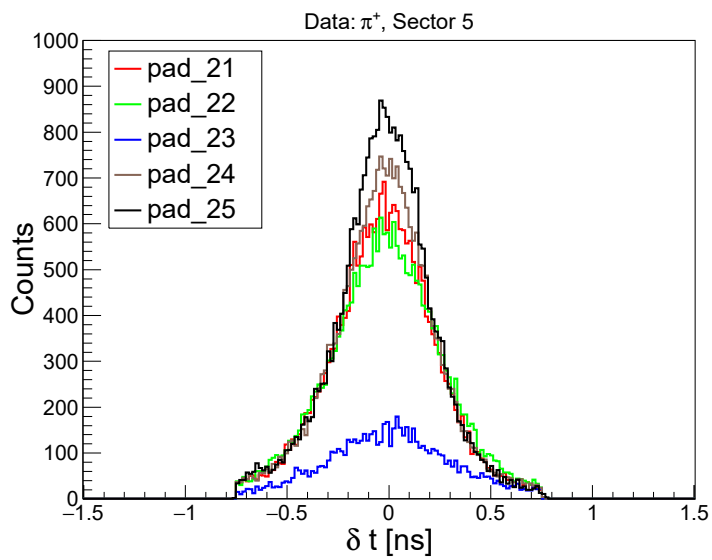

Figure 3.6: The timing distributions of five SC paddles for π^+ in sector 5. The number is events in pad 23 is clearly very less compared to its neighboring pads.

Table 3.4 lists the paddles that were excluded from the analysis. As these paddles represent the physical detector, these were removed from the simulation as well. Plots of δt versus paddle number for π^+, π^- and d are shown in Appendix B.4.

Table 3.4: Table showing paddle numbers which are cut for each particle for all the six sectors. The first line represents bad paddle numbers while second line gives the paddle number beyond which the events were not included.

Particle	Sector 1	Sector 2	Sector 3	Sector 4	Sector 5	Sector 6
π^+	23, 27 ≥ 43	 ≥ 45	11, 13, 23, 31 ≥ 40	23, 33, 35 ≥ 46	23, 29 ≥ 46	23 ≥ 45
π^-	23, 27 ≥ 41	 ≥ 41	11, 15, 16, 23, 31 34-36, ≥ 41	23, 27, 35 ≥ 43	20, 23, 29 ≥ 43	23 ≥ 42
d	23, 27 ≥ 35	23 ≥ 35	11, 22, 23, 31 ≥ 35	23 ≥ 35	23, 29 ≥ 35	23 ≥ 35

3.7 Energy and Momentum Corrections

This section explains about energy and momentum corrections used to improve the data. Tagger corrections were found by S. Stepanyan [S$^+$05] and the corrections are directly applied. Also, the energy loss correction package developed by E. Pasyuk [Pas07] is used in this study. An exclusive $\gamma d \rightarrow \pi^+\pi^- d$ reaction was used to find the momentum corrections. The corrections are explained in the next subsections.

3.7.1 Tagger Corrections

The tagger is used in all photon beam experiments performed by CLAS. It is used to detect recoil electrons after the bremsstrahlung process. Due to sagging of the E-Counters

over time between the supports on the physical structure will lead to slightly shifted energy readout of the tagged photons.

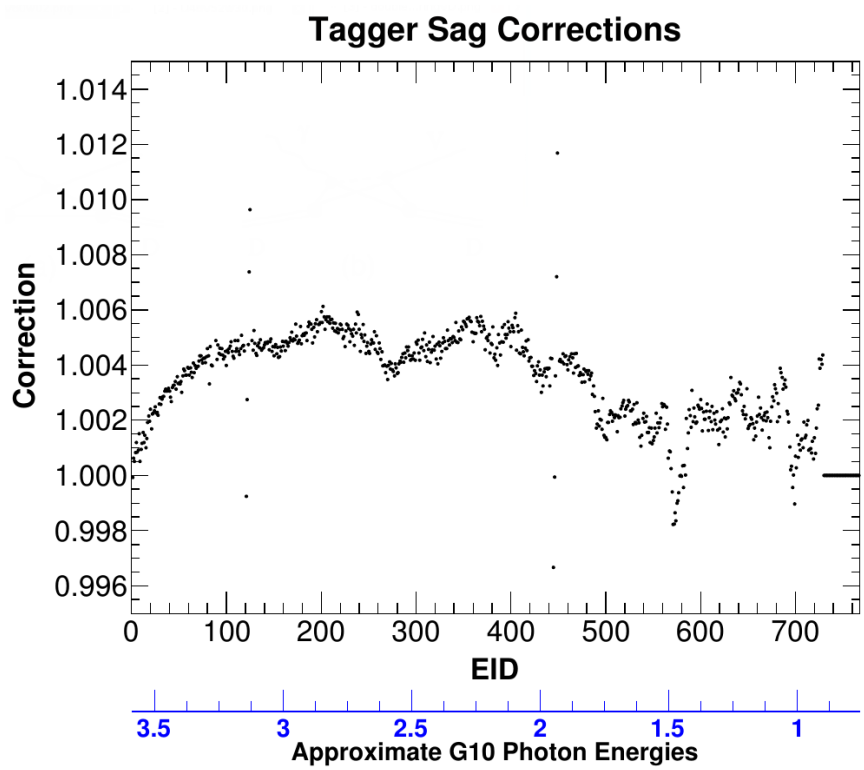

Figure 3.7: The tagger correction factor as a function of E-ID. Image from [Com16].

The sag could potentially change the accepted range of radii of curvature from the scattered electron, and thus change the photon energy corresponding to a specific E-ID. In order to correct for the tagged photon energy, the tagger was calibrated based on the procedure outlined in [S$^+$05] which gives the correction factor for the tagger E-counter relative to each other. As there is a one to one relationship between photon energy and E-ID, the correction factor can then be directly multiplied to the photon energies registered at each of these E-ID. The correction factor as a function of the E-ID is shown in Figure 3.7.

3.7.2 Energy Loss Corrections

Charged particles lose energy when they travel through matter. Before being detected in the drift chambers, charged particles interact with the target cell, start counter and the air molecules inside the CLAS detector. The momentum of the particles are determined, and hence need to be corrected for the analysis. The amount of this correction is calculated by applying the standard energy loss package [Pas07] updated by Eugene Pasyuk for the $g10$ configuration. For a given reconstructed particle momentum and vertex, this package finds the energy loss within CLAS and returns a new 4-vector. This package is a set of FORTRAN subroutines. This package calculates and applies the corrections. Corrections were made to account for energy lost in the target material (liquid Deuterium) and walls, the beam pipe, the start counter and the air gap located between the start counter and the Region 1 drift chambers. The corrected 4-momentum will give a more accurate representation of the reconstructed invariant and missing masses. The correction in energy will cause a shift in the invariant and missing mass peaks towards expected values.

To illustrate the effect of the energy loss correction, the exclusive $\gamma d \rightarrow \pi^+\pi^- d$ channel is used here. After a skim detecting $\pi^+\pi^- d$ as final state particles, a missing mass squared cut $-0.01 < MM^2(\gamma d, \pi^+\pi^- d) < 0.005$ GeV$/c^2$ was applied. This cut boundary was chosen to illustrate the effectiveness of the correction. Those events within this cut include the detected charged pions and the coherent deuteron. If the missing mass of deuteron is plotted for such events then a peak about the deuteron mass is expected. When the energy loss correction was applied to both the data and the simulated events, the peaks shifted towards the expected value. These shifts can be seen in Figure 3.8. One can see that the shift is not enough in case of the simulation which could be due to miscalibration of the detector in the simulation package. In order to reduce this effect, momentum corrections are also performed for data and simulation independently which is described in the next section.

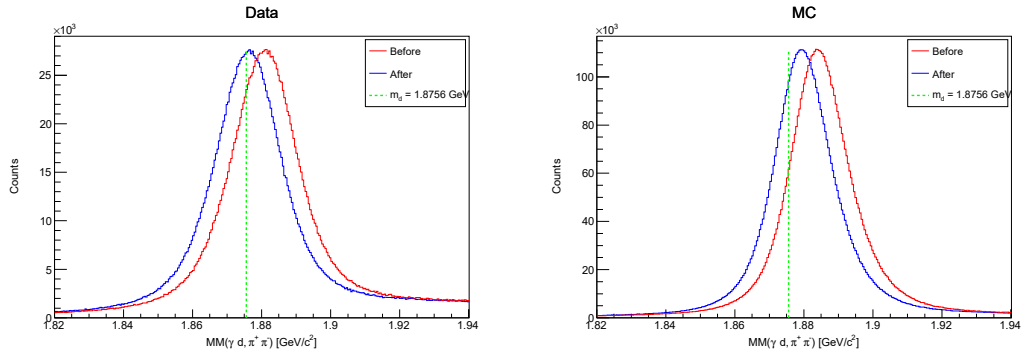

Figure 3.8: Missing mass distributions $MM(\gamma d, \pi^+\pi^-)$ before and after the energy loss correction was applied. The left plot is for the data while the right is that for MC. The dotted line on both represent the expected position of the peak. [Plots are after cut level C1 of Table 3.2 and applying tagger corrections].

3.7.3 Momentum Correction

In addition to the energy loss corrections for charged particles and the correction to the measured photon energy due to the slight gravitational sag in the tagger, experiment-specific momentum corrections can also be made.

The momentum of charged particles in CLAS is determined by tracking them in the magnetic field with the drift chambers. The momentum of detected particles can also have some correction as the CLAS tracking code may not effectively correct for losses along the track. A need for the correction could potentially be seen from the shift of centroids in mass distributions from expected values. The ELOSS package does a very good job in correcting the loss along the track. However, there could be discrepancies in the toroidal magnetic field map and/or in the drift chamber that can lead to inaccurate reconstructed momenta. One can see that the missing mass distribution for the simulation after energy loss correction does not peak at the expected value. Therefore, a momentum correction for

the detected particles will help in extracting information with more certainty than without and reduce the effect of miscalibration in the simulation.

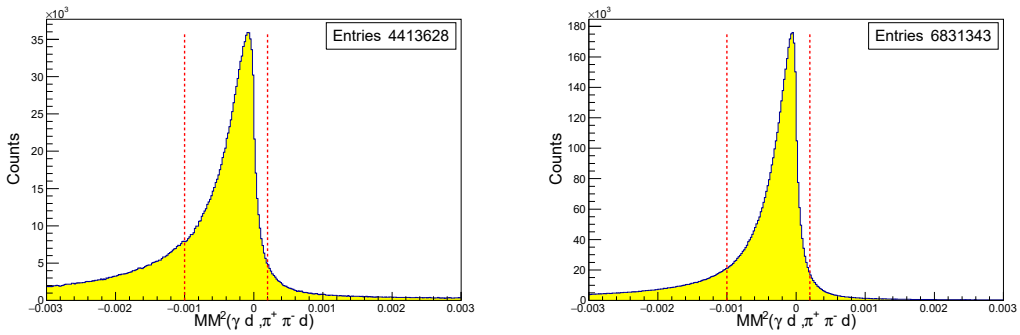

Figure 3.9: Missing mass squared distributions for the reaction $\gamma d \rightarrow \pi^+\pi^- d$) for Data (left) and Simulation (right). The dashed lines show the regions considered for momentum corrections. [Plots are after doing C1 and applying tagger and energy loss corrections]

In order to find the corrections, the exclusive $\gamma d \rightarrow \pi^+\pi^- d$ channel is used again after the application of the tagger and the energy loss corrections. A very narrow missing mass-squared cut around zero will ascertain that one is dealing with the exclusive events only. From Figure 3.9 the asymmetric tail on the negative side of the peak can be seen. This could be attributed to the resolution of momentum measurements by the CLAS drift chambers. Thus when the missing momentum vector has a non-zero magnitude, the missing mass-squared is slightly less than zero as can be seen. The background under this distribution is negligible. A narrow cut, $-0.001 < MM^2(\gamma d, \pi^+\pi^- d) < 0.0002$ (GeV/c^2)^2, is placed to remove a majority of the background events. This cut is tighter and includes a majority of signal events in the missing-mass squared distribution around zero.

In an ideal case, the measured momentum of a particle and the momentum calculated using momentum conservation (difference of incident and other detected particles) are

exactly equal. In other words, their ratio is equal to unity. But this may not be the case considering the discrepancies mentioned. The ratio is the required correction that needs be factored in the measured momentum of the detected particle. Similarly correction factors can be calculated for other detected particles.

For the exclusive reaction, $\gamma d \rightarrow \pi^+\pi^- d$, the correction factor ($C.F.$) for the momentum of π^+, for example, can be mathematically calculated as:

$$C.F.(\pi^+) = \frac{|p_{\pi^+}|}{|(p_\gamma + p_d) - (p_{\pi^-} + p_{d'})|}, \tag{3.7}$$

where d is the target deuteron while d' is the outgoing deuteron and p is the momentum of particle after energy loss and tagger corrections were applied. The correction factor for the other two particles are also calculated in the same way.

Using 4 z-bins, 180 θ-bins, 360 ϕ-bins and 50 $|\vec{p}|$ bins, the correction was calculated. The momenta of the particles are considered within an upper limit of 2 GeV/c ($|\vec{p}_i| < 2$). In each of $4 \times 180 \times 360 \times 50$ bins, an average correction was calculated. However, if there were less than 10 events, the correction factor was set to 1. This condition helped in avoiding over-correction/under-correction due to low statistics in the bins. The correction factor was then recorded and applied to the channels under investigation. Some sample correction plots are shown in Appendix C for the channel $\gamma d \rightarrow \pi^+\pi^- d(\pi^0)$.

To illustrate the affect of the momentum correction, $MM(\gamma d, \pi^+\pi^-)$ for the channel the channel $\gamma d \rightarrow \pi^+\pi^- d$. is plotted again in Figure 3.10 which shows the centroid shift towards expected value.

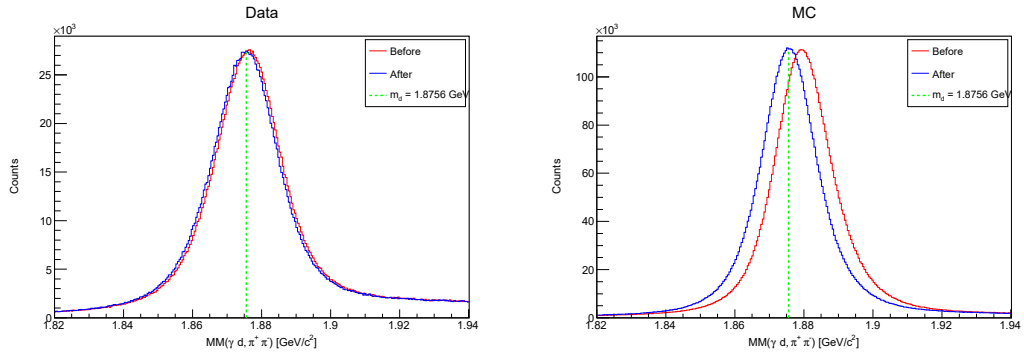

Figure 3.10: Missing mass distributions $MM(\gamma d, \pi^+\pi^-)$ before and after the momentum correction was applied. The left plot is for the data while the right is that for simulation. The dashed line represents the expected position of the peak. [Plots are after cut level C1 of Table 3.2 and applying tagger and energy loss corrections]

3.8 Missing Mass Cut

This study involves investigation of three reaction channels. These channels are separated based on different missing mass cuts. For a fully exclusive reaction, the missing mass distribution under ideal conditions is expected to peak at zero. In case there are other particles that are missed and need be included, one has to cut around that expected particles' mass. The following details the missing mass cuts that are applied to separate the three channels from the same detection sample.

3.8.1 $\gamma d \rightarrow \omega d \rightarrow \pi^+\pi^- d(\pi^0)$

For example, one major background in the present analysis is that from coherent ρ-channel as can be seen from Figure 3.11, where missing mass distributions are plotted on both axes. The colored texts on the figure are shown just to give an idea of the association of the peaks to certain events. Therefore to reduce the ρ background, a missing mass cut around the π^0 mass is made to access the exclusive reaction events [$\gamma d \rightarrow \pi^+\pi^- d(\pi^0)$].

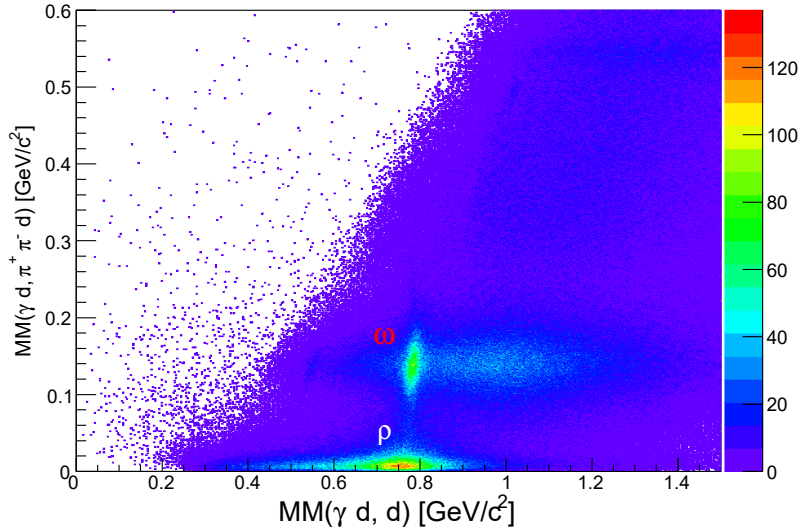

Figure 3.11: A two dimensional plot for the Missing mass distributions for data. The plot is drawn after cut level C1. The ω and ρ are written with respect to the x-axis.

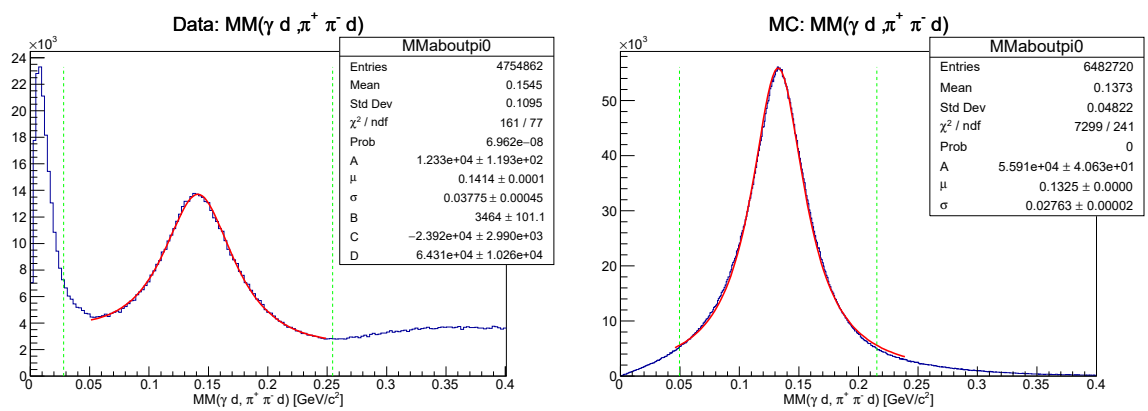

Figure 3.12: The missing mass distribution for data (left) and simulation (right). The dashed lines in green represent the position of the cuts made while the red curve is the fit to the distribution. [Plots are after cut C1 of Table 3.2 and all corrections applied].

The missing mass distribution for this analysis is shown in Figure 3.12. As the data consists of signal as well as background events, the missing pion peak can be estimated by a Lorentzian function sitting on a polynomial background. At this point no effort is made to estimate what physical events form the background. The parametric form of the total fit function is:

$$f(x) = A\left[\frac{\sigma^2}{(x-\mu)^2+\sigma^2}\right] + B + Cx + Dx^2 \tag{3.8}$$

where A, μ, σ, B, C and D are fit parameters. The centroid, μ, and width, σ, of the fit function were extracted and used to estimate the location of cuts. Events within $\mu - 3\sigma < MM(\gamma d, d) < \mu + 3\sigma$ were selected nominally as shown by the dashed green lines. The simulated events are just signal, therefore parameters from the Lorentzian fit were used to make a similar 3σ cut. The centroid and width of the fit functions along with the cut ranges are summarized in Table 3.5.

Table 3.5: Summary of fit parameters used to apply a missing mass cut.

Events	μ	σ	$\mu - 3\sigma$	$\mu + 3\sigma$
Data	0.141392	0.0378032	0.0279821	0.254801
Simulation	0.132503	0.0276202	0.0496429	0.215364

3.8.2 $\gamma d \to \pi^+\pi^- d$

The reactions,

$$\gamma d \to \begin{cases} \rho d \to \pi^+\pi^- d, \\ N\Delta \equiv d^*\pi^\pm \to \pi^+\pi^- d, \end{cases} \tag{3.9}$$

both have the same final state particles and a cut around the zero missing mass squared ensures an exclusive sample along with some background. The missing mass squared

distributions for the data sample and the simulation are shown in Figure 3.13. The objective of this cut is to ensure an exclusive sample of $\pi^+\pi^-d$ events irrespective of where they decayed from. As the cuts are loose, one can expect some background events too in the sample. As the width of this distribution is very narrow (from observation), the background due to this this cut does not make a significant contribution.

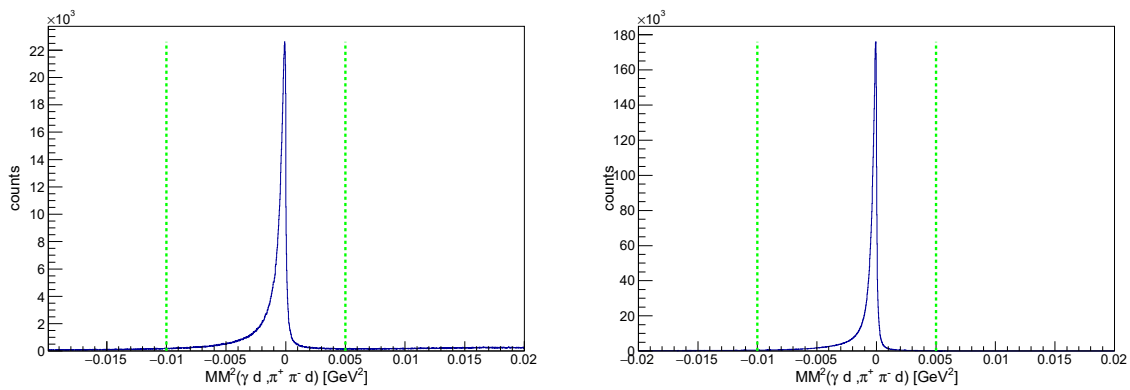

Figure 3.13: The missing mass squared distribution for both data (left) and simulation (right) to select exclusive ρ events along with some background. The dashed lines in green represent the position of the cuts made.

3.9 Summary

This chapter discussed about how the data were skimmed and the channels were separated to extract the signal yield. A number of cuts was applied to reduce the background and enhance the signal. Various corrections were applied to the selected events to incorporate known or speculated discrepancies. The next three chapters will focus on the extraction of signal events along with the production of simulated events for the detector acceptances.

4 Simulation and Acceptance

Measurement of the differential cross-section requires calculation of the acceptance of the CLAS detector. This uses an understanding of not only the detector geometry but also the efficiencies of the detector subsystems. The CLAS acceptance is determined by performing Monte-Carlo (MC) simulation. Although the CLAS detector is designed to provide near 4π coverage, the detector still has blind spots (such as the physical gap in between the calorimeters) or other inefficient regions. These real conditions need to be taken into account to get the true acceptance of the detector for the reactions under investigation.

As the acceptance is reaction dependent, events for the three channels,

$$\gamma d \rightarrow \begin{cases} \rho d \rightarrow \pi^+\pi^- d, \\ \omega d \rightarrow \pi^+\pi^- d(\pi^0), \\ N\Delta \equiv d^*\pi^\pm \rightarrow \pi^+\pi^- d, \end{cases} \tag{4.1}$$

were separately generated. After event generation, the simulated particles were sent through a model of the detector using the GSIM software [Hol]. The result is a file of events that look very similar to the real data, with the same detector blind spots and the same detector tracking and resolution.

4.1 Event Generation

The event generator used in this analysis is `fsgen`, which is a `FORTRAN` code based on `PYTHIA` package [Ste06]. The `fsgen` generates events based on input parameters and settings. These include target material and its position, incident photon energy and the energy range, reaction products, possible decay channels, and the t-slope parameter. The t-slope parameter is an important input for reactions that are diffractive in nature where the differential cross-section varies as an exponential function of the 4-momentum transfer, t.

Agreement between simulated and data events are obtained by the phase space distribution weighted by an exponential t-slope. In the present context, events with final state ωd, ρd and $d^*\pi$ were separately produced leading to the detected final state $\pi^+\pi^- d(\pi^0)$ for the ω-channel and $\pi^+\pi^- d$ for the ρ- and d^*-channels. The branching ratios were not included (since the decays were generated directly by `fsgen`) but were taken into account later in the differential cross section calculation wherever applicable. One thing to note here is that the d^* is a new resonance and the input values for the simulation such as the mass and width were fed based on observation of the signal in the data.

For any diffractive channel, the differential cross section as a function of t can be described mathematically by,

$$\frac{d\sigma}{dt} = \sigma_0 e^{-bt}, \tag{4.2}$$

where $\frac{d\sigma}{dt}$ is the differential cross section, b is the t-slope parameter, and σ_0 is the amplitude of the cross section at $t = 0$. For the ω-channel, the simulations used in the present study use $b = 2.5$ GeV^{-2} and for the ρ-channel the nominal value used is $b = 1.5$ GeV^{-2}. The effect of a different t-slope ($b = 0$ and $b = 1.5$ GeV^{-2}) was also studied for the ω-channel. As the d^* channel is a new one, events were generated with $b = 0$ GeV^{-2} as a first-order approximation.

4.2 Event Processing for Simulated Events

The generated events for the reaction channels under investigation underwent a series of processing, which are briefly discussed below:

`GSIM:` It is a `GEANT` based simulation package used for the simulation of events. It processes the events produced by `fsgen` by propagating the particles through various codes that take into account the physical design of the detector including some known factors such as the blind spots in CLAS. The digitized signal through the simulated detector and its components were then collected and stored.

gpp: The CLAS detector has some known imperfections. These were coded in the GSIM Post Processor (gpp). It adjusted the output of events for detector resolution depending on which subsystem each track would have hit.

user_ana The output of the GPP was then "cooked" by a program called `user_ana` to store information in a format much like that of the data. Additionally, some extra information related to the generated events were included which allows to extract photon energies and initial (vertex) angles associated with each track.

To illustrate an idea of the simulation parameters, the parameters for the MC simulations used for the study of $\gamma d \to \omega d$ are given in Appendix D.

4.3 Acceptance

The acceptance (A) is the ratio of the number of accepted events from the generated data by the total number of generated events given by

$$A = \frac{Y_{acc}}{N_{gen}}, \tag{4.3}$$

where Y_{acc} is the accepted yield of the simulated events and N_{gen} is the total number of generated events. Acceptance is a function of kinematic variable used to describe the observable. For the vector mesons, ρ and ω, the acceptance was calculated as a function of incident photon energy, E_γ and the momentum transfer, t. For the d^* resonance, it was calculated for the center-of-mass energy W binned in cosine of the polar angle, $\cos\theta_{CM}$, of the uncorrelated final state pion. Using the bin convention described in Sec. 5.1 (ω), Sec. 6.1 (ρ) and Section 7.2 (d^*), acceptances were calculated for each bin considered. The t-dependence of the acceptance for different energy bins are shown in Figure 4.1 and Figure 4.2 respectively for ω and ρ channels. Figure 4.3 shows the acceptance of d^{*++}-channel for different W bins as a function of $\cos\theta_{CM}$.

As the generated number of events are independent of any cut or corrections, it can be considered a constant for each kinematic bin. Therefore, the uncertainty associated with

the acceptance (σ_A) was calculated using,

$$\frac{\sigma_A}{A} = \frac{\sigma_{Y_{acc}}}{Y_{acc}} \tag{4.4}$$

where, $\sigma_{Y_{acc}}$ is the uncertainty associated with Y_{acc}. The acceptances for the three channels under investigation are all presented in Appendix E.

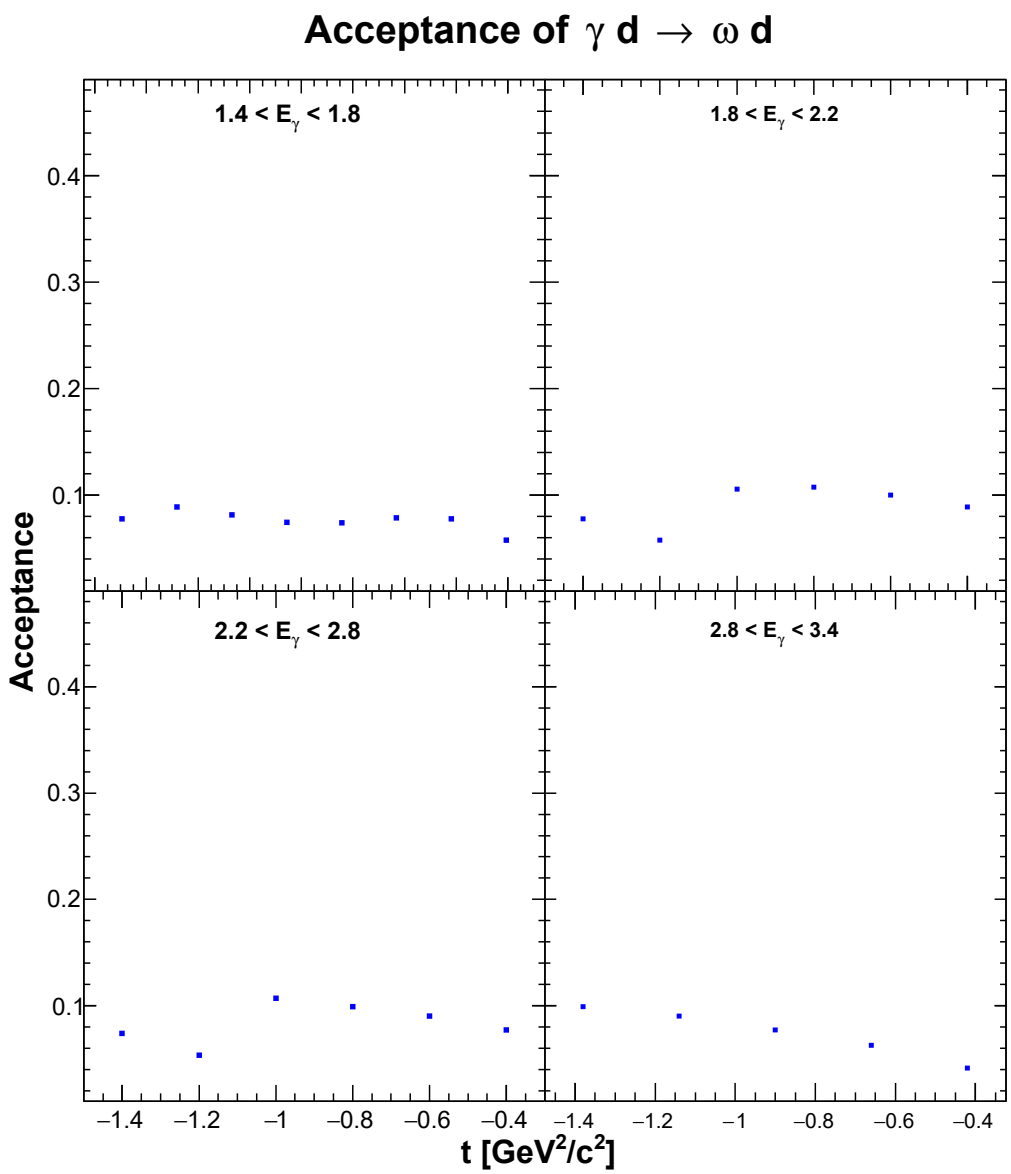

Figure 4.1: Acceptance of $\gamma d \rightarrow \omega d \rightarrow \pi^+\pi^- d(\pi^0)$. The accentance values are listed in Table E.1. The dip at $|t| \sim 1.0$ is due to the requirement of the EC trigger in the simulation as it was used in the data.

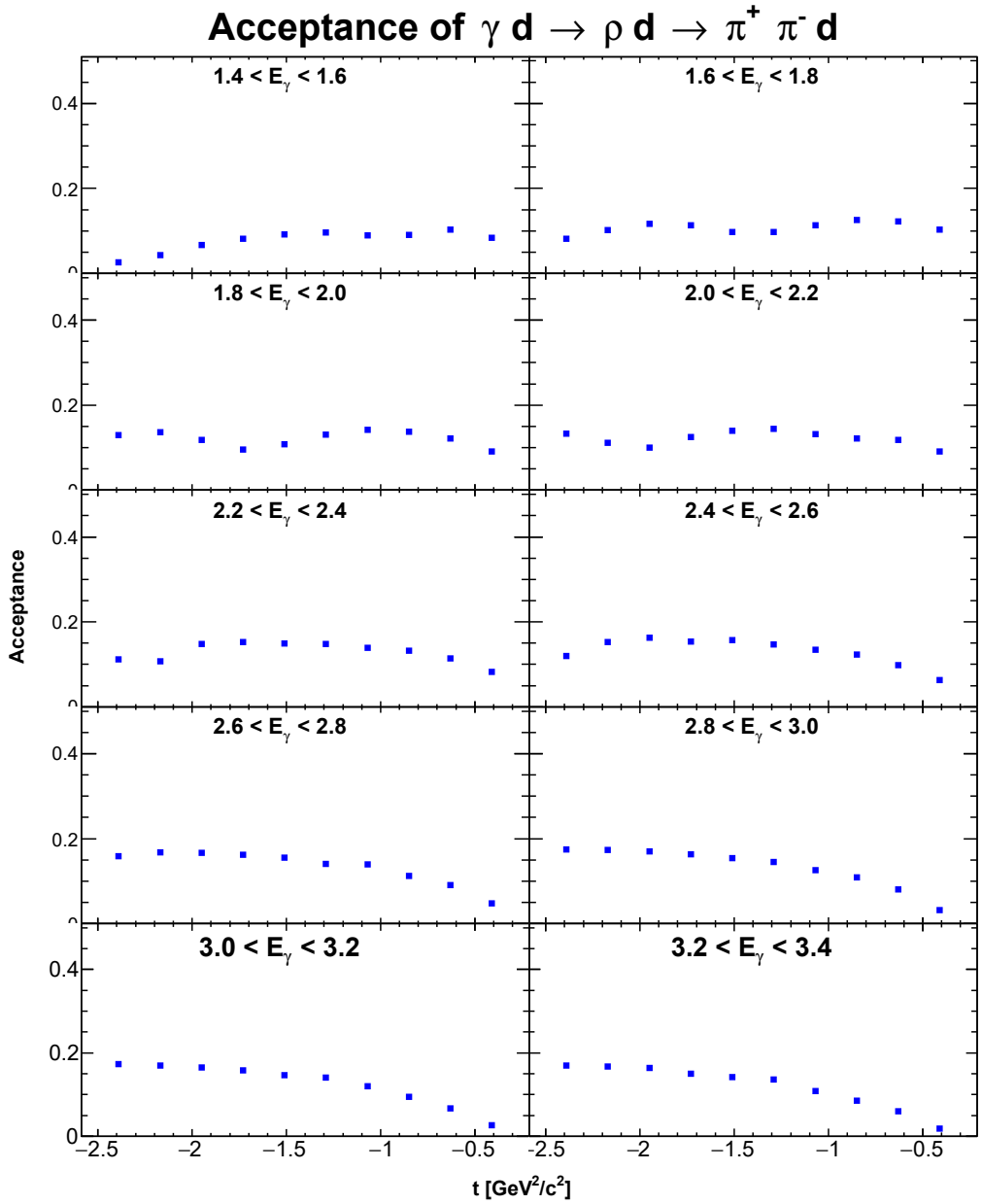

Figure 4.2: Acceptance of $\gamma d \to \rho d \to \pi^+\pi^- d$. The values are listed in Table E.2

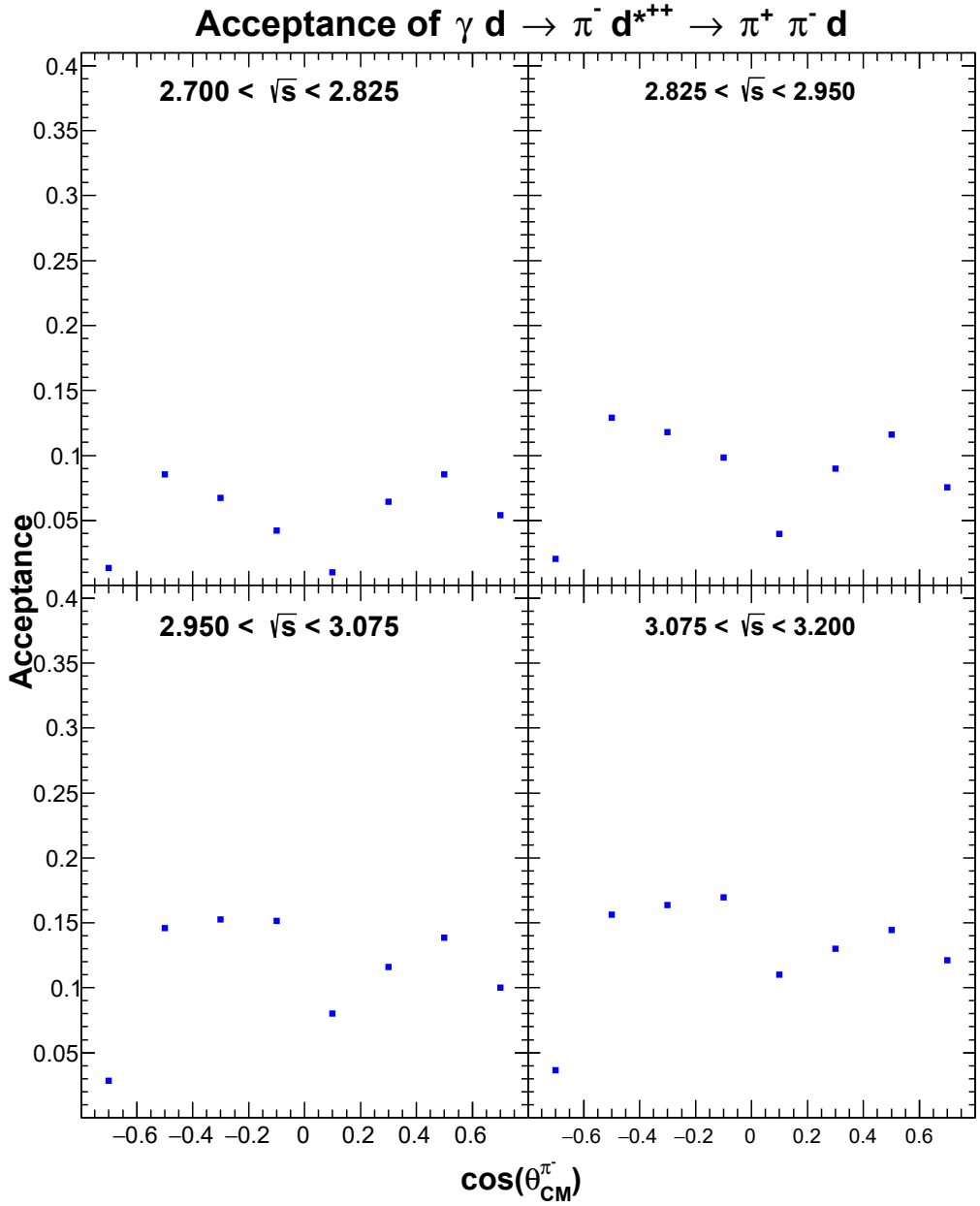

Figure 4.3: Acceptance of $\gamma d \rightarrow \pi^- d^{*++} \rightarrow \pi^+\pi^- d$. The values are listed in Table E.3

4.4 Summary

A detector has physical limits such as physical gaps in between the sectors where no tracking of particle is possible. These kinematic limitations are calculated in the form of the detector acceptance which is used to normalize the signal yield to correctly calculate any physical observables. Even though the same dataset is used with same final state particles, detector acceptance is reaction dependent. This is mainly because of the cuts used to select the events for each channel is different one way or another. As the accepted events should mirror the distributions in the data, the acceptances are different.

This chapter discussed the acceptances of the three channels which were used to calculate the differential cross sections. The following chapters discuss the yield extraction procedure for each reaction channels.

5 Omega Meson Photoproduction

5.1 Kinematic Binning

The events that passed through different cuts and selection were put in bins of incident photon energy (E_γ)and the four-momentum transfer, t, given by,

$$t = (P_\gamma - P_\omega)^2, \tag{5.1}$$

where P_ω is the four-momentum of the reconstructed ω-meson.

For this channel, four E_γ bins which were divided into different t bins in the range $0.3 < -t < 2.5$ were used. In total, the selected events were divided in 25 bins (dependent on E_γ and t). The binning scheme is shown in Figure 5.1 where the 4-momentum transfer is plotted as a function of the incident photon energy. Table 5.1 summarizes the binning scheme used in this analysis.

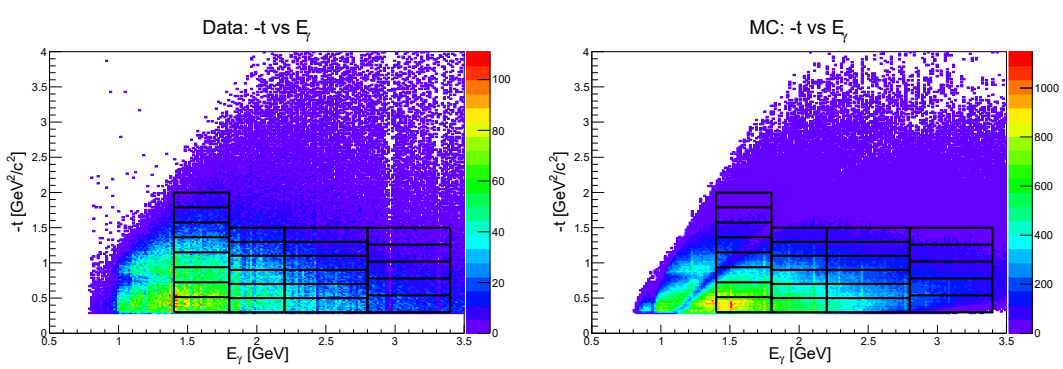

Figure 5.1: Binning scheme used in this analysis. These bins are filled with $-t$ as a function of E_γ.

It may be worthwhile to discuss here the reason for not including lower photon energy range in the analysis. The photon energy threshold for the reaction $\gamma d \rightarrow \omega d'$ can be

calculated using,

$$W_{th} = \sqrt{m_d^2 + 2E_{\gamma th} m_d} \tag{5.2}$$

where $W_{th} = m_{d'} + m_\omega$ is the center of mass energy at the threshold energy $E_{\gamma th}$. Using the PDG values for masses, $E_{\gamma th} \approx 0.94$ GeV. In fact, $1.0 < E_\gamma < 1.4$ GeV should potentially contain events of interest. In addition, the d and π^+, π^- particles need a minimum momentum to be detected. Due to edge effects near the threshold, the acceptance is difficult to simulate with confidence. Because of this, the low energy region ($E_\gamma < 1.4$ GeV) was excluded from the analysis.

Table 5.1: The table lists ranges of incident photon energies for each energy bin considered. Each energy bin is further divided into N_B bins. The 4-momentum ranges are also shown along with the bin width, $\Delta t (= \frac{|t_{max} - t_{min}|}{N_B})$, for the corresponding t-bins.

Energy Bin #	E_γ [GeV]	N_B	t_{min} [(GeV/c)^2]	t_{max} [(GeV/c)^2]	Δt [(GeV/c)^2]
1	1.4 - 1.8	8	-2.0	-0.3	0.2125
2	1.8 - 2.2	6	-1.5	-0.3	0.2
3	2.2 - 2.8	6	-1.5	-0.3	0.2
4	2.8 - 3.4	5	-1.5	-0.3	0.24

5.2 Luminosity

The quantity that measures the ability of a particle accelerator to produce the required number of interactions is called the Luminosity, $\mathscr{L}$. It was calculated from the incident photon flux (N_γ), target density (ρ_T), atomic mass weight (M_d) and length of the target (l_T) using the relation:

$$\mathscr{L}(E_\gamma) = \frac{\rho_T N_A l_T}{M_d} N_\gamma(E_\gamma) \tag{5.3}$$

where N_A is the Avogadro's number. The uncertainty associated with $\mathscr{L}(E_\gamma)$ was calculated using

$$\sigma_{\mathscr{L}} = \mathscr{L} \times \sigma_{N_\gamma} \tag{5.4}$$

Numerical values of these parameters for the g10 experiment are shown in Table 5.2.

Table 5.2: Parameters for the luminosity calculation for the reaction $\gamma d \rightarrow \omega d$.

Name	Description	Value
N_γ	Incident photon flux	Table 5.3
ρ_T	Density of Liquid Deuterium (LH2)	0.163 g/cm^3
M_d	Atomic mass weight of deuteron	2.0140 g/mol
l_T	Length of the g10-target	24 cm
N_A	Avogadro's Number	6.022 $\times 10^{23}$ mol^{-1}

N_γ and σ_{N_γ} were calculated for each energy bin using flux files mentioned in Section 3.2.2 and Appendix B.5. For each energy range, the incident photon flux and luminosity is listed in Table 5.3.

Table 5.3: Incident photon flux (N_γ) and luminosities are listed for the indicated photon energy ranges. The uncertainties were calculated for each energy range. The uncertainties are shown inside the parentheses, which is a shorthand notation to display uncertainties (for example, $5.7535(64) \times 10^{12}$ would mean $5.7535 \times 10^{12} \pm 0.0064 \times 10^{12}$ and so on). See Appendix B.5 for more details about photon flux and associated uncertainties.

Energy Bin #	E_γ [GeV]	$N_\gamma \times 10^{12}$	$\mathscr{L}$ $[pb^{-1}]$
1	1.4–1.8	5.7535(64)	6.9779(78)
2	1.8–2.2	4.0695(53)	4.9355(64)
3	2.2–2.8	5.0866(59)	6.1691(71)
4	2.8–3.4	4.3401(54)	5.2637(65)

5.3 Yield Extraction

This section deals with the yield extraction procedure and discusses about different functions used to fit the signal and the background for the missing mass distribution, $M(\gamma d, d)$. The signal shape is fit using a Voigt function[10],

$$V(x-\mu, \sigma_G, \sigma_L) = G(x, \sigma_G) \otimes L(x, \sigma_L) \tag{5.5}$$

where $\otimes$ represents the convolution between a Gaussian,

$$G(x, \sigma_G) = \frac{1}{\sqrt{2\pi}\sigma_G} e^{-\frac{(x-\mu)^2}{2\sigma^2}} \tag{5.6}$$

and a Lorentzian function,

$$L(x, \sigma_L) = \frac{1}{\pi} \frac{\sigma_L/2}{(x-\mu)^2 + (\sigma_L/2)^2} \tag{5.7}$$

[10] Standard ROOT CERN library function `TMath::Voigt` is used for this purpose [B+].

with $x = MM(\gamma d, d) \equiv M(\pi^+\pi^-\pi^0)$, μ is related to the PDG values of the M_ω and and σs are related to the resolution and the ω-meson decay width respectively.

The main challenge in the yield extraction process was to make a good estimation of the background. A phenomenological 2nd-order polynomial function was nominally used to describe the background[11]. Mathematically, the background function is written as

$$F_{BG}(x) = p_1 + p_2 x + p_3 x^2, \tag{5.8}$$

where p_i's are fit parameters. Therefore the $MM(\gamma d, d)$ distribution was fit using the total function,

$$T(x) = V(x - \mu, \sigma_G, \sigma_L) + F_{BG}(x). \tag{5.9}$$

As the Lorentzian width represents the physical width of ω-meson, therefore σ_L was kept fixed to the PDG value ($\sigma_L = \Gamma_\omega = 0.00849$ GeV) in the final fit.

The yield is then given by

$$Y_D = I_V \times \frac{N_{bins}}{Hist_{range}}, \tag{5.10}$$

where the $Hist_{range}$ is the range of the histogram (in GeV) used for $MM(\gamma d, d)$ distribution in N_{bins} (in Counts/GeV) and the integration of the function I_V,

$$I_V = \left(\int_{\mu-4\sigma_G}^{\mu+4\sigma_G} V(x)dx \right), \tag{5.11}$$

is calculated using standard ROOT functions.

The uncertainty on the yield is given by

$$\sigma_{Y_D} = \sigma_I \times \frac{N_{bins}}{Hist_{range}} \tag{5.12}$$

where the integration error, σ_I, is calculated using the standard ROOT function:

`IntegralError`$(\mu - 4\sigma_G, \mu + 4\sigma_G)$ of $V(x)$.

[11] At this point, no attempt is made to address the physics of the background

5.4 Differential Cross Sections

The differential cross sections were measured in four photon energy bins. In each energy bin, the differential cross sections in momentum transfer bins of width Δt were calculated using the relation:

$$\frac{d\sigma}{dt} = \frac{Y_D}{\Delta t A \mathscr{L}} \times \frac{\Gamma_\omega}{\Gamma_{\omega\to\pi^+\pi^-\pi^0}} \times \gamma_{corr} \tag{5.13}$$

where Y_D is yield, A is the detector acceptance, $\mathscr{L}$ is the target luminosity for the photon energy range considered and $\Gamma_{\omega\to\pi^+\pi^-\pi^0}/\Gamma_\omega$ is the branching ratio. The quantity γ_{corr} is the correction factor due to photon selection condition discussed in Section 3.4 given by

$$\gamma_{corr} = 1 + \frac{N_{N_\gamma>0} - N_{N_\gamma=1}}{N_{N_\gamma>0}}, \tag{5.14}$$

and was found to be $\sim 1.07\%$.

The statistical uncertainty on the differential cross section is given by

$$\sigma_{d\sigma/dt} = \frac{d\sigma}{dt} \times \sqrt{\left(\frac{\sigma_{Y_D}}{Y_D}\right)^2 + \left(\frac{\sigma_A}{A}\right)^2} \tag{5.15}$$

The systematic uncertainty (see Section. 5.5), added in quadrature with the statistical uncertainty gave the total error on the differential cross section values. The differential cross sections for each E_γ and t bins are shown in Figure 5.2. Table F.3 in Appendix F lists the nominal differential cross sections for each energy bin. Note here that the results are plotted as a function of t for each energy bin, where the t values represent the bin centers.

The differential cross section for $\gamma d \to \omega d$ is largest at the lower $|t|$, and decreases with increasing photon energy. This is mainly because the reaction is dominated by natural parity exchange in the t-channel at low $|t|$. Secondary scattering at high $|t|$, where the ω is produced off one nucleon and scatters off from the second enable to extract the vector meson-nucleon scattering cross section ($\sigma_{\omega N}$) using theoretical models. The model used to extract the cross section is explained in Chapter 9.

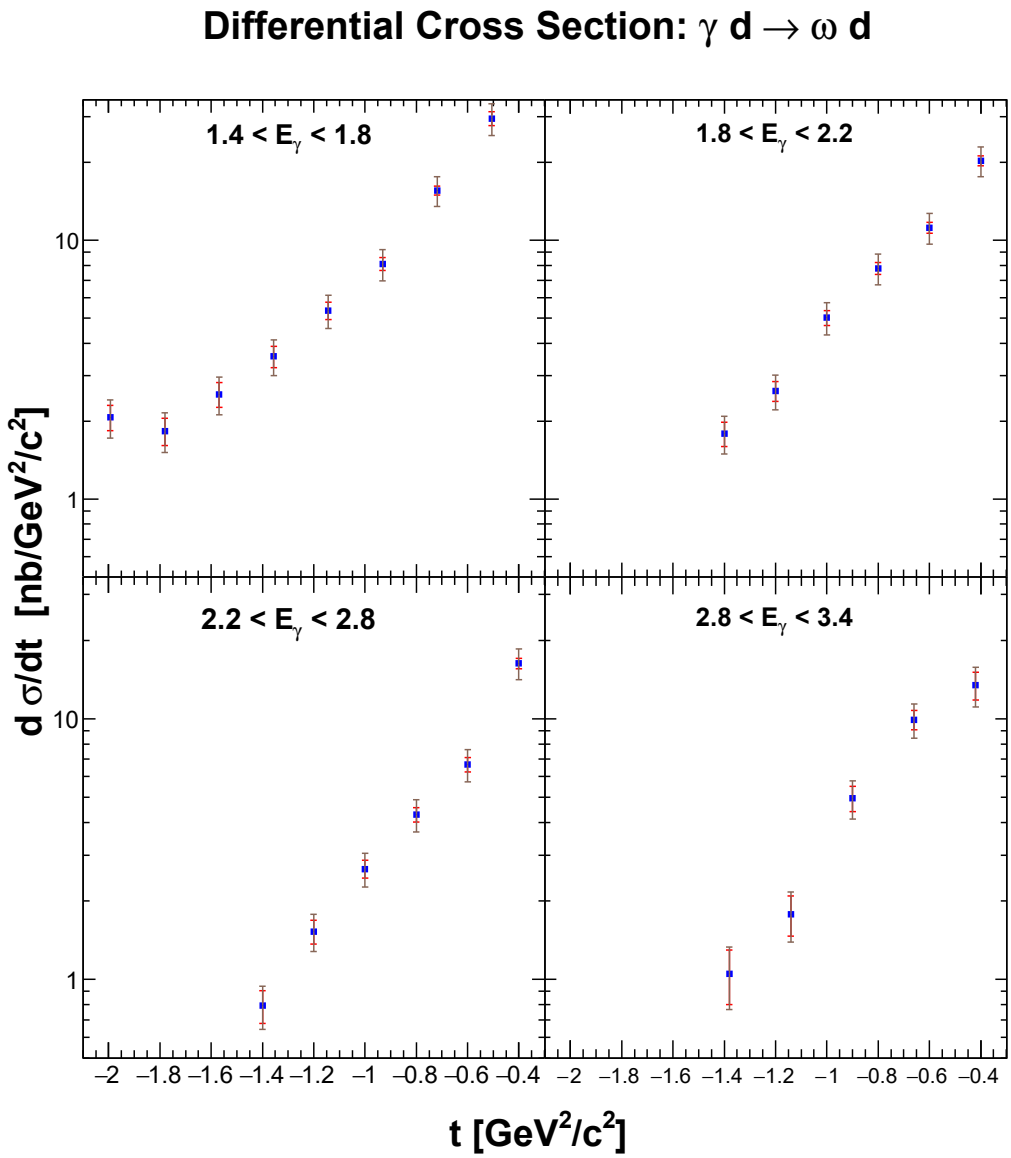

Figure 5.2: The differential cross sections of $\gamma d \rightarrow \omega d$ using the channel $\gamma d \rightarrow \omega d \rightarrow \pi^+\pi^- d(\pi^0)$ as a function of four momentum transfer (t) for different incident photon energy ranges. The outer error bars (in brown) include systematic uncertainties along with statistical errors (shown in red).

5.5 Systematic Uncertainties

$$Relative\ Difference = \frac{R_{Nominal} - R_{variation}}{R_{Nominal}} \tag{5.16}$$

where $R_{Nominal}$ is the differential cross section quoted and $R_{variation}$ is the differential cross section (unless mentioned otherwise in the text) calculated by varying any specific cut.

5.5.1 Flux Consistency/Luminosity

Ideally, as the measured photon flux increases, the extracted yield should also increase. This yield could, in general, be extracted from events by an arbitrary set of cuts employed on all detected tracks. By utilizing a preliminary $d\pi^+\pi^-$ skim, a specific yield was obtained for the number of events with the set of π^+, π^- and d per run. The events that correspond to beam trips were subtracted from this subset. The resultant yield was normalized, or divided, by the total number of incident photons in the run.

The normalized yield $\mathscr{N}$ is defined by the ratio of the yield (events produced) and the incident flux F (incoming photons in this case). Mathematically, it is given by

$$\mathscr{N} = \frac{Y}{F} \tag{5.17}$$

where Y is the yield and F is the incident photon flux. Now, in order to check the consistency, the total normalized yield for each run r is calculated using

$$\mathscr{N}_r = \frac{\sum_r Y}{\sum_r F} \tag{5.18}$$

In this analysis, events that passed the EC flag were only considered. With this flag, $\mathscr{N}_r$ is shown in Figure 5.3 as a function of run number. One can clearly see that the flag helps to remove the inconsistency in the flux by a visible amount. The normalized yield per sub-run is shown in Figure 5.4.

The fluctuation of the normalized yield is in part due to systematic as well as statistical uncertainties. To quote the uncertainty, fluctuation in normalized yield per sub-run was

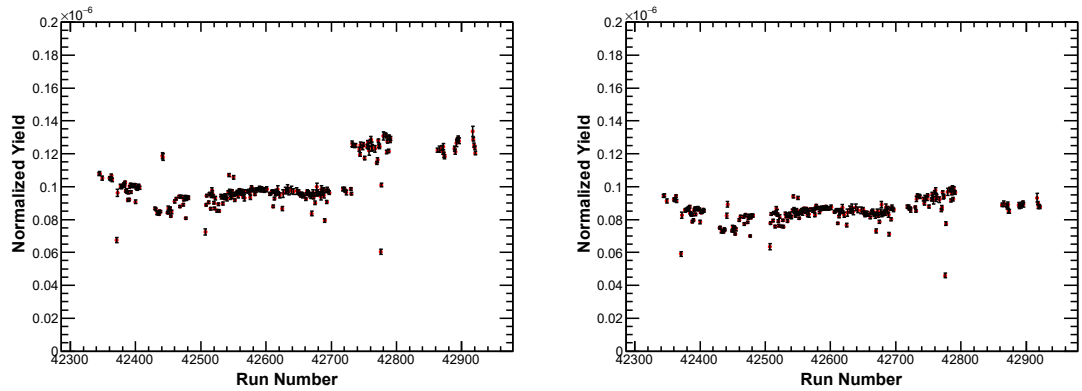

Figure 5.3: The total normalized yield for each run used in this analysis. The left plot is with the EC flag turned OFF while the right is with the flag ON.

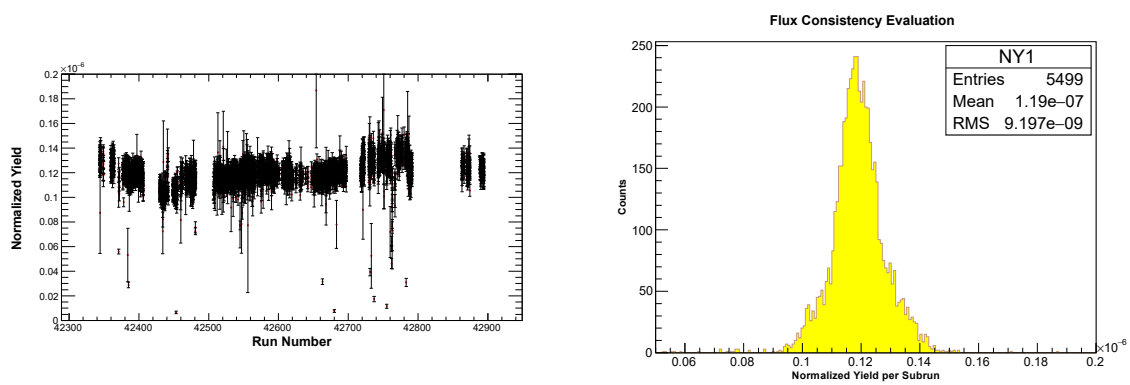

Figure 5.4: On the left, shown is the normalized yield with EC flag ON for each sub-run used in this analysis. The right plot is the y-projection to show the fluctuation in normalized yield per subrun.

used. It is given by

$$\sigma_{NY} = \frac{\sigma}{\mu} \tag{5.19}$$

where μ and σ are the mean and RMS of the distribution shown in Figure 5.4(right). σ_{NY} was found to be less than 8%. Study of systematic uncertainties on the target luminosity

was done by previous analyses using $g10$ data set [CHC14, C$^+$09, Q$^+$09, Mib07]. They quote $5 - 10\%$ systematic effect. As the studies of the flux consistency and the target luminosity are related, we quote 8% systematic effect due the flux inconsistencies and the integrated luminosity.

5.5.2 t-Slope Dependence

The acceptance used in this analysis was calculated using events generated with a t-slope parameter, $b = 2.5$ (e.g. 4.2). The parameter b can be adjusted to different values by a user in `fsgen`, when generating simulation events. A different set of events using t-slope of $b = 0.0$ was generated to observe the effect of adjusting this parameter. The parameter $b = 0.0$ was chosen to see the effect for a set which represents a pure phase space at the extreme end of the possible variations of t-slopes.

In order to calculate the systematic uncertainties, the differential cross sections were calculated using the acceptance from the new simulation. The new simulated events passed through the same corrections and cuts as that of nominal set. The average relative difference of the differential cross sections of the two sets was found to be 4.13% from the Mean as shown in Figure 5.5.

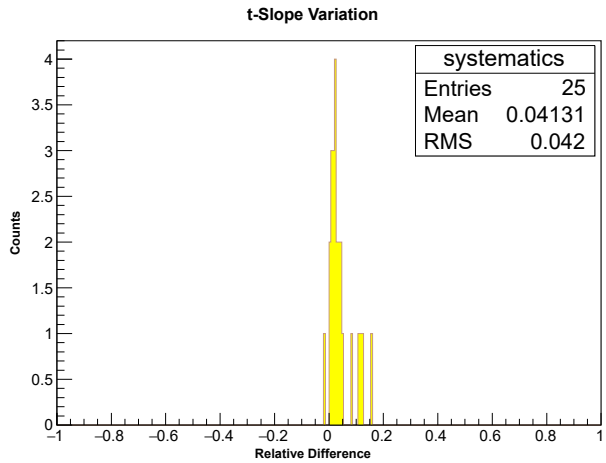

Figure 5.5: The systematic effect of the differential cross sections over all energy and t bins when comparison was made between a generated simulation using $b = 0.0$ and the nominal $b = 2.5$.

5.5.3 Sector Dependence

The sector-dependent uncertainties were determined by computing the acceptance-corrected yields with d hits for a given sector removed from the analysis, and comparing it to the nominal acceptance-corrected yields. SR_i will be used as a notation to refer to the dataset for a given sector, i, removed.

The yield of deuterons at each E_γ and t bin for each SR for data is represented by,

$$N_{data}(d) \pm \sigma_{N_{data}(d)}, \tag{5.20}$$

where

$$\sigma_{N_{data}(d)} = \sqrt{N_{data}(d)} \tag{5.21}$$

The same yield in the simulation for accepted events was also found:

$$N_{MC}(d) \pm \sigma_{N_{MC}(d)}, \tag{5.22}$$

where

$$\sigma_{N_{MC}(d)} = \sqrt{N_{MC}(d)} \tag{5.23}$$

Using these, the accepted-corrected yield R for each SR is then given by

$$R_{SR} = \frac{N_{data}(d)}{N_{MC}(d)}. \tag{5.24}$$

The uncertainty on this ratio was calculated using

$$\sigma_{R_{SR}} = R_{SR} \times \sqrt{\left(\frac{\sigma_{N_{data}(d)}}{N_{data}(d)}\right)^2 + \left(\frac{\sigma_{N_{MC}(d)}}{N_{MC}(d)}\right)^2} \tag{5.25}$$

To investigate the sector dependence, the weighted average of each R_{SR} was calculated using

$$(R_{SR})_{av} = \frac{\sum_{SR=1}^{6} R_{SR}\sigma^2_{R_{SR}}}{\sum_{SR=1}^{6} 1/\sigma^2_{R_{SR}}}. \tag{5.26}$$

When the ratio of the acceptance-corrected yields and their weighted average is plotted, one can expect the values at one. Mathematically, this ratio is given by

$$Ratio(SR) = \frac{R_{SR}}{(R_{SR})_{av}}. \tag{5.27}$$

The weighted average takes into account of individual errors and can therefore be treated as a constant. Therefore the uncertainty associated with this ratio was calculated using

$$\sigma_{Ratio(SR)} = \frac{\sigma_{R_{SR}}}{(R_{SR})_{av}} \tag{5.28}$$

The ratio for each SR is visualized in Figure 5.6. The variation of this ratio with the nominal value of 1 for all bins (25 E_γ and t bins) is shown in Figure 5.7. One can see that there is a variation in the "Mean" listed in the legend of each plot of about 1–2%.

The dependence on each sector can also be found by calculating differential cross sections for each SR. A comparison between the weighted average of the differential cross sections for each SR and the nominal differential cross section is shown in Figure 5.8. A systematic effect of $\sim< 1\%$ is found for this case. From the above discussion, a 2% systematic effect can be safely attributed to the CLAS sectors' variation.

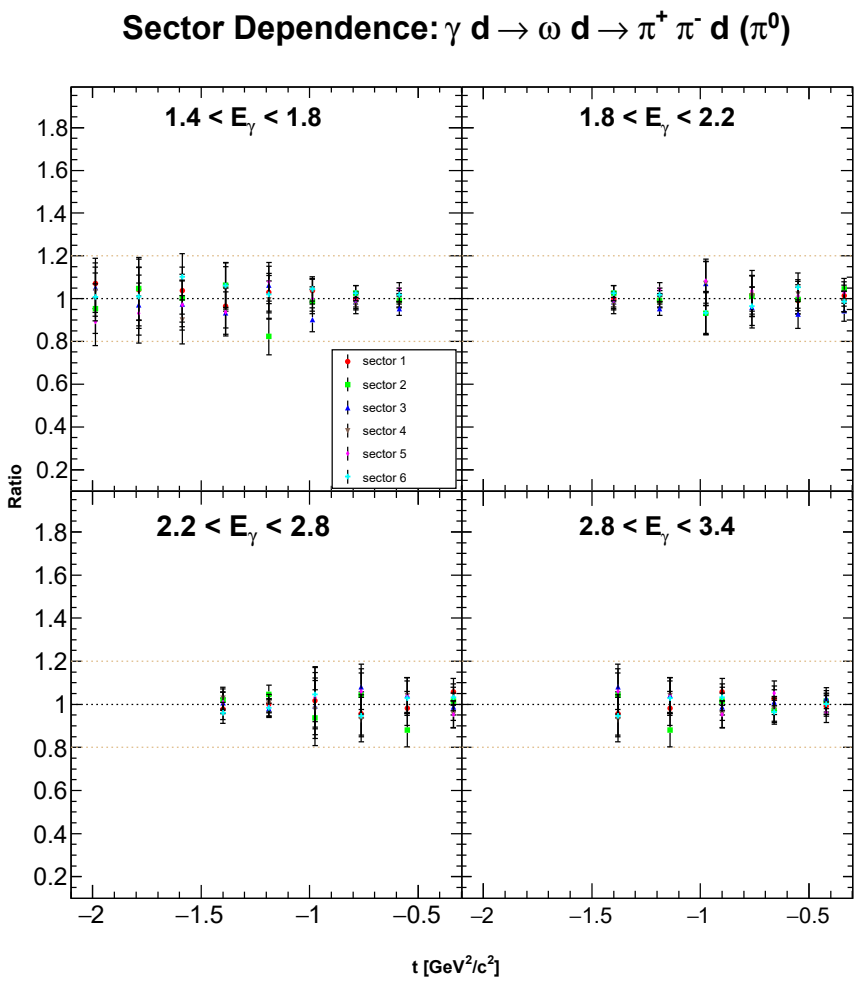

Figure 5.6: The weighted ratio of acceptance-corrected yield for d when a sector was removed. The sector # in the legend represents the corresponding SR.

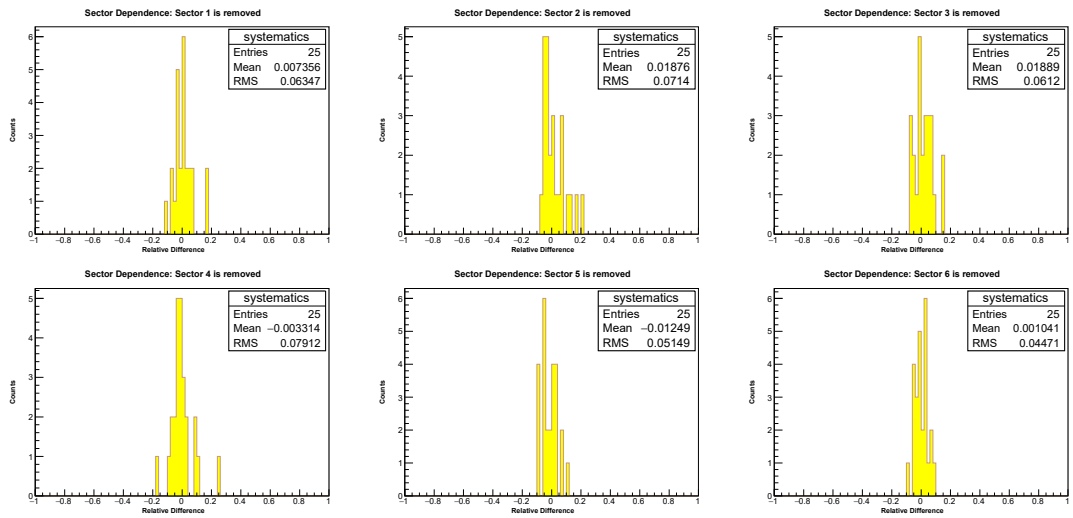

Figure 5.7: The relative differences measured between the weighted ratio of acceptance-corrected yield for d for each sector removed over all E_γ and t bins with respect to their weighted average. These plots are actually the y-projections of Figure 5.6 shifted by 1.0 to center at zero.

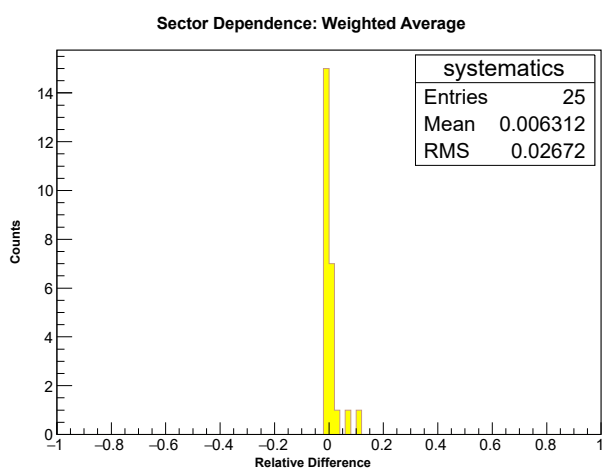

Figure 5.8: The relative differences measured between the weighted ratio of differential cross sections for d for each sector removed over all E_γ and t bins compared with the nominal result.

5.5.4 Timing Cut in PID

The particle identification scheme discussed in Sec. 3.3 could be adjusted to a different cut. The δt cut was expanded from the nominal $3\sigma_{\delta t}$ to a $3.5\sigma_{\delta t}$ to observe the effect. The differential cross section obtained using the new cut was compared to the nominal value. The result was a systematic effect of 0.60% as seen from the "Mean" in Figure 5.9.

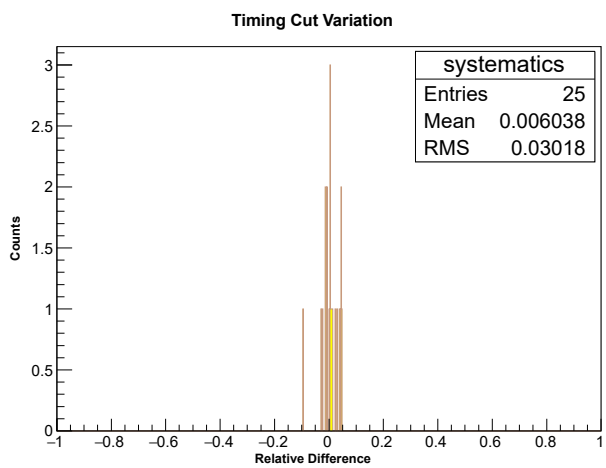

Figure 5.9: The systematic effect over all energy and t bins using the variation in the PID scheme discussed in the text.

5.5.5 Minimum Momentum Cut Variation

When the minimum momentum conditions on the detected particles were removed, the differential cross section obtained was compared to the nominal value. The result was a systematic effect of 0.52% as seen from the mean in Figure 5.10.

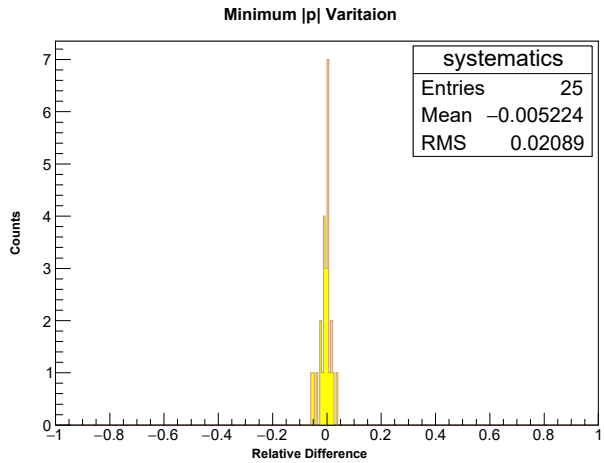

Figure 5.10: The systematic effect over all energy and t bins by removing the minimum momentum condition.

Typically the momentum distribution depends on the polar angles. However, the systematic study suggests that the cuts employed in this analysis have a very small effect. Evidently, majority of the the events of interest were retained by the cut.

5.5.6 Missing Mass Cut

The selection cut of 3σ about the centroid of the fit in the missing mass distribution (Sec. 3.8.1) was changed to study the systematic effect. The variation to a 2.5σ contributes 3.46% to the systematic uncertainties on the result.

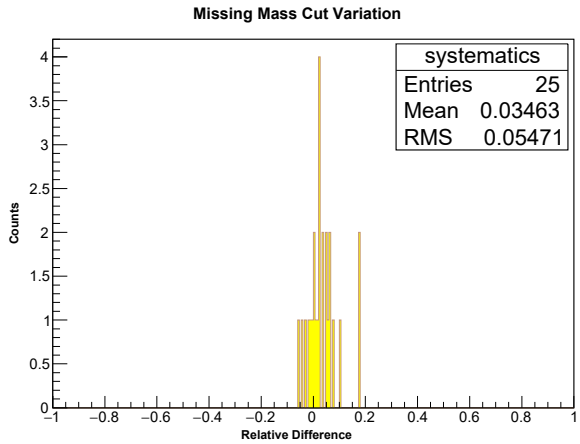

Figure 5.11: The systematic effect over all energy and momentum transfer bins by varying the missing mass cut.

5.5.7 z-Vertex Cut

With a new cut on the target location of $|z + 25| < 11.5$, the systematic effect of 0.73% on the result was found.

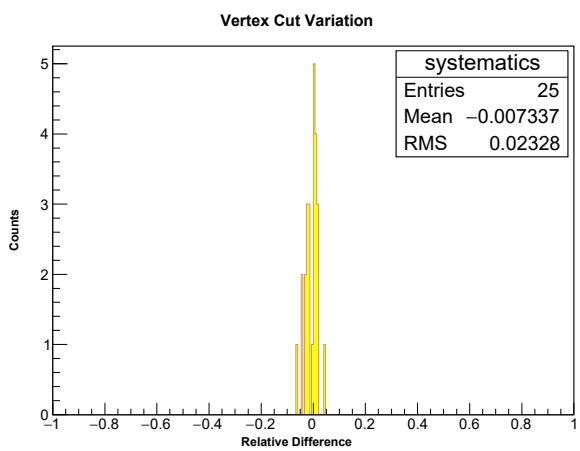

Figure 5.12: The systematic effect over all energy and momentum transfer bins by varying the z-vertex cut.

5.5.8 Fiducial Cut

The cut explained in Sec. 3.6.3 was changed from the nominal 50% cut to a 100% cut (Illustrated in Figure B.9c of Appendix B.2). The result was a sytematic effect of 1.34%.

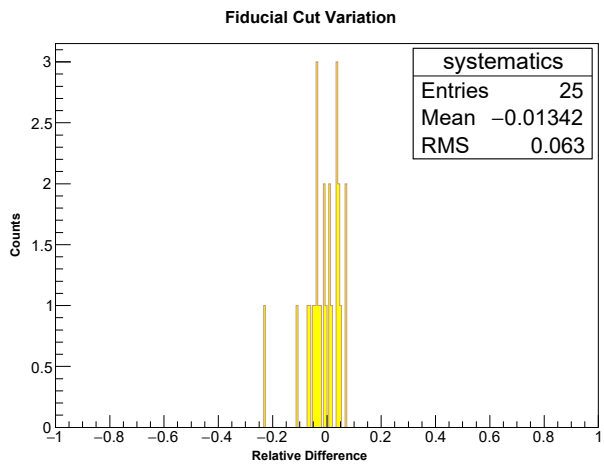

Figure 5.13: The systematic effect over all energy and momentum transfer bins by varying fiducial cut. Few E_γ and t bins show a big variation because of big statistical fluctuations.

5.5.9 Signal Integral Range Variation

In Secs. 5.3 and F.1, a 4σ integral range was considered during the extraction of the yield. When this range was expanded to 5σ, a very small 0.10% systematic effect was seen.

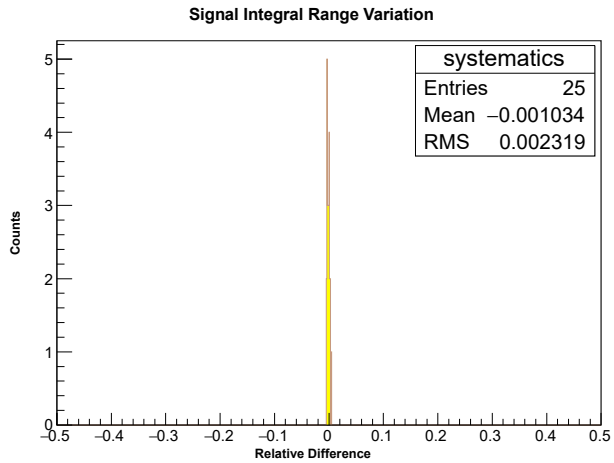

Figure 5.14: The systematic effect over all energy and momentum transfer bins by varying signal integral range.

5.5.10 Background Function

When the background function used nominally was replaced by a polynomial function of the first order given by

$$F_1(x) = p_1 + p_2 x, \tag{5.29}$$

where p_i's are parameters, the result had a systematic effect of 8.59%. This contributes as the highest source of systematic uncertainty in this analysis. Appendix F.3 compares the fits using these two functions.

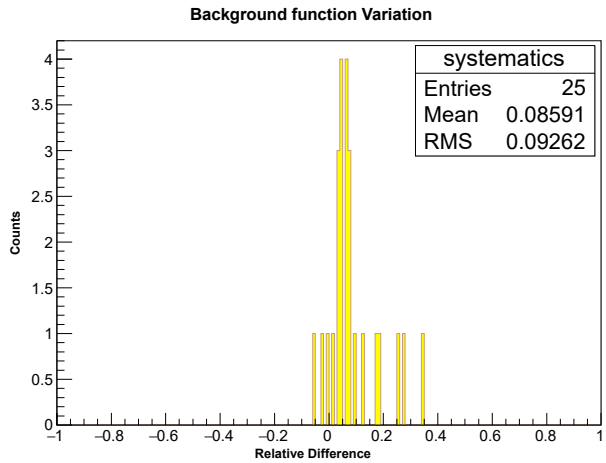

Figure 5.15: The systematic effect in the differential cross section when using a 1st order polynomial function over all E_γ and t bins compared to the nominal value.

5.5.11 Branching Ratio

The three pion decay mode, i.e. $\omega \to \pi^+\pi^-\pi^0$ [O+14] ($\frac{\Gamma_i}{\Gamma} = (89.2 \pm 0.7)\%$) is the major ω-meson decay mode. While generating the simulated events, the branching factor was not taken into account. Therefore, the correct acceptance would be to multiply this factor. As the uncertainty in this factor directly affects all the calculated values equally, this is a systematic effect. Therefore an overall unvertainty of 0.7% was taken as the branching ratio systematic uncertainty.

5.5.12 Systematic Uncertainties Summarized

Table 5.4 summarizes the systematic uncertainties calculated in this analysis. Each systematic effect mentioned in the previous sections contributes to the total systematic uncertainty. Assuming each uncertainty was independent, the total systematic uncertainty was calculated by adding each effect in quadrature.

Table 5.4: Summary of the systematic uncertainties found in this analysis.

Source	**Description**	**Uncertainty**
Flux Consistency/Luminosity	Sec. 5.5.1	8.00%
t-slope dependence	Varied from $b = 2.5$ to $b = 0$	0.04%
Sector Dependence	Sec. 5.5.3	2.00%
Timing Cut	Varied from a 3σ to 3.5σ cut	0.60%
Minimum $\|p\|$ Cut	Removed	0.52%
Missing Mass Cut	Varied from a 3σ to 2.5σ cut	3.46%
z-Vertex Cut	Varied from $\|z + 25\| < 11$ to $\|z + 25\| < 11.5$	0.73%
Fiducial Cut	Varied from a 50% to a 100% cut	1.34%
Signal Integral Range	Varied from 4σ to 5σ	0.10%
Choice of Background function	Sec. 5.5.10	8.59%
Branching Ratio	Reference [O$^+$14]	0.70%
Total Systematic Uncertainty (Added in quadrature)		**12.54%**

5.6 $\omega - N$ Scattering Cross Section

The measured differential cross section presented in Section 5 is compared to the calculated ones from a phenomenological model based on VMD [FKM$^+$97]. This model, as explained in Section 1.2, has been successful in describing the ρ-photoproduction data from SLAC [A$^+$71, FKM$^+$97] and ϕ-photoproduction using the g10 data ([M$^+$07]) off of deuterium target. As this model was initially tested on higher photon energies, we used this model to extract $\sigma_{\omega N}$ for the highest kinematic energy range considered in the analysis of $\gamma d \rightarrow \omega d$, i.e., $2.8 < E_\gamma < 3.4$ GeV. A total of six input parameters can be varied within the model:

1. the ratio of the real to imaginary parts of the corresponding scattering amplitudes, $\alpha_{\gamma N}$ and $\alpha_{\omega N}$;

2. the slope parameters $b_{\gamma N}$ and $b_{\omega N}$;

3. differential cross section of $\gamma N \to \omega N$ at $t = 0$, $\frac{d\sigma}{dt}\Big|_{t=0,\gamma N}$; and

4. the total scattering cross section, $\sigma_{\omega N}$.

In this work, the initial value for $\frac{d\sigma}{dt}\Big|_{t=0,\gamma N}$ was based on published data on $\gamma p \to \omega p$ [B$^+$03]. At intermediate and higher photon energies, VMD assumes the slope factors of the corresponding amplitudes, $b_{\gamma N}$ and $b_{\omega N}$, to be equal i.e., $b_{\gamma N} = b_{\omega N}$. . The variables, $\alpha_{\gamma N}$ and $\alpha_{\omega N}$, were kept fixed and equal to a phenomenological value of -0.4. Therefore, the total parameter space was reduced from six to just three, which were varied to calculate sets of differential cross section values as a function of t for the energy range. These were compared with the data using best fit based on the condition on the reduced chi-squares, χ^2/NDF. The variations of the parameters are shown in Table 5.5 and selective fits are shown in Figure 5.16. From this comparison, it can be concluded the data is consistent with the rescattering model with $30 < \sigma_{\omega N} < 40$ mb in the framework of the VMD model. This study provides the first ever cross section of the $\omega - N$ interaction in the high momentum transfer regime.

Table 5.5: Summary of theory parameters used to compare data for $2.8 < E_\gamma < 3.4$ GeV. The parameters shown here are within 15% of $\chi^2 = 1.0$ (the ideal value). This result was presented in Reference [C+18].

$b_{\gamma N} = b_{\omega N}$ $\left[GeV^{-2}/c^{-2}\right]$	$\frac{d\sigma}{dt}\Big\vert_{t=0,\gamma N}$ $[\mu b/(GeV^2/c^2)]$	$\sigma_{\omega N}$ $[mb]$	χ^2/NDF
7.5	15	31	1.13
8.0	14	34	1.15
8.0	15	33	1.01
8.0	16	32	0.96
8.0	17	31	1.00
8.0	18	30	1.15
8.0	19	30	0.91
8.0	19	31	0.87
8.0	20	30	1.03
8.5	16	35	1.11
8.5	16	39	1.00
8.5	17	34	1.05
8.5	18	33	1.07
9.0	19	39	0.89
9.0	20	38	0.87

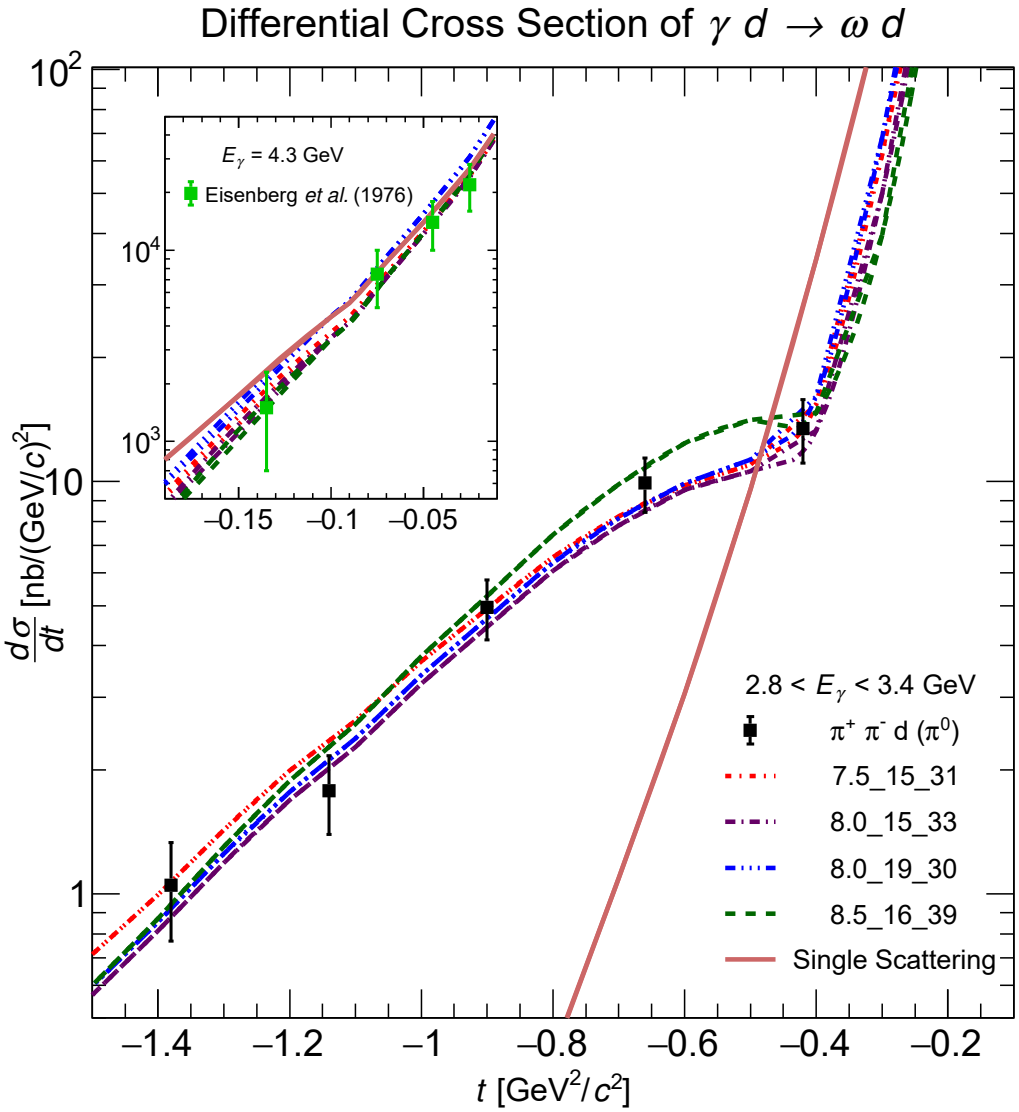

Figure 5.16: Differential cross section of $\gamma d \rightarrow \omega d$ as a function of $|t|$ for $2.8 < E_\gamma < 3.4$ GeV compared to that of a calculation based on [FKM+97]. Each curve corresponds to a specific b, $\frac{d\sigma}{dt}\Big|_{t=0,\gamma N}$ and $\sigma_{\omega N}$ value, as listed in Table 5.5. The legend for each curve is defined respectively for these parameters. The solid brown curve represents the contribution of the single scattering for input parameters corresponding to that of the red dashed-dotted curve. In the inset, the solid points are the results from [EHK+76] for an incident photon energy of 4.3 GeV. Image Source: [C+18].

5.7 Summary

This chapter presented the first measurement of the differential cross-section for the incident photon energies and 4-momentum transfer ranges considered. The $d\sigma/dt$ exhibits a smooth fall-off with t for all energies, as expected for a t-dependent reaction mechanism. The ω can be produced in two ways: single and double scattering off the nucleons. The single scattering is dominant at low momentum transfer. However, at higher $|t|$ the production of ω can be attributed mainly to the double scattering mechanism. At photon energies close to 3 GeV, a rescattering model based on VMD successfully parametrizes the vector meson production amplitude [FKM+97], allowing the extraction of $\sigma_{\omega N}$. For $2.8 < E_\gamma < 3.4$ GeV and in the high momentum transfer region, the total scattering cross section, $\sigma_{\omega N}$ was found to be within $30 - 40$ mb in the framework of the VMD.

6 ρ Meson Photoproduction

This chapter primarily focuses on the extraction of differential cross section for the channel $\gamma d \to \rho d$, where ρ decays nearly 100% of the time into π^+ and π^-.

6.1 Kinematic Binning

Similar to that of the ω-channel, the events that passed through different cuts and selection were put in 10 E_γ bins within $1.4 < E_\gamma < 3.4$ GeV. Each of these energy bins were further divided in 10 t bins each within $0.3 < |t| < 2.5$ GeV^2, where $t = (P_\gamma - P_\rho)^2$ with P_i being the 4-momentum of particle i. In other words, the selected events were divided in a total of 100 bins. The binning scheme is shown in Figure 6.1, where the 4-momentum transfer is plotted as a function of the incident photon energy and is summarized in Table 6.1.

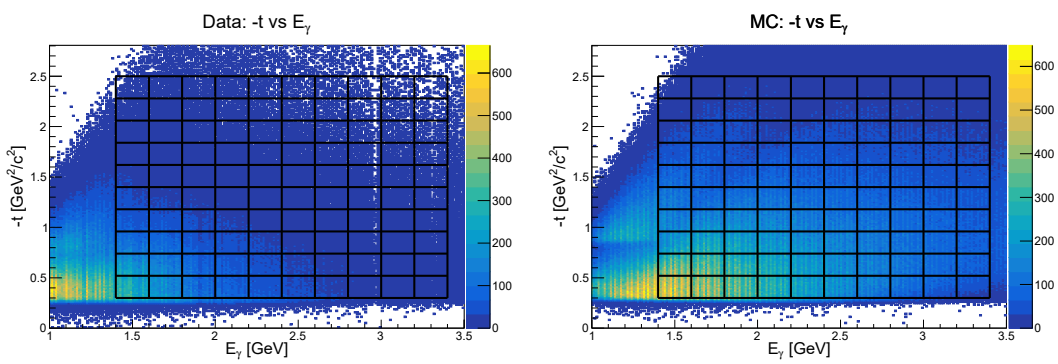

Figure 6.1: Binning scheme used for $\gamma d \to \rho d$ events filled as a function of E_γ and $-t$.

The binning region did not extend to low E_γ in the analysis due to the production threshold of the ρ-meson. Due to edge effects near the threshold along with the requirement of minimum momentum of the detected particles, it becomes very difficult to confidently simulate particles.

Due to some bad regions in the tagger, the energy distribution for the data and simulation do not exactly match. These regions are removed in the form of detector cuts from the simulated events.

Table 6.1: The kinematic ranges of E_γ and $|t|$ considered. Each of the 10 energy bins are further divided into 10 t bins.

Bin #		1	2	3	4	5	6	7	8	9	10
E_γ [GeV]	low	1.4	1.6	1.8	2.0	2.2	2.4	2.6	2.8	3.0	3.2
	high	1.6	1.8	2.0	2.2	2.4	2.6	2.8	3.0	3.2	3.4

Bin #		1	2	3	4	5	6	7	8	9	10
$\|t\|$ [GeV^2]	low	2.50	2.28	2.06	1.84	1.62	1.40	1.18	0.96	0.74	0.52
	high	2.28	2.06	1.84	1.62	1.40	1.18	0.96	0.74	0.52	0.30

6.2 Luminosity

The Luminosity, $\mathscr{L}$, is calculated from the incident photon flux (N_γ), target density (ρ_T), atomic mass weight (M_d) and length of the target (l_T) using Equation 5.3. The luminosities for each E_γ-bin is listed in Table 6.2 using the same method described in Section 5.2.

Table 6.2: Incident photon flux (N_γ) and luminosities are listed for the indicated photon energy ranges. The uncertainties are calculated for each energy range.

Energy Bin #	E_γ [GeV]	$N_\gamma \times 10^{12}$	$\mathscr{L}$ [pb^{-1}]
1	1.4-1.6	3.1037(48)	3.7642(58)
2	1.6-1.8	2.6506(44)	3.2147(53)
3	1.8-2.0	2.0384(37)	2.4722(45)
4	2.0-2.2	2.0316(37)	2.4640(45)
5	2.2-2.4	1.8553(36)	2.2501(43)
6	2.4-2.6	1.6656(34)	2.0201(41)
7	2.6-2.8	1.5663(33)	1.8997(39)
8	2.8-3.0	1.6816(34)	2.0395(41)
9	3.0-3.2	1.3728(30)	1.6649(36)
10	3.2-3.4	1.3133(29)	1.5928(36)

6.2.1 Yield Extraction

This section discusses the procedure that was used to extract the signal events for the reaction $\gamma d \rightarrow \rho d$, with $\rho \rightarrow \pi^+\pi^-$ as the only decay channel considered. Therefore, the invariant mass distribution of the detected pions, $M(\pi^+\pi^-)$ was used for the purpose.

The signal shape is fit using a Voigt function[12],

$$V(x-\mu, \sigma_G, \sigma_L) = G(x, \sigma_G) \otimes L(x, \sigma_L) \tag{6.1}$$

[12] Standard ROOT CERN library function `TMath::Voigt` is used for this purpose [B+].

where $\otimes$ represents the convolution between a Gaussian,

$$G(x, \sigma_G) = \frac{1}{\sqrt{2\pi}\sigma_G} e^{-\frac{(x-\mu)^2}{2\sigma^2}} \tag{6.2}$$

and a Lorentzian function,

$$L(x, \sigma_L) = \frac{1}{\pi} \frac{\sigma_L/2}{(x-\mu)^2 + (\sigma_L/2)^2} \tag{6.3}$$

with $x = M(\pi^+\pi^-)$, μ is related to the PDG values of the M_ρ and and σs are related to the resolution and the ρ-meson decay width respectively.

The main challenge in the yield extraction process is to make a good estimation of the background. A phenomenological 3rd-order polynomial function is nominally used to describe the background[13]. Mathematically, the background function is written as

$$F_{BG}(x) = p_1 + p_2 x + p_3 x^2 + p_4 x^3, \tag{6.4}$$

where p_i's are fit parameters. Therefore the invariant mass distribution is fit using the total function,

$$T(x) = V(x-\mu, \sigma_G, \sigma_L) + F_{BG}(x). \tag{6.5}$$

As the Lorentzian width represents the physical width of ρ-meson, therefore σ_L is kept fixed to the PDG value ($\sigma_L = \Gamma_\rho = 0.1491$ GeV) in the final fit.

The yield is then given by

$$Y_D = I_V \times \frac{N_{bins}}{Hist_{range}}, \tag{6.6}$$

where the $Hist_{range}$ is the range of the histogram used for $M(\pi^+\pi^-)$ distribution in N_{bins} and the integration of the function I_V,

$$I_V = \left(\int_{\mu-2\sigma_L}^{\mu+2\sigma_L} V(x)dx \right), \tag{6.7}$$

is calculated using standard ROOT functions.

[13] At this point, no attempt is made to address the physics of the background

The uncertainty on the yield is given by

$$\sigma_{Y_D} = \sigma_I \times \frac{N_{bins}}{Hist_{range}} \tag{6.8}$$

where the integration error, σ_I, is calculated using the standard ROOT function:

`IntegralError`$(\mu - 2\sigma_L, \mu + 2\sigma_L)$ of $V(x)$.

A few sample fits are shown in Figure 6.2

6.3 Differential Cross Sections

The differential cross sections are measured in ten photon energy bins. In each energy bin, the differential cross sections in momentum transfer bins of width Δt are calculated using the relation:

$$\frac{d\sigma}{dt} = \frac{Y_D}{\Delta t A \mathscr{L}} \tag{6.9}$$

where Y_D is yield, A is the detector acceptance, $\mathscr{L}$ is the target luminosity for the photon energy range considered. The statistical uncertainty on the differential cross section is given by

$$\sigma_{d\sigma/dt} = \frac{d\sigma}{dt} \times \sqrt{\left(\frac{\sigma_{Y_D}}{Y_D}\right)^2 + \left(\frac{\sigma_A}{A}\right)^2} \tag{6.10}$$

The result is plotted in Figure 6.3 and the differential cross sections are listed in Table 6.3 for each energy bin considered. Note here that the results are plotted as a function of t for each energy bin. The t values represent the bin centers of the t-bins considered.

The differential cross sections in each energy bin increase with t. The values are the highest for low $|t|$ as expected for a t-channel diffractive process. A smooth fall off with increase in $|t|$ can be seen especially at higher photon energies. However, at lower energies, due to lower statistics and perhaps due to the interference of other channels such as the d^*, the $d\sigma/dt$ is not as expected.

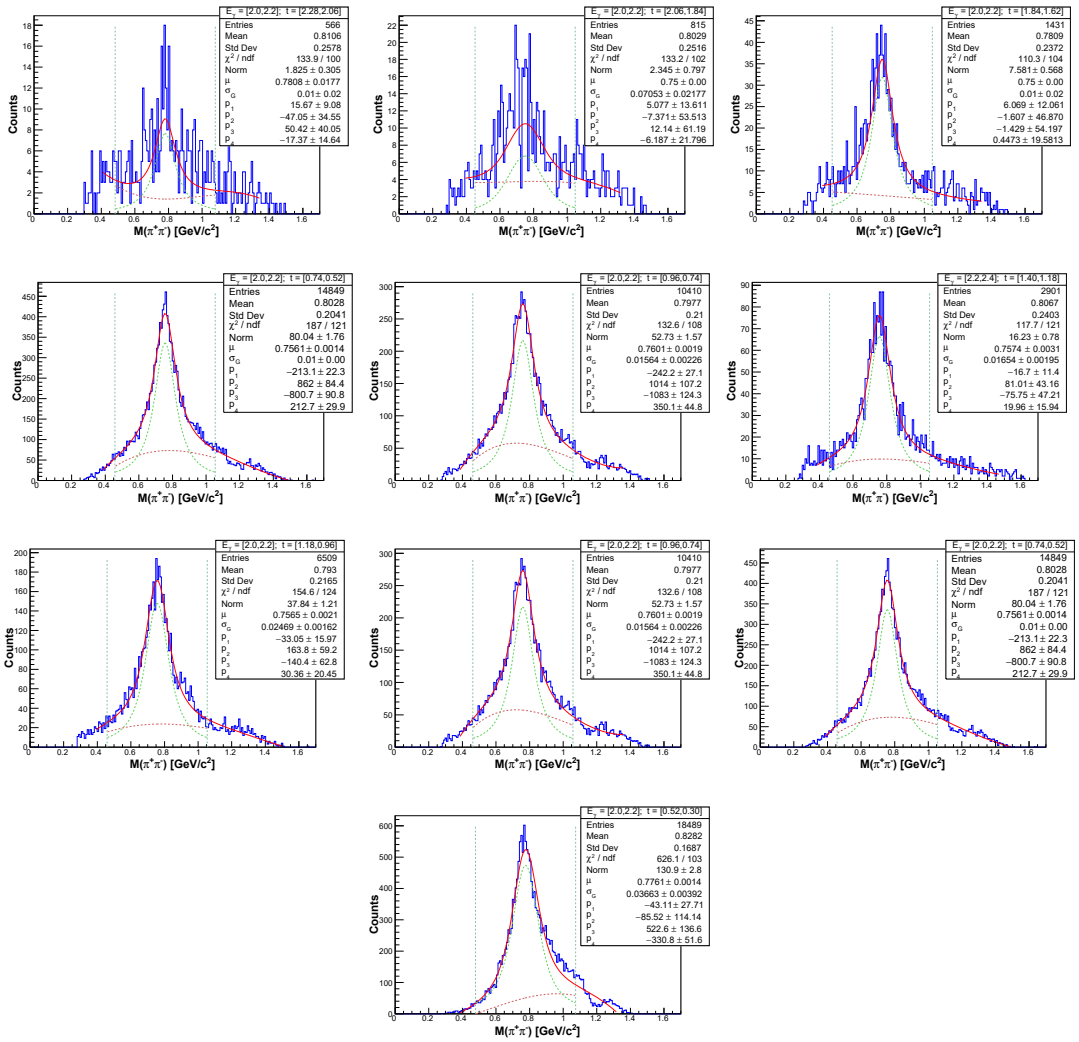

Figure 6.2: The invariant mass distributions for 10 momentum transfer bins in $E_\gamma = [2.0, 2.2]$ GeV. The signal is shown by dashed green curve. The vertical lines represent 2σ integration range. A third order polynomial `Pol3` is used to describe the background.

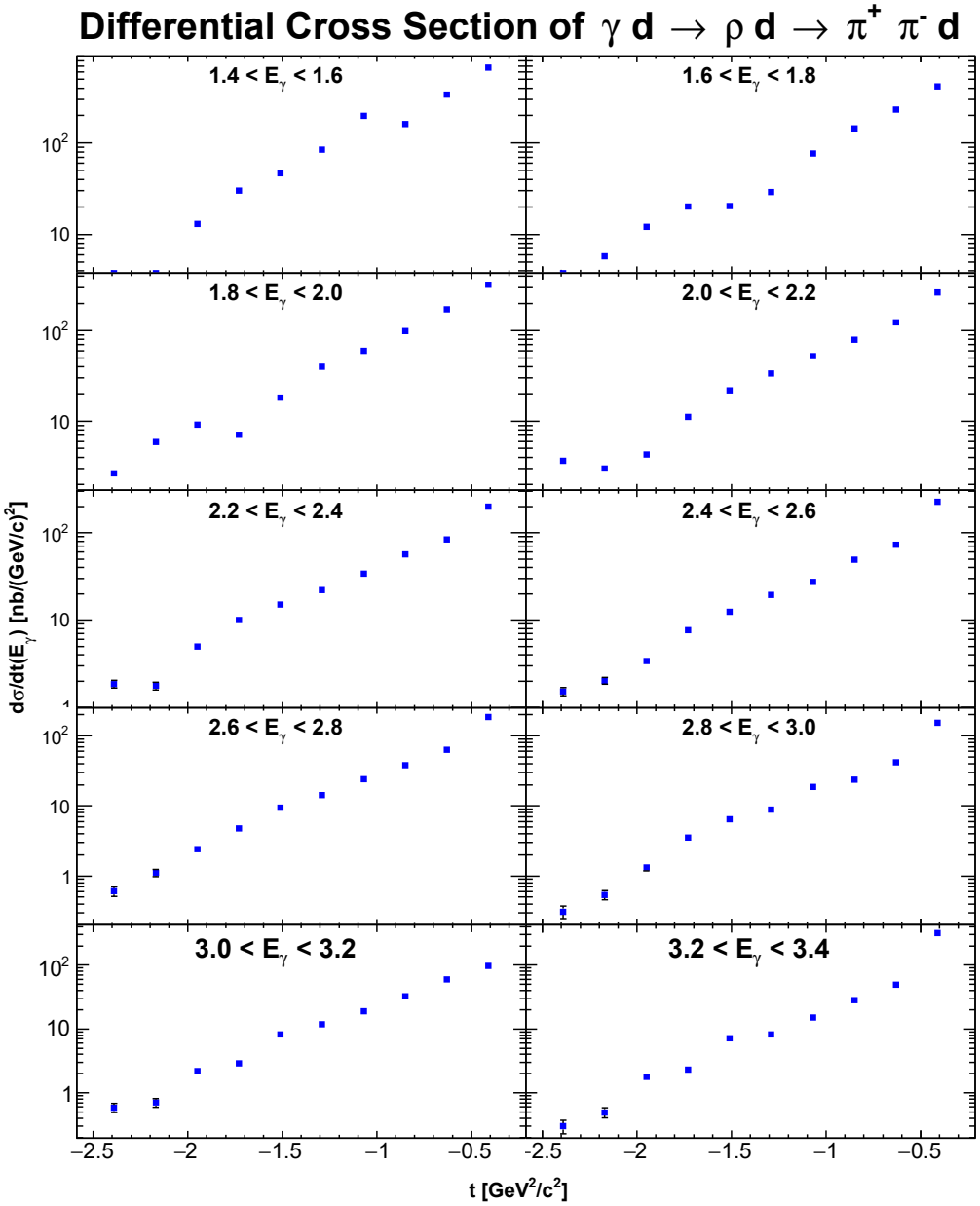

Figure 6.3: Differential cross section of $\gamma d \rightarrow \rho d$ using the channel $\gamma d \rightarrow \rho d \rightarrow \pi^+\pi^- d$ as a function of four momentum transfer (t) for different incident photon energy ranges.

Table 6.3: Differential cross section values for $\gamma d \rightarrow \rho d$. For some bins where the fit was not good (based on reduced χ^2), shows null result.

E_γ [GeV]		t [GeV^2]		$\frac{d\sigma}{dt}$ [nb/(GeV/c)^2]	$\sigma_{d\sigma/dt}$ [nb/(GeV/c)^2]
low	high	low	high		
1.4	1.6	-2.5	-2.28	-	-
1.4	1.6	-2.28	-2.06	-	-
1.4	1.6	-2.06	-1.84	13.06	0.516821
1.4	1.6	-1.84	-1.62	30.2491	0.739229
1.4	1.6	-1.62	-1.4	46.9449	0.872631
1.4	1.6	-1.4	-1.18	84.736	1.18081
1.4	1.6	-1.18	-0.96	198.066	2.00891
1.4	1.6	-0.96	-0.74	161.977	1.67594
1.4	1.6	-0.74	-0.52	340.423	2.40614
1.4	1.6	-0.52	-0.3	668.75	3.97703
1.6	1.8	-2.5	-2.28	-	-
1.6	1.8	-2.28	-2.06	5.79919	0.294377
1.6	1.8	-2.06	-1.84	12.1368	0.406931
1.6	1.8	-1.84	-1.62	20.3075	0.538318
1.6	1.8	-1.62	-1.4	20.4755	0.572072
1.6	1.8	-1.4	-1.18	28.9978	0.68326
1.6	1.8	-1.18	-0.96	76.7088	1.07706
1.6	1.8	-0.96	-0.74	145.354	1.44615
1.6	1.8	-0.74	-0.52	234.086	1.89411
1.6	1.8	-0.52	-0.3	415.863	2.84082

Table 6.3: Differential cross section values for $\gamma d \rightarrow \rho d$. For some bins where the fit was not good (based on reduced χ^2), shows null result.

E_γ [GeV]		t [GeV^2]		$\frac{d\sigma}{dt}$ [nb/(GeV/c)^2]	$\sigma_{d\sigma/dt}$ [nb/(GeV/c)^2]
low	high	low	high		
1.8	2	-2.5	-2.28	2.64874	0.197928
1.8	2	-2.28	-2.06	5.91381	0.29218
1.8	2	-2.06	-1.84	9.15439	0.391449
1.8	2	-1.84	-1.62	7.10655	0.376908
1.8	2	-1.62	-1.4	18.3096	0.580935
1.8	2	-1.4	-1.18	39.9191	0.797532
1.8	2	-1.18	-0.96	59.8997	0.942427
1.8	2	-0.96	-0.74	99.3068	1.25
1.8	2	-0.74	-0.52	171.658	1.77184
1.8	2	-0.52	-0.3	319.657	2.86389
2	2.2	-2.5	-2.28	3.6443	0.233006
2	2.2	-2.28	-2.06	3.01012	0.228213
2	2.2	-2.06	-1.84	4.26719	0.286995
2	2.2	-1.84	-1.62	11.1245	0.421406
2	2.2	-1.62	-1.4	21.7928	0.565402
2	2.2	-1.4	-1.18	33.6737	0.695472
2	2.2	-1.18	-0.96	52.4112	0.913783
2	2.2	-0.96	-0.74	79.3928	1.17758
2	2.2	-0.74	-0.52	123.434	1.49743
2	2.2	-0.52	-0.3	262.562	2.58068

Table 6.3: Differential cross section values for $\gamma d \rightarrow \rho d$. For some bins where the fit was not good (based on reduced χ^2), shows null result.

E_γ [GeV]		t [GeV^2]		$\frac{d\sigma}{dt}$ [nb/(GeV/c)^2]	$\sigma_{d\sigma/dt}$ [nb/(GeV/c)^2]
low	high	low	high		
2.2	2.4	-2.5	-2.28	1.85204	0.186451
2.2	2.4	-2.28	-2.06	1.77045	0.184406
2.2	2.4	-2.06	-1.84	4.98709	0.267806
2.2	2.4	-1.84	-1.62	10.048	0.378588
2.2	2.4	-1.62	-1.4	15.0139	0.468307
2.2	2.4	-1.4	-1.18	21.9429	0.569068
2.2	2.4	-1.18	-0.96	33.9732	0.734447
2.2	2.4	-0.96	-0.74	56.4416	0.977747
2.2	2.4	-0.74	-0.52	84.0726	1.29039
2.2	2.4	-0.52	-0.3	198.712	2.40679
2.4	2.6	-2.5	-2.28	1.52911	0.172092
2.4	2.6	-2.28	-2.06	2.02572	0.175508
2.4	2.6	-2.06	-1.84	3.40471	0.220651
2.4	2.6	-1.84	-1.62	7.68739	0.344688
2.4	2.6	-1.62	-1.4	12.4232	0.435031
2.4	2.6	-1.4	-1.18	19.5032	0.566985
2.4	2.6	-1.18	-0.96	27.3453	0.700307
2.4	2.6	-0.96	-0.74	49.1181	0.991683
2.4	2.6	-0.74	-0.52	72.3813	1.34934
2.4	2.6	-0.52	-0.3	225.785	3.12958

Table 6.3: Differential cross section values for $\gamma d \rightarrow \rho d$. For some bins where the fit was not good (based on reduced χ^2), shows null result.

E_γ [GeV]		t [GeV^2]		$\frac{d\sigma}{dt}$ [nb/(GeV/c)^2]	$\sigma_{d\sigma/dt}$ [nb/(GeV/c)^2]
low	high	low	high		
2.6	2.8	-2.5	-2.28	0.607612	0.0961686
2.6	2.8	-2.28	-2.06	1.10952	0.126633
2.6	2.8	-2.06	-1.84	2.41863	0.188633
2.6	2.8	-1.84	-1.62	4.7653	0.269471
2.6	2.8	-1.62	-1.4	9.40928	0.390013
2.6	2.8	-1.4	-1.18	14.3475	0.50723
2.6	2.8	-1.18	-0.96	23.9601	0.661065
2.6	2.8	-0.96	-0.74	38.1642	0.934394
2.6	2.8	-0.74	-0.52	63.5118	1.3486
2.6	2.8	-0.52	-0.3	186.393	3.31862
2.8	3	-2.5	-2.28	0.308428	0.0629763
2.8	3	-2.28	-2.06	0.538962	0.0837056
2.8	3	-2.06	-1.84	1.31614	0.132342
2.8	3	-1.84	-1.62	3.53061	0.222608
2.8	3	-1.62	-1.4	6.44628	0.311692
2.8	3	-1.4	-1.18	8.84384	0.375675
2.8	3	-1.18	-0.96	18.7851	0.592892
2.8	3	-0.96	-0.74	23.7118	0.714704
2.8	3	-0.74	-0.52	41.7752	1.11032
2.8	3	-0.52	-0.3	153.224	3.53112

Table 6.3: Differential cross section values for $\gamma d \rightarrow \rho d$. For some bins where the fit was not good (based on reduced χ^2), shows null result.

E_γ [GeV]		t [GeV^2]		$\frac{d\sigma}{dt}$ [nb/(GeV/c)^2]	$\sigma_{d\sigma/dt}$ [nb/(GeV/c)^2]
low	high	low	high		
3	3.2	-2.5	-2.28	0.583148	0.0963544
3	3.2	-2.28	-2.06	0.70235	0.106993
3	3.2	-2.06	-1.84	2.18127	0.192174
3	3.2	-1.84	-1.62	2.86852	0.225198
3	3.2	-1.62	-1.4	8.18839	0.399992
3	3.2	-1.4	-1.18	11.829	0.490315
3	3.2	-1.18	-0.96	18.8907	0.671519
3	3.2	-0.96	-0.74	32.3472	0.996619
3	3.2	-0.74	-0.52	59.6224	1.61987
3	3.2	-0.52	-0.3	96.5411	3.33001
3.2	3.4	-2.5	-2.28	0.300703	0.0713574
3.2	3.4	-2.28	-2.06	0.493743	0.0920266
3.2	3.4	-2.06	-1.84	1.76289	0.17719
3.2	3.4	-1.84	-1.62	2.29029	0.210802
3.2	3.4	-1.62	-1.4	7.17558	0.386769
3.2	3.4	-1.4	-1.18	8.17702	0.42137
3.2	3.4	-1.18	-0.96	15.0416	0.640759
3.2	3.4	-0.96	-0.74	28.1687	0.993882
3.2	3.4	-0.74	-0.52	49.5238	1.5898
3.2	3.4	-0.52	-0.3	315.191	8.04035

6.4 $\rho - N$ Scattering Cross Section

The theoretical model based on VMD described in Section 1.2 was used to extract $\sigma_{\rho N}$ from the data with some modifications. For the ρ-photoproduction in the single scattering region, the model uses the differential cross section at $t = 0$ from [BSYP78] given by

$$\frac{d\sigma}{dt}\Big|_{t=0,\gamma N} = 563.87 - 259.58e_g + 57.71e_g^2 - 5.71e_g^3 + 0.21e_g^4, \tag{6.11}$$

where e_g is an energy variable given by

$$e_g = \frac{m_d^2 + 2m_d E_\gamma - m_N^2}{2m_N}. \tag{6.12}$$

Here m_d is the deuteron mass and the mass of a nucleon is m_N. In the calculation, proton mass is used for m_N. As can be seen from this equation that it e_g a function of the photon energy, E_γ. Therefore, this quantity becomes a constant for a particular energy. As explained in [BSYP78], the parametrization of this quantity is based on differential cross sections from a variety of experiments using a proton target.

The model assumed the slope parameter in the single and double scattering amplitudes to be of equal value, i.e., $b_{\gamma N} = b_{\rho N}$. This is the first variable. Another input in the calculation was the scattering cross section $\sigma_{\rho N}$ that included the final state interaction representing the scattering of the ρ-meson twice between the nucleons.

In the intermediate energy ranges such as the E_γ considered, the ratio of the real part of the scattering amplitudes for proton and neutron targets is not 1, but the model omits this difference considering the fact that the isospin averaged amplitudes dominate coherent photoproduction of the vector meson from deuterium. Therefore, the parameters $\alpha_{\gamma N}$ and $\alpha_{\rho N}$ were set equal to an empirical value of -0.4 in this model [FKM+97]. These parameters are being defined with respect to Equation 1.3 that defined the scattering amplitude for the reaction $\gamma N \to \rho N$ (see Section 1.2).

For the photon energy, $E_\gamma = 3.3$ GeV (bin center), the two parameters were varied to produce a set of differential cross sections. Each set was then compared with the measured

values. The comparison was done in the similar way as that of the $\sigma_{\omega N}$ based on the χ^2-test. If the reduced χ^2 was within 20% of unity, the parameters were accepted. The selected set of $\sigma_{\rho N}$ and the slope parameter along with associated χ^2 value per degrees of freedom (NDF) is shown in Table 6.4.

Table 6.4: Summary of the parameters used to compare the result from the data for the highest energy bin $3.2 < E_\gamma < 3.4$ GeV in the present analysis using $\gamma d \to \pi^+\pi^- d$ channel. The result from these parameters shown here are within 20% of $\chi^2 = 1.0$ (the ideal value) when compared with the data.

Trials	$b_{\gamma N} = b_{\rho N}$ [GeV^{-2}]	$\sigma_{\rho N}$ [mb]	$\lvert\chi^2/NDF\rvert$
1	6	12	0.90
2	6	13	1.14
3	6.5	16.4	0.98
4	6.5	16.5	1.09
5	7	20	1.13
6	7.5	20	0.81
7	7.5	23	0.85
8	8	24	0.90
9	8	25	0.81
10	8	26	1.15

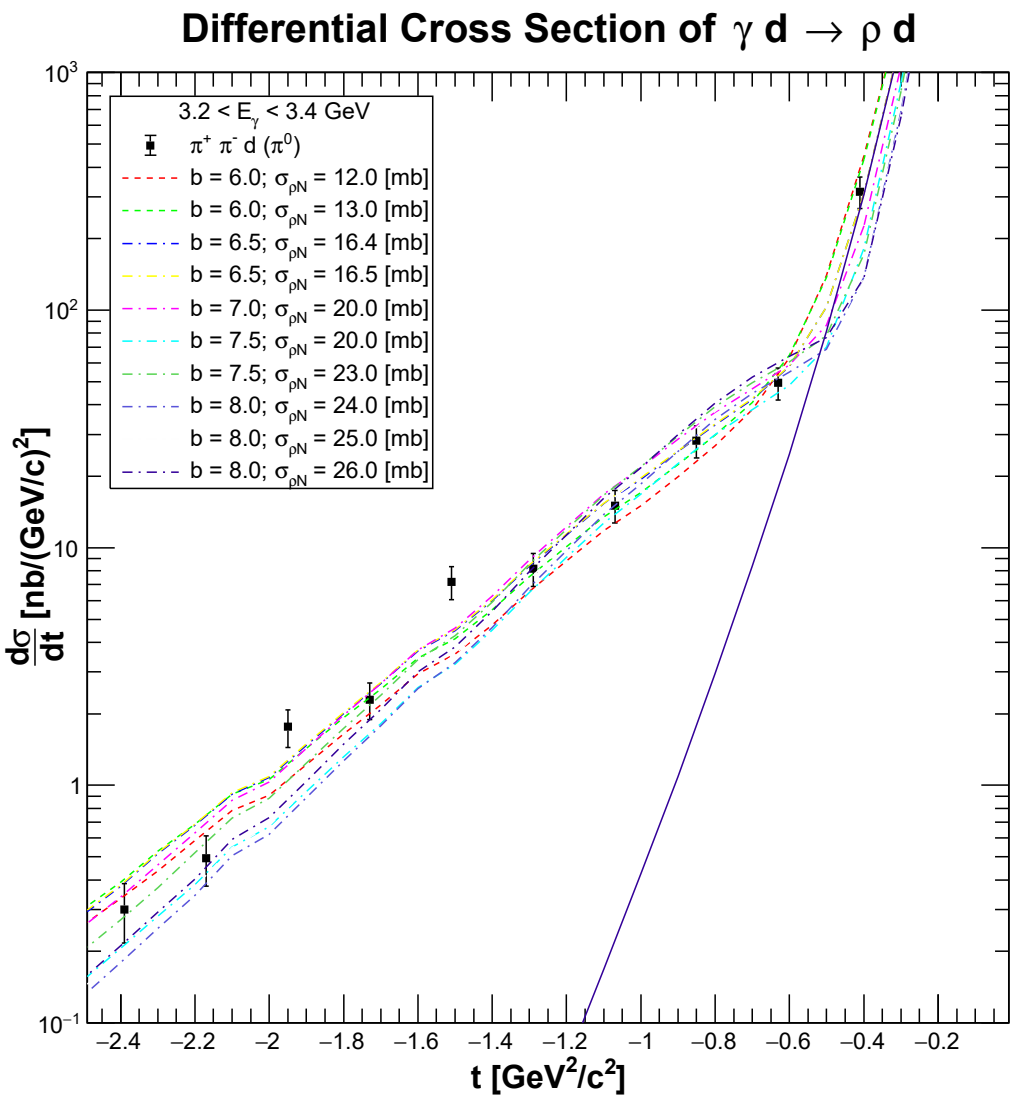

Figure 6.4: Differential cross section of $\gamma d \rightarrow \rho d$ as a function of $|t|$ for $3.2 < E_\gamma < 3.4$ GeV compared to that of a calculation based on [FKM+97]. Each curve corresponds to a specific slope parameter b and $\sigma_{\omega N}$ value, as listed in Table 5.5. The legend for each curve is also defined respectively for these parameters. The solid violet curve represents the contribution of the single scattering for input parameters corresponding to that of the violet dashed-dotted curve calculated using $b = 8.0$ GeV^{-2} and $\sigma_{\rho N} = 26.0$ mb.

Figure 6.4 presents $d\sigma/dt$ for $3.2 < E_\gamma < 3.4$ GeV. The error bars on the data represent a 15% systematic uncertainty[14] added in quadrature with the statistical uncertainties. The $\sigma_{\rho N}$ in the kinematic domain where the ρ photoproduction cross section was known to be sensitive to the rescattering amplitude was found to be $20 < \sigma_{\rho N} < 26$ mb for the slope parameters $7.0 < b < 8.0$ GeV^{-2}. It is evident that the model based on VMD successfully describes the measured data. Furthermore, at $|t| \gtrsim 0.5$ GeV^2, significant contributions from the double scattering is observed. The single scattering contribution for one parameter set is also shown in the plot, which is significant at low $|t|$ and drops sharply at higher momentum transfer regime. For $|t| > 0.6$ GeV^2, the differential cross section is entirely controlled by the double scattering. The result obtained here is comparable with the value of about 26-29 mb found (using a different model) in the SLAC data taken for higher photon energies (see Figure 1.4).

This finding reconfirms the concept presented in Figure 1.3 and the result from ω meson photoproduction. The ρ meson is created at the first vertex from the scattering from a nucleon which is dominant at low $|t|$ and the strength of the second scattering increases with $|t|$ enabling us to extract the ρ-N interaction total cross section.

6.5 Summary

This chapter presented the procedure to calculate the differential cross section for the ρ-meson photoproduction using the reaction $\gamma d \to \rho d \to \pi^+\pi^- d$. Various components in Equation 6.9 such as the luminosity and acceptances were used to calculate the differential cross section which was summarized in Table 6.3.

The observed t-dependence is characteristic feature for a diffractive process on deuterium. As mentioned in Chapter 1, there is a rapid fall off in the $d\sigma/dt$ with increasing

[14] The systematic uncertainties calculated from several analyses on the g10 dataset typically range between 10-15% [Com16, C$^+$18, M$^+$07]. We used the upper limit of this range for the systematic uncertainty of this analysis.

$|t|$ up to about $t \approx -0.5$ GeV^2. This region was kinematically not coverable with the present dataset. However, the results presented here are the first measurement for a region where the cross section is dominated by the contributions from the double scattering terms over various photon energy bins. This range is important in the determination of the ρ-N scattering cross section ($\sigma_{\rho N}$) by making use of a physics model.

7 $N\Delta$ Resonance

In the previous chapters, we covered the details involving event selection, acceptance and normalization for the d^* channels. Additional analysis procedures required to extract these measurements will be documented in this chapter. A few Dalitz plot distributions will be shown motivating the reader to follow the three charge states for the same decay final state. A preliminary differential cross section of the $d^{*++} \rightarrow d\pi^+$ decay using the reaction $\gamma d \rightarrow \pi^+\pi^- d$ will be presented. An outlook for other charge states will be presented in Chapter 9.

7.1 First Look at the Resonances

There are three possible charge states for the d^* resonances that have been seen in the g10 dataset using the detected final state particles of d, π^+ and π^-. The first combination is that the π^- scatters off at the first vertex and the resonance state decays into π^+ and a bound deuteron as shown by the Feynman diagram in Figure 7.1a. We define this state as the d^{*++} resonance.

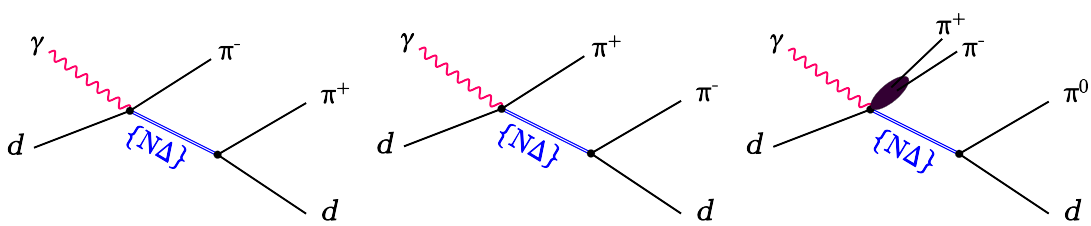

(a) d^{*++} (b) d^{*0} (c) d^{*+}

Figure 7.1: Feynman diagrams for the possible $N\Delta$ resonances using the same detected final states.

Similarly, the decay of the resonance in π^- and d at the second vertex with the same detection sample suggests the possibility of a neutral resonance state, d^{*0}. This is shown in Figure 7.1b. The third charge state, d^{*+} shown in Figure 7.1c is possible when it decays into d and π^0, where π^0 is reconstructed from the missing mass of the same detection sample.

With three detected particles, one way to investigate the first two charge states is to plot the squares of the invariant mass of the detected particles in a Dalitz-like plot. Figure 7.2 shows on the vertical axis, the square of the invariant mass of π^+ and the outgoing deuteron, $M^2(d\pi^+)$. The horizontal axis represents the square of the invariant mass of the deuteron and the other pion, $M^2(d\pi^-)$.

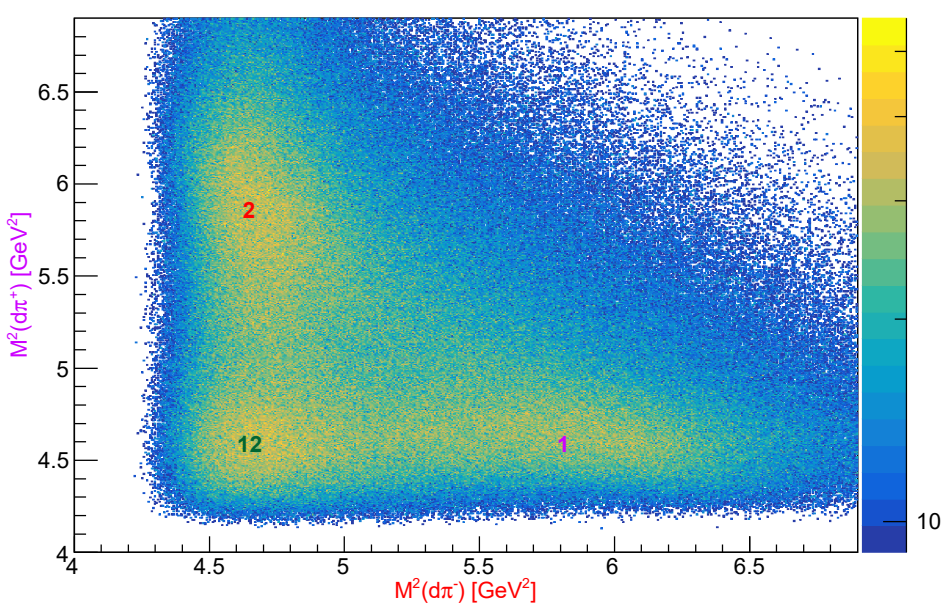

Figure 7.2: Dalitz-like distribution of the final state particles. Three prominent peaks at regions 1, 2 and 12 can be seen. Region 12 is the intersection of the regions 1 and 2, where many of the $\pi^+\pi^-$ events are located.

The distribution is suggestive of three prominent peaks (regions 1, 2 and 12). Region 1 shows the correlated events for the d and π^+, while region 2 corresponds to the events that may have decayed from a resonance, d^{*0}. Region 12 is the overlap of the regions 1 and 2 suggesting the correlation between the pions. Region other than the marked in this plot represents the correlated ρ-meson events and the uncorrelated events in the phase space containing the three detected particles.

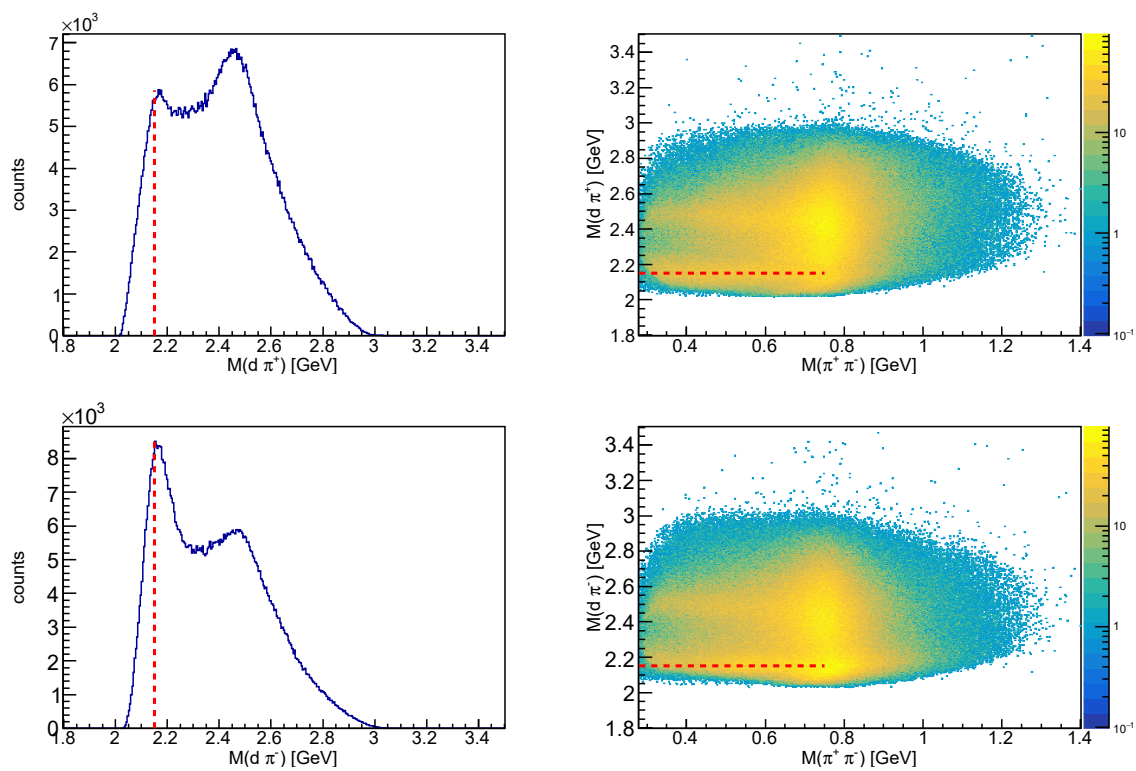

Figure 7.3: The mass distributions and their corresponding projections for the d^{*++} and d^{*0}. The x-axis on both 2D plot is the invariant mass of the two detected pions peaking at the mass of the ρ meson.

In order to look more closely at the suggested correlations, invariant masses for $d\pi$ are shown versus those of the pions in Figure 7.3. The plots on the left are the Y-projections of the plots on the right. The X-projection is the distribution of two pions peaking at the ρ mass. The dashed-lines in red on the left plots are drawn just to guide the eye. A peak at about 2150 MeV for both mass distributions can be seen. The bump at about 2.5 GeV is just a reflection of the other peak. Although the plots in themselves do not prove anything, but there are two take-aways – peaks at about the same mass value ~2150 MeV and the ρ is the major background in both the cases.

When a π^0 is included using the missing mass distribution of the detected particles, the third charge state of the resonance can be studied. In Figure 7.4, the missing mass for the detected deuteron ($MM(\gamma d, d)$) is shown on the horizontal axis. This distribution yielded the ω-meson events (Chapter 5). The missing mass distribution for two pions, i.e. $MM(\gamma d, \pi^+\pi^-)$ is on the y-axis and the projection of this axis is shown on the left. The dashed line in red is to guide the eye to give the location of the peak. Interestingly, this peak is at about the same same mass of 2150 MeV suggesting the possibility of the third resonance channel, d^{*+} that decays into a π^0 and deuteron.

From a first look at various mass distributions using the detected final states, the location of the peak is at the same mass as the possible dibaryon resonances. The validation of the resonances will involve a complete partial wave analysis for each channel, which is not covered in this document. This chapter, however, focuses on extracting a preliminary differential cross section for the d^{*++}-channel only.

7.2 Kinematic Binning

The $d\pi^+$ events after various detector selection cuts were distributed in various bins of the center-of-mass (CM) energy. The CM energy for the process $\gamma d \rightarrow d^{*++}\pi^-$ given by

$$W \equiv \sqrt{s} = (P_\gamma + P_d)^2, \tag{7.1}$$

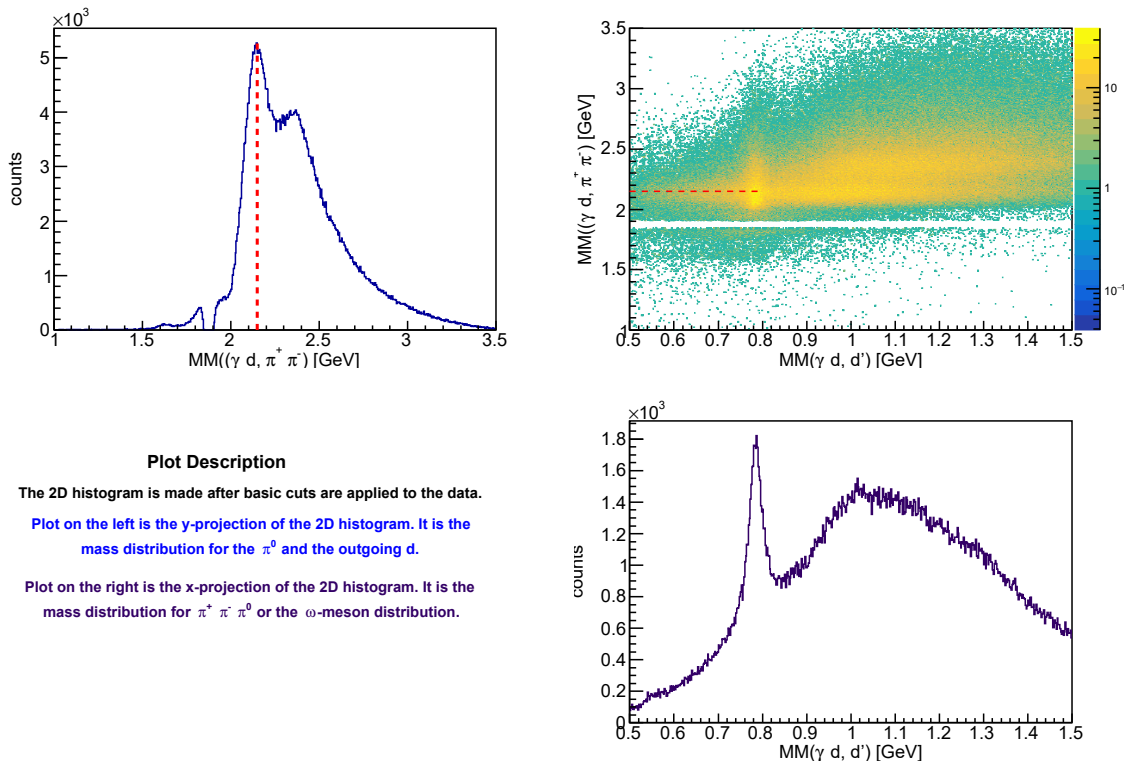

Figure 7.4: The missing mass distributions and their corresponding projections. The x-axis on the 2D plots is the missing mass of detected deuteron. This projection was used to extract ω signal events. The y-axis is the missing mass of the detected charged pions, namely, π^+ and π^-. The projection of this distribution is shown on the top left plot, where a peak at around 2150 Mev can be seen in the missing mass distribution. The dashed line in red is shown to guide the eye.

where P_d is the four-momentum of the outgoing deuteron. Another independent variable, the CM angle for the outgoing π^-, was used to bin further that describes the kinematics without affecting the signal. The angular distribution ($\cos\theta^{\pi^-}_{CM}$) and the energy in the center of mass frame is shown in Figure 7.5 where the bins are separated by black solid lines. The binning scheme is summarized in Table 7.1. For this analysis, four W bins which were divided into 8 angular bins in the range $-0.8 < \cos\theta^{\pi^-}_{CM} < 0.8$ are used.

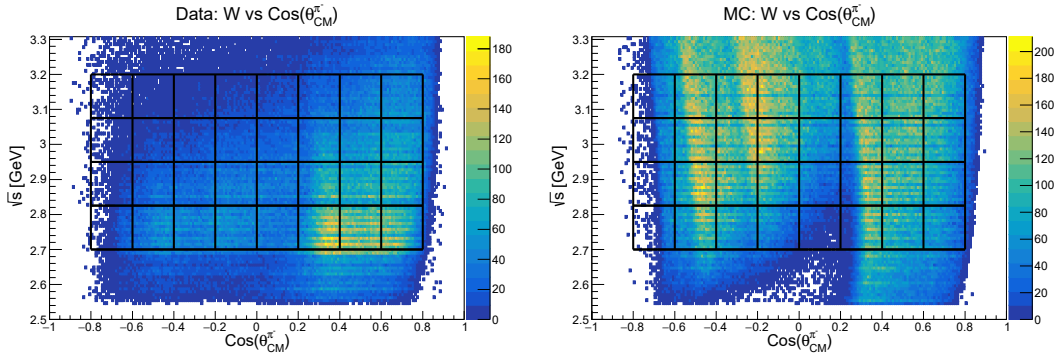

Figure 7.5: The energy versus angular distributions of π^- in the CM frame. The distribution on the left is for data, while the left plot is for the simulated events.

Table 7.1: Kinematic ranges of W and $\cos\theta^{\pi^-}_{CM}$ used in the analysis of the d^{*++} channel.

Energy Bin #		1	2	3	4
W [GeV]	low	2.700	2.825	2.950	3.075
	high	2.825	2.950	3.075	3.200

Angle Bin #		1	2	3	4	5	6	7	8
$\cos\theta^{\pi^-}_{CM}$	low	-0.8	-0.6	-0.4	-0.2	0.0	0.2	0.4	0.6
	high	-0.6	-0.4	-0.2	0.0	0.2	0.4	0.6	0.8

As previously discussed in Chapter 4, simulation of the d^{*++} required an estimation of its mass and width, which were provided based on the $d\pi^+$ distribution in the data. Using μ = 2150 MeV for the mass and a width of 100 MeV as first order approximation, events were generated. A slight discrepancy between the data and simulation at low W can be seen in Figure 7.5. Therefore, this region was not used for the analysis.

7.3 Luminosity

The CM energy for the channel under investigation can be written as a function of incident photon energy using the direct relation

$$W^2 = m_d^2 + 2E_\gamma m_d, \tag{7.2}$$

where m_d is the mass of deuteron. As there is direct correspondence to the photon flux (N_γ) for each energy range, the photons flux can therefore be evaluated for any W range. N_γ and σ_{N_γ} were calculated for each energy bin using the flux files mentioned in Section 3.2.2 and Appendix B.5. The correspondence and the photon flux and related uncertainty values are listed in Table 7.2. The luminosity, $\mathscr{L}$, can then can calculated as a function of W using

$$\mathscr{L}(W) = \frac{\rho_T N_A l_T}{M_d} N_\gamma(W), \tag{7.3}$$

where the definition and the values of the parameters ρ_T, M_d, l_T and N_A are provided in Table 5.2. Table 7.2 lists the luminosity in this case.

Table 7.2: Incident photon flux (N_γ) and luminosities are listed for the indicated photon energy ranges. These photon energies correspond to the CM energies considered in this analysis. The uncertainties were calculated for each energy range.

E_γ [GeV]		W [GeV]		$N_\gamma \times 10^{12}$	$\sigma_{N_\gamma} \times 10^{12}$	$\mathscr{L}(W)$ $[pb^{-1}]$	$\sigma_{\mathscr{L}}$ $[pb^{-1}]$
low	high	low	high				
1.0056	1.1897	2.700	2.825	4.0309	0.0055	4.8887	0.0067
1.1897	1.3821	2.825	2.950	3.5567	0.0051	4.3136	0.0062
1.3821	1.5829	2.950	3.075	3.0628	0.0047	3.7146	0.0057
1.5829	1.7920	3.075	3.200	2.8314	0.0045	3.4340	0.0055

7.4 Yield Extraction

Usually the yield extraction procedure involves estimation of signal and background using phenomenological functions such as a Gaussian, Lorentzian, Voigtian or some higher order polynomial functions. This process works as long as the background process involved do not vary much over bins and the signal sits on top of it. Sometimes, one may need to consider physics models to estimate the background processes involved and eliminate them by various techniques. As no physics model was available, this analysis used some assumptions as explained next.

Figure 7.6 shows the mass distributions for $d\pi^+$, $d\pi^+$ and $\pi^+\pi^-$ respectively binned in angles for the first W bin. The rows represent the same number of events and hence they can be referred to as the projections of pairs in a 3D space[15]. The expected mass peak at about 2150 MeV in the $M(d\pi^+)$ becomes more prominent in the forward angles while the reflection (bump at about 2350 MeV) in $M(d\pi^+)$ flattens. Similarly, there is an inverse correlation in the signal and the reflection in the $M(d\pi^-)$ distribution as well. From this observation, it can be inferred that the peaks in each distribution act as the second bump and hence can be considered as a major background for each other. Other sources of background as discussed previously from the Dalitz-like plot in Figure 7.2 are the ρ and the uncorrelated $\pi^+\pi^-$ events. There could be other unknown backgrounds as well that may contribute. Figures 7.7, 7.8 and 7.9 show the projections for the rest of W-bins.

[15] For a set of three individual particles, $\{xyz\}$, subset of possible pairs are $\{xy\}$, $\{xz\}$ and $\{yz\}$. These are referred here as the projections.

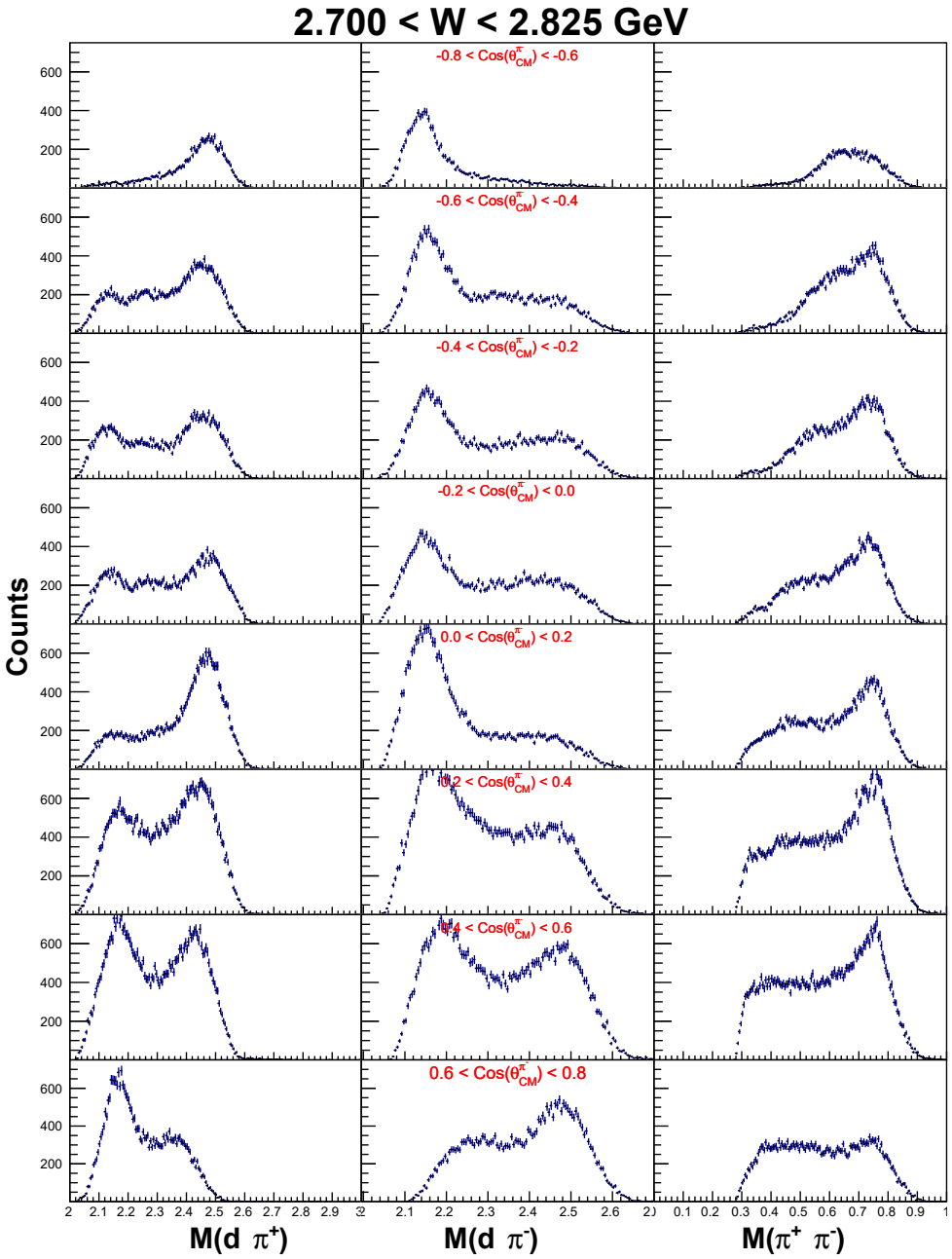

Figure 7.6: Invariant mass distributions for each pair of the final state detected particles for different angular bins in $2.7 < W < 2.825$ GeV.

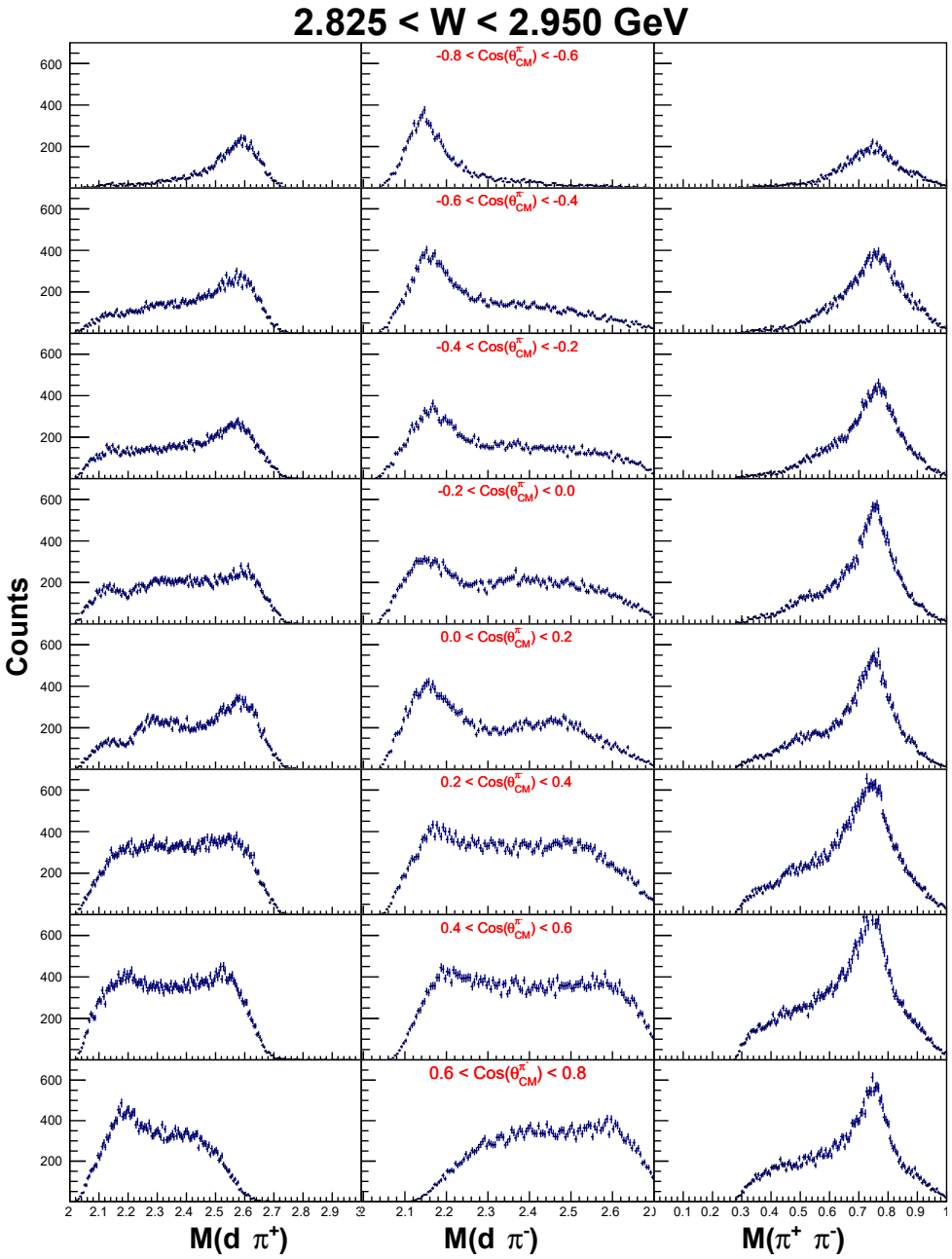

Figure 7.7: Invariant mass distributions for each pair of the final state detected particles for different angular bins in $2.825 < W < 2.950$ GeV.

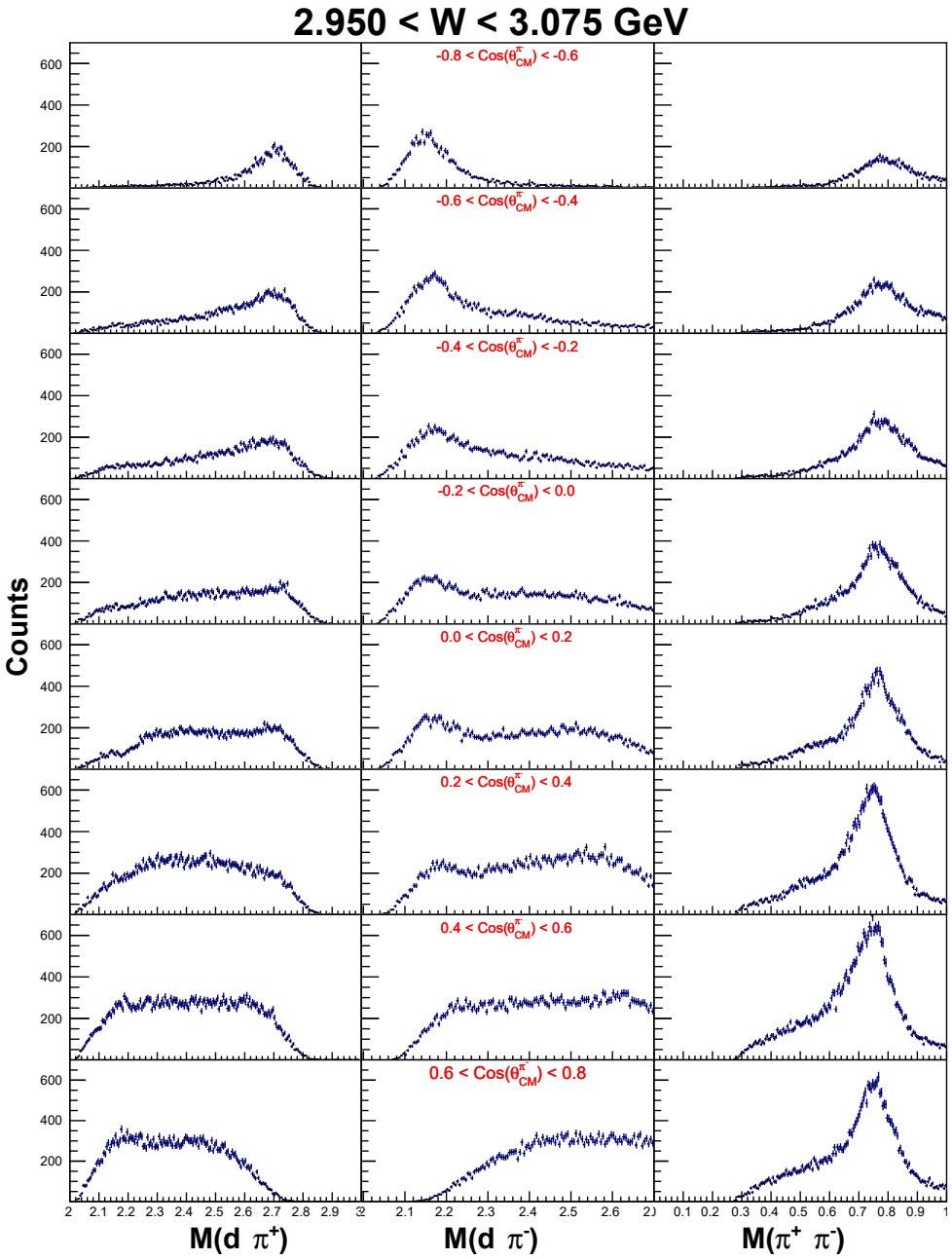

Figure 7.8: Invariant mass distributions for each pair of the final state detected particles for different angular bins in $2.950 < W < 3.075$ GeV.

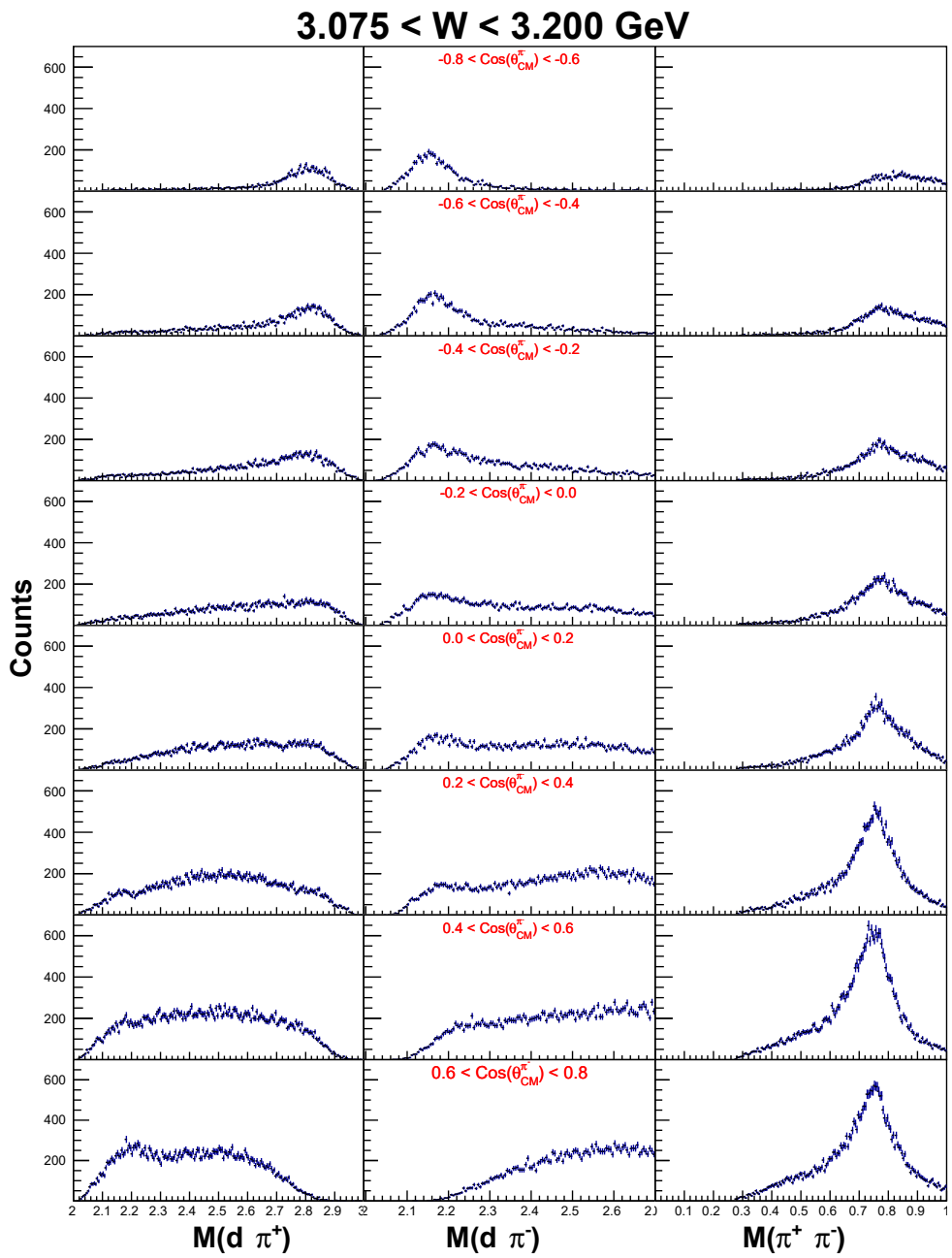

Figure 7.9: Invariant mass distributions for each pair of the final state detected particles for different angular bins in $3.075 < W < 3.2$ GeV.

As separating these events piece by piece was not possible without a clear physics understanding of all the background processes involved, we made first-order assumptions about them. Assuming d^{*0}, ρ and $\pi^+\pi^-d$ events formed the bulk of the background in the $M(d\pi^+)$ distribution and the contribution from other unknown sources of background negligible, simulations for each set of reactions were performed. The events for the signal ($d^{*++}\pi^- \rightarrow d\pi^+\pi^-$) were generated with mass, $\mu = 2.15$ GeV and width, $\Gamma = 100$ MeV. Similarly, the reflection ($d^{*0}\pi^+ \rightarrow d\pi^-\pi^+$) used the same μ and Γ. The events for ρ were the same from the ρ-photoproduction analysis (Chapters 4 and 6). Phase space events ($\gamma d \rightarrow \pi^+\pi^-d$) were also generated. Ideally the total mass distribution from the simulation should describe the distribution in the data. Therefore, the next step was to fit the data using the simulation.

The function used to fit the data is of the form,

$$x_D = f_1x_1 + f_2x_2 + f_3x_3 + f_4x_4, \tag{7.4}$$

where $x \equiv M(d\pi^+)$ and f is the fraction of the simulated events for each process. The subscripts represent the distribution sample - D: data; 1: simulated d^{*++}; 2: simulated d^{*0}; 3: simulated ρ; 4: simulated phase space.

All the three projections ($M(d\pi^+)$, $M(d\pi^-)$ and $M(\pi^+\pi^-)$) were fit simultaneously for each energy and angle bin. From the overall fit, the parameters f_i gave the fraction of events in the data contributed by a process i, $i = 1, 2, 3$ or 4. Therefore the number of d^{*++} events for each bin was calculated as

$$Y_D = f_1 \times N_D, \tag{7.5}$$

where N_D is the total number of events in the binned data distribution. The uncertainty associated with the yield was given by

$$\sigma_{Y_D} = \sigma_{f_1} \times N_D. \tag{7.6}$$

where σ_{f_1} is the uncertainty from the fit for parameter f_1.

A sample fit is shown in Figure 7.10. The yield for each bin is given in Table 7.3.

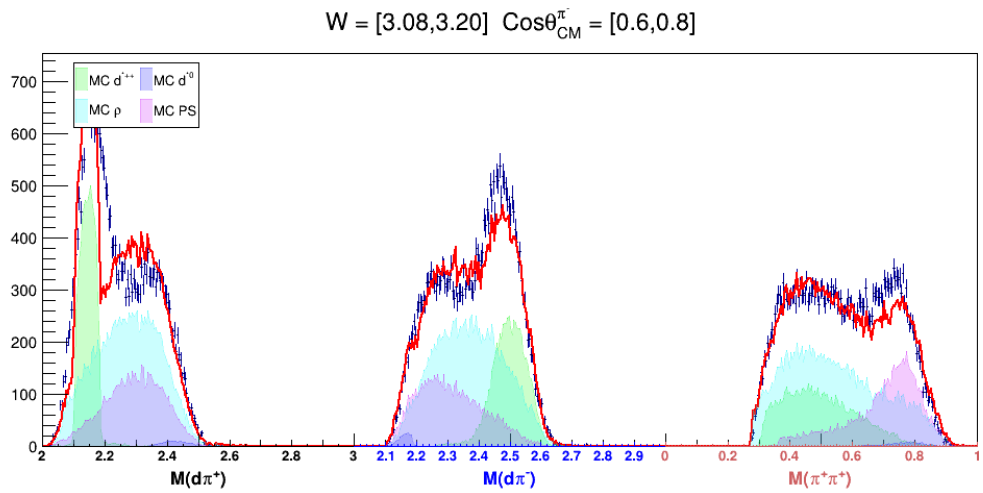

Figure 7.10: Fit for the first W bin for the most forward angle. The red curve is the overall fit to the data distribution in blue. The three projections as separately labeled are plotted on the same horizontal axis. The contributions from each simulation are also shown.

7.5 Differential Cross Sections

The differential cross sections were measured for W and $\cos\theta^{\pi^-}_{CM}$ bins. In each energy bin, the differential cross sections in each angular bins of width $\Delta\cos\theta^{\pi^-}_{CM} = 0.2$ were calculated using the relation:

$$\frac{d\sigma}{d\cos\theta^{\pi^-}_{CM}} = \frac{Y_D}{\Delta\cos\theta^{\pi^-}_{CM} A\mathscr{L}} \tag{7.7}$$

where Y_D is yield, A is the detector acceptance, $\mathscr{L}$ is the target luminosity for the W ranges considered.

The statistical uncertainty on the differential cross section is given by

$$\sigma_{d\sigma/d\cos\theta^{\pi^-}_{CM}} = \frac{d\sigma}{d\cos\theta^{\pi^-}_{CM}} \times \sqrt{\left(\frac{\sigma_{Y_D}}{Y_D}\right)^2 + \left(\frac{\sigma_A}{A}\right)^2 + \left(\frac{\sigma_{\mathscr{L}}}{\mathscr{L}}\right)^2} \tag{7.8}$$

Using these equations and the quantities calculated from previous sections, the differential cross sections were calculated. The preliminary result is shown in Figure 7.11.

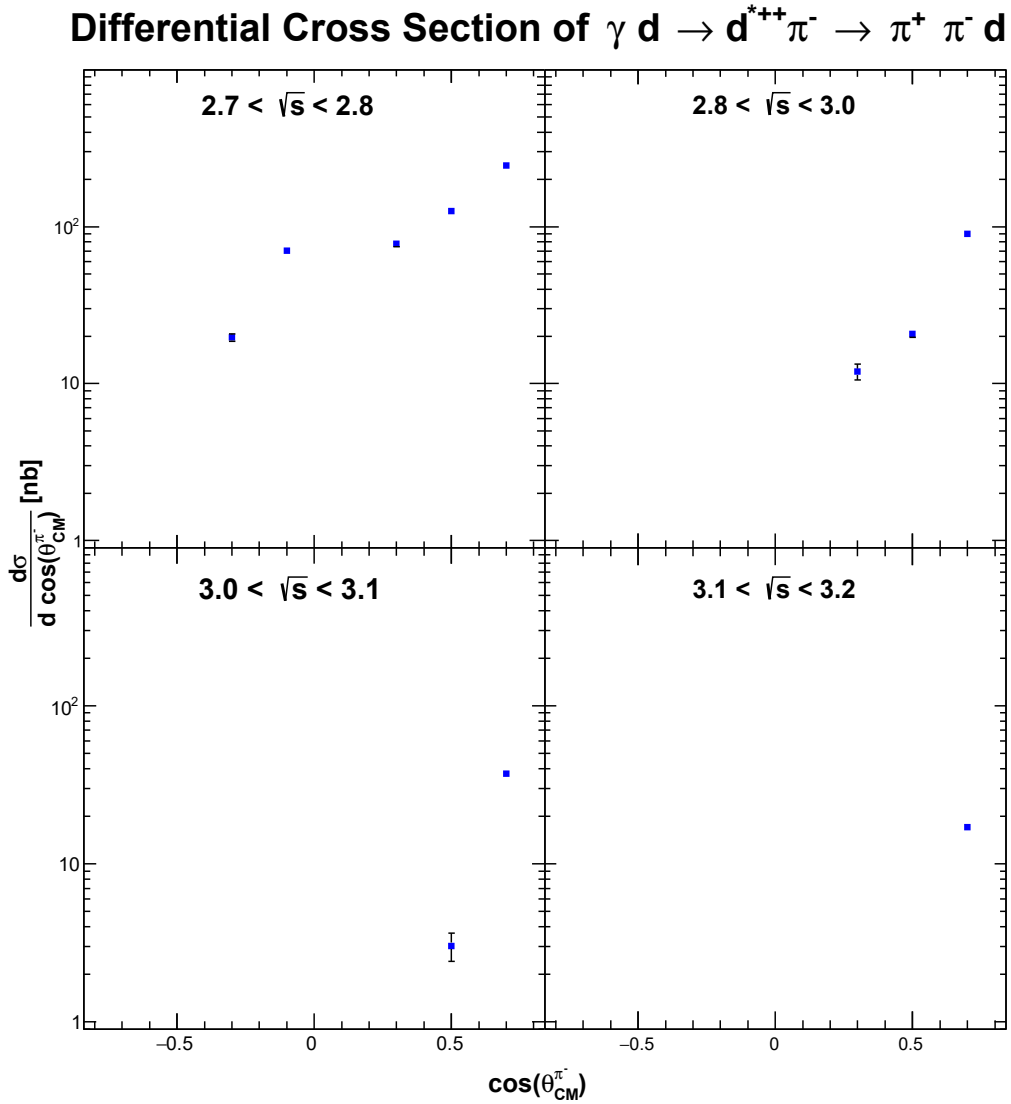

Figure 7.11: Differential cross sections of $\gamma d \rightarrow d^{*++}\pi^-$ using the channel $\gamma d \rightarrow d^{*++}\pi^- \rightarrow \pi^+\pi^- d(\pi^0)$ as a function of angle of the outgoing π^- for different CM energy ranges. The error bars represent the statistical uncertainties.

The differential cross section values for each of the W and $\cos\theta^{\pi^-}_{CM}$ bins are listed in Table 7.3. In general, the d^{*++} differential cross sections show an increasing trend at forward angles implying a potential t-channel dominant behavior for the π^- associated with the d^{*++} production. When the energy is farther from the threshold, i.e., for higher W, the signal was very weak and barely visible in many kinematic bins (Figures 7.7, 7.7 and 7.7), slightly prominent in the forward angles. As a result, we were able to extract the differential cross sections for the forward angles only. In order to better visualize the result in hand, a plot for the differential cross section values as a function of W was plotted for the angular range, $0.6 < \cos\theta^{\pi^-}_{CM} < 0.8$, shown in Figure 7.12. The $\frac{d\sigma}{d\cos\theta^{\pi^-}_{CM}}$ decreases with the increase in the center of mass energy. In this kinematic range, within the assumption, the differential cross sections ranged from about 17-246 nb.

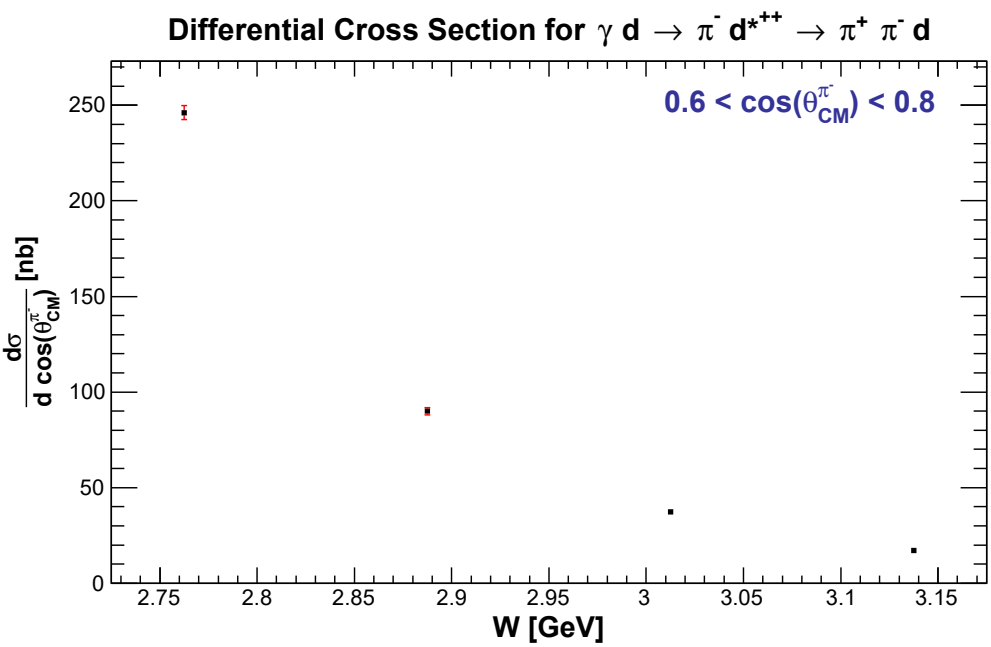

Figure 7.12: The differential cross sections of $\gamma d \rightarrow d^{*++}\pi^-$ using the channel $\gamma d \rightarrow d^{*++}\pi^- \rightarrow \pi^+\pi^- d(\pi^0)$ as a function of W for the most forward angular bin, i.e. $0.6 < \cos\theta^{\pi^-}_{CM} < 0.8$. The graph is plotted against the bin centers of the W-bins.

Table 7.3: Listed are the differential cross section values for the possible resonance d^{*++}. The kinematic bins where the fit produced unreasonable reduced χ^2 were removed. A general trend of good fits in the forward angles can be seen.

W [GeV]		$\cos\theta^{\pi^-}_{CM}$		Y_D	σ_{Y_D}	$\frac{d\sigma}{d\cos\theta^{\pi^-}_{CM}}$ $[nb]$	$\sigma_{d\sigma/d\cos\theta^{\pi^-}_{CM}}$ $[nb]$
low	high	low	high				
2.7	2.825	-0.8	-0.6	-	-	-	-
2.7	2.825	-0.6	-0.4	2.76026	214.241	0.0330585	2.56588
2.7	2.825	-0.4	-0.2	1296.35	67.143	19.671	1.02977
2.7	2.825	-0.2	0	2900.27	118.451	70.1827	2.94173
2.7	2.825	0	0.2	-	-	-	-
2.7	2.825	0.2	0.4	4924.54	229.008	78.0967	3.68188
2.7	2.825	0.4	0.6	10487	184.372	125.625	2.36916
2.7	2.825	0.6	0.8	12986.8	162.088	246.111	3.70511
2.825	2.95	-0.8	-0.6	-	-	-	-
2.825	2.95	-0.6	-0.4	-	-	-	-
2.825	2.95	-0.4	-0.2	-	-	-	-
2.825	2.95	-0.2	0	-	-	-	-
2.825	2.95	0	0.2	-	-	-	-
2.825	2.95	0.2	0.4	921.623	106.288	11.9131	1.3765
2.825	2.95	0.4	0.6	2070.94	98.2509	20.6784	0.989751
2.825	2.95	0.6	0.8	5849.28	112.705	89.9254	1.86508
2.95	3.075	-0.8	-0.6	-	-	-	-
2.95	3.075	-0.6	-0.4	-	-	-	-
2.95	3.075	-0.4	-0.2	-	-	-	-

Table 7.3: Listed are the differential cross section values for the possible resonance d^{*++}. The kinematic bins where the fit produced unreasonable reduced χ^2 were removed. A general trend of good fits in the forward angles can be seen.

W [GeV]		$\cos\theta^{\pi^-}_{CM}$		Y_D	σ_{Y_D}	$\frac{d\sigma}{d\cos\theta^{\pi^-}_{CM}}$ $[nb]$	$\sigma_{d\sigma/d\cos\theta^{\pi^-}_{CM}}$ $[nb]$
low	high	low	high				
2.95	3.075	-0.2	0	-	-	-	-
2.95	3.075	0	0.2	-	-	-	-
2.95	3.075	0.2	0.4	-	-	-	-
2.95	3.075	0.4	0.6	311.446	62.6361	3.02523	0.608705
2.95	3.075	0.6	0.8	2778.33	82.2297	37.3178	1.13575
3.075	3.2	-0.8	-0.6	-	-	-	-
3.075	3.2	-0.6	-0.4	-	-	-	-
3.075	3.2	-0.4	-0.2	-	-	-	-
3.075	3.2	-0.2	0	-	-	-	-
3.075	3.2	0	0.2	-	-	-	-
3.075	3.2	0.2	0.4	-	-	-	-
3.075	3.2	0.4	0.6	-	-	-	-
3.075	3.2	0.6	0.8	1420.88	61.5463	17.0604	0.74811

7.6 Summary

This chapter presented a first look of the possible $N\Delta$ resonances called as the d^{*++}, d^{*0} and d^{*+} based on their charges. Each of them decayed into a deuteron and a pion. The g10 data was able to show a first look at these possible states. A preliminary analysis for the extraction of the differential cross section for the doubly-

charged d^{*++} resonance was presented by performing Monte-Carlo simulations for the major backgrounds assuming these backgrounds dominate the distribution. As a first order approximation, the assumption suggests that these were indeed the major backgrounds. However, due to low statistics in higher energies especially at backward angles, differential cross section extraction was not possible for all the kinematic range considered. A dedicated theoretical model would help solve this puzzle.

8 CLAS12 Preshower Calorimeter

Any collaboration functions smoothly and efficiently when its members provide constant service work. CLAS collaboration is no different, where members provide their service in the various ways. Apart from taking shifts during an experimental run, while some members work directly in setting up of hardware or the physical set up of detectors, others develop related software or work in groups to calibrate the detectors. It is due to the collaborative work from all the members of CLAS during the 6 GeV era, that everyone (including former and current members) are able to make use of the data and prepare for future experiments.

As a member at the CLAS Collaboration, I participated in the calibration of a detector subsystem, the Pre-Shower Calorimeter (PCAL), which is an important part of the upgraded CLAS detector (called CLAS12, where 12 is referred to the acceleration of the electrons from CEBAF up to 12 GeV). I have created and helped in implementing a method to calibrate the PCAL unit in collaboration with Cole Smith and Nicholas Compton [Com16]. This calibration helped to reduce backgrounds and improve the resolution to desired level for data taking. I helped in creating a software in `Java`, that was originally written in `C++`. The transition to a software based on `Java` was important to be consistent to other software and to better visualize calibrated data in graphical format. Also, the software libraries were easy to access from a common repository created by a dedicated software group at JLab. This chapter describes the design of PCAL, explains the method to calibrate and summarizes the results.

8.1 Geometry

With the 12 GeV electron beam, the detection of high energy electrons and neutral pions is very challenging for the CLAS EC. Therefore, the PCAL detector was built and installed for full reconstruction of the high-energy showers and to separate high energy

photons and π^0s. The unit is placed just before the EC along the beamline as can be seen in Figure 8.1.

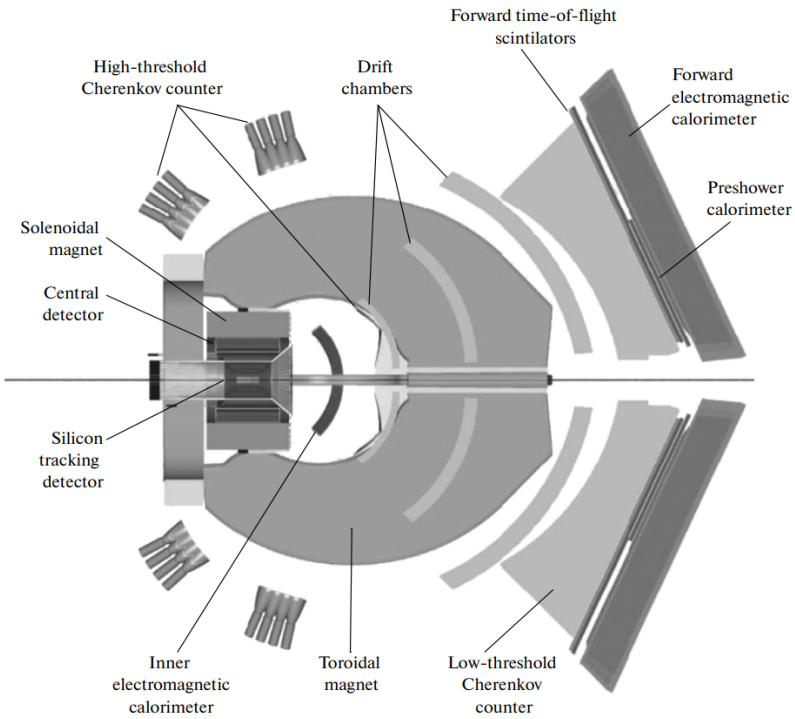

Figure 8.1: Side view of the CLAS12 detector displaying its major subsystems. The PCAL and the EC units have azimuthal symmetry. Image source: [VKMR10]. Springer Nature License Number: 4506171355129

The PCAL has a geometry similar as that of the EC (see Section 2.3.7). There are six PCAL modules around the beamline, each of which is triangular in shape. Figure 8.2 shows the triangular shape and the dimensions of one of the modules. Each PCAL module is composed of 15 scintillator layers sandwiched with layers of lead. Between each lead sheet there are three different alternating stereo readout planes for the layers. These readout planes of the scintillator strips are known as the U, V and W layers. In other words, these

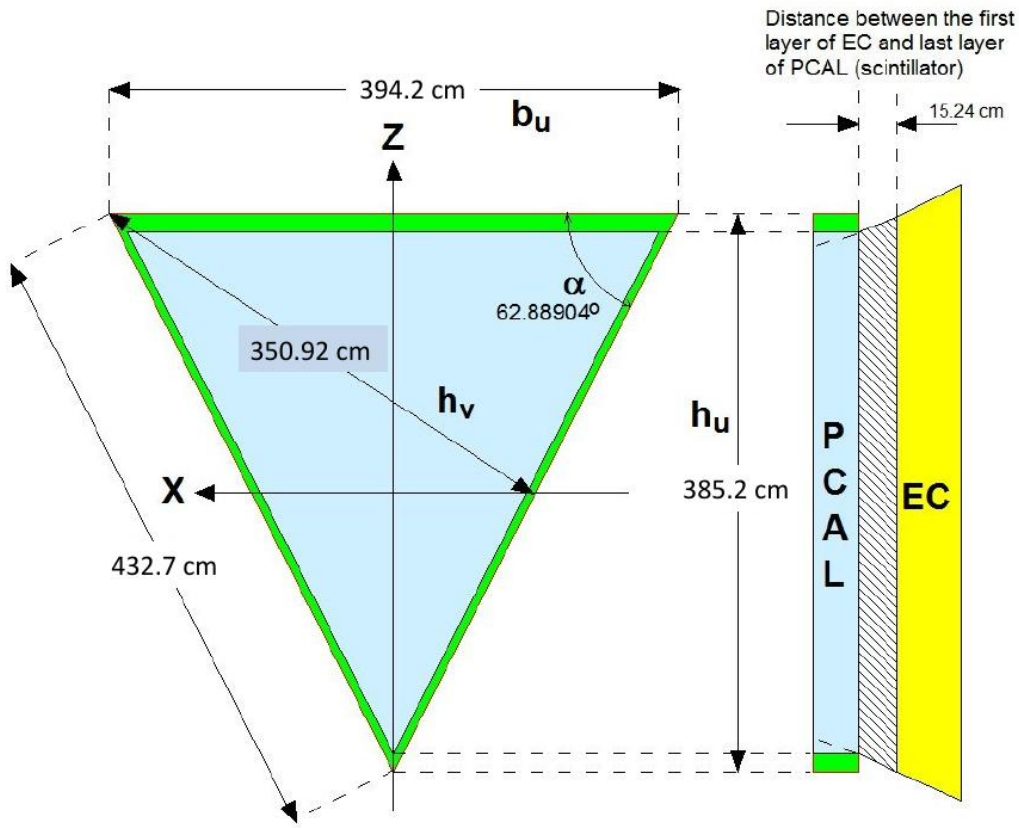

Figure 8.2: A schematic plot showing dimensions of a PCAL module. Image source: [A+15b]

layers repeat five times. Each repeating layer signal is coupled to the same Photomultiplier tube (PMT). The scintillator strips for the U-view, for example, are parallel to the base of the triangle, which is the farthest from the beamline. The strips in the W layer are parallel to the side which contains the PMTs for the U-layer and for those in the V layer are aligned parallel to the third side.

Because of the isosceles shape, the number of scintillator strips in the V and W layers are 77 each. Each of the 47 longer strips are connected to individual PMTs and the remaining 30 strips are coupled to 15 individual PMTs. In other words, there are 62

readout channels in the U and V layers. On the other hand, there are a total of 84 strips in the U plane, where 52 of the shorter strips are read out to a single PMT and other 32 longer strips are paired into 16 channels making a total of 68 readout channels. The alignment of the inner U, V and W layers can be seen in Figure 8.3.

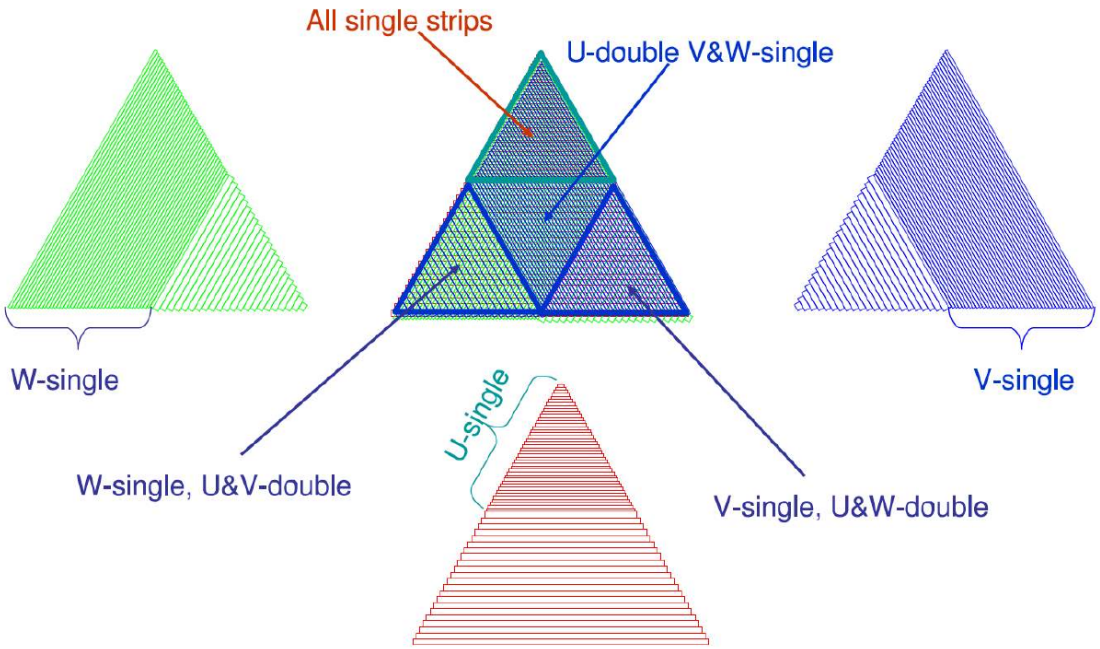

Figure 8.3: Arrangement of readout channels for U (red), V (blue) and W (green) layers. The upper middle plot shows the superposition of all three views. The U PMTs are mounted on the left side of the triangle, as seen in this view from the target, while the V and W PMTs are mounted along the base. Image source: [A+15b]

Strips in each view are numbered for easy identification and calibration purposes (U1-U68, V1-62 and W1-W62 based on the PMT readout). The higher numbered strips are the longer strips while shorter ones are the lower. For example, in the U plane, U1 is the shortest and U68 is the longest strip. The strip convention was originally used in the PCAL

Geometry Note [A+15b] and is used throughout this document for consistency. The layout shown in Figure 8.4 helps to better visualize this convention.

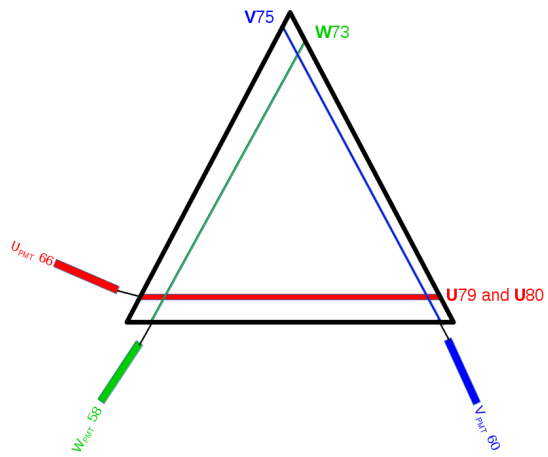

Figure 8.4: This drawing shows the layout of the PMT readout for different views.

To ensure the readout represents the true light attenuation, it is important to extract the attenuation coefficients evaluated from Analog-to-digital converter (ADC) values as a function of distance of hit from the PMT readout. The extraction of these coefficients are explained in the following sections.

8.2 Calibration

In order to calibrate the PCAL unit of the CLAS12 detector, one can think of dividing each PCAL module into bins based on the overlapping shapes. These shapes can be of two types. The first type is a 3-strip pixel in which all the views superimpose on each other, while the other shape is formed from the overlap of two strips from two different views (i.e. UV, VW or UW). The latter is called the 2-strip pixel. Figure 8.5 shows the mapping of all possible overlap conditions mentioned.

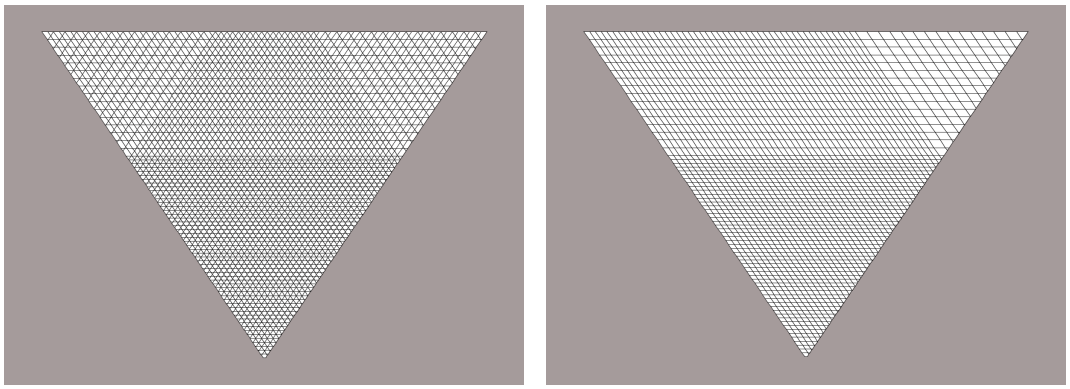

(a) Pixel map.

(b) UW overlap map.

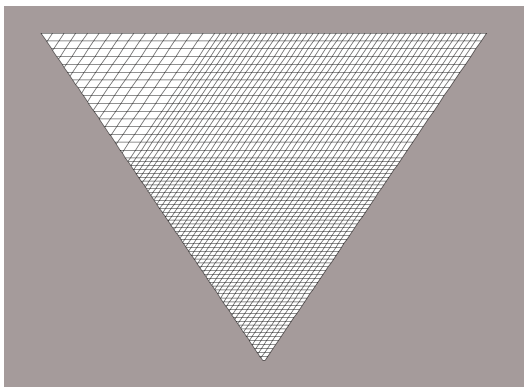

(c) UV overlap map.

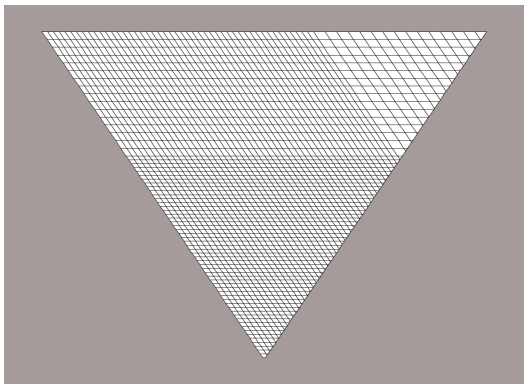

(d) WU overlap map.

Figure 8.5: Shown are the different ways overlaps can be considered in a single PCAL module.

The data used for the calibration was collected using cosmic ray muons before the PCAL unit was installed as a part of the CLAS12 detector subsystem. For these data, the PCAL sectors were oriented in the horizontal plane. As the muons travel through the scintillator strips, light is emitted. Because the light produced had a small attenuation length and may not reach the PMT, wavelength shifting fibers were used in the scintillators. The fibers converted the original blue light into green light increasing the attenuation length to more than three meters enabling the detection of light at the PMT. For each hit in the

bins, one might expect a peak at ADC values corresponding to the minimum ionizing hit of the muons.

The calibration process involved four steps. The first step was to calculate the distance (x) from the hit to the PMT. The sum of physical widths from the bin center to the edge of the PCAL unit for a particular view provided the distance. The next step was to extract the centroid of the ADC distribution. The distribution contained unknown backgrounds which were reduced by applying various cuts. This enhanced the signal peak, which was fit using a Gaussian function. This provided the peak centroids. In the third step, the centroids were plotted as a function of the distances from the first step. This is the attenuation curve. The shape of curve was fit with a function

$$I(x) = Ae^{-Bx} + C, \tag{8.1}$$

where A, B and C are the fit parameters. These parameters constitute the attenuation coefficients.

The final step was to make sure the method was reproducible within reasonable uncertainty. For this, events were simulated using given calibration coefficients. A total of 3 million events were generated in the module 2 of the PCAL unit in order to do the simulation studies and check the established method.

8.2.1 Calculation of the Distance

A 3-strip pixel could be of an odd geometrical shape. The distance for each 3-strip pixel with respect to the corresponding PMT in a view was formulated using a pixel map created by N. Compton [Com16]. This map was developed based on the PCAL geometry in the CLAS Calibration DataBase (CCDB). The outline of the map is shown in Figure 8.5a. The pixel map provided the distance from the bin center to the edge in any required view (U, V or W).

On the other hand, a 2-strip pixel is usually a trapezoid. One example bin is shown in Figure 8.6. If w is the width of a strip ($\approx$ 4.5 cm), then its width s can be found by using,

$$s = \frac{w}{\sin\alpha} \tag{8.2}$$

where α is the base angle of a PCAL module.

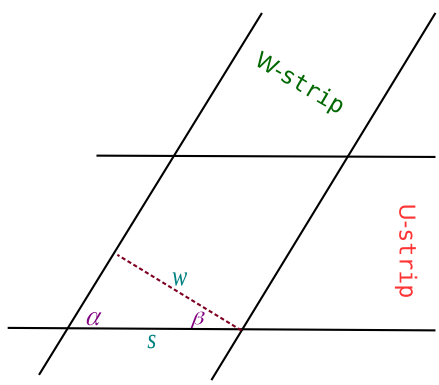

Figure 8.6: Outline of a generic intersection of a u and w strip. The distance between the trapezoidal area and the PCAL edge can be represented by a linear function of s. Note here that α is the same angle shown in Figure 8.2.

If a hit in the overlap of V60 and U66, for example, is registered then the distance x is given by the distance from the bin center of the overlap to the U-PMT

8.2.2 Extraction of Centroids

Various cuts were applied to the data to ensure a more accurate calibration.

Multiplicity cut: Any physical event cannot have more than three PMT readouts. Therefore, a multiplicity cut was used to remove any event that contained more than one readout in each layer. Cosmic ray trajectory may not be always perpendicular to the face of the PCAL unit. Applying this cut ensured the removal for events. The accepted range of angles (different from perpendicular to the PCAL face) varies as a function of strip number

and is not uniform in all directions. This multiplicity cut also helps in removing events where multiple cosmic rays hit the detector within the same time interval, due to possible firing of more PMTs.

Dalitz cut: The Dalitz condition implies that if a point inside a triangle is chosen, no matter the location, the sum of the distances to each edge will be unchanged. This distance was empirically found to be two units relative to the size of the triangle for any hit location. If this condition was not satisfied, then the hit recorded was most likely electronic noise, an indirect hit, or multiple cosmic ray hits recorded at once and hence removed from the analysis.

Removal of Unphysical Events: Using the pixel map, a correlation between the layers was set up, where events in low U-strips never correlated with those in the low V-strips, for example. Using this correlation, unphysical events were removed from the data.

Shape of the signal: Once all the above cuts are applied, the ADC distribution showed a peak over a smooth background in most of the bins. One sample bin is shown in Figure 8.7, where the Gaussian function was used to fit the peak and the background was estimated by an exponential function. The Gaussian mean was recorded for all the bins in each view.

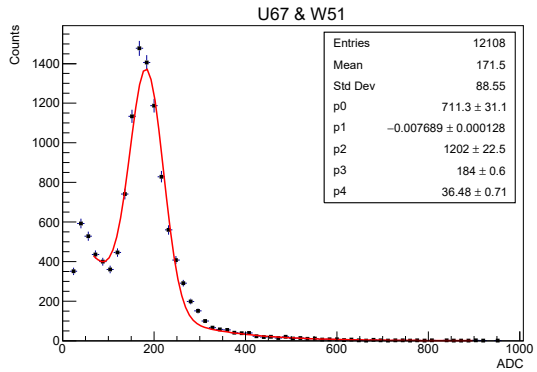

Figure 8.7: An example of the distribution of the ADC readout from one u/w trapezoidal bin (overlap of U67 and W51). The fit (exponential combined with Gaussian) is shown by the red curve.

8.2.3 Attenuation Coefficients

In the final step, the centroids were plotted as a function of distance for each bin center. The curve was then fit using the function described in Equation 8.1. The extracted parameters were used to restrict the ADC distribution in the next iteration. After multiple iterations, the ADC distribution was much cleaner and the attenuation curve could be described well with the fit parameters and reliable attenuation coefficients were obtained (Figure 8.8).

The attenuation coefficients A, B and C extracted from the fits were then saved to the CLAS12 Calibration Database for each module.

8.2.4 Reproducibility

Near the PMT ($x = 0$), ideally no light attenuation is expected so that the light intensity from Equation 8.1 becomes

$$I(x) = A + C. \tag{8.3}$$

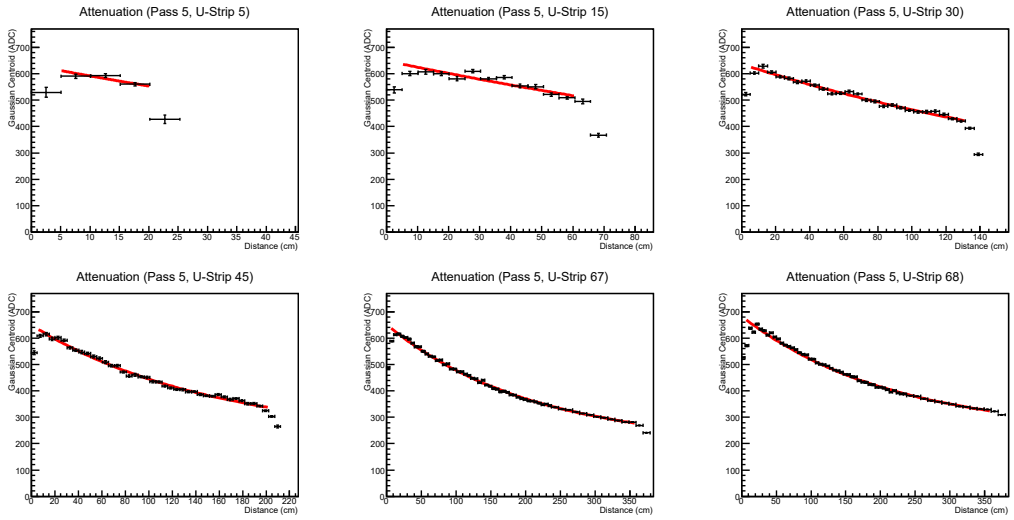

Figure 8.8: The attenuation fits for selected U-strips are shown (U5, U15, U30, U45, U67, and U68). Image Source: [Com16].

This quantity is known as the gain. The gain was normalized to an *ad hoc* value of 100. The normalized values were fed as the generation input in the GEant4 Monte Carlo (GEMC) simulation [Ung]. As this was a simulation, no background is expected. Nonetheless, similar cuts as data were applied to the generated events.

The events that passed the initial cuts were binned in the same way as the data. In most of these bins a Gaussian function described the ADC distribution reasonably well (reduced χ^2 within 10% of unity). The centroids for such bins were approximated from the Gaussian fits. However, it was also found that some bins have very small number of counts and the Gaussian function could not define the distribution accurately. To account for that, a fit condition was employed. If the number of events was less than 20, the statistical mean was used as the centroid. The process was repeated for every strip in each view. The ADC distributions and the Gaussian fits for U67 are shown in Figure 8.9.

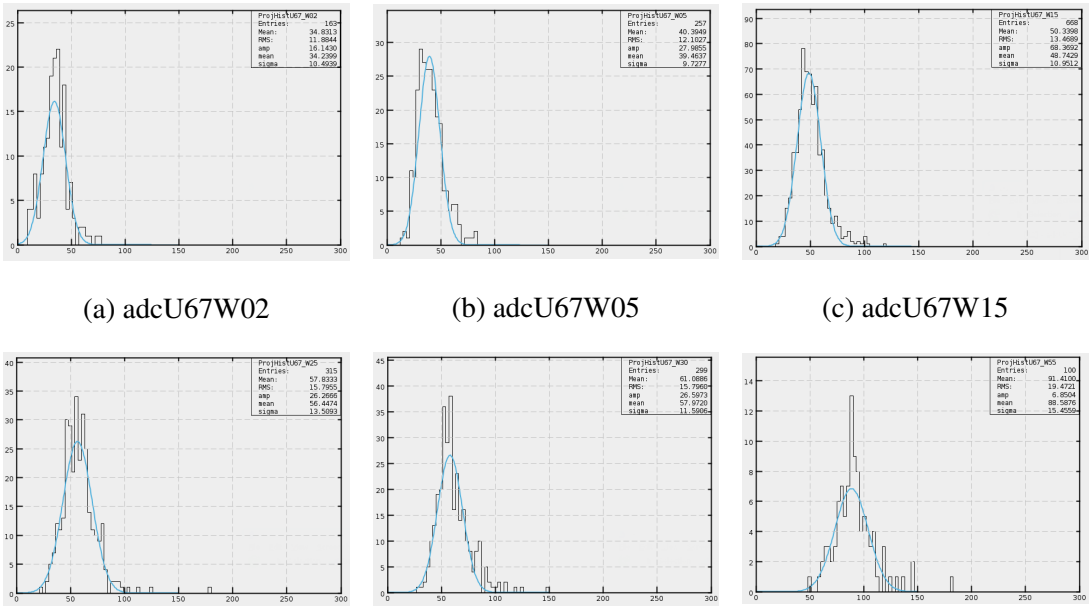

(a) adcU67W02 (b) adcU67W05 (c) adcU67W15

(d) adcU67W25 (e) adcU67W30 (f) adcU67W55

Figure 8.9: ADC distribution for U67 for some W bins for the GEMC events. The last two digits in the caption of each figure represent the bin number based on the W strip. Blue curve is the Gaussian fit.

In the similar way, centroids for other U-strips were extracted and stored. After calculating the corresponding distances from the center of these bins, the centroids were plotted. The resulting plot was fit using Equation 8.1 to extract the fit parameters. This process is repeated for each strip in each view so that a set of 68 U, 62 V and W coefficients are recorded. To illustrate the process, the fit (blue curve) for U67 is shown in Figure 8.10. A curve representing y_{Gen} for U67 is drawn in red.

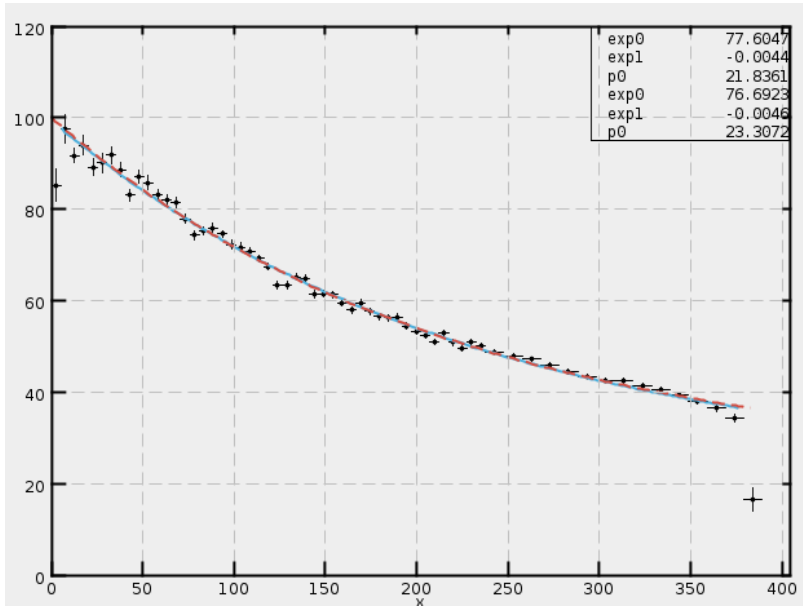

Figure 8.10: Exponential fit for U67. The first set of three coefficients are from the fit and the next set of three are the coefficients used in the event generation.

The calibration coefficients from the CCDB and the ones extracted from simulation were in very good visual agreement. One way to test the results is to compare the input and the output coefficients. However, the coefficients cannot be directly compared to one another as different coefficients can define the same exponential form as in Equation 8.1 fairly well. Therefore, for a given distance x, the light intensities were separately calculated and compared using

$$\frac{\Delta y}{y_{Gen}} = \frac{y_{Gen} - y_{calc}}{y_{Gen}} \tag{8.4}$$

where $y \equiv y(x) = Ae^{-Bx} + C$. This ratio was calculated as a function of distance and the variation for the U view can be seen in Figure 8.11. From the variation, it can be concluded that the coefficients were reproduced within 3% for longer strips. Some shorter strips, however, were not reproduced that well. The major reason was due to a very low number of events in each bin for such strips. Nonetheless, the overall average variation using the

new software based on `Java` to reproduce the coefficients was within 5% for all views. This

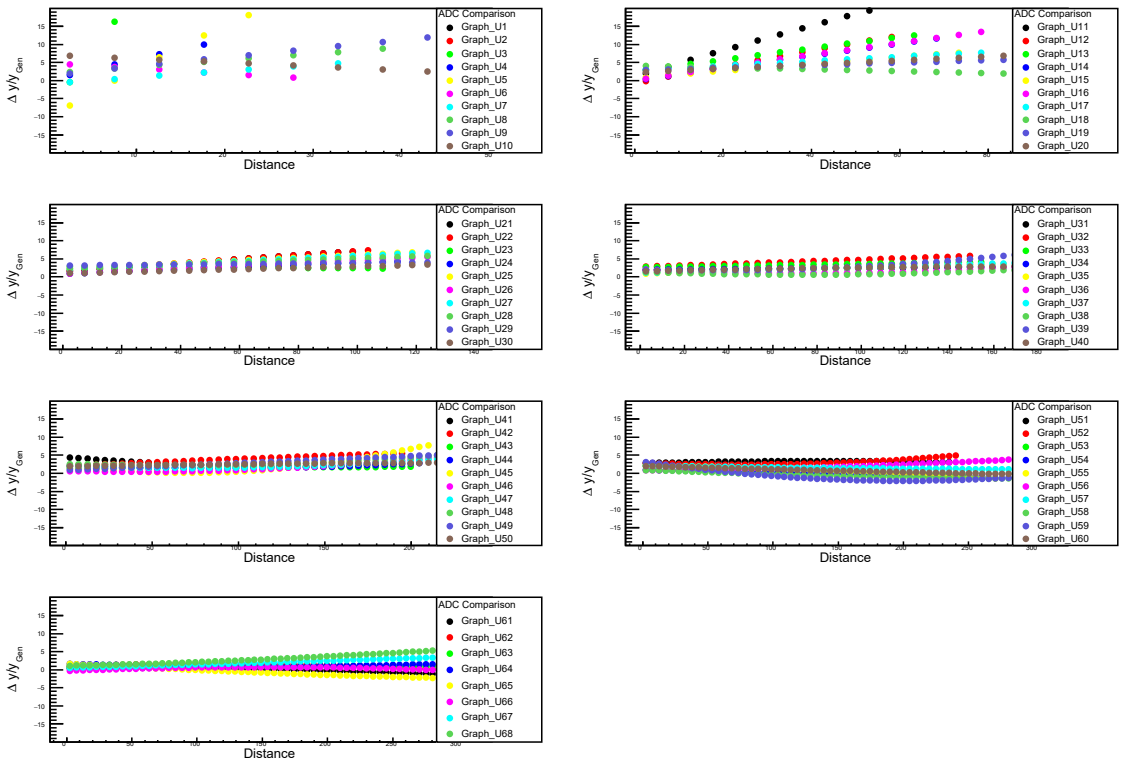

Figure 8.11: Difference of the generated and calculated attenuation curves as a function of distance for all strips in the U view.

test provided a check of the method that was used to calculate the calibration coefficients previously using `C++`.

8.3 Summary

As a member of the CLAS collaboration, I worked together with various other members and contributed in the development of the PCAL calibration software. This `Java`-based software not only performed the calibration at a real time but also presented the progress in the form of various figures (ADC distribution, fits, centroid plot versus

distance, gain, etc.) in the Graphical User Interface. One major accomplishment was the ability to reproduce the attenuation coefficients used as input during the simulation. This verification tested the geometry as well as various methods implemented in the extraction of the coefficients from cosmic data using C++ based codes. It is because of quality of these coefficients that during the Key Performance Parameter run in the Spring of 2017 with the upgraded detector, the PCAL unit was shown to reproduce pions from the invariant mass of the two photons with a good resolution [KPP17]. The data taking runs started in the Fall of 2018 with the upgraded detector.

9 Conclusion

Understanding the mechanics of the strong force within a hadron arising due to the quark-gluon or the gluon-gluon interactions is one of the most challenging problem for the particle physics community. In the low energy or the non-perturbative energy regime, the origins of quark confinement is not well understood. Similarly, another aspect of the problem lies with the asymptotic freedom of the quarks. In order to solve these problems, an insight into this non-perturbative regime is necessary. Although the non-perturbative solution is technically possible with the lattice QCD, due to computational limits, it is still a distant reality. Even with its possibility, we would need input from experimental observations for the validation and extension of the lattice calculations. Therefore, physicists rely on tools such as the hadron spectroscopy. That said, this tool also has its challenges and limitations to present a full understanding of different kinematics. Therefore, it is important to extract observables such as the differential cross sections and make physical interpretations. This thesis adds to the world data, differential cross sections of three channels, where the first two are t-channel processes (ρ and ω photoproduction) and the third one deals with a possible dibaryon resonance using the same data sample from the g10 experiment at the Hall B of Jefferson Lab.

The study of the vector meson channels provided similar insight about the double scattering process that is dominant at higher momentum transfer. For the highest photon energies in the vector meson studies, the scattering cross section for the $\omega - N$ interaction was found to be larger than that of the $\rho - N$ interaction. This may be due to the isospin of the two vector mesons. The ω is an isosinglet (isospin 0) meson while the ρ has isospin 1. Within isospin symmetry, the interaction of the ρ meson allows the exchange of other non-isosinglets such as the pseudoscalar mesons(pions) making the t-channel process more complicated. Complexities near the production threshold for the ρ-meson may also arise due to nucleon resonances in the s-channel. The ω photoproduction, however, avoids such

complications. As the final state ωd are isosinglets, the exchange of non-isosinglets is restricted in the ω photoproduction off of the deuterium. In this thesis, the data was found to be consistent with the rescattering model with $30 < \sigma_{\omega N} < 40$ mb for the process $\gamma d \to \omega d$ in the framework of the VMD model. The same model with different set of parameters for the photoproduction of the ρ-meson was measured to be $20 < \sigma_{\rho N} < 26$ mb for the slope parameters $7.0 < b < 8.0$ GeV^{-2}. Both of the results are the first world measurements in the kinematic range selected in this work for the lower mass vector mesons.

Experimental information on σ_{VN} is of interest currently due to progress within lattice QCD, which can now extract meson-meson scattering phase shifts directly [WBnD$^+$15]. This is a significant advance because it connects QCD calculations to experimental observables, such as the total cross sections. Such a direct connection between non-perturbative QCD and experiment has been rare and hence measurements of the scattering cross section of these light vector mesons (which are fairly stable on the lattice compared with massive mesons or other baryons) can be soon compared with predictions from LQCD calculations.

The g10 data is full of many potential research avenues. Besides the vector meson channels, which are t-channel processes, this thesis also investigated other s-channel resonances demonstrating the richness of the g10 dataset. The presence of three possible dibaryon states ($N\Delta$ configuration) defined as d^{*++}, d^{*0} and d^{*+} from the detected final state $d\pi^+\pi^-$ is a unique find with a matching mass of about 2150 MeV for each structure. The Dalitz plot of the $d\pi^+$ invariant mass-squared versus the $d\pi^-$ invariant mass-squared exhibits a pronounced broad resonance line symmetric in both invariant mass systems at about 2150 MeV, slightly below the nominal $N\Delta$ threshold. This mass aligns with previously observed resonance structure in the SAID partial wave analysis [ASWB93] and from the predictions of Dyson and Xuong [DX64].

Furthermore, a preliminary differential cross section was measured for the doubly charged state, d^{*++} decaying into coherent d and π^+. The assumption that the background processes $\gamma d \rightarrow d^{*0}\pi^-$, $\gamma d \rightarrow \rho d$ and the phase space $\gamma d \rightarrow d\pi^+\pi^-$ along with the signal was found to reasonably describe the data within a first order approximation. The differential cross sections for the most forward angular bin, $0.6 < \cos\theta^{\pi^-}_{CM} < 0.8$, showed a decreasing trend from the energy close to the threshold to higher energies in the center of mass reference frame ($2.7 < W < 3.2$ GeV). In this kinematic range, within the assumption, the differential cross sections ranged from about 17-246 nb. Although a physical interpretation of the result is pending, it is still an achievement for future analysis of these exotic channels. A complete understanding warrants a full partial wave analysis on these channels which will help disentangle the resonant contributions. Measuring the properties of these new states will illuminate in our understanding of the basic structure of matter.

References

[A+71] R. L. Anderson et al. Determination of the ρ-meson-nucleon cross section from elastic ρ photoproduction on deuterium. *Phys. Rev. D*, 4:3245–3250, Dec 1971. URL: http://link.aps.org/doi/10.1103/PhysRevD.4.3245, doi:10.1103/PhysRevD.4.3245

[A+11] P. Adlarson et al. Abashian-booth-crowe effect in basic double-pionic fusion: A new resonance? *Phys. Rev. Lett.*, 106:242302, Jun 2011. URL: https://link.aps.org/doi/10.1103/PhysRevLett.106.242302, doi:10.1103/PhysRevLett.106.242302

[A+13] P. Adlarson et al. Measurement of the $pn \to pp\pi^0\pi^-$ reaction in search for the recently observed resonance structure in $d\pi^0\pi^0$ and $d\pi^+\pi^-$ systems. *Phys. Rev. C*, 88:055208, Nov 2013. URL: https://link.aps.org/doi/10.1103/PhysRevC.88.055208, doi:10.1103/PhysRevC.88.055208

[A+15a] R. Aaij et al. Observation of $j/\psi p$ resonances consistent with pentaquark states in $\Lambda_b^0 \to j/\psi K^- p$ decays. *Phys. Rev. Lett.*, 115:072001, Aug 2015. URL: https://link.aps.org/doi/10.1103/PhysRevLett.115.072001, doi:10.1103/PhysRevLett.115.072001

[A+15b] G. Asryan et al. The geometry of the clas12 pre-shower calorimeter. *CLAS12-NOTE*, (2), 2015. URL: https://clasweb.jlab.org/wiki/images/d/d0/Pcal_geometry_note.pdf

[A+17] R. Aaij et al. Observation of $j/\psi\phi$ structures consistent with exotic states from amplitude analysis of $B^+ \to j/\psi\phi K^+$ decays. *Phys. Rev. Lett.*, 118:022003, Jan 2017. URL: https://link.aps.org/doi/10.1103/PhysRevLett.118.022003, doi:10.1103/PhysRevLett.118.022003

[AAB+01] M. Amarian, G. Asryan, K. Beard, W. Brooks, V. Burkert, T. Carstens, A. Coleman, R. Demirchyan, Yu. Efremenko, H. Egiyan, K. Egiyan, H. Funsten, V. Gavrilov, K. Giovanetti, R.M. Marshall, B. Mecking, R.C. Minehart, H. Mkrtchan, M. Ohandjanyan, Yu. Sharabian, L.C. Smith, S. Stepanyan, W.A. Stephens, T.Y. Tung, and C. Zorn. The clas forward electromagnetic calorimeter. *Nuclear Instruments and Methods in Physics Research Section A: Accelerators, Spectrometers, Detectors and Associated Equipment*, 460(2):239 – 265, 2001. URL: http://www.sciencedirect.com/science/article/pii/S0168900200009967, doi:https://doi.org/10.1016/S0168-9002(00)00996-7

[ABC+01] G. Adams, V. Burkert, R. Carl, T. Carstens, V. Frolov, L. Houghtlin, G. Jacobs, M. Kossov, M. Klusman, B. Kross, M. Onuk, J. Napolitano, J.W. Price, C. Riggs, Y. Sharabian, A. Stavinsky, L.C. Smith, W.A.

Stephens, P. Stoler, W. Tuzel, K. Ullrich, A. Vlassov, A. Weisenberger, M. Witkowski, B. Wojtekhowski, P.F. Yergin, and C. Zorn. The clas cherenkov detector. *Nuclear Instruments and Methods in Physics Research Section A: Accelerators, Spectrometers, Detectors and Associated Equipment*, 465(2):414 – 427, 2001. URL: http://www.sciencedirect.com/science/article/pii/S0168900200013139, doi:https://doi.org/10.1016/S0168-9002(00)01313-9

[ASWB93] Richard A. Arndt, Igor I. Strakovsky, Ron L. Workman, and David V. Bugg. Analysis of the reaction π^+d→pp to 500 mev. *Phys. Rev. C*, 48:1926–1938, Oct 1993. URL: https://link.aps.org/doi/10.1103/PhysRevC.48.1926, doi:10.1103/PhysRevC.48.1926

[B$^+$] Rene Brun et al. TMath. https://root.cern.ch/root/html534/src/TMath.cxx.html#PzREtB. Accessed: January 14, 2019.

[B$^+$74] P. Benz et al. Photoproduction of ρ^0, ω and ρ^- mesons on deuterons at energies between 1 and 5 gev. *Nuclear Physics B*, 79(1):10 – 37, 1974. URL: http://www.sciencedirect.com/science/article/pii/055032137490176X, doi:http://dx.doi.org/10.1016/0550-3213(74)90176-X

[B$^+$77] P. Bapu et al. Photoproduction of ρ^0 and ρ^- mesons at 3 gev. *Phys. Rev. D*, 15:26–35, Jan 1977. URL: http://link.aps.org/doi/10.1103/PhysRevD.15.26, doi:10.1103/PhysRevD.15.26

[B$^+$03] M. Battaglieri et al. Photoproduction of the ω meson on the proton at large momentum transfer. *Phys. Rev. Lett.*, 90:022002, Jan 2003.

[BCD$^+$11] S. R. Beane, E. Chang, W. Detmold, B. Joo, H. W. Lin, T. C. Luu, K. Orginos, A. Parreño, M. J. Savage, A. Torok, and A. Walker-Loud. Evidence for a bound h dibaryon from lattice qcd. *Phys. Rev. Lett.*, 106:162001, Apr 2011. URL: https://link.aps.org/doi/10.1103/PhysRevLett.106.162001, doi:10.1103/PhysRevLett.106.162001

[BLTW70] H. J. Behrend, F. Lobkowicz, E. H. Thorndike, and A. A. Wehmann. Photoproduction of 8-gev rho mesons from nuclei. *Phys. Rev. Lett.*, 24:336–340, Feb 1970. *Ibid.* 24:1246-1251, June 1970. URL: http://link.aps.org/doi/10.1103/PhysRevLett.24.336, doi:10.1103/PhysRevLett.24.336

[BP05] J. Ball and E. Pasyuk. Photon flux determination through "out-of-time" sampling of out-of-time hits with the hall b photon tagger. *CLAS-Note*, 002, 2005.

[BSYP78] T. H. Bauer, R. D. Spital, D. R. Yennie, and F. M. Pipkin. The hadronic properties of the photon in high-energy interactions. *Rev. Mod. Phys.*,

50:261–436, Apr 1978. URL: https://link.aps.org/doi/10.1103/RevModPhys.50.261, doi:10.1103/RevModPhys.50.261

[C+09] W. Chen, , et al. Measurement of the differential cross section for the reaction $\gamma n \rightarrow \pi^- p$ from deuterium. *Phys. Rev. Lett.*, 103:012301, Jul 2009. URL: http://link.aps.org/doi/10.1103/PhysRevLett.103.012301, doi:10.1103/PhysRevLett.103.012301

[C+18] T. Chetry et al. Differential cross section for dd using clas at jefferson lab. *Physics Letters B*, 782:646 – 651, 2018. URL: http://www.sciencedirect.com/science/article/pii/S0370269318304489, doi:https://doi.org/10.1016/j.physletb.2018.06.003

[CHC14] N. Compton, K. Hicks, and M. Camp. Cross sections of $\gamma d \rightarrow k^0\Lambda(p)$ from g10. *CLAS-Note*, 2014. URL: https://www.jlab.org/Hall-B/shifts/admin/paperreviews/2014/k0lamv4-9309054-2014-11-18-v8.0.PDF

[Che10] W. Chen. A measurement of the differential cross section for the reaction $\gamma n \rightarrow \pi^- p$ from deuterium. *PhD. Thesis*, 2010.

[Com16] N. Compton. The differential cross section Λ recoil polarization from $\gamma d \rightarrow k^0\Lambda(p)$. *PhD. Thesis*, 2016.

[DX64] Freeman J. Dyson and Nguyen-Huu Xuong. $y = 2$ states in su(6) theory. *Phys. Rev. Lett.*, 13:815–817, Dec 1964. URL: https://link.aps.org/doi/10.1103/PhysRevLett.13.815, doi:10.1103/PhysRevLett.13.815

[ea14] P. Adlarson et. al. Evidence for a new resonance from polarized neutron-proton scattering. *Phys. Rev. Lett.*, 112:202301, May 2014. URL: http://link.aps.org/doi/10.1103/PhysRevLett.112.202301, doi:10.1103/PhysRevLett.112.202301

[EHK+76] Y. Eisenberg, B. Haber, E. Kogan, U. Karshon, E.E. Ronat, A. Shapira, and G. Yekutieli. Vector meson production by 4.3 gev polarized photons on deuterium. *Nuclear Physics B*, 104(1):61 – 97, 1976.

[EMWW61] A. R. Erwin, R. March, W. D. Walker, and E. West. Evidence for a $\pi - \pi$ resonance in the $i = 1$, $j = 1$ state. *Physical Reveiw Letters*, 6:628, 1961.

[FG66] V. Franco and R. J. Glauber. High-energy deuteron cross sections. *Physical Reveiw*, 4(11):1195–1214, 1966.

[FKM+97] L. Frankfurt, W. Koepf, J. Mutzbauer, G. Piller, M. Sargsian, and M. Strikman. Coherent photo- and lepto-production of vector mesons from deuterium. *Nuclear Physics A*, 622(4):511 – 537, 1997. URL: http://www.sciencedirect.com/science/article/pii/S0375947497806975, doi:http://dx.doi.org/10.1016/S0375-9474(97)80697-5

[G+76] V. P. Gupta et al. Coherent photoproduction of vector mesons on deuterium at 5.5 gev. *Phys. Rev. D*, 14:42–54, July 1976. URL: http://link.aps.org/doi/10.1103/PhysRevD.14.42, doi:10.1103/PhysRevD.14.42

[GMZ61] Murray Gell-Mann and Fredrik Zachariasen. Form factors and vector mesons. *Phys. Rev.*, 124:953–964, Nov 1961. URL: http://link.aps.org/doi/10.1103/PhysRev.124.953, doi:10.1103/PhysRev.124.953

[Gri08] David J Griffiths. *Introduction to elementary particles; 2nd rev. version*. Physics textbook. Wiley, New York, NY, 2008. URL: https://cds.cern.ch/record/111880

[GS94] W. Greiner and A. Schäfer. *Quantum Chromodynamics*. Springer-Verlag Berlin Heidelberg New York, 1994.

[Hol] M. Holtrop. GSIM: CLAS GEANT Simulation. URL: http://nuclear.unh.edu/~maurik/Gsim/gsim_info.shtml

[Hos92] Norio Hoshizaki. S-matrix poles and phase shifts for nΔ scattering. *Phys. Rev. C*, 45:R1424–R1427, Apr 1992. URL: https://link.aps.org/doi/10.1103/PhysRevC.45.R1424, doi:10.1103/PhysRevC.45.R1424

[Hos93] Norio Hoshizaki. S-matrix poles for unstable-particle scattering. *Progress of Theoretical Physics*, 89(1):245–250, 1993. URL: http://dx.doi.org/10.1143/ptp/89.1.245, doi:10.1143/ptp/89.1.245

[IIA+11] Takashi Inoue, Noriyoshi Ishii, Sinya Aoki, Takumi Doi, Tetsuo Hatsuda, Yoichi Ikeda, Keiko Murano, Hidekatsu Nemura, and Kenji Sasaki. Bound *h* dibaryon in flavor su(3) limit of lattice qcd. *Phys. Rev. Lett.*, 106:162002, Apr 2011. URL: https://link.aps.org/doi/10.1103/PhysRevLett.106.162002, doi:10.1103/PhysRevLett.106.162002

[Jaf77] R. L. Jaffe. Perhaps a stable dihyperon. *Physical Review Letters*, 38(5):195–198, 1977.

[KPP17] KPP Run, 2017. URL: https://wiki.jlab.org/clas12-run/index.php/KPP_Run

[LDK01] Christoph W. Leemann, David R. Douglas, and Geoffrey A. Krafft. The continuous electron beam accelerator facility: Cebaf at the jefferson laboratory. *Annual Review of Nuclear and Particle Science*, 51(1):413–450, 2001. URL: https://doi.org/10.1146/annurev.nucl.51.101701.132327, arXiv:https://doi.org/10.1146/annurev.nucl.51.101701.132327, doi:10.1146/annurev.nucl.51.101701.132327

[M+03] B. A. Mecking et al. The cebaf large acceptance spectrometer (clas). *Nuclear Instruments and Methods in Physics Research A*, 3:513–533, 2003.

[M+07] T. Mibe et al. Measurement of coherent ϕ-meson photoproduction from the deuteron at low energies. *Phys. Rev. C*, 76:052202, Nov 2007. URL: http://link.aps.org/doi/10.1103/PhysRevC.76.052202, doi:10.1103/PhysRevC.76.052202

[McK06] B. McKinnon. Study for the Θ^+ pentaquark in the reaction $\gamma d \to pK^+K^-n$ with clas. *PhD. Thesis*, 2006.

[Mib07] T. Mibe. Coherent ϕ-meson photoproduction on deuterium. *CLAS-Note*, 110, 2007.

[MS08] B. R. Martin and G. Shaw. *Particle Physics*. John Wiley & Sons Ltd, third edition, 2008.

[O+14] K. A. Olive et al. Review of Particle Physics. *Chin. Phys.*, C38:090001, 2014. doi:10.1088/1674-1137/38/9/090001

[Pas07] E. Pasyuk. Energy loss corrections for charged particles in clas. *CLAS-Note*, 016, 2007. URL: https://misportal.jlab.org/ul/physics/hall-b/clas/viewFile.cfm/2007-016.pdf?documentId=423

[Q+09] X. Qian et al. The extraction of total cross section from. *Physics Letters B*, 680(5):417 – 422, 2009. URL: http://www.sciencedirect.com/science/article/pii/S0370269309010934, doi:http://dx.doi.org/10.1016/j.physletb.2009.09.024

[S+05] S. Stepanyan et al. Energy calibration of the hall b bremsstrahlung tagging system using a magnetic pair spectrometer. *CLAS-Note*, 012, 2005.

[Sak60] J.J Sakurai. Theory of strong interactions. *Annals of Physics*, 11(1):1 – 48, 1960. URL: http://www.sciencedirect.com/science/article/pii/0003491660901263, doi:http://dx.doi.org/10.1016/0003-4916(60)90126-3

[SCD+99] E.S. Smith, T. Carstens, J. Distelbrink, M. Eckhause, H. Egiyan, L. Elouadrhiri, J. Ficenec, M. Guidal, A.D. Hancock, F.W. Hersman, M. Holtrop, D.A. Jenkins, W. Kim, K. Loukachine, K. MacArthur, C. Marchand, B. Mecking, G. Mutchler, D. Schutt, L.C. Smith, T.P. Smith, S. Taylor, T.Y. Tung, A. Weisenberger, and R.E. Welsh. The time-of-flight system for clas. *Nuclear Instruments and Methods in Physics Research Section A: Accelerators, Spectrometers, Detectors and Associated Equipment*, 432(2):265 – 298, 1999. URL: http://www.sciencedirect.com/science/article/pii/S0168900299004842, doi:https://doi.org/10.1016/S0168-9002(99)00484-2

[SCL+00] D.I. Sober, Hall Crannell, Alberto Longhi, S.K. Matthews, J.T. O'Brien, B.L. Berman, W.J. Briscoe, Philip L. Cole, J.P. Connelly, W.R. Dodge,

L.Y. Murphy, S.A. Philips, M.K. Dugger, D. Lawrence, B.G. Ritchie, E.S. Smith, James M. Lambert, E. Anciant, G. Audit, T. Auger, C. Marchand, M. Klusman, J. Napolitano, M.A. Khandaker, C.W. Salgado, and A.J. Sarty. The bremsstrahlung tagged photon beam in hall b at jlab. *Nuclear Instruments and Methods in Physics Research Section A: Accelerators, Spectrometers, Detectors and Associated Equipment*, 440(2):263 – 284, 2000. URL: http://www.sciencedirect.com/science/article/pii/S0168900299007846, doi:https://doi.org/10.1016/S0168-9002(99)00784-6

[Ste06] S. Stepanyan. Generic event generator fsgen. *CLAS-CVS*, 2006.

[TAD+01] S Taylor, S Ahmad, J Distelbrink, G.S Mutchler, E Smith, and T Smith. The clas start counter. *Nuclear Instruments and Methods in Physics Research Section A: Accelerators, Spectrometers, Detectors and Associated Equipment*, 462(3):484 – 493, 2001. URL: http://www.sciencedirect.com/science/article/pii/S0168900200011256, doi:https://doi.org/10.1016/S0168-9002(00)01125-6

[UBM32] Harold C. Urey, F. G. Brickwedde, and G. M. Murphy. A hydrogen isotope of mass 2. *Phys. Rev.*, 39:164–165, Jan 1932. URL: https://link.aps.org/doi/10.1103/PhysRev.39.164, doi:10.1103/PhysRev.39.164

[Ung] M. Ungaro. GEant4 Monte-Carlo. URL: https://gemc.jlab.org/gemc/html/index.html

[VKMR10] A. G. Voronin, D. E. Karmanov, M. M. Merkin, and S. V. Rogozhin. First results in studying the readout electronics of the silicon tracking system for upgrading the clas12 experiment. *Instruments and Experimental Techniques*, 53(6):805–811, Nov 2010. URL: https://doi.org/10.1134/S0020441210060072, doi:10.1134/S0020441210060072

[WBnD+15] David J. Wilson, Raúl A. Briceño, Jozef J. Dudek, Robert G. Edwards, and Christopher E. Thomas. Coupled $\pi\pi$, $k\overline{K}$ scattering in p-wave and the ρ resonance from lattice qcd. *Phys. Rev. D*, 92:094502, Nov 2015. URL: https://link.aps.org/doi/10.1103/PhysRevD.92.094502, doi:10.1103/PhysRevD.92.094502

Appendix A: g10 Data Run

This analysis used 278 runs and a total of 5667 sub-runs. Listed are the run numbers used:

42344	42345	42349	42360	42361	42362	42363	42364	42371	42372
42377	42378	42380	42381	42382	42383	42384	42385	42386	42387
42388	42389	42390	42391	42392	42393	42394	42395	42396	42397
42398	42399	42400	42401	42402	42403	42404	42405	42406	42430
42431	42433	42434	42435	42436	42437	42438	42441	42442	42449
42450	42451	42452	42453	42454	42455	42460	42462	42467	42468
42469	42470	42473	42474	42475	42476	42477	42478	42479	42480
42481	42507	42508	42509	42512	42513	42514	42515	42516	42517
42518	42519	42520	42521	42522	42525	42527	42528	42531	42532
42533	42534	42535	42536	42537	42538	42539	42540	42541	42542
42543	42544	42545	42546	42547	42548	42549	42550	42551	42552
42553	42554	42555	42556	42557	42558	42559	42560	42561	42562
42563	42564	42565	42566	42567	42570	42573	42574	42575	42576
42577	42578	42579	42580	42583	42584	42585	42586	42587	42589
42590	42591	42592	42593	42594	42597	42598	42601	42606	42607
42609	42610	42611	42612	42613	42614	42615	42616	42617	42618
42619	42621	42625	42626	42630	42631	42632	42633	42635	42639
42642	42647	42650	42651	42652	42653	42654	42655	42656	42658
42661	42662	42663	42664	42665	42666	42667	42668	42669	42670
42671	42672	42673	42674	42675	42677	42678	42679	42680	42681
42683	42684	42685	42686	42687	42688	42689	42690	42692	42693
42694	42695	42697	42718	42719	42720	42721	42722	42723	42730

Table A.1 continued from previous page

42731	42732	42733	42736	42737	42743	42744	42745	42748	42749
42751	42755	42756	42757	42758	42760	42761	42762	42763	42767
42770	42771	42772	42773	42774	42776	42777	42780	42783	42784
42785	42786	42787	42788	42789	42790	42791	42863	42866	42870
42871	42872	42873	42874	42889	42890	42892	42893	42894	42895
42896	42917	42918	42919	42920	42921	42922			

Table A.1: List of run numbers used.

Appendix B: Selection of Events

B.1 PID: Timing Plots

Figure B.1 shows the timing distribution before any specific cuts were applied. This plot shows accidentals sneaking in in the distribution. To provide a sample of what we expect, Figure B.2 shows the timing distribution of the detected deuteron before and after the cut was applied. Figs B.1 and B.2 are generated for the first five run numbers listed in Table A.1.

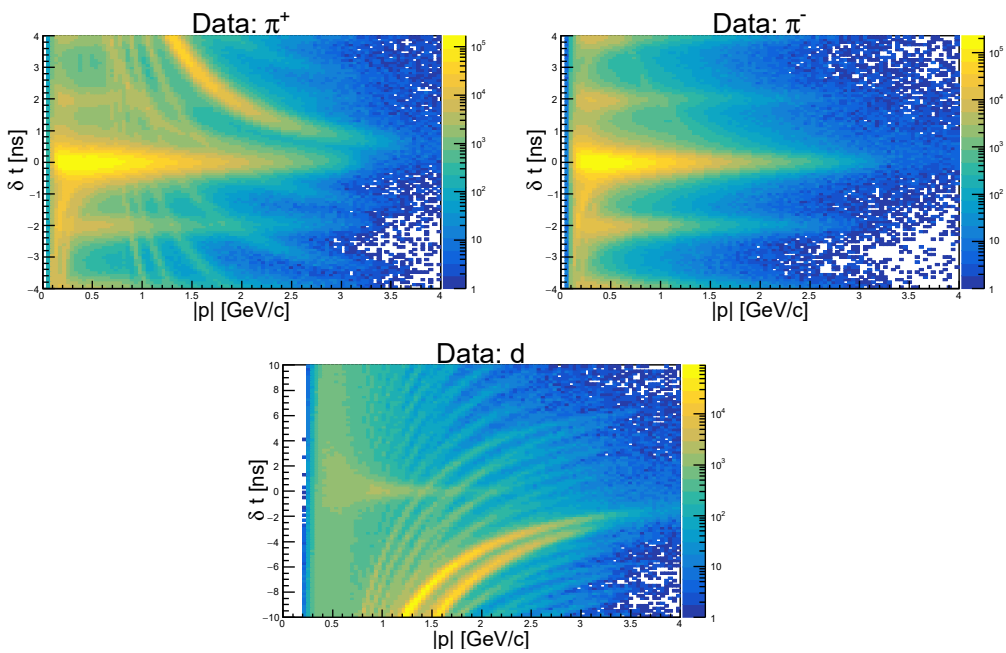

Figure B.1: Timing distribution used for particle identification before any coincidence requirement was imposed.

This section deals with how the accidentals were removed and how the particles were cleanly identified.

A pre-skim on the exclusive reaction channel $\gamma d \rightarrow \pi^+\pi^- d$ was done with wide δt cuts. Using this pre-skimmed data, a momentum dependent timing study was performed to

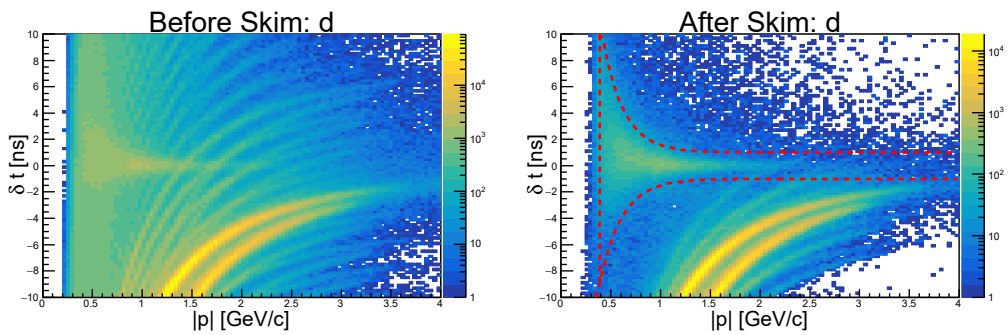

Figure B.2: Timing distribution for the detected deuteron before and after the skim. The number of accidentals are greatly reduced. The dashed curves represent a cut level C1 of Table C1 of Table 3.2; No energy loss correction was made at this point.]

apply new cuts to the current channel $\gamma d \rightarrow \omega d \rightarrow \pi^+\pi^- d(\pi^0)$. This cut was obtained by making preliminary straight cuts ($|\delta t_{\pi^\pm}| < 1$ ns and $|\delta t_d| < 4$ ns) for the detected particles. The events were then iteratively fit and applied new timing cuts. The events were binned in several momentum bins. Using a Gaussian fitting function, centroid and width of the distribution for each momentum bin were extracted. Exponential functions of the form,

$$\delta t_\mu = p0_\mu e^{p1_\mu |p|} + p2_\mu, \tag{B.1}$$

and

$$\delta t_\sigma = p0_\sigma e^{p1_\sigma |p|} + p2_\sigma \tag{B.2}$$

were then used to extract fit parameters $p0$, $p1$ and $p2$ for the Gaussian centroids (μ) and widths (σ) when fit. A 3σ timing cut means that events satisfying the condition

$$\delta t_\mu - 3\delta t_\sigma < \delta t < \delta t_\mu + 3\delta t_\sigma, \tag{B.3}$$

are only kept, ie, events outside of this limit were rejected from the analysis. Similar procedure was followed to extract the cut for the simulated events also. Sample Gaussian along with the exponential fits for final state d in data and simulation are shown here:

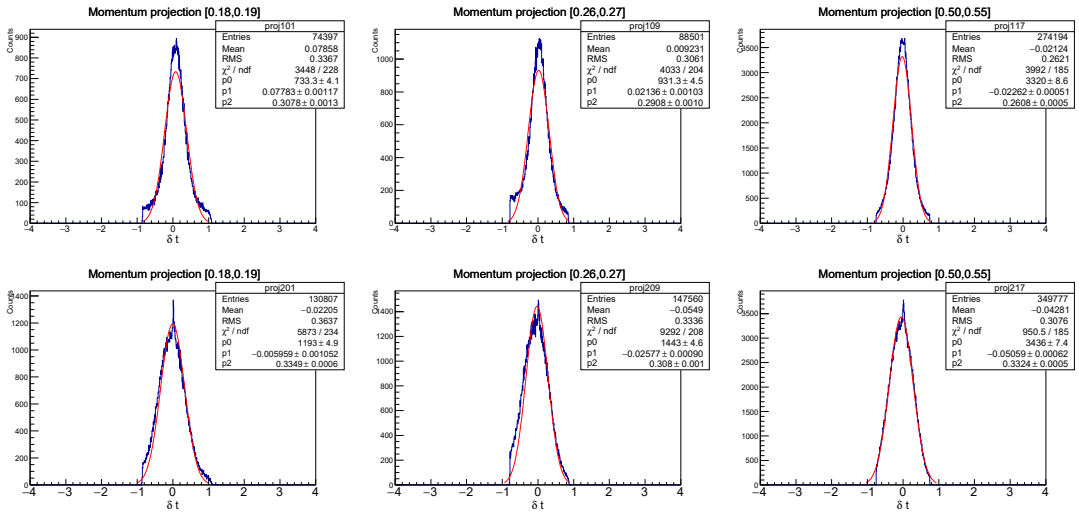

Figure B.3: The top row of plots the timing distributions are for π^+ in Simulation for a few bins. In the bottom row, the MC distributions are shown.

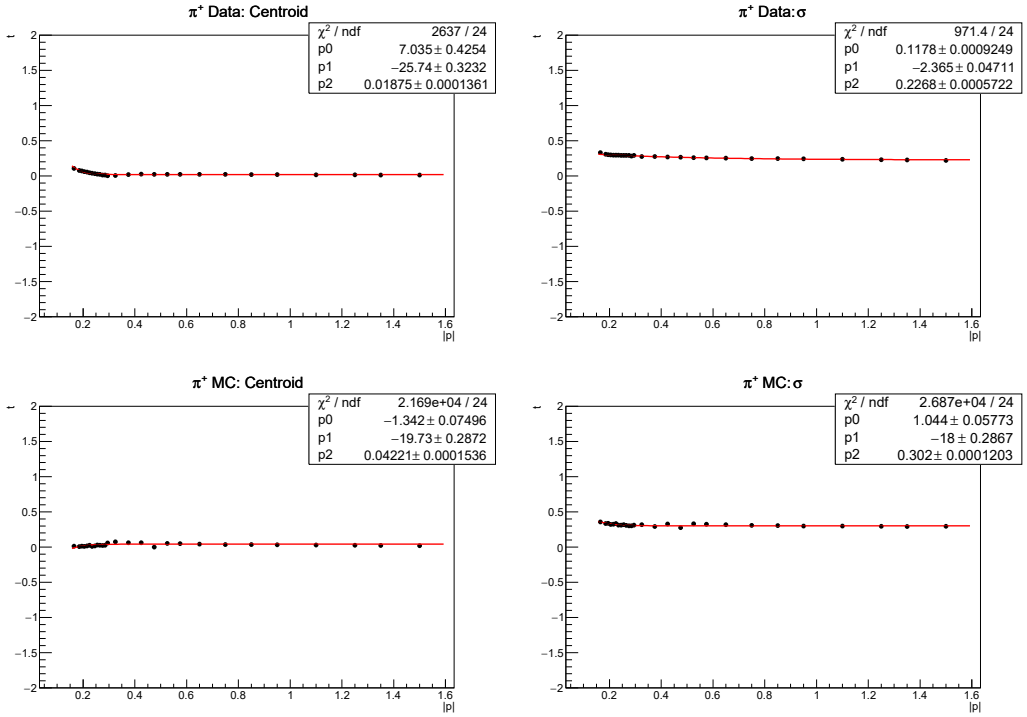

Figure B.4: Centroids and widths from the fits for π^+ (top row: data; bottom row: MC).

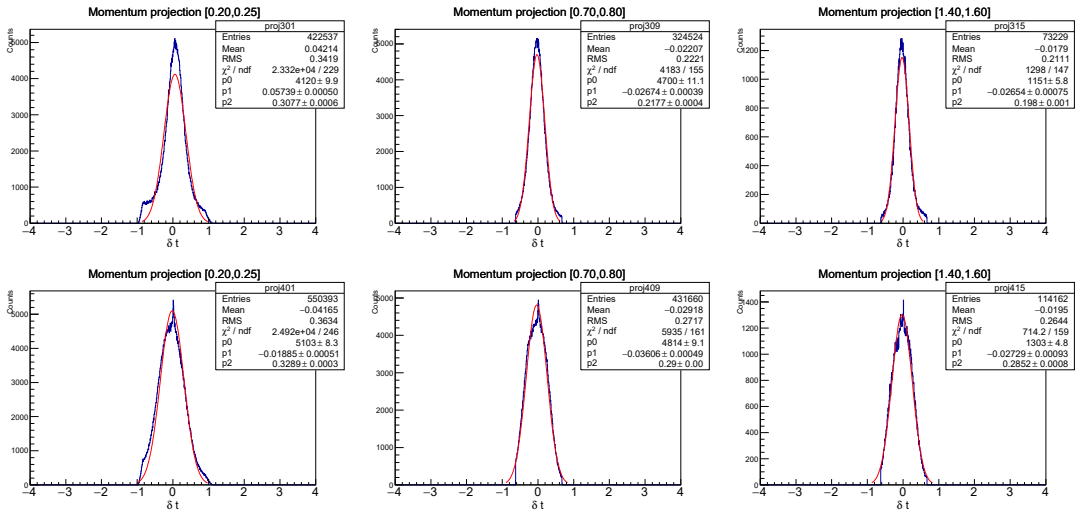

Figure B.5: Timing distributions for π^- for a few bins (top row: data; bottom row: MC).

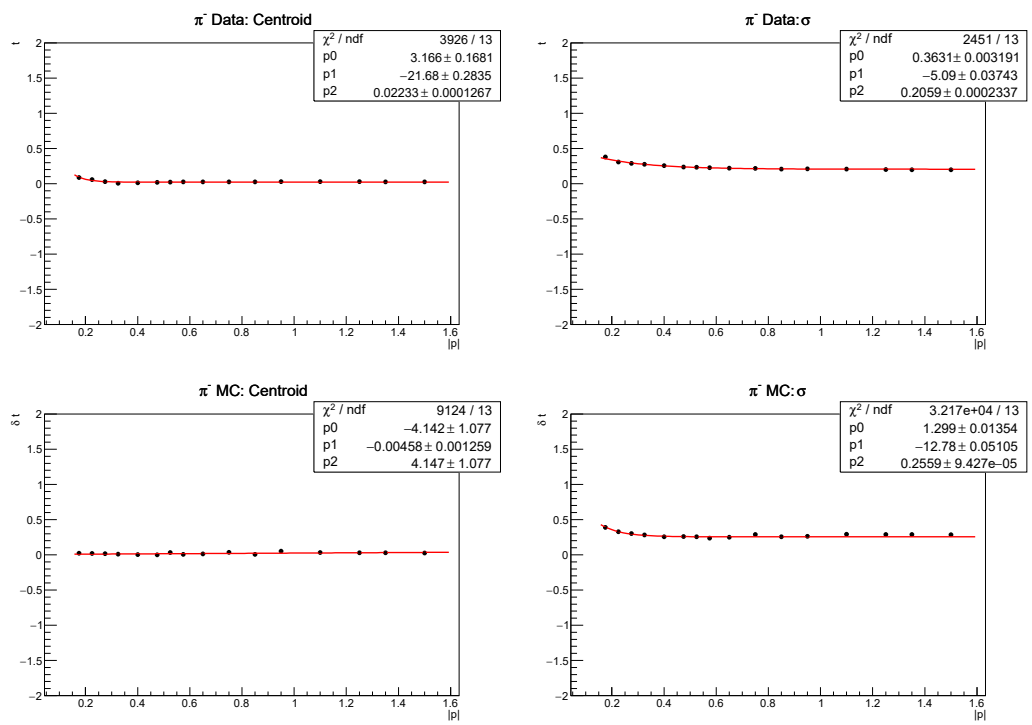

Figure B.6: Centroids and widths from the fits for π^- (top row: data; bottom row: MC).

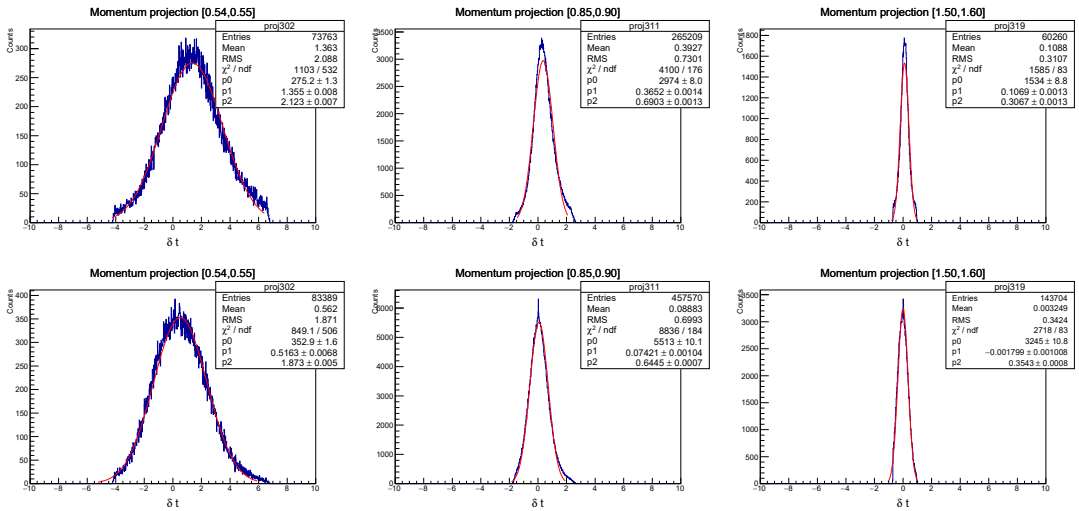

Figure B.7: Timing distributions for d for a few bins (top row: data; bottom row: MC).

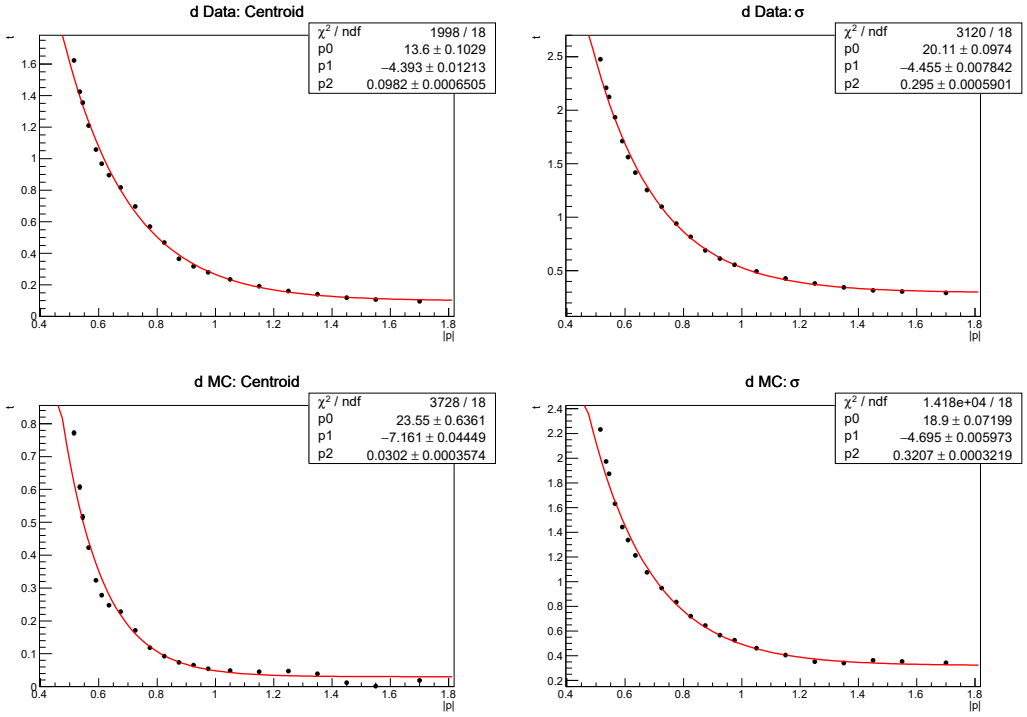

Figure B.8: Centroids and widths from the fits for d (top row: data; bottom row: MC).

B.2 Fiducial Cuts: Plots

Figure B.9a shows the ϕ^{CLAS} distributions for π^- for complete polar angular range. For one of the 50 θ^{CLAS}-bins considered for this study, the distribution can be seen in Figure B.9b. Taking one sector, $-\pi/6 < \phi < \pi/6$, ϕ corresponding to 50% of the height of the distribution was recorded for each θ-bin. This is shown in Figure B.9c. These points were then fit using an exponential function of the form,

$$\phi = ae^{b\theta} + c \tag{B.4}$$

where a, b and c are the fit parameters. Figure B.9d shows the fit for π^-. Once the parameters were found, events outside of $|\phi^{CLAS}| < ae^{b\theta} + c$ were rejected from each sector. This process was repeated for all the detected particles. The cut parameters for each detected particle are listed in Table B.1.

Table B.1: Parameters extracted from the exponential fits for a 50% and a 100% cut for the detected particles.

Particles	Parameters 50% cut			Parameters 100% cut		
	a	b	c	a	b	c
π^+	-0.277437	-4.29357	0.471889	-0.352442	-4.1795	0.444513
π^-	-0.472211	-4.0925	0.440119	-0.4866127	-4.53718	0.39701
d	-0.275288	-4.07023	0.467217	-0.373674	-5.00008	0.423615

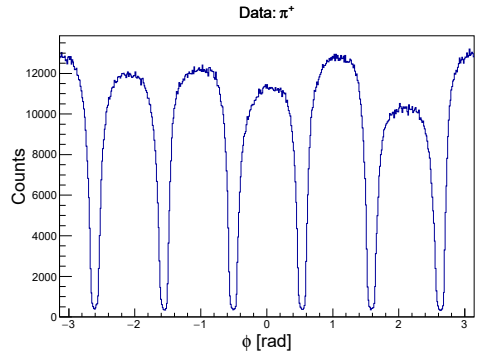

(a) ϕ^{CLAS} distributions for all detected π^- in $0 < \theta^{CLAS} < \pi$ $[rad]$.

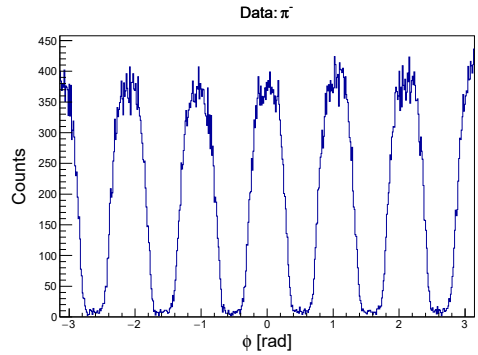

(b) ϕ^{CLAS} distributions for all detected π^- in $0.314159 < \theta^{CLAS} < 0.37699$ $[rad]$.

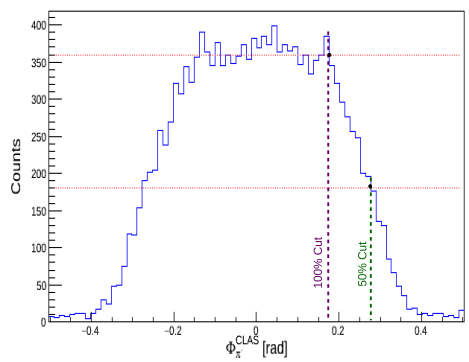

(c) ϕ^{CLAS} distributions for all detected π^- in $0.314159 < \theta^{CLAS} < 0.37699$ $[rad]$.

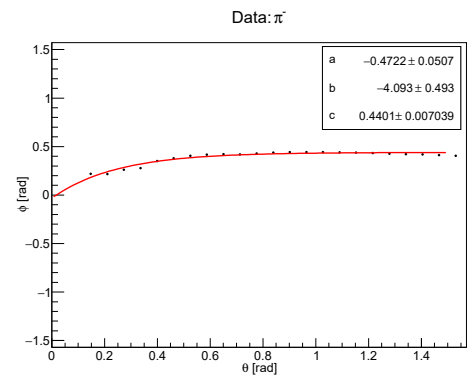

(d) Exponential fit showing the fit parameters a, b and c for π^- for a 50% cut.

Figure B.9: Plots are after cut C1 of Table 3.2; No energy loss correction was made at this point.

B.3 Momentum Distribution: Simulation

Similar prescription explained in Sec. 3.6.1 was followed for the simulation. Figure B.10 shows an example for the $\gamma d \rightarrow \omega d \rightarrow \pi^+\pi^- d$ channel, where the momentum distribution for the simulation along with the position of the minimum momentum cuts are specified.

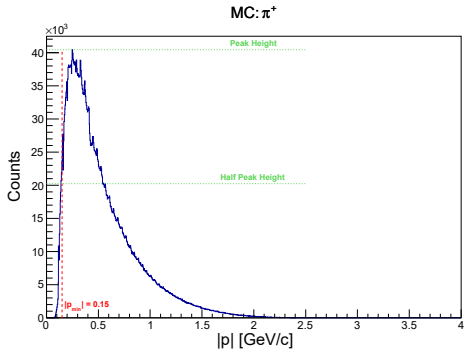

(a) Minimum Momentum Cut for π^+ in MC.

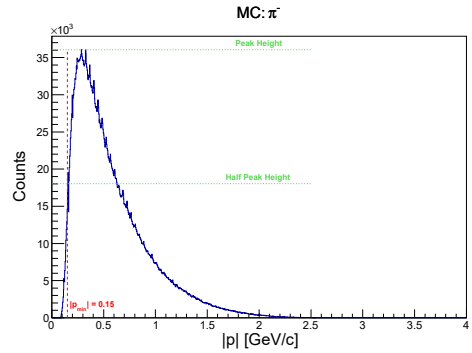

(b) Minimum Momentum Cut for π^- in MC.

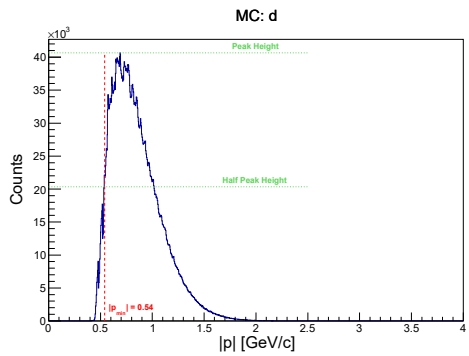

(c) Minimum Momentum Cut for d in MC.

Figure B.10: Momentum distributions in MC. [Plots shown here are drawn after cut C1 and C6 of Table 3.2. Momentum and energy loss corrections were applied.]

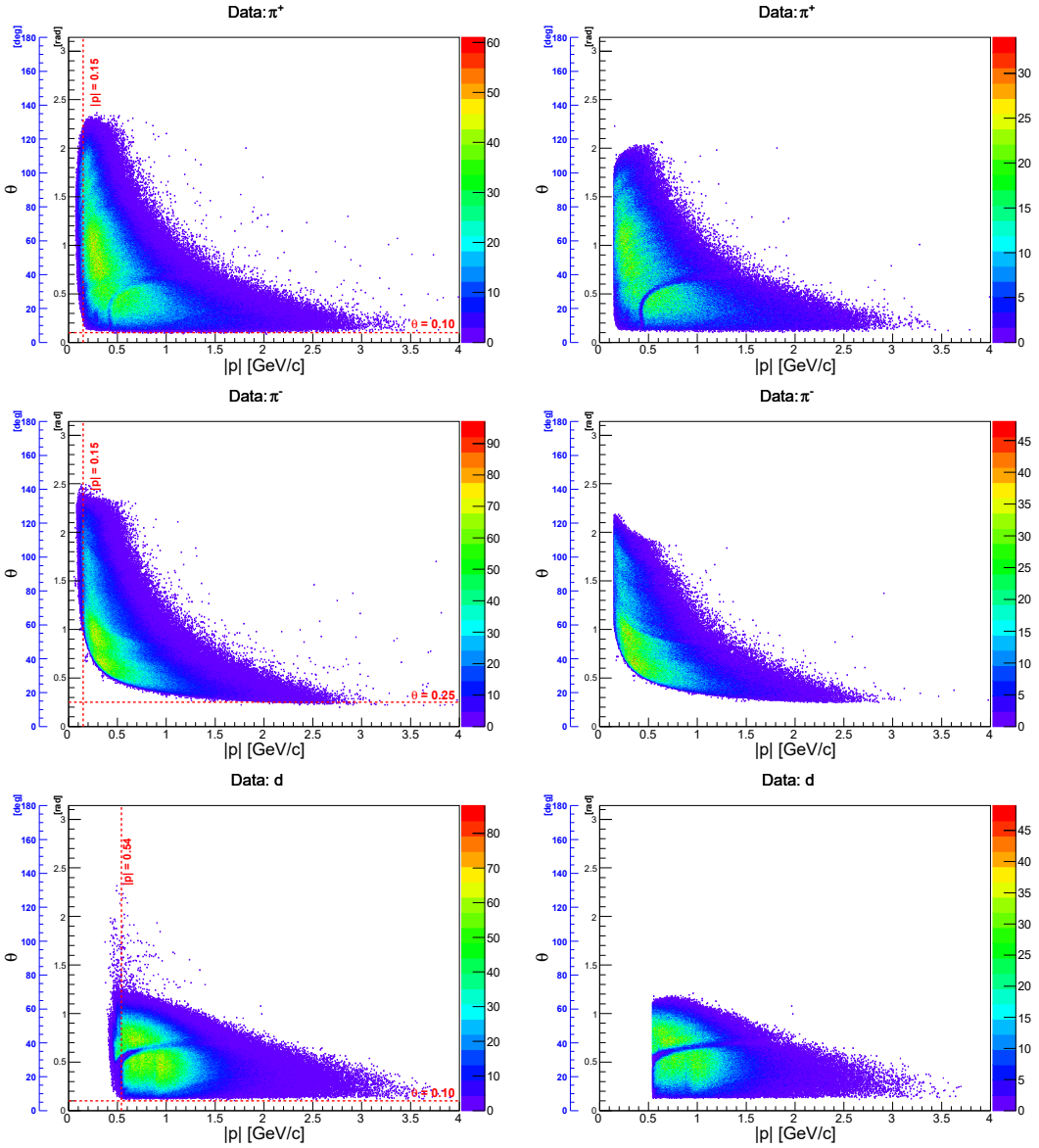

Figure B.11: Polar angle versus momentum distributions for the detected particles in the data. Plots on the left are made after cut levels C1 and C6 of Table 3.2 while those on the right are after cuts C1-C6. Momentum and energy loss corrections were applied prior to the application of the cuts.

B.4 SC: Bad Paddles

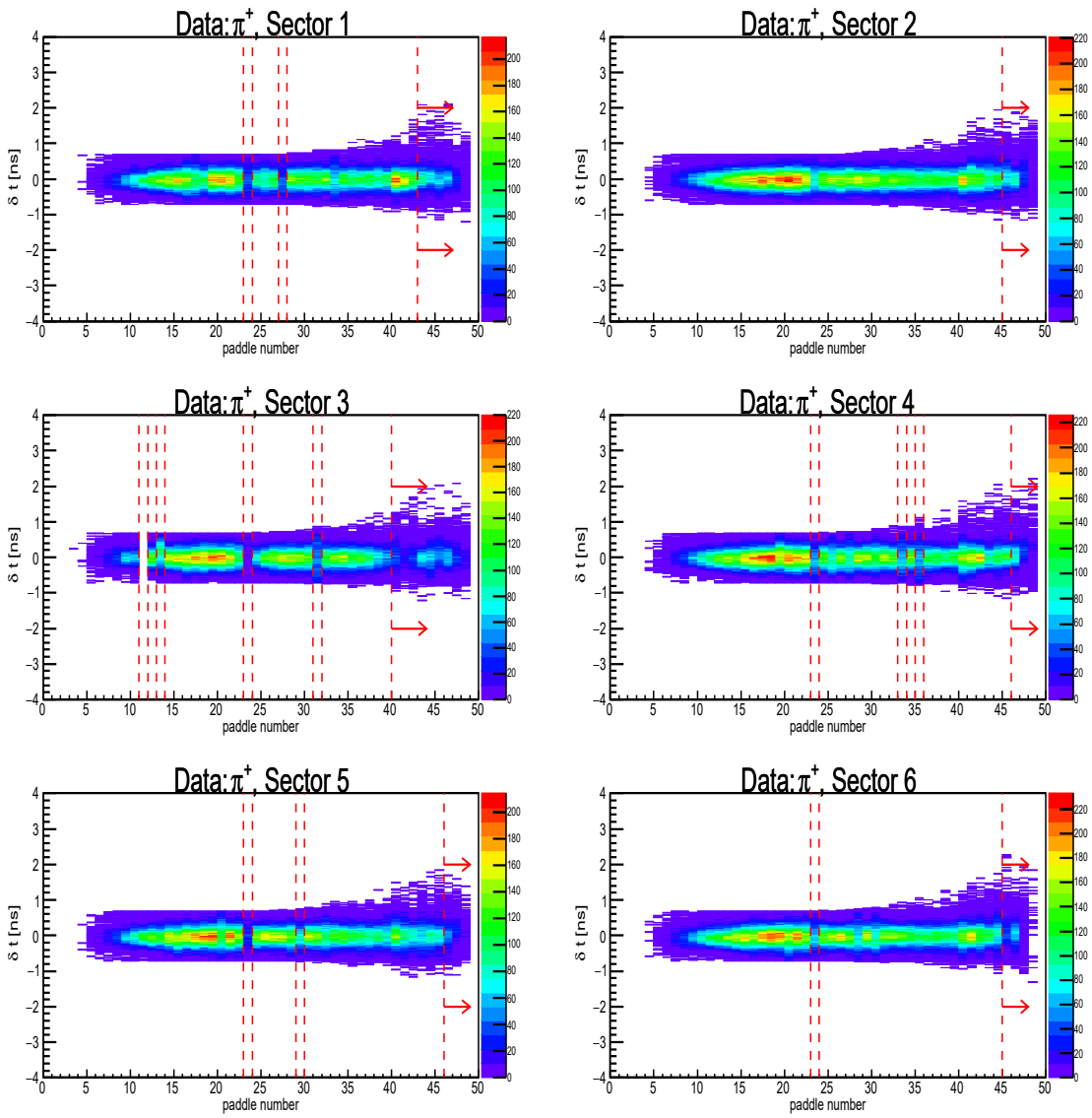

Figure B.12: δt vs paddle number distributions for all the sectors of π^+. Bad SCs are enclosed by the vertical lines (Also listed in Table 3.4). The arrows mean the paddles in that direction are all excluded. [Plots are after cut C1 of Table 3.2; No energy loss correction was made at this point.]

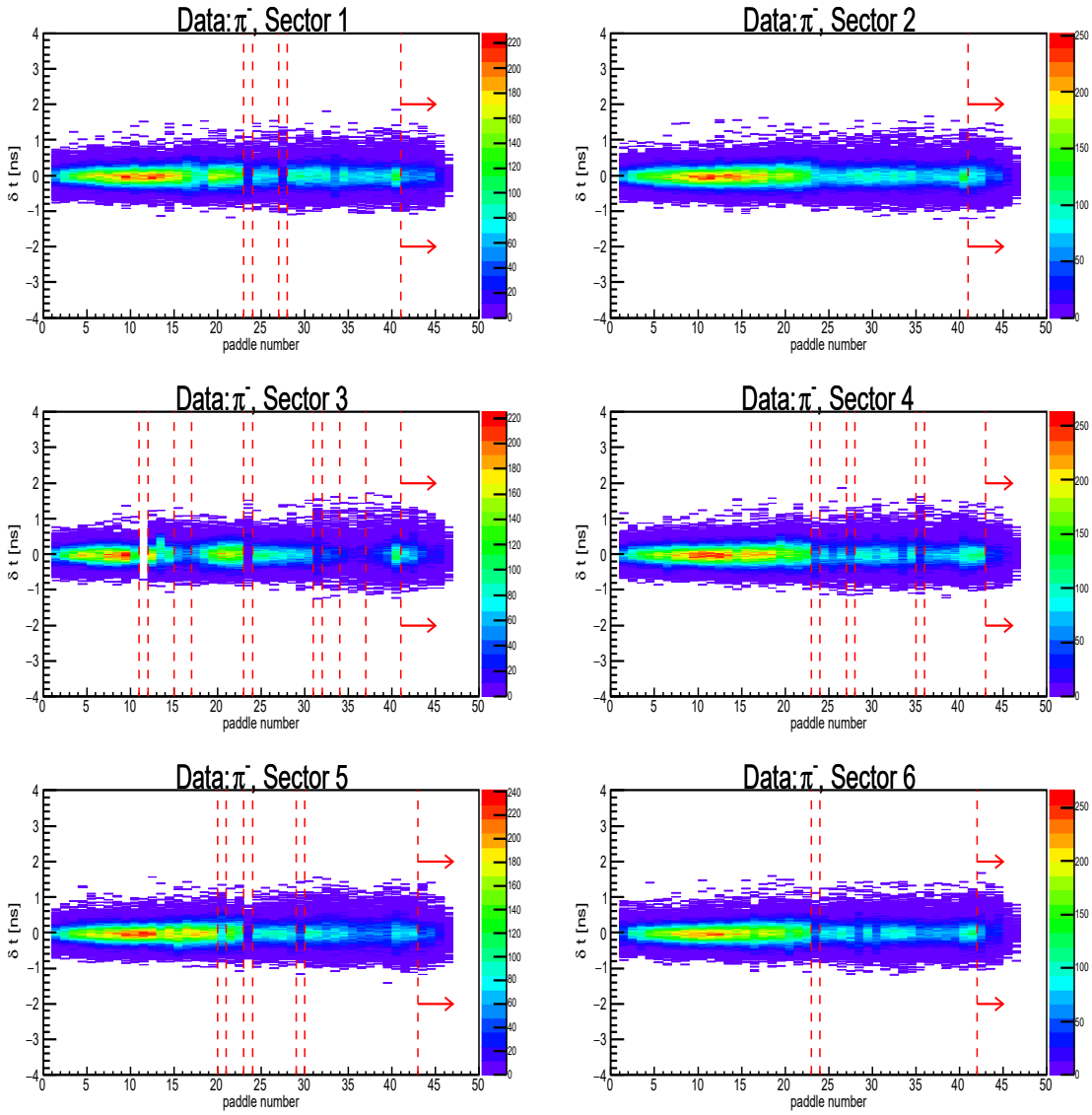

Figure B.13: δt vs paddle number distributions for all the sectors of π^-. Bad SCs are enclosed by the vertical lines (Also listed in Table 3.4). The arrows mean the paddles in that direction are all excluded. [Plots are after cut C1 of Table 3.2; No energy loss correction was made at this point.]

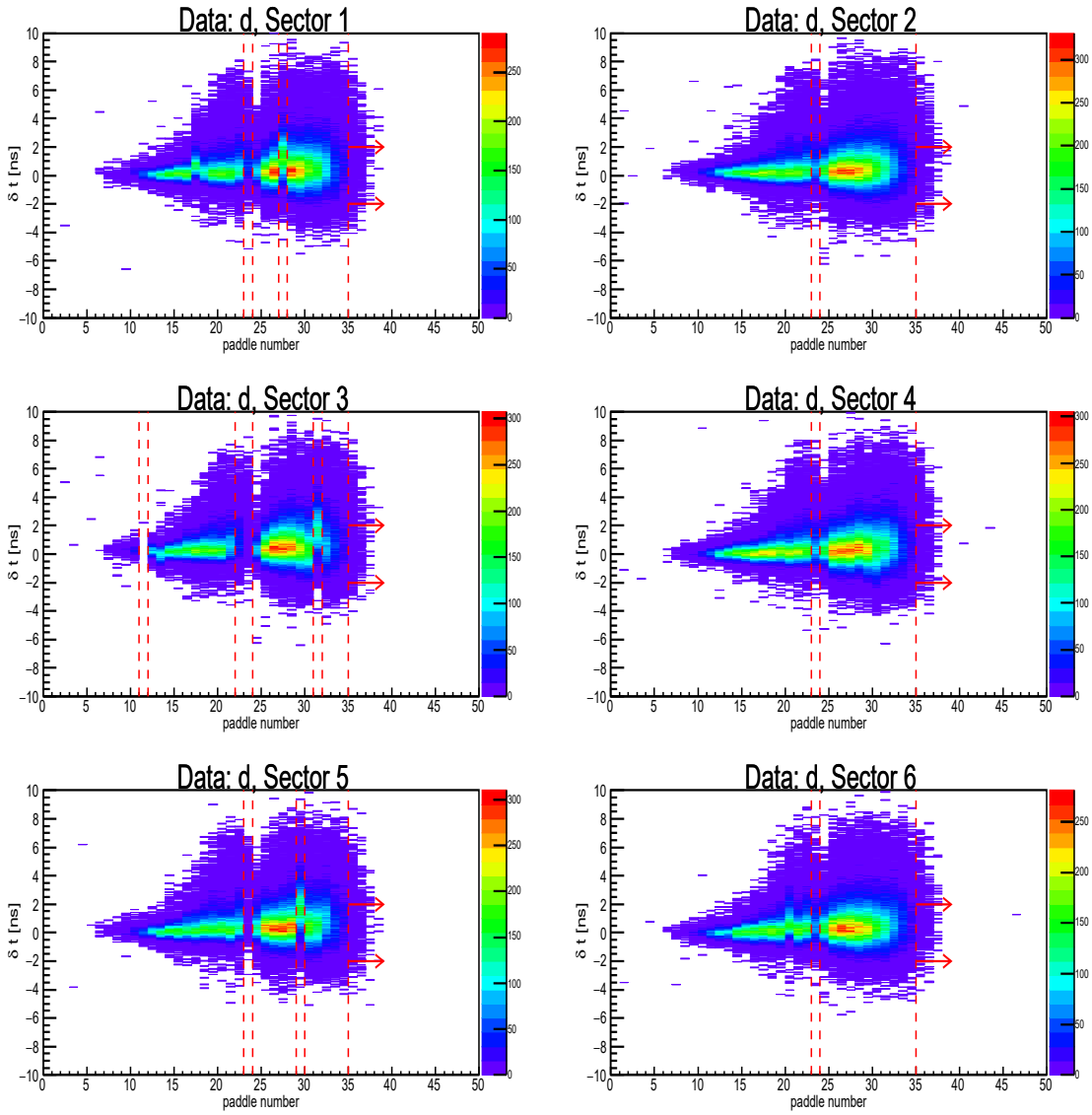

Figure B.14: δt vs paddle number distributions for all the sectors of d. Bad SCs are enclosed by the vertical lines (Also listed in Table 3.4). The arrows mean the paddles in that direction are all excluded. [Plots are after cut C1 of Table 3.2; No energy loss correction was made at this point.]

B.5 Flux

Each *gflux* file consists of two column of numbers. The first column represents the number, ($N_\gamma(\Delta E)$), of "good" photons in an E-ID bin. There are 767 E-ID bins and can be mapped to the incident photon energy (There is a one-to-one relationship between them as seen in Figure B.15. Using the energy and E-ID map, the number of photons for a specific energy range is calculated by adding the corresponding number of photons of each E-ID within that range. The second column is the uncertainty associated with the corresponding number in the first column. The uncertainty on the number of photons in each energy range is calculated by adding the associated uncertainties in quadrature for the energy range considered. If N_i represent the number of photons in E-ID bin i in any energy range, then the photon flux $N_\gamma(E_1)$ for that bin E_1 is calculated mathematically as,

$$N_\gamma(E_1) = \sum_{i=1}^{m} N_i, \tag{B.5}$$

with m as the total number of E-ID bins in E_1. The uncertainty associated with this number is calculated using

$$\sigma_{N_\gamma}(E_1) = \sqrt{\sum_{i=1}^{m} \sigma_{N_i}^2} \tag{B.6}$$

The uncertainties σ_{N_i} are provided in the flux files. Refer to [BP05] for more details on how photon flux and the associated uncertainties are calculated for each E-ID.

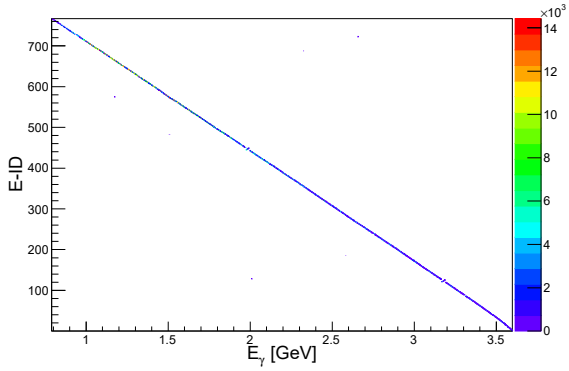

Figure B.15: This plot represents the relation between E-ID and incident photon energy

Appendix C: Momentum Corrections

There are $4 \times 180 \times 360 \times 50$ bins for the correction factor for four variables considered as explained in sub-section 3.7.3. These can be shown using a two-dimensional plot of azimuthal and particle momentum with the corrections scaling on the z-axis (color scale). Some sample plots for the detected particles are shown in Figure C.1 - Figure C.3 for both data and simulation. One point to note about these plots is that the correction factor 1 is shown in color white.

A big majority of corrections are small in both data and simulation. From the plots it may seem that there are more corrections for simulation than data. This is due to the restriction on the number of counts in each bin used while finding the corrections. In each of $4 \times 180 \times 360 \times 50$ bins considered, if the number of events is less than 10, then the correction was set to 1 (as explained in Section 3.7.3). This happened more often in data than in simulation. Therefore, it appears to have more correction than that of data but in reality this is due to statistics.

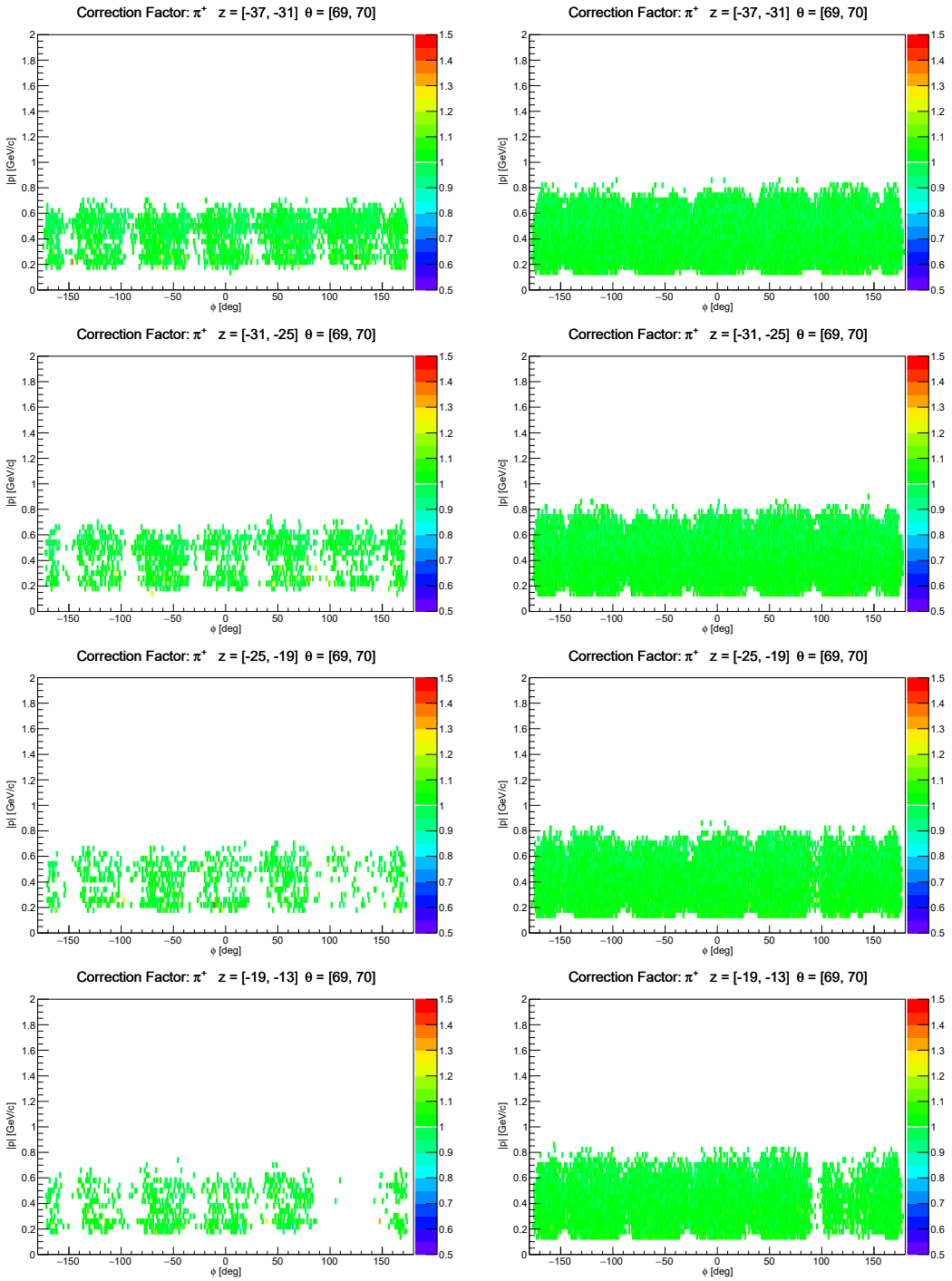

Figure C.1: Momentum Corrections for π^+. Left: Data, right: Simulation. The white space in the plots represents a correction factor of 1.

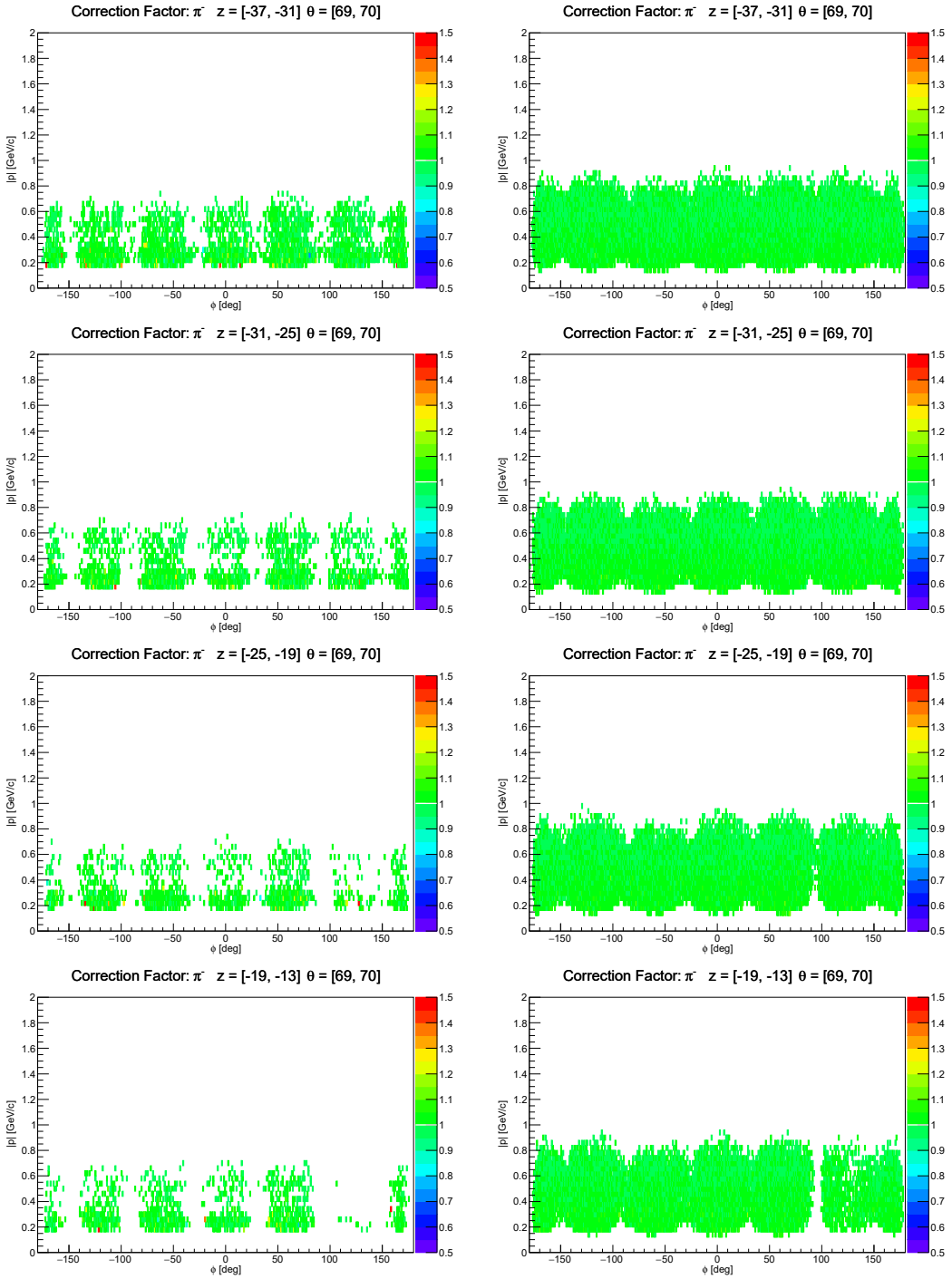

Figure C.2: Momentum Corrections for π^-. Left: Data, right: Simulation. The white space in the plots represents a correction factor of 1.

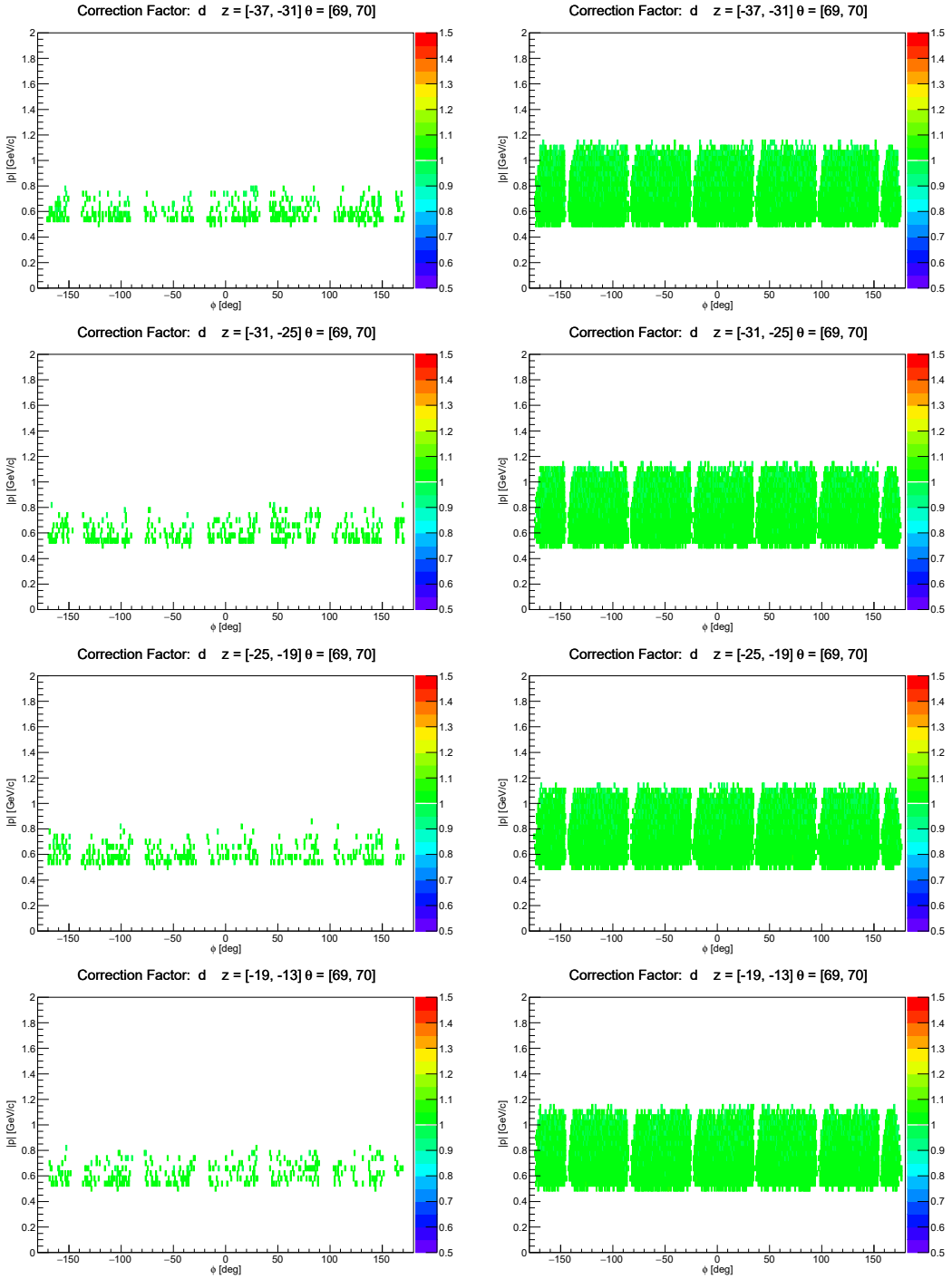

Figure C.3: Momentum Corrections for d. Left: Data, right: Simulation. The white space in the plots represents a correction factor of 1.

Appendix D: Parameters for Monte Carlo Simulation

This section describes different parameters used to simulate events for the $g10$ low field data with beam current $I = 2250\ A$.

D.0.1 `fsgen` Script

```
50000           / number of (gp) interactions to be generated
250       000   / first variable-> number of output files with above number
/ of events, second variable-> bos file number to start
1               / number of final states per (gp) interaction to be generated
3.767           / incident electron energy
0.8, 3.65       / total hadron mass or real photon energy range
0.,0.           / photon mass (for real photons =0.)
0.,0.           / X Bjorken
45 0 0          / target-material   target-nucleon  spectator-nucleon, if last
/ two are =0, target is the first one ("target-material")
/ Log file
outfile.log
/ On the following lines (input BOS file, output BOs file & N-tuple file) 0=.true.
1         test_in.evt
0         gd_omega1_
1         test.hbook
/ distribution parameters
0                / Power of Q2 dependence, if <0 user suplied function is needed
0   0.0  15.0    / first parameter->slop of t-dipendance, if <0 user suplied
/ function is needed, second and third are |t_min| and |t_max|
1                / Genbod kgenev, =1 for constant weights, =2 for Fermi energy
/ dependent weights
'list'           / 'list' or 'notlist'  prints to standart out
'decay'          / decay or not final decayed particles
'noedit'         / edit or not final LUND data buffer
/ Final state that should be generated /
2                               / number of outgoing particles
45      0    0  0   0   0  0.0  / particle code for deuteron
223     712  0  0   0   0  0.0  / omega / cos theta is with respect to the 2nd entry
/ (which is generally the meson)
/ Decay channels for some of decay products /
3                           /Just the number of defined particles
```

```
-211  0  0  0   0   0   0 /pi-
211  0  0  0   0   0   0 /pi+
111  0  0  0   0   0   0 /pi0
/ RANMAR integer sequence number (1 to 900000000) for initialization.
412546217
/ Run number (default 1)
1
/ Target pozition (Z)
-37.0 -13.0 0.15
/ crate or not TAGR bank
0
/ Some fiducial acceptances
8           / number of lines below
11   0. 6. 0. 180. -180. 180.  0
2212 0.3 6. 5. 180. -180. 180.  0
2112 0.3 6. 8. 180. -180. 180.  0
45 0. 6. 0. 180. -180. 180. 0
211 0. 6. 0. 180. -180. 180. 0
-211 0. 6. 0. 180. -180. 180.  0
321 0.2 6. 5. 180. -180. 180.  0
-321 0. 6. 10. 180. -180. 180.  0
/ Format in above PID pmin pmax thmin thmax phmin phmax flag
/ No fiducial cuts if flag =0; uses max min of angles if 1; needs user
/ fiducial function if -1
1         test.txt
```

The above provided script was used to simulated events. It was originally created by [Ste06]. This script creates `.evt` files which are the inputs for `GSIM`.

D.0.2 `GSIM` Command

More information about `GSIM` can be found at [Hol]. The command line is given below:

```
gsim\_bat -ffread /volatile/clas/clasg10/taya/mc/GSIM/ffread-g10-2250.in
-mcin gd.evt -kine 1 -bosout gsim.evt
```

D.0.3 GSIM FFREAD card

Details in the ffread card:

```
AUTO 1
MAGTYPE 2
MAGSCALE 0.583 0.0
TARGET 'g10a'
BEAM 3.777
RUNG 42430
GEOM 'ST  '
STZOFF -22.
TGPOS 0. 0. -3.
STOP
```

D.0.4 gpp Command

```
gpp -P0x1b -R42430 -Y -ogpp.bos  gsim.evt
ln -s gpp.bos infile
```

D.0.5 user_ana Command

```
user_ana -t /volatile/clas/clasg10/taya/mc/GSIM/rec_2250.tcl
```

and the rec_2250.tcl contains the following information:

```
source /group/clas/builds/src/clas-trunk/reconstruction/recsis/recsis_proc.tcl
# define packages
turnoff ALL;
global_section off;
turnon seb tof egn trk user pid;
set lst_do -1;
set ltime_do -1;
set ltagger_do -1;
set st_tagger_match 10.;
set def_adc -1;
set def_tdc -1;
set def_atten -1;
set def_geom -1;
inputfile infile;
setc chist_filename hist.hbook;
```

```
setc log_file_name logfile;
setc outbanknames(1) "HEADTAGRCL01HEVTEVNTDCPBECPBECHBSCPBCCPBSTPBTGPBTBERTBTRSCRCSTR \
                      PARTTBIDGPIDTDPLEPICMCTKMCVX";
outputfile clas.out PROC1 2047;
set lseb_nt_do -1;
set lall_nt_do -1;
set lgpid_do -1;
set lpid_nost_do -1;
set lmctk_nt_do -1;
set torus_current 2250;
set mini_torus_current 0;
set poltarget_current 0;
set TargetPos(3) -25.;
setc prlink_file_name "prlink_2250_g10.bos";
set dc_xvst_choice 0;
set trk_minhits(1) 2;
set trk_prfit_chi2 70.;
set trk_lrambfit_chi2 50.;
set trk_tbtfit_chi2 65.;
set trk_minlramb 4;
# tbt stuff realistic curve for drift time to drift distance.
# tell FPACK not to stop if it thinks you are running out of time
fpack "timestop -9999999999"
# do not send events to event display
set lscat $false;
set ldisplay_all $false;
#set nevt_to_skip  500000;
# how many events to SKIP set to .le. 0 to NOT SKIP
# tell recsis to pause or go
setc rec_prompt "CLASCHEF_recsis> ";
#setc rec_prompt "[exec whoami]_recsis> ";
go 10000000;
exit_pend;
```

Appendix E: Acceptance Tables

Table E.1: Acceptance values for ω.

E_γ [GeV]		t [GeV^2]		Accepted		Generated	Acceptance	
low	high	low	high	Y_{acc}	$\sigma_{Y_{acc}}$	Y_{gen}	A	σ_A
1.40	1.80	-2.00	-1.79	6783.81	81.47	87363	0.0777	0.0009
1.40	1.80	-1.79	-1.58	13380.50	114.11	150775	0.0887	0.0008
1.40	1.80	-1.57	-1.36	20790.10	142.10	254746	0.0816	0.0006
1.40	1.80	-1.36	-1.15	32482.60	177.42	435624	0.0746	0.0004
1.40	1.80	-1.15	-0.94	54957.60	230.62	741908	0.0741	0.0003
1.40	1.80	-0.94	-0.72	98592.10	308.20	1257710	0.0784	0.0002
1.40	1.80	-0.73	-0.51	166537.00	399.71	2139450	0.0778	0.0002
1.40	1.80	-0.51	-0.30	209895.00	450.70	3642490	0.0576	0.0001
1.80	2.20	-1.50	-1.30	22845.20	150.04	216497	0.1055	0.0007
1.80	2.20	-1.30	-1.10	38431.20	194.40	357405	0.1075	0.0005
1.80	2.20	-1.10	-0.90	58728.30	239.99	587447	0.1000	0.0004
1.80	2.20	-0.90	-0.70	85865.00	289.72	968333	0.0887	0.0003
1.80	2.20	-0.70	-0.50	118321.00	340.01	1594900	0.0742	0.0002
1.80	2.20	-0.50	-0.30	141304.00	372.42	2628740	0.0538	0.0001
2.20	2.80	-1.50	-1.30	27258.80	166.41	254217	0.1072	0.0007
2.20	2.80	-1.30	-1.10	41550.70	203.07	419439	0.0991	0.0005
2.20	2.80	-1.10	-0.90	62240.90	248.31	688136	0.0904	0.0004
2.20	2.80	-0.90	-0.70	87089.10	293.26	1128720	0.0772	0.0003
2.20	2.80	-0.70	-0.50	117286.00	340.10	1861590	0.0630	0.0002
2.20	2.80	-0.50	-0.30	126878.00	354.20	3077800	0.0412	0.0001

Table E.1: Acceptance values for ω.

E_γ [GeV]		t [GeV^2]		Accepted		Generated	Acceptance	
low	high	low	high	Y_{acc}	$\sigma_{Y_{acc}}$	Y_{gen}	A	σ_A
2.80	3.40	-1.50	-1.26	7996.22	89.47	255042	0.0314	0.0004
2.80	3.40	-1.26	-1.02	14461.40	120.06	457337	0.0316	0.0003
2.80	3.40	-1.02	-0.78	19958.60	140.89	838611	0.0238	0.0002
2.80	3.40	-0.78	-0.54	29384.90	170.76	1530610	0.0192	0.0001
2.80	3.40	-0.54	-0.30	25170.40	158.05	2786760	0.0090	0.0001

Table E.2: Acceptance values for ρ.

E_γ [GeV]		t [GeV^2]		Accepted		Generated	Acceptance	
low	high	low	high	Y_{acc}	$\sigma_{Y_{acc}}$	Y_{gen}	A	σ_A
1.40	1.60	-2.50	-2.28	866.24	29.43	32848	0.0264	0.0009
1.40	1.60	-2.28	-2.06	2417.76	49.17	55980	0.0432	0.0009
1.40	1.60	-2.06	-1.84	5702.63	75.52	85044	0.0671	0.0009
1.40	1.60	-1.84	-1.62	10108.70	100.54	124139	0.0814	0.0008
1.40	1.60	-1.62	-1.40	16388.30	128.02	177679	0.0922	0.0008
1.40	1.60	-1.40	-1.18	24042.50	155.06	250715	0.0959	0.0006
1.40	1.60	-1.18	-0.96	31551.00	177.63	353726	0.0892	0.0005
1.40	1.60	-0.96	-0.74	44740.60	211.52	496254	0.0902	0.0004
1.40	1.60	-0.74	-0.52	70754.50	266.00	685471	0.1032	0.0004
1.40	1.60	-0.52	-0.30	78340.80	279.89	934141	0.0839	0.0003
1.60	1.80	-2.50	-2.28	3166.22	56.27	38602	0.0820	0.0015
1.60	1.80	-2.28	-2.06	5674.02	75.33	55443	0.1023	0.0014
1.60	1.80	-2.06	-1.84	9085.44	95.32	78086	0.1164	0.0013
1.60	1.80	-1.84	-1.62	12478.20	111.71	109939	0.1135	0.0011
1.60	1.80	-1.62	-1.40	14822.20	121.75	151652	0.0977	0.0008
1.60	1.80	-1.40	-1.18	20613.50	143.57	212202	0.0971	0.0007
1.60	1.80	-1.18	-0.96	33109.50	181.96	293750	0.1127	0.0007
1.60	1.80	-0.96	-0.74	51573.70	227.10	409034	0.1261	0.0006
1.60	1.80	-0.74	-0.52	69810.10	264.22	570884	0.1223	0.0005
1.60	1.80	-0.52	-0.30	81353.90	285.23	792229	0.1027	0.0004
1.80	2.00	-2.50	-2.28	4596.11	67.79	35344	0.1300	0.0020

Table E.2: Acceptance values for ρ.

E_γ [GeV]		t [GeV^2]		Accepted		Generated	Acceptance	
low	high	low	high	Y_{acc}	$\sigma_{Y_{acc}}$	Y_{gen}	A	σ_A
1.80	2.00	-2.28	-2.06	6713.20	81.93	49051	0.1369	0.0018
1.80	2.00	-2.06	-1.84	8165.13	90.36	68765	0.1187	0.0014
1.80	2.00	-1.84	-1.62	9126.66	95.53	94991	0.0961	0.0011
1.80	2.00	-1.62	-1.40	14325.40	119.69	132577	0.1081	0.0010
1.80	2.00	-1.40	-1.18	24069.00	155.14	184034	0.1308	0.0009
1.80	2.00	-1.18	-0.96	36435.50	190.88	256632	0.1420	0.0008
1.80	2.00	-0.96	-0.74	48814.00	220.94	356316	0.1370	0.0007
1.80	2.00	-0.74	-0.52	60289.20	245.54	494964	0.1218	0.0005
1.80	2.00	-0.52	-0.30	63035.50	251.07	689932	0.0914	0.0004
2.00	2.20	-2.50	-2.28	4166.56	64.55	31410	0.1327	0.0022
2.00	2.20	-2.28	-2.06	4857.84	69.70	43748	0.1110	0.0017
2.00	2.20	-2.06	-1.84	6088.47	78.03	61161	0.0995	0.0013
2.00	2.20	-1.84	-1.62	10581.40	102.87	84780	0.1248	0.0013
2.00	2.20	-1.62	-1.40	16565.10	128.71	118251	0.1401	0.0012
2.00	2.20	-1.40	-1.18	23755.70	154.13	164069	0.1448	0.0010
2.00	2.20	-1.18	-0.96	30162.40	173.67	228322	0.1321	0.0008
2.00	2.20	-0.96	-0.74	38757.30	196.87	318679	0.1216	0.0007
2.00	2.20	-0.74	-0.52	52468.00	229.06	441807	0.1188	0.0005
2.00	2.20	-0.52	-0.30	55958.70	236.56	614116	0.0911	0.0004
2.20	2.40	-2.50	-2.28	3171.29	56.31	28448	0.1115	0.0021
2.20	2.40	-2.28	-2.06	4257.07	65.25	39505	0.1078	0.0017

Table E.2: Acceptance values for ρ.

E_γ [GeV]		t [GeV^2]		Accepted		Generated	Acceptance	
low	high	low	high	Y_{acc}	$\sigma_{Y_{acc}}$	Y_{gen}	A	σ_A
2.20	2.40	-2.06	-1.84	8158.48	90.32	55246	0.1477	0.0018
2.20	2.40	-1.84	-1.62	11670.20	108.03	76673	0.1522	0.0015
2.20	2.40	-1.62	-1.40	15876.60	126.00	106258	0.1494	0.0013
2.20	2.40	-1.40	-1.18	22112.60	148.70	149071	0.1483	0.0011
2.20	2.40	-1.18	-0.96	28726.60	169.49	206626	0.1390	0.0009
2.20	2.40	-0.96	-0.74	38077.20	195.13	287616	0.1324	0.0007
2.20	2.40	-0.74	-0.52	45589.10	213.52	400608	0.1138	0.0006
2.20	2.40	-0.52	-0.30	45865.90	214.16	555366	0.0826	0.0004
2.40	2.60	-2.50	-2.28	3105.19	55.72	25967	0.1196	0.0023
2.40	2.60	-2.28	-2.06	5493.84	74.12	36089	0.1522	0.0022
2.40	2.60	-2.06	-1.84	8202.08	90.57	50366	0.1628	0.0019
2.40	2.60	-1.84	-1.62	10756.20	103.71	69938	0.1538	0.0016
2.40	2.60	-1.62	-1.40	15316.50	123.76	97306	0.1574	0.0014
2.40	2.60	-1.40	-1.18	19805.30	140.73	135144	0.1466	0.0011
2.40	2.60	-1.18	-0.96	25427.70	159.46	188883	0.1346	0.0009
2.40	2.60	-0.96	-0.74	32301.30	179.73	262910	0.1229	0.0007
2.40	2.60	-0.74	-0.52	35827.90	189.28	365202	0.0981	0.0005
2.40	2.60	-0.52	-0.30	31874.90	178.53	507854	0.0628	0.0004
2.60	2.80	-2.50	-2.28	3807.66	61.71	23927	0.1591	0.0028
2.60	2.80	-2.28	-2.06	5592.92	74.79	33241	0.1683	0.0024
2.60	2.80	-2.06	-1.84	7774.05	88.17	46619	0.1668	0.0020

Table E.2: Acceptance values for ρ.

E_γ [GeV]		t [GeV^2]		Accepted		Generated	Acceptance	
low	high	low	high	Y_{acc}	$\sigma_{Y_{acc}}$	Y_{gen}	A	σ_A
2.60	2.80	-1.84	-1.62	10500.30	102.47	64555	0.1627	0.0017
2.60	2.80	-1.62	-1.40	14039.00	118.49	90306	0.1555	0.0014
2.60	2.80	-1.40	-1.18	17566.30	132.54	124807	0.1407	0.0011
2.60	2.80	-1.18	-0.96	24404.60	156.22	174612	0.1398	0.0010
2.60	2.80	-0.96	-0.74	27210.00	164.96	242414	0.1122	0.0007
2.60	2.80	-0.74	-0.52	30461.30	174.53	335597	0.0908	0.0005
2.60	2.80	-0.52	-0.30	22279.50	149.26	468560	0.0475	0.0003
2.80	3.00	-2.50	-2.28	3857.80	62.11	22095	0.1746	0.0030
2.80	3.00	-2.28	-2.06	5357.28	73.19	30965	0.1730	0.0026
2.80	3.00	-2.06	-1.84	7335.26	85.65	43106	0.1702	0.0021
2.80	3.00	-1.84	-1.62	9811.71	99.05	59946	0.1637	0.0018
2.80	3.00	-1.62	-1.40	12845.90	113.34	83527	0.1538	0.0015
2.80	3.00	-1.40	-1.18	16884.10	129.94	116348	0.1451	0.0012
2.80	3.00	-1.18	-0.96	20375.60	142.74	161583	0.1261	0.0009
2.80	3.00	-0.96	-0.74	24462.90	156.41	224648	0.1089	0.0007
2.80	3.00	-0.74	-0.52	25060.30	158.30	311565	0.0804	0.0005
2.80	3.00	-0.52	-0.30	13852.70	117.70	434848	0.0319	0.0003
3.00	3.20	-2.50	-2.28	3629.17	60.24	20913	0.1735	0.0031
3.00	3.20	-2.28	-2.06	4914.37	70.10	29038	0.1692	0.0026
3.00	3.20	-2.06	-1.84	6594.34	81.21	39964	0.1650	0.0022
3.00	3.20	-1.84	-1.62	8857.43	94.11	56142	0.1578	0.0018

Table E.2: Acceptance values for ρ.

E_γ [GeV]		t [GeV^2]		Accepted		Generated	Acceptance	
low	high	low	high	Y_{acc}	$\sigma_{Y_{acc}}$	Y_{gen}	A	σ_A
3.00	3.20	-1.62	-1.40	11332.60	106.45	77669	0.1459	0.0015
3.00	3.20	-1.40	-1.18	15111.80	122.93	107554	0.1405	0.0012
3.00	3.20	-1.18	-0.96	18075.10	134.44	150289	0.1203	0.0009
3.00	3.20	-0.96	-0.74	19744.40	140.51	209100	0.0944	0.0007
3.00	3.20	-0.74	-0.52	19528.00	139.74	291492	0.0670	0.0005
3.00	3.20	-0.52	-0.30	10504.80	102.49	405685	0.0259	0.0003
3.20	3.40	-2.50	-2.28	3275.75	57.23	19314	0.1696	0.0032
3.20	3.40	-2.28	-2.06	4604.61	67.86	27474	0.1676	0.0027
3.20	3.40	-2.06	-1.84	6169.69	78.55	37785	0.1633	0.0022
3.20	3.40	-1.84	-1.62	7793.79	88.28	52067	0.1497	0.0018
3.20	3.40	-1.62	-1.40	10426.40	102.11	73294	0.1423	0.0015
3.20	3.40	-1.40	-1.18	13721.20	117.14	101148	0.1357	0.0012
3.20	3.40	-1.18	-0.96	15352.80	123.91	141003	0.1089	0.0009
3.20	3.40	-0.96	-0.74	16829.20	129.73	196082	0.0858	0.0007
3.20	3.40	-0.74	-0.52	16291.80	127.64	272968	0.0597	0.0005
3.20	3.40	-0.52	-0.30	6842.98	82.72	379379	0.0180	0.0002

Table E.3: Acceptance values for d^{*++}.

W [GeV]		$\cos\theta^{\pi^-}_{CM}$		Accepted		Generated	Acceptance	
low	high	low	high	Y_{acc}	$\sigma_{Y_{acc}}$	Y_{gen}	A	σ_A
2.70	2.83	-0.80	-0.60	3793.00	61.59	282779	0.0134	0.0002
2.70	2.83	-0.60	-0.40	24041.00	155.05	281519	0.0854	0.0006
2.70	2.83	-0.40	-0.20	19064.00	138.07	282840	0.0674	0.0005
2.70	2.83	-0.20	0.00	11982.00	109.46	283493	0.0423	0.0004
2.70	2.83	0.00	0.20	2852.00	53.40	283125	0.0101	0.0002
2.70	2.83	0.20	0.40	18289.00	135.24	283582	0.0645	0.0005
2.70	2.83	0.40	0.60	24292.00	155.86	284517	0.0854	0.0006
2.70	2.83	0.60	0.80	15280.00	123.61	283122	0.0540	0.0004
2.83	2.95	-0.80	-0.60	5138.00	71.68	252851	0.0203	0.0003
2.83	2.95	-0.60	-0.40	32737.00	180.93	254091	0.1288	0.0008
2.83	2.95	-0.40	-0.20	29787.00	172.59	252339	0.1180	0.0007
2.83	2.95	-0.20	0.00	24841.00	157.61	252815	0.0983	0.0007
2.83	2.95	0.00	0.20	9946.00	99.73	250659	0.0397	0.0004
2.83	2.95	0.20	0.40	22576.00	150.25	251761	0.0897	0.0006
2.83	2.95	0.40	0.60	29333.00	171.27	252683	0.1161	0.0007
2.83	2.95	0.60	0.80	18933.00	137.60	251113	0.0754	0.0006
2.95	3.08	-0.80	-0.60	6507.00	80.67	228349	0.0285	0.0004
2.95	3.08	-0.60	-0.40	33167.00	182.12	227452	0.1458	0.0009
2.95	3.08	-0.40	-0.20	34849.00	186.68	228275	0.1527	0.0009
2.95	3.08	-0.20	0.00	34470.00	185.66	227491	0.1515	0.0009
2.95	3.08	0.00	0.20	18252.00	135.10	227447	0.0802	0.0006

Table E.3: Acceptance values for d^{*++}.

W [GeV]		$\cos\theta^{\pi^-}_{CM}$		Accepted		Generated	Acceptance	
low	high	low	high	Y_{acc}	$\sigma_{Y_{acc}}$	Y_{gen}	A	σ_A
2.95	3.08	0.20	0.40	26448.00	162.63	227856	0.1161	0.0008
2.95	3.08	0.40	0.60	31500.00	177.48	227314	0.1386	0.0008
2.95	3.08	0.60	0.80	22967.00	151.55	229179	0.1002	0.0007
3.08	3.20	-0.80	-0.60	7674.00	87.60	209769	0.0366	0.0004
3.08	3.20	-0.60	-0.40	32622.00	180.62	208741	0.1563	0.0009
3.08	3.20	-0.40	-0.20	34081.00	184.61	208251	0.1637	0.0010
3.08	3.20	-0.20	0.00	35454.00	188.29	208992	0.1696	0.0010
3.08	3.20	0.00	0.20	23135.00	152.10	209826	0.1103	0.0008
3.08	3.20	0.20	0.40	27209.00	164.95	208942	0.1302	0.0008
3.08	3.20	0.40	0.60	30211.00	173.81	209203	0.1444	0.0009
3.08	3.20	0.60	0.80	25421.00	159.44	209629	0.1213	0.0008

Appendix F: Tables and Plots: $\gamma d \to \omega d$

F.1 Simulation: Accepted Events

This section deals with the yield extraction for simulated events. As only signal is generated, the distribution is fit using a Voigt function only. In other words, the generated events have zero background and therefore the use of a polynomial function will overfit the distribution and is therefore avoided.

The fitting procedure is the same as the data. As the Lorentzian width represents the physical width of ω-meson, therefore σ_L is kept fixed to the PDG value ($\sigma_L = \Gamma_\omega = 0.0849$ GeV) in the fit. The accepted yield is given by,

$$Y_{acc} = I_V \times \frac{N_{bins}}{Hist_{range}}, \tag{F.1}$$

where the $Hist_{range}$ is the range of the histogram used for $MM(\gamma d, d)$ distribution in N_{bins} and the integration of the function I_V,

$$I_V = \left(\int_{\mu-4\sigma_G}^{\mu+4\sigma_G} V(x)dx \right), \tag{F.2}$$

is calculated using standard ROOT functions.

The uncertainty on the yield is given by

$$\sigma_{Y_{acc}} = \sigma_I \times \frac{N_{bins}}{Hist_{range}} \tag{F.3}$$

where the integration error, σ_I, is calculated using the standard ROOT function:

`IntegralError`$(\mu - 4\sigma_G, \mu + 4\sigma_G)$.

The range along with the fits are shown in Figs. F.1-F.4.

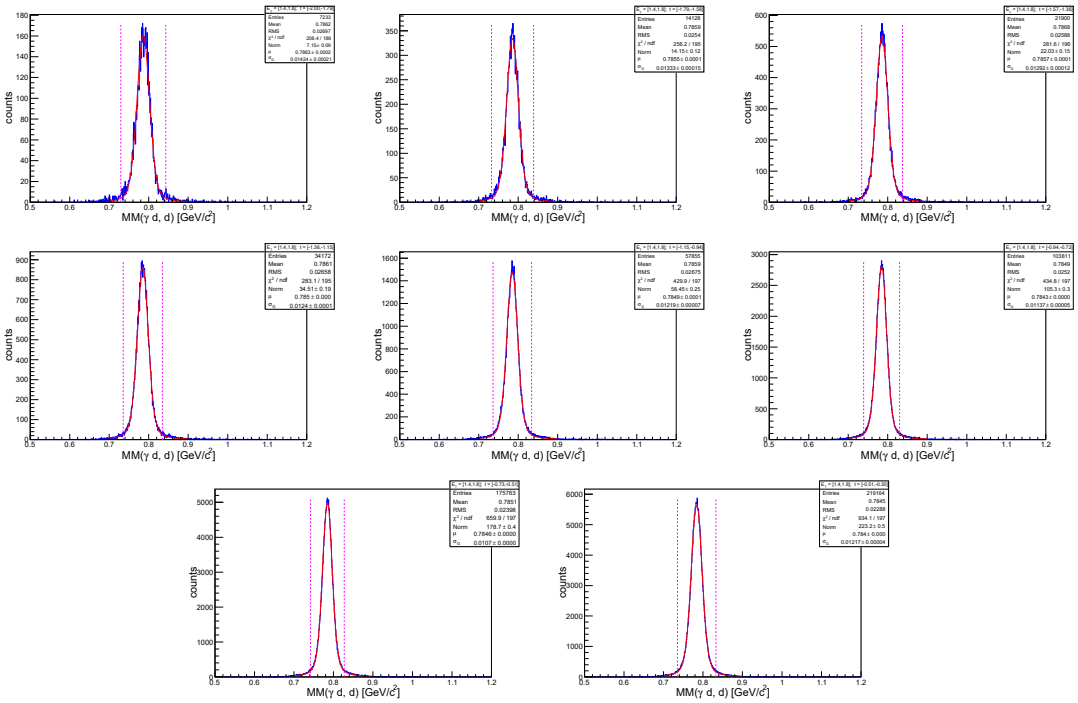

Figure F.1: Missing mass distributions of accepted events for different momentum transfer bins in $E_\gamma = [1.4, 1.8]$. The signal is shown by dashed green curve. The vertical lines represent 4σ integration range with respect to the Gaussian centroid.

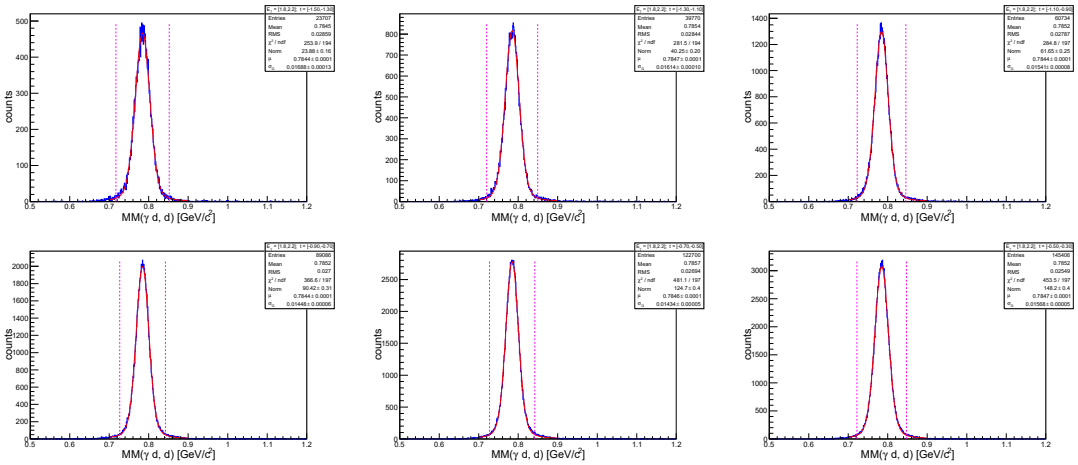

Figure F.2: Missing mass distributions of accepted events for different momentum transfer bins in $E_\gamma = [1.8, 2.2]$. The signal is shown by dashed green curve. The vertical lines represent 4σ integration range with respect to the Gaussian centroid.

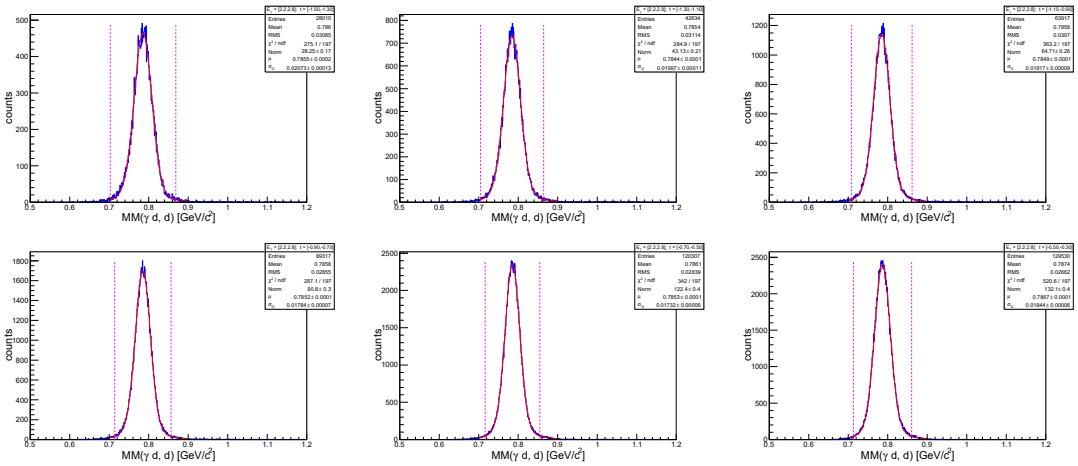

Figure F.3: Missing mass distributions of accepted events for different momentum transfer bins in $E_\gamma = [2.2, 2.8]$. The signal is shown by dashed green curve. The vertical lines represent 4σ integration range with respect to the Gaussian centroid.

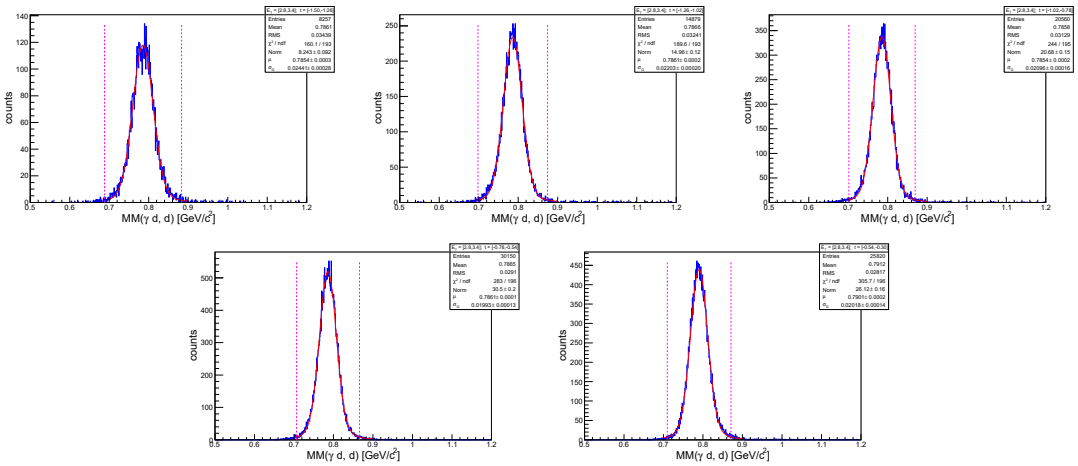

Figure F.4: Missing mass distributions of accepted events for different momentum transfer bins in $E_\gamma = [2.8, 3.4]$. The signal is shown by dashed green curve. The vertical lines represent 4σ integration range with respect to the Gaussian centroid.

$1.4 < E_\gamma < 1.8$ [GeV]			
t [GeV$^2/c^2$]		Y_{acc}	$\sigma_{Y_{acc}}$
Low	High		
-2.00	-1.79	6783.81	81.47
-1.79	-1.58	13380.48	114.11
-1.57	-1.36	20790.14	142.10
-1.36	-1.15	32482.64	177.42
-1.15	-0.94	54957.61	230.62
-0.94	-0.72	98592.09	308.20
-0.73	-0.51	166537.34	399.72
-0.51	-0.30	209895.48	450.70

$1.8 < E_\gamma < 2.2$ [GeV]			
t [GeV$^2/c^2$]		Y_{acc}	$\sigma_{Y_{acc}}$
Low	High		
-1.50	-1.30	22845.22	150.04
-1.30	-1.10	38431.19	194.40
-1.10	-0.90	58728.25	239.99
-0.90	-0.70	85865.01	289.72
-0.70	-0.50	118321.04	340.01
-0.50	-0.30	141304.35	372.42

$2.2 < E_\gamma < 2.8$ [GeV]			
t [GeV$^2/c^2$]		Y_{acc}	$\sigma_{Y_{acc}}$
Low	High		
-1.50	-1.30	27258.81	166.41
-1.30	-1.10	41550.67	203.07
-1.10	-0.90	62240.87	248.31
-0.90	-0.70	87089.12	293.26
-0.70	-0.50	117286.14	340.10
-0.50	-0.30	126877.87	354.20

$2.8 < E_\gamma < 3.4$ [GeV]			
t [GeV$^2/c^2$]		Y_{acc}	$\sigma_{Y_{acc}}$
Low	High		
-1.50	-1.26	7996.22	89.47
-1.26	-1.02	14461.37	120.06
-1.02	-0.78	19958.57	140.89
-0.78	-0.54	29384.89	170.76
-0.54	-0.30	25170.40	158.05

Table F.1: Accepted Events

F.2 Simulation: Generated Events

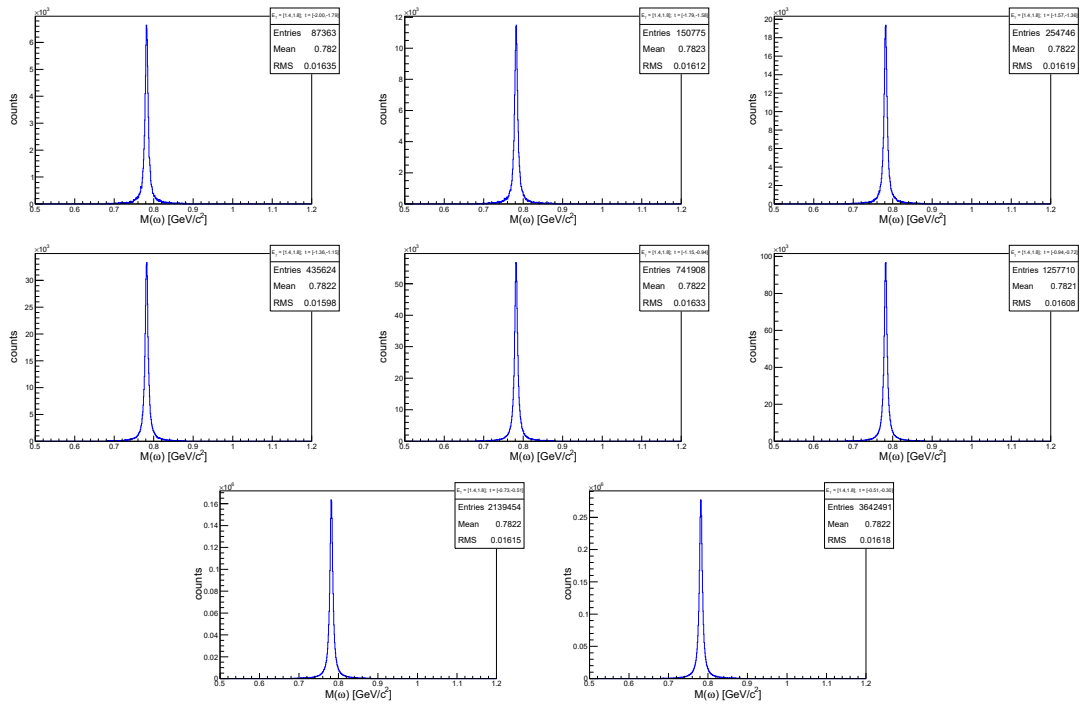

Figure F.5: Mass distributions of generated events for different momentum transfer bins in $E_\gamma = [1.4, 1.8]$.

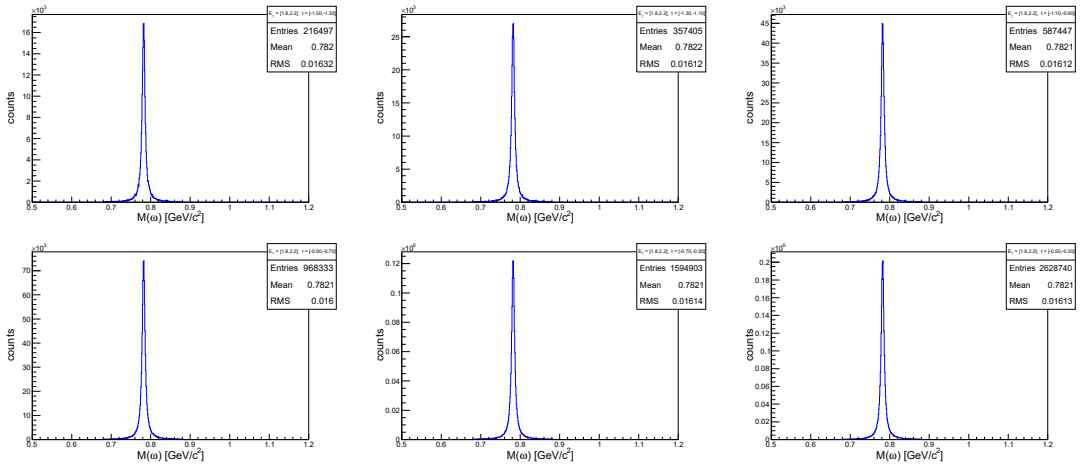

Figure F.6: Mass distributions of generated events for different momentum transfer bins in $E_\gamma = [1.8, 2.2]$.

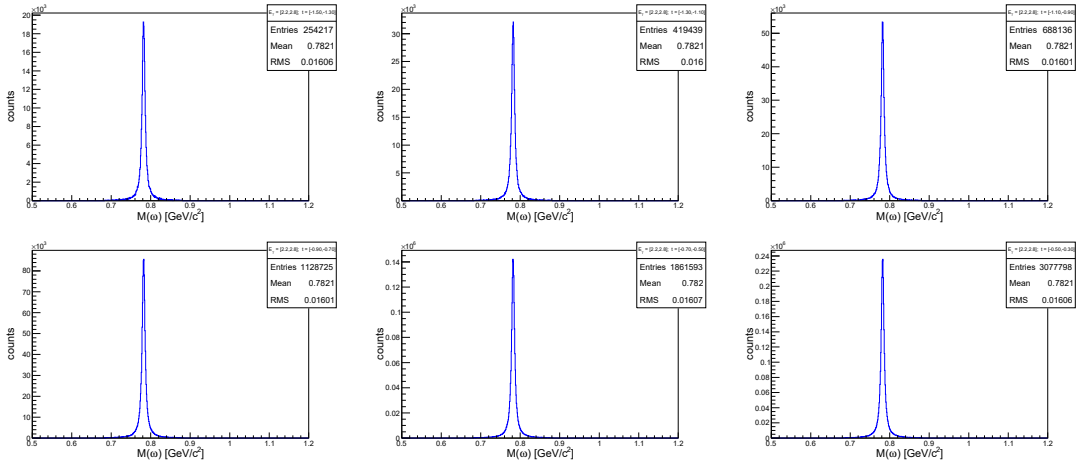

Figure F.7: Mass distributions of generated events for different momentum transfer bins in $E_\gamma = [2.2, 2.8]$.

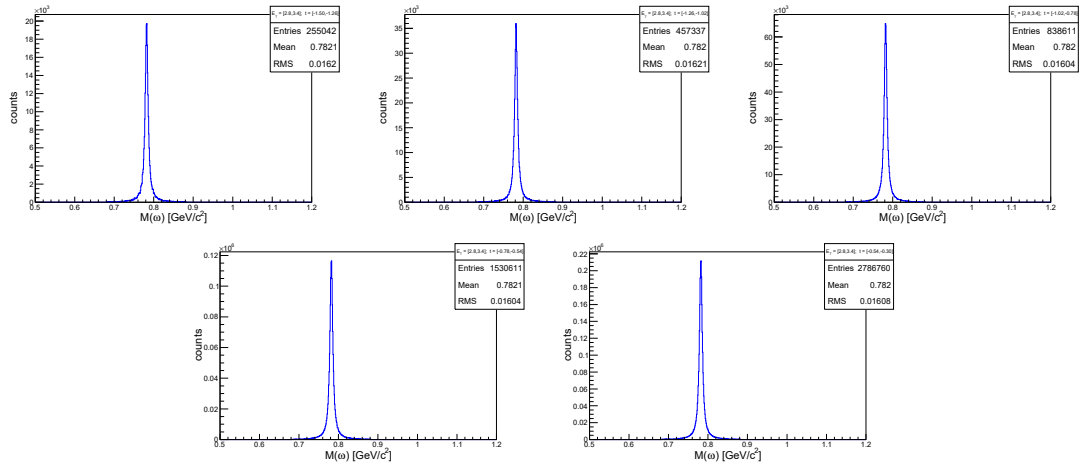

Figure F.8: Mass distributions of generated events for different momentum transfer bins in $E_\gamma = [2.8, 3.4]$.

$1.4 < E_\gamma < 1.8$ [GeV]		
t [GeV$^2/c^2$]		Y_{gen}
Low	High	
-2.00	-1.79	87363.00
-1.79	-1.58	150775.00
-1.57	-1.36	254746.00
-1.36	-1.15	435624.00
-1.15	-0.94	741908.00
-0.94	-0.72	1257710.00
-0.73	-0.51	2139454.00
-0.51	-0.30	3642491.00

$1.8 < E_\gamma < 2.2$ [GeV]		
t [GeV$^2/c^2$]		Y_{gen}
Low	High	
-1.50	-1.30	216497.00
-1.30	-1.10	357405.00
-1.10	-0.90	587447.00
-0.90	-0.70	968333.00
-0.70	-0.50	1594903.00
-0.50	-0.30	2628740.00

$2.2 < E_\gamma < 2.8$ [GeV]		
t [GeV$^2/c^2$]		Y_{gen}
Low	High	
-1.50	-1.30	254217.00
-1.30	-1.10	419439.00
-1.10	-0.90	688136.00
-0.90	-0.70	1128725.00
-0.70	-0.50	1861593.00
-0.50	-0.30	3077798.00

$2.8 < E_\gamma < 3.4$ [GeV]		
t [GeV$^2/c^2$]		Y_{gen}
Low	High	
-1.50	-1.26	255042.00
-1.26	-1.02	457337.00
-1.02	-0.78	838611.00
-0.78	-0.54	1530611.00
-0.54	-0.30	2786760.00

Table F.2: Generated Events

One can also calculate lifetime using the uncertainty relation. It comes out to be of the order of 10^{-23} seconds using the uncertainty relation and the Lorentzian width extracted from the fit.

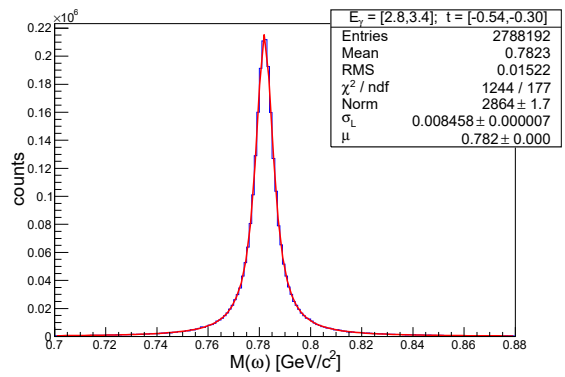

Figure F.9: Generated mass distribution for one energy and t bin is fit using a Lorentzian function.

F.3 Background Function Fit Comparison

Two background functions are used for systematic study. A second order polynomial function (left plots) is used as the nominal while a linear function (right plots) is used to study the systematic variation.

F.4 Differential cross section values for $\gamma d \to \omega d$

Table F.3: Differential cross section values for $\gamma d \to \omega d$.

E_γ GeV		t [GeV^2/c^2]		$\frac{d\sigma}{dt}$ [nb/(GeV/c)^2]	$\sigma_{d\sigma/dt}$ [nb/(GeV/c)^2]
Low	High	Low	High		
1.40	1.80	-2.00	-1.79	2.0708	0.2324
1.40	1.80	-1.79	-1.58	1.8322	0.2225

Table F.3: Differential cross section values for $\gamma d \rightarrow \omega d$.

E_γ GeV		t [GeV^2/c^2]		$\frac{d\sigma}{dt}$ [nb/(GeV/c)^2]	$\sigma_{d\sigma/dt}$ [nb/(GeV/c)^2]
Low	High	Low	High		
1.40	1.80	-1.57	-1.36	2.5413	0.2780
1.40	1.80	-1.36	-1.15	3.5593	0.3404
1.40	1.80	-1.15	-0.94	5.3532	0.4031
1.40	1.80	-0.94	-0.72	8.1024	0.4665
1.40	1.80	-0.73	-0.51	15.5927	0.6128
1.40	1.80	-0.51	-0.30	29.5789	1.8064
1.80	2.20	-1.50	-1.30	1.7887	0.1933
1.80	2.20	-1.30	-1.10	2.6154	0.2345
1.80	2.20	-1.10	-0.90	5.0196	0.3266
1.80	2.20	-0.90	-0.70	7.7891	0.4200
1.80	2.20	-0.70	-0.50	11.1939	0.5584
1.80	2.20	-0.50	-0.30	20.2993	0.9027
2.20	2.80	-1.50	-1.30	0.7929	0.1131
2.20	2.80	-1.30	-1.10	1.5265	0.1584
2.20	2.80	-1.10	-0.90	2.6537	0.2089
2.20	2.80	-0.90	-0.70	4.2889	0.2793
2.20	2.80	-0.70	-0.50	6.6754	0.4160
2.20	2.80	-0.50	-0.30	16.3323	0.7450
2.80	3.40	-1.50	-1.26	1.0493	0.2480
2.80	3.40	-1.26	-1.02	1.7796	0.3150
2.80	3.40	-1.02	-0.78	4.9525	0.5450

Table F.3: Differential cross section values for $\gamma d \rightarrow \omega d$.

E_γ GeV		t [GeV^2/c^2]		$\frac{d\sigma}{dt}$ [nb/(GeV/c)^2]	$\sigma_{d\sigma/dt}$ [nb/(GeV/c)^2]
Low	High	Low	High		
2.80	3.40	-0.78	-0.54	9.9142	0.8381
2.80	3.40	-0.54	-0.30	13.4432	1.6286

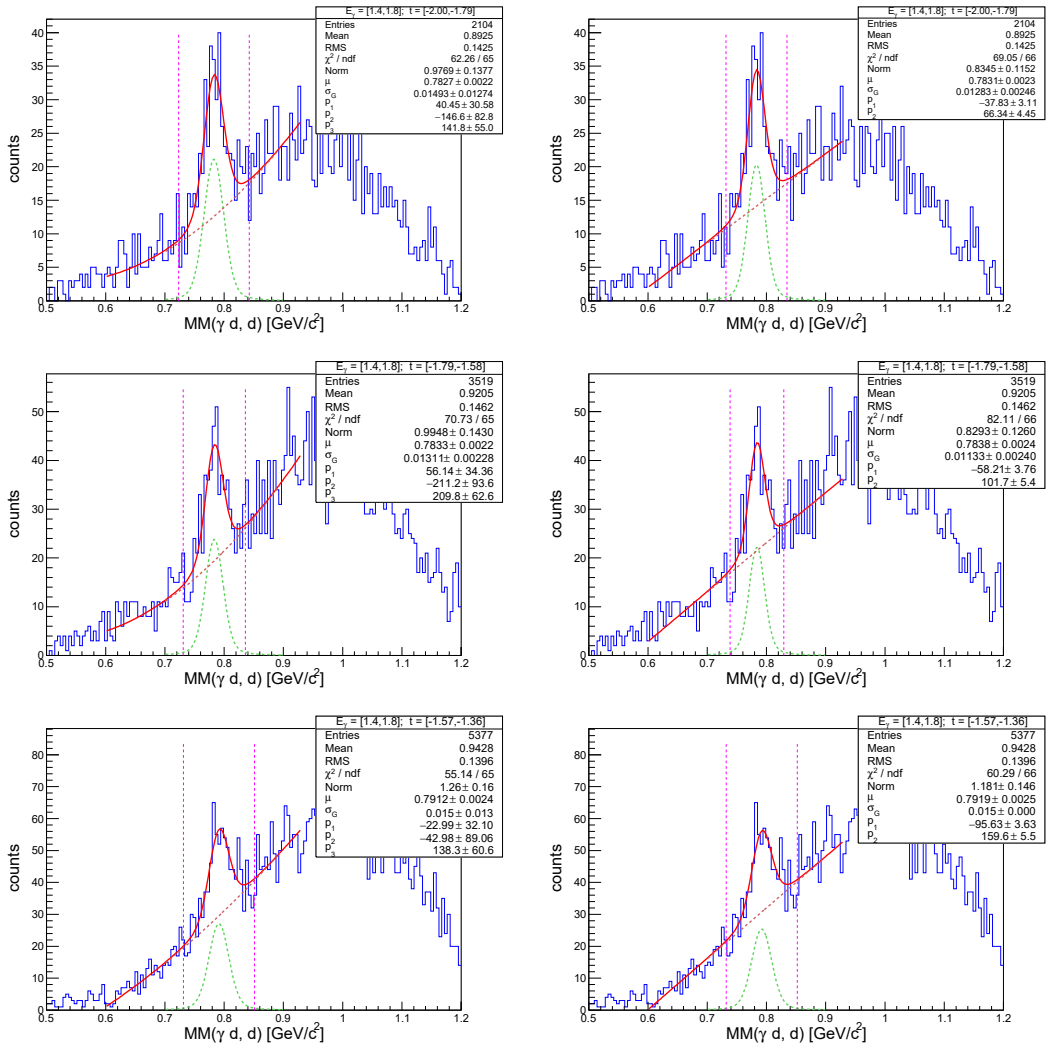

Figure F.10: Missing mass distributions for different momentum transfer bins in $E_\gamma = [1.4, 1.8]$. The signal is shown by dashed green curve. The vertical lines represent 4σ integration range with respect to the Gaussian centroid. Left plots use `pol2`, right plots show `pol1`.

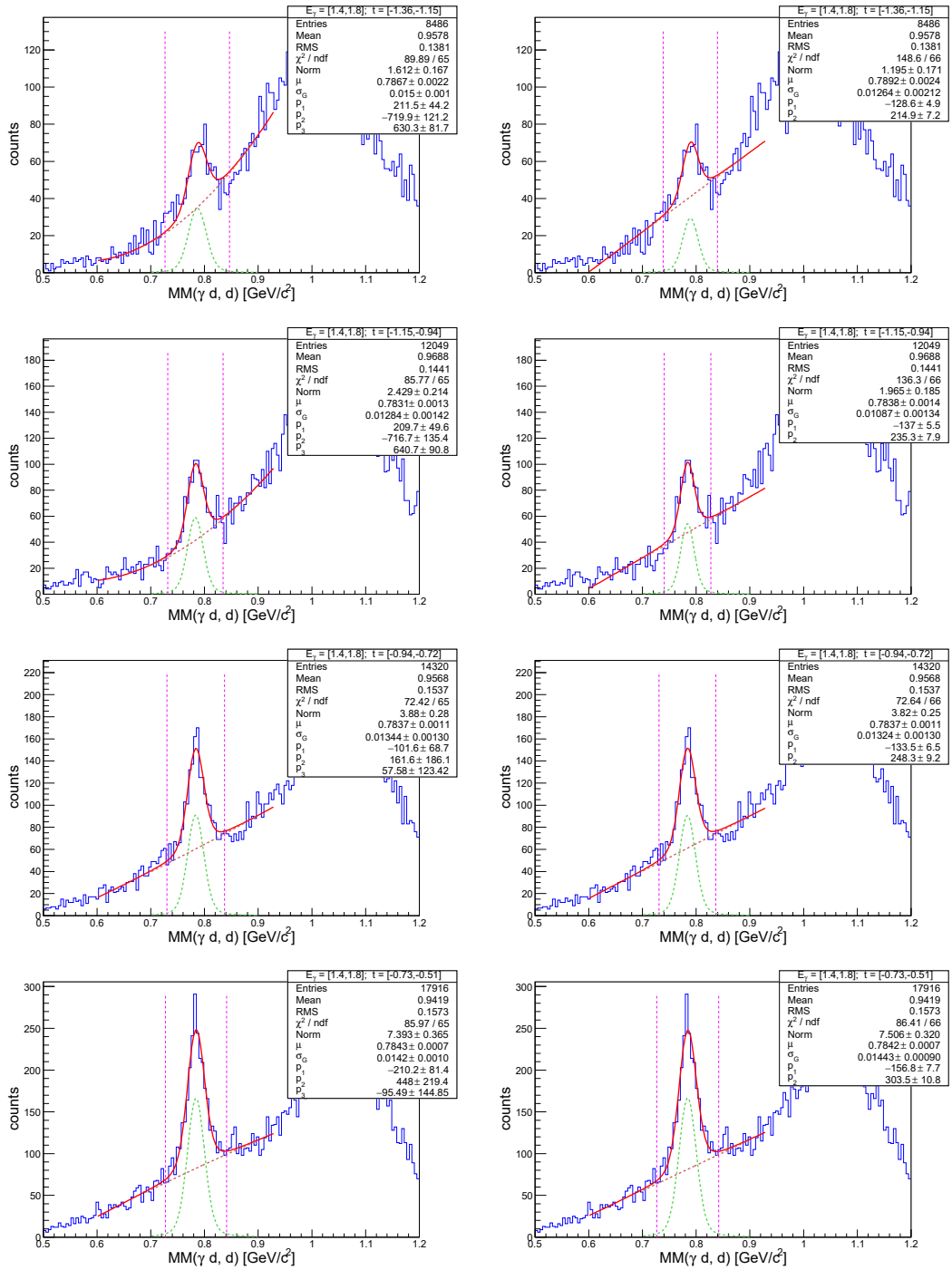

Figure F.10: Missing mass distributions for different momentum transfer bins in $E_\gamma = [1.4, 1.8]$. The signal is shown by dashed green curve. The vertical lines represent 4σ integration range with respect to the Gaussian centroid. Left plots use `pol2`, right plots show `pol1`.

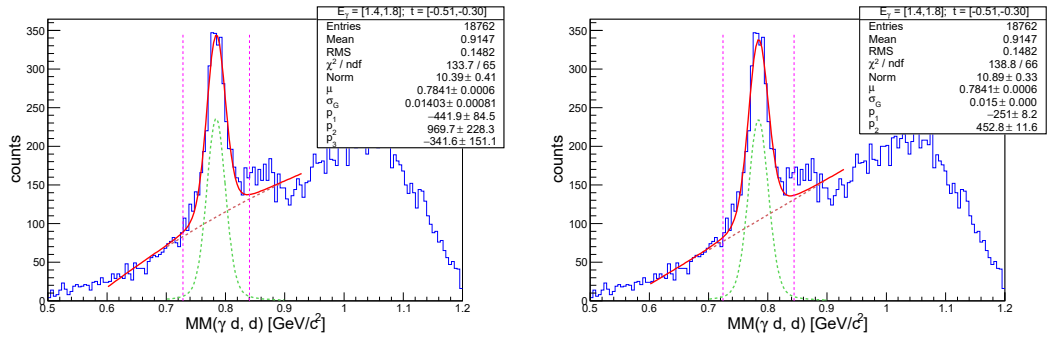

Figure F.10: Missing mass distributions for different momentum transfer bins in $E_\gamma = [1.4, 1.8]$. The signal is shown by dashed green curve. The vertical lines represent 4σ integration range with respect to the Gaussian centroid. Left plots use `pol2`, right plots show `pol1`.

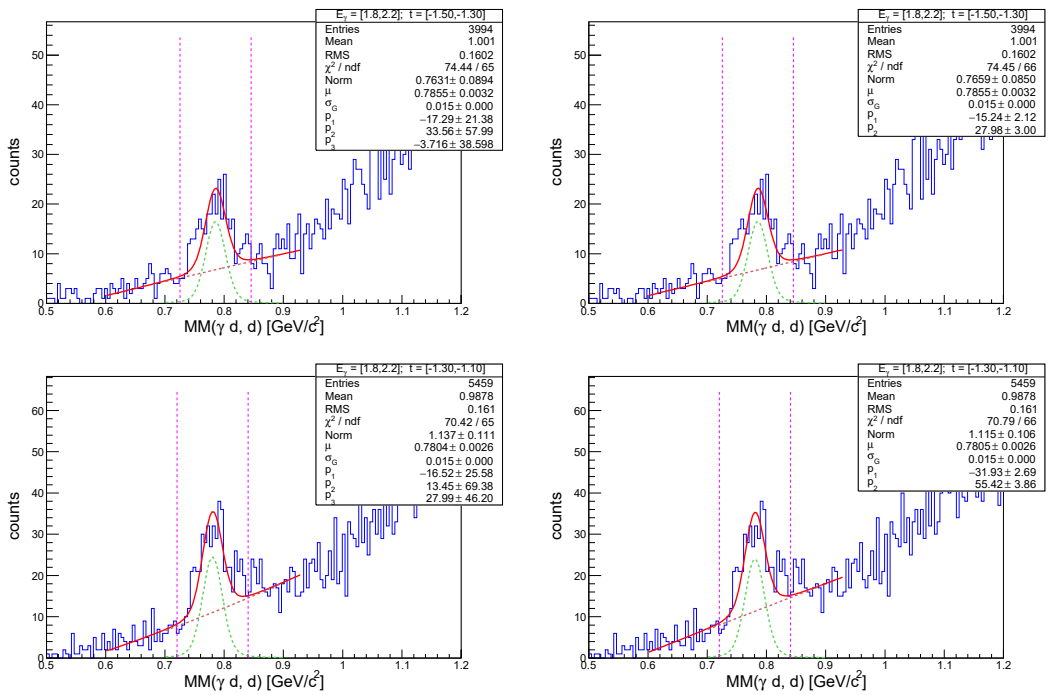

Figure F.11: Missing mass distributions for different momentum transfer bins in $E_\gamma = [1.8, 2.2]$. The signal is shown by dashed green curve. The vertical lines represent 4σ integration range with respect to the Gaussian centroid. Left plots use `pol2`, right plots show `pol1`.

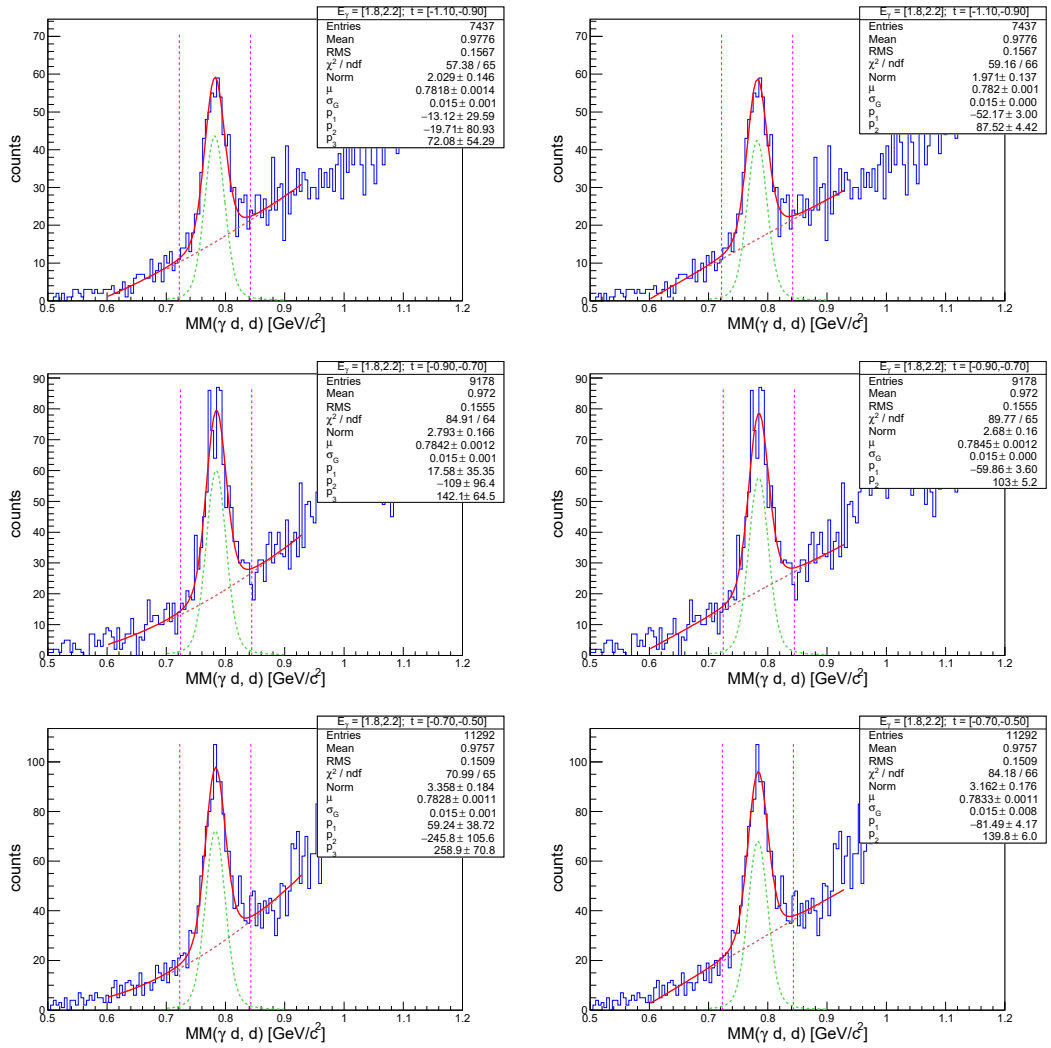

Figure F.11: Missing mass distributions for different momentum transfer bins in $E_\gamma = [1.8, 2.2]$. The signal is shown by dashed green curve. The vertical lines represent 4σ integration range with respect to the Gaussian centroid. Left plots use `pol2`, right plots show `pol1`.

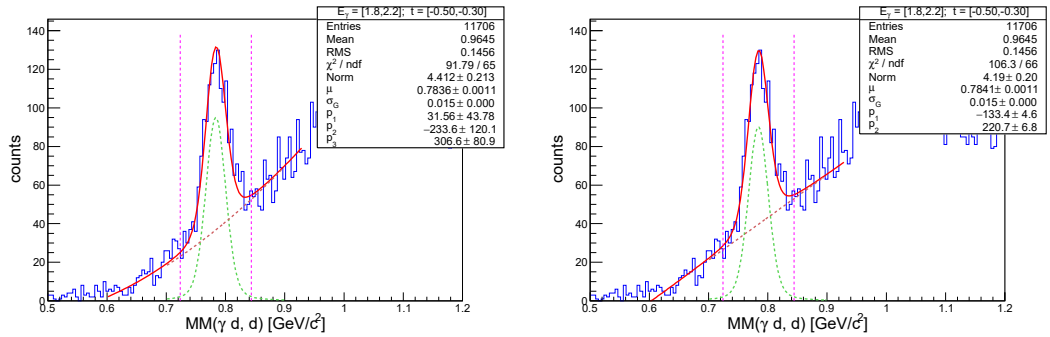

Figure F.11: Missing mass distributions for different momentum transfer bins in $E_\gamma = [1.8, 2.2]$. The signal is shown by dashed green curve. The vertical lines represent 4σ integration range with respect to the Gaussian centroid. Left plots use `pol2`, right plots show `pol1`.

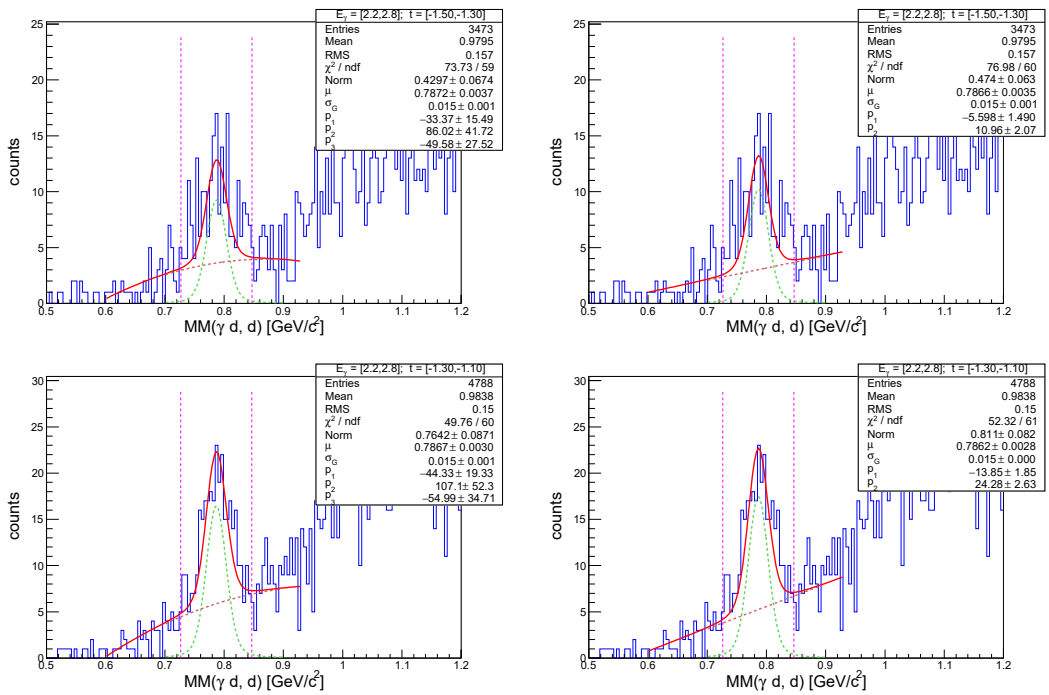

Figure F.12: Missing mass distributions for different momentum transfer bins in $E_\gamma = [2.2, 2.8]$. The signal is shown by dashed green curve. The vertical lines represent 4σ integration range with respect to the Gaussian centroid. Left plots use `pol2`, right plots show `pol1`.

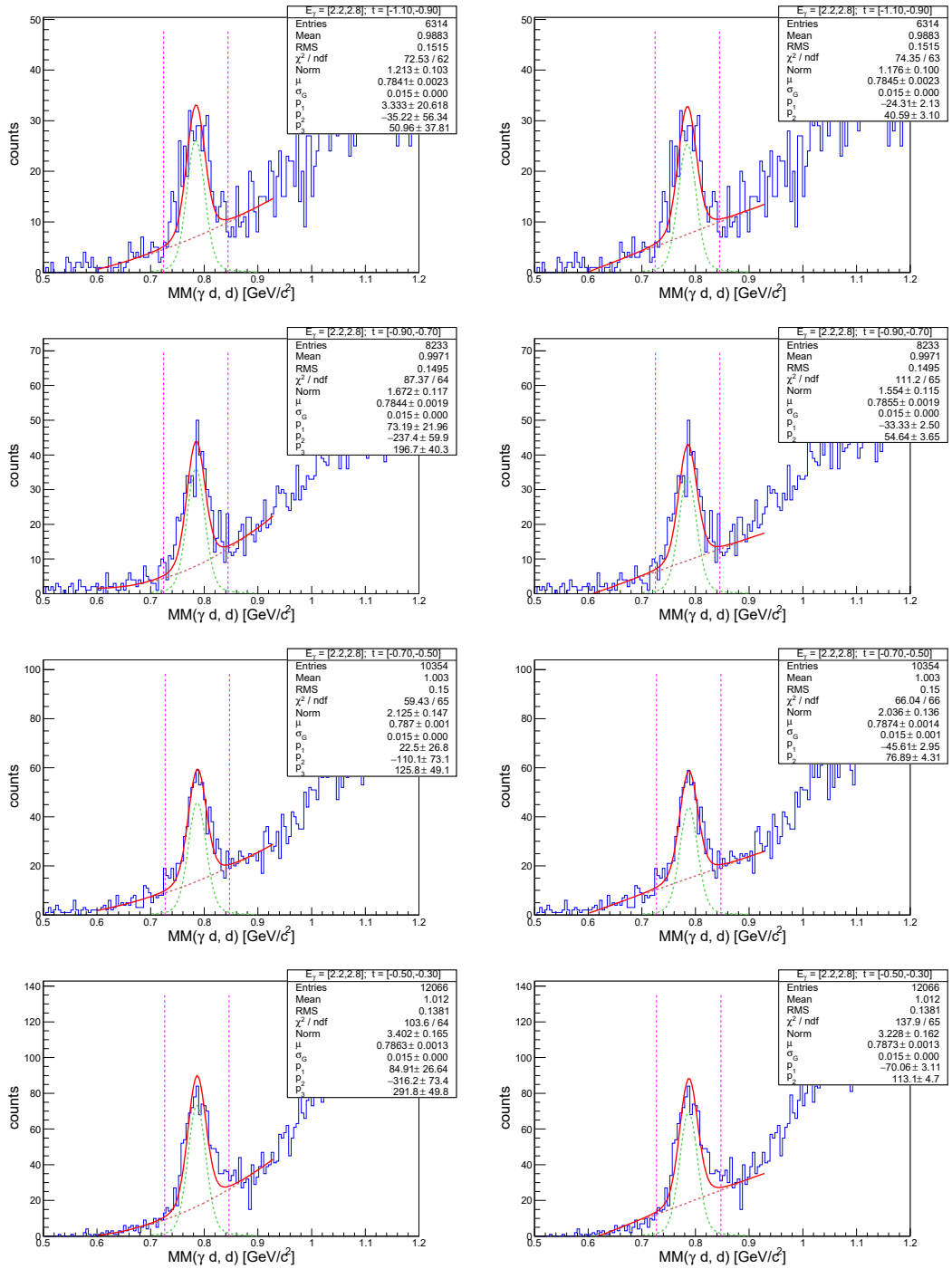

Figure F.12: Missing mass distributions for different momentum transfer bins in $E_\gamma = [2.2, 2.8]$. The signal is shown by dashed green curve. The vertical lines represent 4σ integration range with respect to the Gaussian centroid. Left plots use `pol2`, right plots show `pol1`.

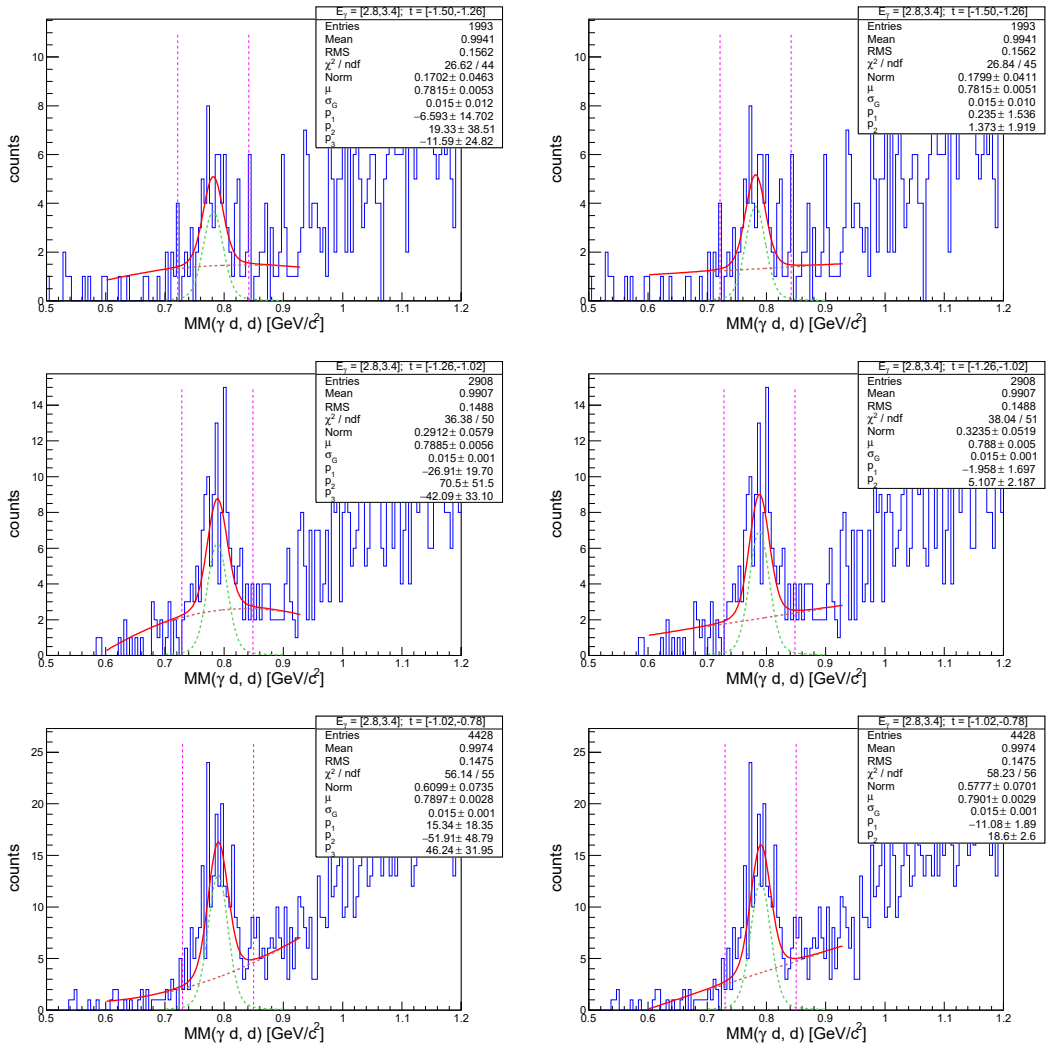

Figure F.13: Missing mass distributions for different momentum transfer bins in $E_\gamma = [2.8, 3.4]$. The signal is shown by dashed green curve. The vertical lines represent 4σ integration range with respect to the Gaussian centroid. Left plots use `pol2`, right plots show `pol1`.

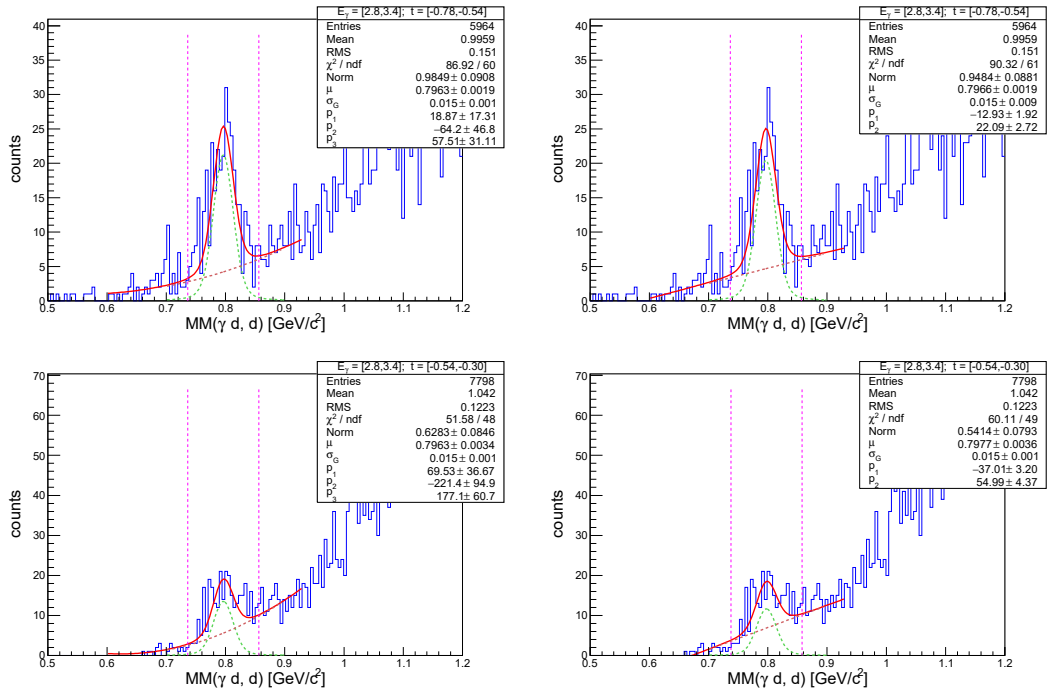

Figure F.13: Missing mass distributions for different momentum transfer bins in $E_\gamma = [2.8, 3.4]$. The signal is shown by dashed green curve. The vertical lines represent 4σ integration range with respect to the Gaussian centroid. Left plots use `pol2`, right plots show `pol1`.